frontiers | Research Topics

Digital technologies by empowered sustainable electrical energy development

Edited by
Yushuai Li, Bonan Huang, Jianhua Zhang and Yingchun Wang

Coordinated by
Tianyi Li

Published in
Frontiers in Energy Research

FRONTIERS EBOOK COPYRIGHT STATEMENT

The copyright in the text of individual articles in this ebook is the property of their respective authors or their respective institutions or funders. The copyright in graphics and images within each article may be subject to copyright of other parties. In both cases this is subject to a license granted to Frontiers.

The compilation of articles constituting this ebook is the property of Frontiers.

Each article within this ebook, and the ebook itself, are published under the most recent version of the Creative Commons CC-BY licence. The version current at the date of publication of this ebook is CC-BY 4.0. If the CC-BY licence is updated, the licence granted by Frontiers is automatically updated to the new version.

When exercising any right under the CC-BY licence, Frontiers must be attributed as the original publisher of the article or ebook, as applicable.

Authors have the responsibility of ensuring that any graphics or other materials which are the property of others may be included in the CC-BY licence, but this should be checked before relying on the CC-BY licence to reproduce those materials. Any copyright notices relating to those materials must be complied with.

Copyright and source acknowledgement notices may not be removed and must be displayed in any copy, derivative work or partial copy which includes the elements in question.

All copyright, and all rights therein, are protected by national and international copyright laws. The above represents a summary only. For further information please read Frontiers' Conditions for Website Use and Copyright Statement, and the applicable CC-BY licence.

ISSN 1664-8714
ISBN 978-2-8325-5518-7
DOI 10.3389/978-2-8325-5518-7

About Frontiers

Frontiers is more than just an open access publisher of scholarly articles: it is a pioneering approach to the world of academia, radically improving the way scholarly research is managed. The grand vision of Frontiers is a world where all people have an equal opportunity to seek, share and generate knowledge. Frontiers provides immediate and permanent online open access to all its publications, but this alone is not enough to realize our grand goals.

Frontiers journal series

The Frontiers journal series is a multi-tier and interdisciplinary set of open-access, online journals, promising a paradigm shift from the current review, selection and dissemination processes in academic publishing. All Frontiers journals are driven by researchers for researchers; therefore, they constitute a service to the scholarly community. At the same time, the *Frontiers journal series* operates on a revolutionary invention, the tiered publishing system, initially addressing specific communities of scholars, and gradually climbing up to broader public understanding, thus serving the interests of the lay society, too.

Dedication to quality

Each Frontiers article is a landmark of the highest quality, thanks to genuinely collaborative interactions between authors and review editors, who include some of the world's best academicians. Research must be certified by peers before entering a stream of knowledge that may eventually reach the public - and shape society; therefore, Frontiers only applies the most rigorous and unbiased reviews. Frontiers revolutionizes research publishing by freely delivering the most outstanding research, evaluated with no bias from both the academic and social point of view. By applying the most advanced information technologies, Frontiers is catapulting scholarly publishing into a new generation.

What are Frontiers Research Topics?

Frontiers Research Topics are very popular trademarks of the *Frontiers journals series*: they are collections of at least ten articles, all centered on a particular subject. With their unique mix of varied contributions from Original Research to Review Articles, Frontiers Research Topics unify the most influential researchers, the latest key findings and historical advances in a hot research area.

Find out more on how to host your own Frontiers Research Topic or contribute to one as an author by contacting the Frontiers editorial office: frontiersin.org/about/contact

Digital technologies by empowered sustainable electrical energy development

Topic editors
Yushuai Li — Aalborg University, Denmark
Bonan Huang — Northeastern University, China
Jianhua Zhang — Clarkson University, United States
Yingchun Wang — Northeastern University, China

Topic coordinator
Tianyi Li — Aalborg University, Denmark

Citation
Li, Y., Huang, B., Zhang, J., Wang, Y., Li, T., eds. (2024). *Digital technologies by empowered sustainable electrical energy development*.
Lausanne: Frontiers Media SA. doi: 10.3389/978-2-8325-5518-7

Table of contents

frontiers | Frontiers in Energy Research

TYPE Original Research
PUBLISHED 05 May 2023
DOI 10.3389/fenrg.2023.1194139

Check for updates

OPEN ACCESS

EDITED BY
Yushuai Li,
University of Oslo, Norway

REVIEWED BY
Yihuan Li,
North China Electric Power University, China
Peiyuan Guan,
University of Oslo, Norway
Chenhui Song,
Changsha University of Science and Technology, China

*CORRESPONDENCE
Shaokun Zou,
zoukun@sungrowpower.com

RECEIVED 26 March 2023
ACCEPTED 17 April 2023
PUBLISHED 05 May 2023

CITATION
Zou S, Zhang N and Wei B (2023), A capacity optimization and scheduling scheme of a multi-energy complementary power station considering energy trading.
Front. Energy Res. 11:1194139.
doi: 10.3389/fenrg.2023.1194139

COPYRIGHT
© 2023 Zou, Zhang and Wei. This is an open-access article distributed under the terms of the Creative Commons Attribution License (CC BY). The use, distribution or reproduction in other forums is permitted, provided the original author(s) and the copyright owner(s) are credited and that the original publication in this journal is cited, in accordance with accepted academic practice. No use, distribution or reproduction is permitted which does not comply with these terms.

A capacity optimization and scheduling scheme of a multi-energy complementary power station considering energy trading

Shaokun Zou[1]*, Ning Zhang[2] and Baoze Wei[3]

[1]Sungrow Renewables Development Co., Ltd., Hefei, China, [2]School of Electrical Engineering and Automation, Anhui University, Hefei, China, [3]Department of Energy Technology, Aalborg University, Aalborg, Denmark

Digital technology is rapidly advancing, and the resulting digitization of energy is becoming an inevitable trend. Integrating digital technology with energy planning can enable efficient utilization of renewable energy (RE); the fluctuation of RE generation, such as wind and photovoltaic (PV), can be reduced, and the reliability of the power grid can be ensured. A better solution for RE utilization and planning based on digital technology is proposed in this paper. First, an operation mechanism of a multi-energy complementary power station is proposed based on the complementary characteristics of multiple energy sources in the power generation process. The current status and related issues of multi-energy complementary power stations are studied in this paper. Second, a two-layer model of optimization that integrates the complementary features of multiple energy sources and system planning requirements is developed in this paper based on the aforementioned power station operation mechanism. The two layers of the model are nested with each other to realize the operation of the power station. The upper model includes the RE utilization rate and the benefits of the energy storage (ES) system. The lower model includes the operating cost of the power station. The solution model includes the highest utilization rate of RE and the lowest operation cost. Finally, the simulation operation is performed based on the data on a provincial power grid. The model and operation strategy of the multi-energy complementary power station based on digital technology proposed by this paper are verified.

KEYWORDS

digital technology, multi-energy complementary, optimization planning, renewable energy, energy trading, energy storage system

1 Introduction

The green and low-carbon economy has received considerable global attention as a result of resource and environmental limitations. Numerous countries are presently investigating strategies to attain a low-carbon economy by confronting these challenges (Li et al., 2021; Li et al., 2022; Zhang et al., 2022). RE plays a critical role in realizing this goal. Nevertheless, the inherently unpredictable characteristics of wind and PV power generation may lead to substantial resource wastage (Joseph and Balachandra, 2020). Digital technologies are being used effectively to accurately model and optimize various processes (Li et al., 2020; Song

et al., 2021; Yang et al., 2023). Thus, to enhance the utilization of RE resources and encourage efficient energy consumption, establishing a coordination mechanism for multi-energy complementation through digital technologies is imperative.

Due to its cost-saving and environmentally friendly advantages, RE is positioned to become the primary power source in the future. However, in order to achieve low-carbon development, the fluctuation of RE output must be addressed (Li et al., 2019; Olsen et al., 2019; Sanjari et al., 2020). To this end, the adoption of multi-energy complementarity represents a crucial step forward in promoting energy modernization and the creation of a green and efficient energy system (Tan and Novosel, 2017; Li et al., 2020; Auguadra et al., 2023). The field of research related to RE is currently in a phase of rapid development. However, several issues need to be addressed in order to optimize the planning, construction, scheduling, operational technology, and institutional mechanisms. These issues can be broadly categorized as follows: first, there is a need to determine the optimal combination of wind, PV, hydro, and thermal storage to achieve the best operating results. Second, reducing energy waste and improving the utilization of RE are critical challenges that require further research. Third, the instability of RE sources, such as wind and PV, due to weather fluctuations during power generation, can lead to reduced power generation efficiency. Strategies for mitigating this instability and replacing the output of conventional power stations with RE to minimize costs must be developed. Fourth, determining the appropriate pricing mechanism for electricity generated from RE sources remains a key issue that needs to be addressed.

At present, scholars have studied the multi-energy complementary coordination mechanism. An optimal operation strategy for an independent regional grid based on the synergistic operation of wind–PV–water-storage during the dry period is proposed, as seen in Liu et al. (2019). This strategy mitigates the impact of seasonal and daily fluctuations in RE output on power supply reliability while also avoiding the risk of decreased hydroelectric generation during dry periods due to water shortages. In the paper by shafiei and Ghasemi-Marzbali (2023), a fast-charging station model is developed by integrating RE and ES systems. The uncertainty of RE is reduced, and the profitability of the charging station is improved. A grid-interactive microgrid based on a DC–DC multi-source converter configuration consisting of PV, wind, and hybrid ES is proposed in an article by Ravada et al. (2021). It can effectively reduce the fluctuations in generation caused by wind and PV. A coordinated optimization model for a hybrid water–wind–solar system based on the uncertainty of scenic power generation is proposed by Wei et al. (2019). The proposed operation strategy can improve the efficiency of RE utilization and reduce environmental pollution at the same time. An agent-based transactive energy trading platform is proposed in the article by Nunna et al. (2020) to integrate ES systems into the energy management system of a microgrid. The proposed model can effectively improve the system's revenue. In the paper by Sun et al. (2017), a scenario-based stochastic model is proposed for dispatching a power system that integrates battery-based ES and transportation. The model aims to minimize the operating cost of the power system by reducing the amount of wind and electricity that is abandoned. An interconnected power system water–thermal–wind–PV complementary operation model is proposed by Wang et al. (2018). This model couples the complementary features of multi-energy and multi-area operations to optimize the utilization of RE sources and minimize carbon emissions. Additionally, this model mitigates the issue of abandonment in multi-energy and multi-regional power systems. A collaborative energy management strategy based on on-the-fly prediction is proposed in an article by Bazmohammadi et al. (2019). The proposed strategy solves the coupling constraint problem. It achieves multi-energy complementarity and improves energy utilization. A multi-energy supply geothermal–solar–wind RE hub framework was established by Xu et al. (2022). This framework maximizes the complementary features of the geothermal–PV–wind hybrid RE system, resulting in improved economic performance. A scheduling strategy structure that considers the stochastic characteristics caused by wind power and PV is proposed in the paper by Dong et al. (2020). A coordinated dispatching model with optimization objectives and profit maximization is developed in this paper. The proposed scheduling strategy can effectively improve the system's revenue. In the paper by Oskouei et al. (2021), a unified decision structure consisting of network partitioning and optimal operational planning problems is proposed. The structure determines the optimal allocation of wind, PV, and ES systems. The RE utilization is increased, and the abandonment rate is reduced. A techno–economic–environmental energy dispatch framework for a multi-energy microgrid system is presented in an article by Karimi et al. (2023). The model improves the flexibility and reliability of the microgrid system. It also optimizes the operational cost, carbon emission, groundwater extraction, and independence of the multi-energy system. The independence of the multi-energy microgrid system is improved.

In this paper, a planning model is developed to facilitate the integration of multiple energy sources, specifically wind, PV, hydro, thermal, and storage. The proposed model encompasses the storage of electricity during periods of low RE generation, which can be utilized during peak periods for the regulation of peak loads. Moreover, surplus power generated during low-energy periods can be exchanged with the power grid. In situations where the energy supply is insufficient, power can be procured from suppliers by comparing prices to select the most viable option. The implementation of this planning model for multi-energy complementarity power stations is anticipated to enhance the utilization of RE, lower operational costs, and advance low-carbon development.

Its contributions can be briefly expressed as follows:

1. A power station operation mechanism that takes into account wind, PV, water, thermal, and ES is proposed by considering the coupling relationship between several different energy sources. Digital techniques are utilized to optimize the economic performance of the multi-energy complementary power station and to maximize the profitability of the station.
2. In this paper, a multi-energy complementary power station model is developed that takes into account the operating costs of the station, the revenue of the ES system, and the utilization of RE. The model is segmented into two parts: upper and lower. Different optimization algorithms are used to solve the model separately.
3. A power station planning model based on digital technology proposed in this paper reduces the waste of resources and supports the development of RE. At the same time, it solves the problem of low utilization of RE, which is in line with the green and low-carbon development goal.

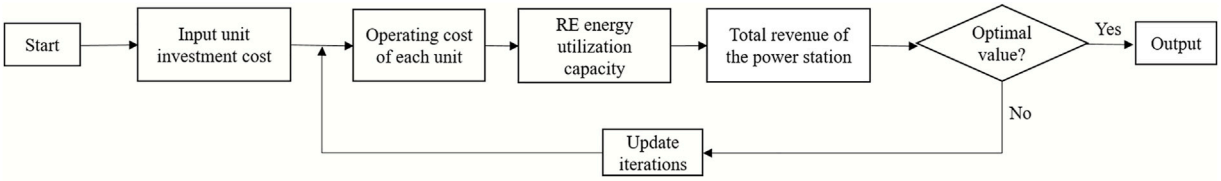

FIGURE 1
Planning flow chart.

The remaining sections can be summarized as follows: in Section 2, the master planning model of the multi-energy complementary power station is presented, and an objective function is established to maximize the power station's benefits at minimum cost. Section 3 discusses the simulation results and validates the model's feasibility. The paper concludes with the main findings in Section 4.

2 Materials and methods

2.1 Planning flow chart

The power station planning process is shown in Figure 1. The operation strategy that enables the power station to be economically optimal can be obtained by following the planning steps in Figure 1. The planning process is as follows: first, the operating cost of each unit is calculated by inputting the cost of each unit. Next, the RE utilization capacity is calculated, and finally, the sum return of the power station is calculated. If the calculated value is optimal, it is outputted. Otherwise, the process iteratively updates the particle until the optimal value is obtained.

2.2 Objective function

The objective function of the multi-energy complementary power station is established as follows:

$$C = \max\left(C_{yx} - K - F - A - B - D\right). \tag{1}$$

The objective function C represents the relationship between the total revenue of the power station and the cost of each unit. The objective function is established by maximizing the total revenue of the power station and minimizing the cost of each unit (Li et al., 2021).

2.2.1 ES system operating benefit and cost model C_{yx}

2.2.1.1 ES system operating income model

The primary source of revenue for ES systems is to store electricity during peak usage periods and sell it to the power grid, earning the price differential.

$$C_{sy} = \sum_{t=1}^{T}\left(\eta_f P_{price,sell} P_{St}^{f} - \eta_c P_{price,buy} P_{St}^{c}\right) \tag{2}$$

The formula for calculating the revenue generated by the ES system during operation is given in Eq. 2. Since the ES system cannot both charge and discharge at the same time, one of P_{St}^{f} and P_{St}^{c} must be 0 in Eq. 2, which is given in the constraints section of the paper.

2.2.1.2 ES system operating cost model

The operating cost of an ES system consists of three components, which are investment cost, operation and maintenance (O&M) cost, and kWh cost.

$$C_{cb} = C_{In} + C_{OM} + C_{ESS}, \tag{3}$$

$$C_{In} = C(r,n)\left(C_P C_{ESS} + C_E E_{ESS}\right), \tag{4}$$

$$C(r,n) = \frac{r(1+r)^n}{(1+r)^n - 1}, \tag{5}$$

$$C_{OM} = \lambda_O P_{ESS} + \lambda_M Q_{ESS}. \tag{6}$$

If it is not possible to determine, the aforementioned cost factors are generally approximated by a percentage of the initial investment to calculate the O&M costs, that is,

$$C_{OM} = \mu C_{In}, \tag{7}$$

$$C_{ESS} = \frac{C_{In} + C_{OM}}{Q_{ESS}}, \tag{8}$$

$$Q_{ESS} = \eta_{ESS} P_{ESS} H_{ESS}. \tag{9}$$

The formula for calculating the annual power generation of the ES system is given in Eq. 9, and the annual power generation is calculated by the conversion efficiency of the ES station and the annual utilization hours of the electricity storage of the ES station.

Therefore, the model with the greatest operating benefits of the ES system is

$$C_{yx} = C_{sy} - C_{cb}. \tag{10}$$

The relationship between the benefits and costs of the ES system is given in Eq. 10 as total benefits equal to operating benefits minus costs.

2.2.2 Thermal power unit cost F

2.2.2.1 O&M costs f_1

$$f_d = P_{zj} \frac{\sum_{i=1}^{365} E_i r(1+r)^M}{T_y k (1+r)^M - 1}. \tag{11}$$

The formula for calculating the average annual cost is given in Eq. 11. The equivalent annual value of the cost of a thermal power station can be calculated by Eq. 11.

$$f_1 = \lambda_1 f_d, \tag{12}$$

where λ_1 is the O&M coefficient.

The relationship between O&M costs and investment costs of thermal power units is represented by Eq. 12.

2.2.2.2 Fuel costs f_2

$$f_2 = \sum_{i=1}^{365} E_i W_{fuel} P_{fuel}. \tag{13}$$

The formula for calculating the cost of fuel consumed by thermal power units during peaking is given in Eq. 13.

To sum up, the charge for the thermal power turbine is

$$F = f_1 + f_2. \tag{14}$$

2.2.3 Wind turbine cost A

$$A = \lambda_2 A_{IN}, \tag{15}$$

where λ_2 is the O&M factor of the wind turbines.

2.2.4 Hydropower unit cost B

$$B = \lambda_3 B_{IN}, \tag{16}$$

where λ_3 is the O&M coefficient of the hydropower unit.

2.2.5 Cost of PV unit D

$$D = \lambda_4 D_{IN}, \tag{17}$$

where λ_4 is the O&M coefficient of the PV unit.

2.2.6 RE utilization capacity K

The ability to consume RE resources is expressed by the abandoned wind, PV, and water. The less wind, PV, and water are discarded, the higher the ability to consume RE resources in the system, and the opposite is lower.

$$K = \sum_{t=1}^{T}\sum_{w=1}^{N_w}\left(x_w P_{q,w,t}^{wind}\Delta t\right) + \sum_{t=1}^{T}\sum_{g=1}^{N_g}\left(x_g P_{q,g,t}^{PV}\Delta t\right) + \sum_{t=1}^{T}\sum_{s=1}^{N_s}\left(x_s P_{q,s,t}^{hydro}\Delta t\right), \tag{18}$$

where Δt is the duration of the time section.

K denotes the penalty price for wasting RE. When more electricity is abandoned, the larger K is, and the lower the utilization rate of RE will be. When the abandoned electricity is less, the smaller K means a higher utilization rate of RE. Therefore, in the planning process, the smaller the K, the better, that is, the smaller the abandoned power, the higher the energy utilization.

2.3 Binding conditions

2.3.1 Power balance constraint

$$\sum_{i=1}^{\Omega} P_{i,t} + \sum_{w=1}^{N_w} P_{w,t}^{wind} + \sum_{s=1}^{N_s} P_{s,t}^{hydro} + \sum_{g=1}^{Ng} P_{g,t}^{PV} + P_{St}^{f} = P_t^{load} + P_{St}^{c}. \tag{19}$$

The whole system needs to satisfy the law of energy conservation. The power balance equation is given by Eq. 19, where the power generated by each unit at moment t is equal to the load power, which is also equivalent to the load when the ES system is charged and to the generator set when it is discharged (Yang et al., 2022).

2.3.2 Thermal power output constraints

$$P_{t,\min} \le P_{i,t} \le P_{t,\max}, \tag{20}$$

where $P_{t,\min}$ is the minimum power output of the thermal turbine at time t. $P_{t,\max}$ is the thermal turbine's maximum electrical output at time t.

2.3.3 Wind turbine output constraint

$$0 \le P_{w,t}^{wind} \le P_{w,t,\max}^{wind}, \tag{21}$$

where $P_{w,t,\max}^{wind}$ is the wind turbine's max output power at time t.

2.3.4 Hydroelectric turbine output constraint

$$0 \le P_{s,t}^{hydro} \le P_{s,t,\max}^{hydro}, \tag{22}$$

where $P_{s,t,\max}^{hydro}$ is the hydroelectric turbine's max output power at moment t.

2.3.5 PV turbine output constraint

$$0 \le P_{g,t}^{PV} \le P_{g,t,\max}^{PV}, \tag{23}$$

where $P_{g,t,\max}^{PV}$ is the PV turbine's max output power at moment t.

2.3.6 ES constraints

2.3.6.1 Charge state constraints

$$\begin{cases} S_t = S_{t-1} + \dfrac{\eta_c P_{St}^{c}}{P_{ESS}}\Delta t - \dfrac{P_{St}^{f}}{\eta_f P_{ESS}}\Delta t, \\ S_{\min} \le S_t \le S_{\max}. \end{cases} \tag{24}$$

Since the ES capacity of the ES system cannot be zero, the maximum and minimum ES capacities at moment t are limited, as shown in Eq. 24. The ES capacity at moment t increases as the ES system is charged and decreases as the ES system is discharged. When the RE output is enough to meet the load, the ES system charges to store the excess electricity and the electricity can be sold when the storage is not enough. When the RE output is not enough

TABLE 1 Main economic parameters of various types of power sources in a multi-energy complementary power station.

Power supply type	Stand-alone capacity/MW	Unit investment cost/ (Yuan·kW^{-1})	Annual fixed O&M costs/ (Yuan·kW^{-1})	Operating life/ year
PV	0.5	8,000	96	25
Wind power	2	7,000	195	20
Hydropower	125	11,450	240	50
ES	200	6,000	80	30
Thermal	300	5,000	105	15

to meet the load, the ES system discharges, and if it is not enough, the electricity needs to be purchased.

2.3.6.2 Charge and discharge power constraints

$$\begin{cases} 0 \le P_{St}^{f} \le P_{St,\max}^{f}, \\ 0 \le P_{St}^{c} \le P_{St,\max}^{c}, \\ P_{St}^{f} \cdot P_{St}^{c} = 0. \end{cases} \tag{25}$$

The charging and discharging power of the ES system is limited and cannot be infinitely charged or discharged, so some constraints should be added, as shown in Eq. 25.

2.3.6.3 Electricity price constraint

In a multi-party bidding situation, when the power grid tariff is higher than the tariff of other power companies, the option is to sell the excess power to the power grid.

$$\begin{cases} 0 < \min P_{others}^{sell} < P_{price,sell}, \\ 0 < P_{price,buy} < \min P_{others}^{buy}. \end{cases} \tag{26}$$

The bidding relationship between the grid and the power supply company is represented by Eq. 26. The power station always selects the party with the most favorable price. If the price of buying electricity from the grid is higher than the price of the other power supply companies, it chooses to buy electricity from the other companies. It chooses to sell power to the grid if the price of buying power from the grid is higher than the price of the other supply companies.

3 Results

This paper analyses a modified example of an actual system at a provincial level in China. The planning of multi-energy complementary power stations in the next 5 years is studied in this paper based on the current established commissioning plan situation of the province. The main economic parameters of each type of power source in the built multi-energy complementary power stations are indicated in Table 1. In Table 1, it can be seen that, for the time being, relatively few RE sources, such as wind turbines and PV units, have been put into operation because their power generation is unstable, and therefore, the utilization of RE sources is currently limited.

3.1 Parameter setting

The overview diagram of the power plant operation scenario is shown in Figure 2. A multi-energy complementary power station consists of wind turbines, photovoltaic units, hydroelectric units, thermal units, and energy storage systems. The power station supplies power to the load, and excess power can be stored until the power supply is low and the energy storage is discharged. The power balance can also be maintained by trading power with the power supplier to gain benefits.

The main economic parameters of the units selected for wind, PV, water, thermal power, and ES systems are illustrated in Table 1. During the simulation process, the selected units' economic parameters should be characterized by moderate cost and long service life. Due to the advantages of large installed capacity, high stability, long continuous discharge time, and wide regulation range, ES systems choose pumped storage. By using pumped storage power stations, the electricity system's stability can be effectively improved and the utilization of its RE capacity can be enhanced.

Figure 3 shows the wind, PV, and hydropower output curves for a typical day in spring.

In Figure 3, it can be seen that PV turbines mainly work from 12: 00 to 14:00 and their output power peaks at 13:00. Hydropower units mainly work from 22:00 to 10:00 of the following day, and the output power peaks at 9:00. The wind turbines mainly work from 9:00 to 12: 00, and the output power peaks at 15:00.

Figure 4 shows the wind, PV, and hydropower output curves for a typical day in summer.

In Figure 4, it can be seen that PV turbines mainly work from 6: 00 to 18:00 and their output power peaks at 12:00. Hydropower units mainly work from 19:00 to 10:00 of the following day, and the output power peaks at 23:00. The wind turbines mainly work from 10:00 to 24:00, and the output power peaks at 13:00.

Figure 5 shows the wind, PV, and hydropower output curves for a typical day in autumn.

In Figure 5, it can be seen that PV turbines mainly work from 6: 00 to 18:00, and their output power peaks at 12:00. Hydropower units mainly work from 19:00 to 14:00 of the following day, and the output power peaks at 20:00. The wind turbines mainly work from 8: 00 to 24:00, and the output power peaks at 10:00 and 23:00.

Figure 6 shows the wind, PV, and hydropower output curves for a typical day in winter.

In Figure 6, it can be seen that PV turbines mainly work from 10: 00 to 16:00, and their output power peaks at 13:00. Hydropower

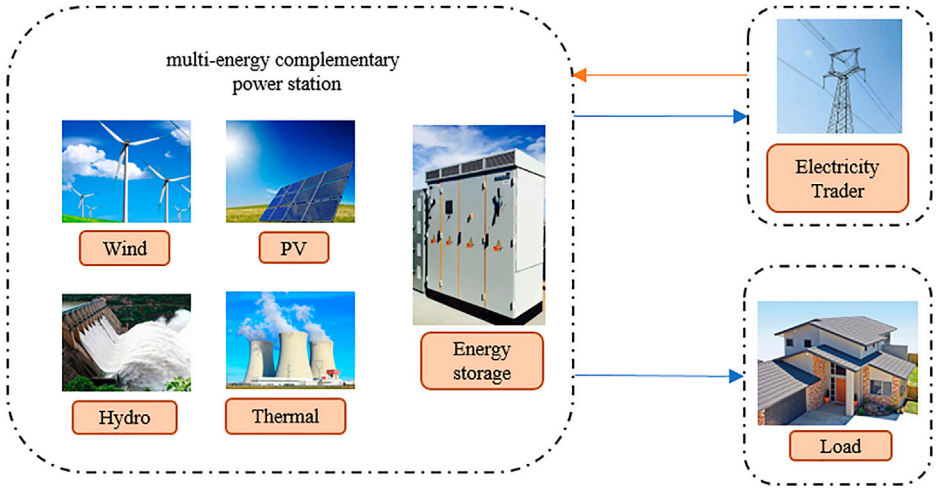

FIGURE 2
Overview diagram of the power plant operation scenario.

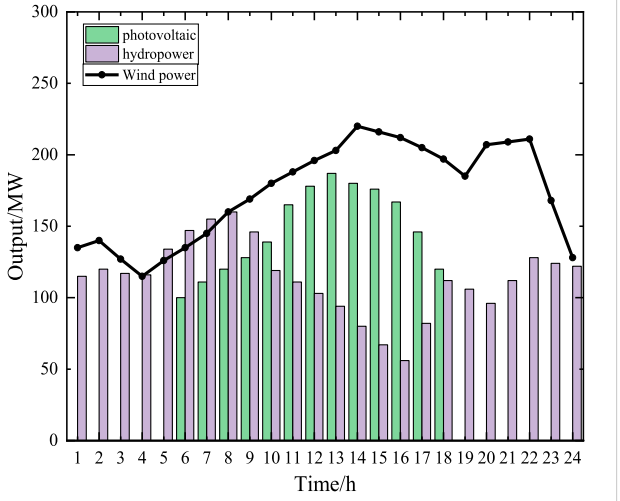

FIGURE 3
Daily output curve in spring.

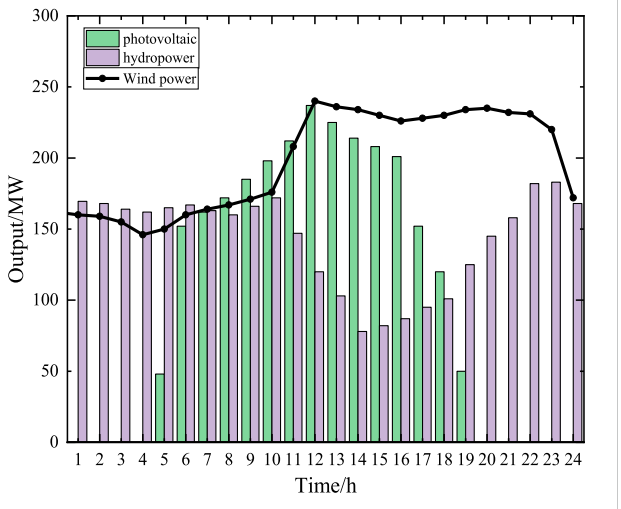

FIGURE 4
Daily output curve in summer.

units mainly work from 18:00 to 24:00, and the output power peaks at 20:00. The wind turbines mainly work from 9:00 to 24:00, and the output power peaks at 24:00.

As the typical day is highly representative, the criterion for selecting the typical day for all seasons is based on the day with the highest daily load. The RE output data for this typical day are then used as input data to more accurately reflect the operation of the power station.

By comparing the output curves for a typical day in spring, summer, autumn, and winter, it can be seen that the complementary situation of the three renewable resources is obvious and that the fluctuations in power generation can be reduced by making full use of the complementary t characteristics of the energy sources. This also illustrates again the indeterminate of RE and the necessity of establishing multi-energy complementary power stations. Therefore, the reasonable coordination of several energy sources can improve the utilization of RE and reduce the waste of resources.

3.2 The results by projection analysis

Based on the original data on the province, the planning results can be obtained, and the added installed capacity of various electricity sources in the province is shown in Table 2. It can be found that wind power and PV have been put into operation every year during the planning period, and the capacity has been

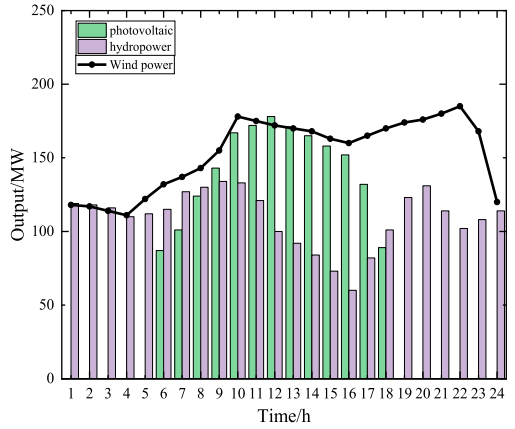

FIGURE 5
Daily output curve in autumn.

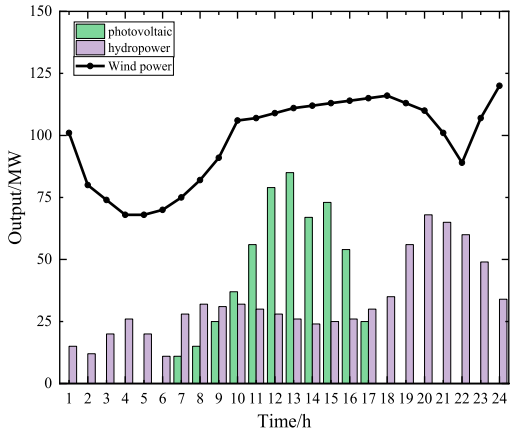

FIGURE 6
Daily output curve in winter.

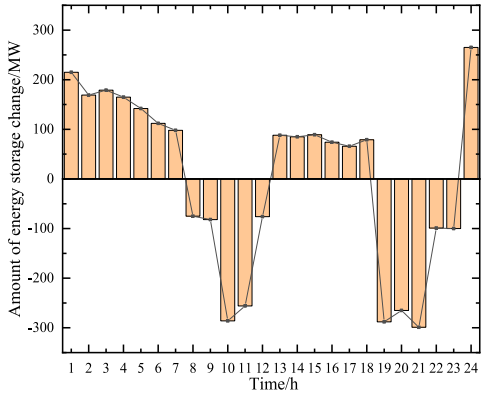

FIGURE 7
ES operation results in summer.

increasing year by year, which also shows that the development prospect of renewable resources is good and applicable. Thermal power is mainly used to take the basic load and part of the peak load of the system and has a relatively stable installed capacity during the planning period. Due to the influence of the construction period, independent hydropower units are not put into operation in the first 3 years of the planning period, while 490 MW and 1530 MW are put into operation in years 4 and 5, respectively. As shown in Table 2, ES units were commissioned according to the original plan of the province, and 800MW and 280 MW were commissioned in years 3 and 4 of the planning period, which were separate. The ES units were not put into operation in the fifth year. This is due to the optimization of the operating economy of the power station, which had already been optimized to the maximum in the third and fourth years, and further input is not conducive to the operation of the power station. Therefore, ES units are only put into operation in years 3 and 4.

From the aforementioned details, we can see that in the next 5 years, thermal power, wind power, and PV will become the leading power generation methods of the system, while the share of wind and PV power connected to the grid is expected to increase annually. The reason is that the incorporation of ES fully utilizes the complementary nature of various energy sources, improves the use of RE, and reduces the waste of renewable resources, which is an extremely important step in achieving low-carbon development in countries around the world.

Taking the fifth year as an example, the discharge curves of the typical days of ES in summer and winter are shown in Figures 7, 8. It can be observed that the peak discharge periods of ES in summer are mainly from 8:00 to 13:00 and 19:00 to 23:00, and the peak discharge periods of ES in winter are mainly from 10:00 to 11:00 and 19:00 to 23:00. The price of electricity is higher than usual during these periods, and the power station can sell electricity during these periods to generate increased revenue. Therefore, it is possible to

TABLE 2 New production capacity of various power supplies during the planning period.

Year	Wind Power/MW	PV/MW	Hydropower/MW	Thermal power/MW	ES/MW
First year	1,431	1,012	0	2,607	0
Second year	2075	1,398	0	3,911	0
Third year	4,011	1879	0	3,923	800
Fourth year	3,169	2011	490	4,915	280
Fifth year	4,156	2,654	1,530	5,809	0

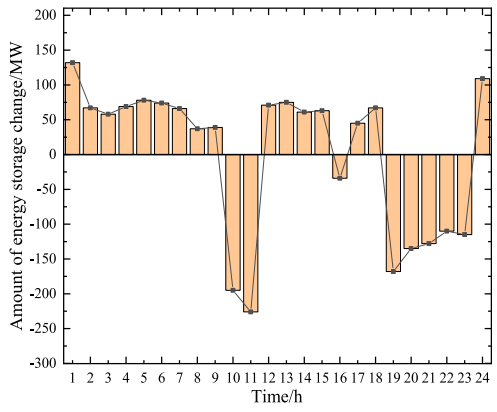

FIGURE 8
ES operation results in winter.

get a clear picture of the operating revenue of the whole power station through the hourly operation of the ES system during a typical day.

4 Discussion

On the premise of promoting low-carbon development and improving the utilization of RE, a planning model is established in this article based on the characteristics of energy complementarity. The model takes full advantage of the complementarity of energy sources. Furthermore, the capacity changes of various types of installed energy devices in different time periods are analyzed, while the flexibility of the system is improved. By simulating the model, it is clear from the simulation results in Section 3 that in the next 5 years, energy complementarity will be fully utilized due to the access to the multi-energy complementary power station, and the use of renewable resources for power generation will increase.

The model of a multi-energy complementary power station based on digital technology developed in this study can improve the capacity of RE consumption. In contrast to existing models, the model in this study is more comprehensive in consideration. With a large number of RE sources connected to the grid, using the complementary relationship between energy sources to improve energy utilization has practical implications for reducing environmental pollution and for the electricity market.

Data availability statement

The original contributions presented in the study are included in the article/Supplementary Material; further inquiries can be directed to the corresponding author.

Author contributions

SZ: responsible for research direction establishment, methodology design, writing—original draft preparation, and project administration. NZ: writing—original draft preparation, software, implementation of specific algorithms, investigation, and analysis of results. BW: data curation, analysis of results, visualization, validation, and writing—reviewing and editing.

Funding

The paper is supported by the National Natural Science Foundation of China (Project No. 62203004).

Conflict of interest

SZ was employed by Sungrow Renewables Development Co., Ltd.

The remaining authors declare that the research was conducted in the absence of any commercial or financial relationships that could be construed as a potential conflict of interest.

Publisher's note

All claims expressed in this article are solely those of the authors and do not necessarily represent those of their affiliated organizations, or those of the publisher, the editors, and the reviewers. Any product that may be evaluated in this article, or claim that may be made by its manufacturer, is not guaranteed or endorsed by the publisher.

References

Auguadra, M., Ribó-Pérez, D., and Gómez-Navarro, T. (2023). Planning the deployment of energy storage systems to integrate high shares of renewables: The Spain case study. *Energy* 264, 126275. doi:10.1016/j.energy.2022.126275

Bazmohammadi, N., Tahsiri, A., Anvari-Moghaddam, A., and Guerrero, J. M. (2019). Stochastic predictive control of multi-microgrid systems. *IEEE Trans. Industry Appl.* 55 (5), 5311–5319. doi:10.1109/TIA.2019.2918051

Dong, H., Li, S., Dong, H., Tian, Z., and Hillmansen, S. (2020). Coordinated scheduling strategy for distributed generation considering uncertainties in smart grids. *IEEE Access* 8, 86171–86179. doi:10.1109/ACCESS.2020.2992342

Joseph, A., and Balachandra, P. (2020). Smart grid to energy internet: A systematic review of transitioning electricity systems. *IEEE Access* 8, 215787–215805. doi:10.1109/ACCESS.2020.3041031

Karimi, H., Jadid, S., and Hasanzadeh, S. (2023). Optimal-sustainable multi-energy management of microgrid systems considering integration of renewable energy resources: A multi-layer four-objective optimization. *Sustain. Prod. Consum.* 36, 126–138. doi:10.1016/j.spc.2022.12.025

Li, T., Chen, L., Jensen, C. S., Pedersen, T. B., Gao, Y., and Hu, J. "Evolutionary clustering of moving objects," in Proceedings of the IEEE 38th International Conference on Data Engineering (ICDE)), Kuala Lumpur, Malaysia, May 2022, 2399–2411.

Li, T., Huang, R., Chen, L., Jensen, C. S., and Pedersen, T. B. (2020a). Compression of uncertain trajectories in road networks. *Proc. VLDB Endow.* 13 (7), 1050–1063. doi:10.14778/3384345.3384353

Li, Y., Gao, D. W., Gao, W., Zhang, H., and Zhou, J. (2021). A distributed double-Newton descent algorithm for cooperative energy management of multiple energy

bodies in energy internet. *IEEE Trans. Industrial Inf.* 17 (9), 5993–6003. doi:10.1109/TII.2020.3029974

Li, Y., Gao, D. W., Gao, W., Zhang, H., and Zhou, J. (2020). Double-mode energy management for multi-energy system via distributed dynamic event-triggered Newton-raphson algorithm. *IEEE Trans. Smart Grid* 11 (6), 5339–5356. doi:10.1109/TSG.2020.3005179

Li, Y., Gao, W., Huang, S., Wang, R., Yan, W., Gevorgian, V., et al. (2021a). Data-driven optimal control strategy for virtual synchronous generator via deep reinforcement learning approach. *J. Mod. Power Syst. Clean Energy* 9 (4), 919–929. doi:10.35833/MPCE.2020.000267

Li, Y., Zhang, H., Liang, X., and Huang, B. (2019). Event-triggered-based distributed cooperative energy management for multienergy systems. *IEEE Trans. Industrial Inf.* 15 (4), 2008–2022. doi:10.1109/TII.2018.2862436

Liu, Z., Zhang, Z., Zhuo, R., and Wang, X. (2019). Optimal operation of independent regional power grid with multiple wind-solar-hydro-battery power. *Appl. Energy* 235, 1541–1550. doi:10.1016/j.apenergy.2018.11.072

Nunna, H. S. V. S. K., Sesetti, A., Rathore, A. K., and Doolla, S. (2020). Multiagent-based energy trading platform for energy storage systems in distribution systems with interconnected microgrids. *IEEE Trans. Industry Appl.* 56 (3), 3207–3217. doi:10.1109/TIA.2020.2979782

Olsen, D. J., Zhang, N., Kang, C., Ortega-Vazquez, M. A., and Kirschen, D. S. (2019). Planning low-carbon campus energy hubs. *IEEE Trans. Power Syst.* 34 (3), 1895–1907. doi:10.1109/TPWRS.2018.2879792

Oskouei, M. Z., Mohammadi-Ivatloo, B., Erdinç, O., and Erdinç, F. G. (2021). Optimal allocation of renewable sources and energy storage systems in partitioned power networks to create supply-sufficient areas. *IEEE Trans. Sustain. Energy* 12 (2), 999–1008. doi:10.1109/TSTE.2020.3029104

Ravada, B. R., Tummuru, N. R., and Ande, B. N. L. (2021). Photovoltaic-wind and hybrid energy storage integrated multisource converter configuration-based grid-interactive microgrid. *IEEE Trans. Industrial Electron.* 68 (5), 4004–4013. doi:10.1109/TIE.2020.2984437

Sanjari, M. J., Gooi, H. B., and Nair, N. K. C. (2020). Power generation forecast of hybrid PV–wind system. *IEEE Trans. Sustain. Energy* 11 (2), 703–712. doi:10.1109/TSTE.2019.2903900

shafiei, M., and Ghasemi-Marzbali, A. (2023). Electric vehicle fast charging station design by considering probabilistic model of renewable energy source and demand response. *Energy* 267, 126545. doi:10.1016/j.energy.2022.126545

Song, C., Xiao, J., Zu, G., Hao, Z., and Zhang, X. (2021). Security region of natural gas pipeline network system: Concept, method and application. *Energy* 217, 119283. doi:10.1016/j.energy.2020.119283

Sun, Y., Zhong, J., Li, Z., Tian, W., and Shahidehpour, M. (2017). Stochastic scheduling of battery-based energy storage transportation system with the penetration of wind power. *IEEE Trans. Sustain. Energy* 8 (1), 135–144. doi:10.1109/TSTE.2016.2586025

Tan, D., and Novosel, D. (2017). Energy challenge, power electronics and systems (PEAS) technology and grid modernization. *CPSS Trans. Power Electron. Appl.* 2 (1), 3–11. doi:10.24295/CPSSTPEA.2017.00002

Wang, X., Chang, J., Meng, X., and Wang, Y. (2018). Short-term hydro-thermal-wind-photovoltaic complementary operation of interconnected power systems. *Appl. Energy* 229, 945–962. doi:10.1016/j.apenergy.2018.08.034

Wei, H., Hongxuan, Z., Yu, D., Yiting, W., Ling, D., and Ming, X. (2019). Short-term optimal operation of hydro-wind-solar hybrid system with improved generative adversarial networks. *Appl. Energy* 250, 389–403. doi:10.1016/j.apenergy.2019.04.090

Xu, D., Yuan, Z.-L., Bai, Z., Wu, Z., Chen, S., and Zhou, M. (2022). Optimal operation of geothermal-solar-wind renewables for community multi-energy supplies. *Energy* 249, 123672. doi:10.1016/j.energy.2022.123672

Yang, L., Li, X., Sun, M., and Sun, C. (2023). Hybrid policy-based reinforcement learning of adaptive energy management for the energy transmission-constrained island group. *IEEE Trans. Industrial Inf.*, 1–12. doi:10.1109/TII.2023.3241682

Yang, L., Sun, Q., Zhang, N., and Li, Y. (2022). Indirect multi-energy transactions of energy internet with deep reinforcement learning approach. *IEEE Trans. Power Syst.* 37 (5), 4067–4077. doi:10.1109/TPWRS.2022.3142969

Zhang, N., Sun, Q., Yang, L., and Li, Y. (2022). Event-triggered distributed hybrid control scheme for the integrated energy system. *IEEE Trans. Industrial Inf.* 18 (2), 835–846. doi:10.1109/TII.2021.3075718

Glossary

RE	renewable energy
PV	photovoltaic
ES	energy storage
O&M	operation and maintenance
C	benefits of the model
K	abandonment penalty for RE
F	cost of thermal turbines
A	cost of wind turbines
B	cost of hydropower turbines
D	cost of PV turbines
C_{sy}	running revenue of the ES system
η	efficiency of the ES system
F	discharge
c	charging
P_{St}	power of the ES system
$P_{price,sell}$	price of electricity sold to the power grid
$P_{price,buy}$	price of electricity purchased from the power grid
C_{cb}	operating cost of the ES system
C_{In}	investment cost of the ES system
C_{OM}	O&M cost of the ES system
C_{ESS}	cost of ES system kilowatt-hour costs
C_P	power unit investment of ES
C_E	capacity unit investment of ES
P_{ESS}	installed capacity of the ES power station
$C(r,n)$	equivalent annual value coefficient
r	benchmark discount rate
n	duration of ES operation (life, in years)
λ	O&M cost factor for ES
Q_{ESS}	annual power generation of ES
μ	O&M cost coefficient
H_{ESS}	annual utilization hours of electricity
f_d	annual equivalent of installed cost investment in thermal power
P_{zj}	installed cost per unit of thermal power unit capacity
T_y	annual operating time
k	rate of the fundamental peak regulation capacity of thermal power to the maximum output power
M	service life
E_i	peak regulation discharge power of ES on day i
IN	installed cost
$P_{q,t}$	discarded power occurring in period t
x	abandoned penalty price
w	wind turbine
g	PV turbine
s	hydro turbine
N	number of turbines
Ω	quantity of thermal turbines
$P_{i,t}$	*i*th thermal unit's output power at moment t
$P_{,t}$	actual power connected to the power grid
S_t	battery power stored in the ES device in time period t
$S_{\min}$	minimum stored power of the charging state
$S_{\max}$	maximum stored power of the charging state
P_{others}^{buy}	price of selling electricity to other power supply companies
P_{others}^{sell}	price of electricity sold by the power grid

frontiers | Frontiers in Energy Research

TYPE Original Research
PUBLISHED 13 June 2023
DOI 10.3389/fenrg.2023.1215786

Check for updates

OPEN ACCESS

EDITED BY
Yushuai Li,
University of Oslo, Norway

REVIEWED BY
Xiaofeng Li,
Anhui University, China
Bingyu Wang,
North China Electric Power University, China

*CORRESPONDENCE
Xinyu Ke,
848618850@qq.com

RECEIVED 02 May 2023
ACCEPTED 31 May 2023
PUBLISHED 13 June 2023

CITATION
Liu X, Chen X and Ke X (2023), Based on the difference of Newton's method integrated energy system distributed collaborative optimization.
Front. Energy Res. 11:1215786.
doi: 10.3389/fenrg.2023.1215786

COPYRIGHT
© 2023 Liu, Chen and Ke. This is an open-access article distributed under the terms of the Creative Commons Attribution License (CC BY). The use, distribution or reproduction in other forums is permitted, provided the original author(s) and the copyright owner(s) are credited and that the original publication in this journal is cited, in accordance with accepted academic practice. No use, distribution or reproduction is permitted which does not comply with these terms.

Based on the difference of Newton's method integrated energy system distributed collaborative optimization

Xinying Liu[1], Xu Chen[2] and Xinyu Ke[3]*

[1]Faculty of Electrical and Control Engineering, Liaoning Technical University, Huludao, China, [2]College of Mechanical and Electrical Engineering, Xinjiang Agricultural University, Urumqi, China, [3]The Electrical Engineering College, Guizhou University, Guiyang, China

With the integration of renewable energy into the grid, the traditional power system stability faced by huge challenges, and the development of integrated energy system, it is of essence to improve the coupling of multiple integrated energy systems of different types, management in the integrated energy system and reduce the pressure of communication and computing, in this paper, we construct a distributed Newton algorithm based on Newton's method to accelerate the solving speed, which decreases the times of iterations to reduce the pressure of communication and calculation, saving the cost of operation. Besides, privacy protection is particularly important for a distributed control system, under the premise that calculation speed is guaranteed, meanwhile, privacy protection of all agents in an integrated energy system is also critical. This study uses annular directed distributed algorithm to enhance the privacy of integrated distributed energy systems in the intelligent body, so as to fully ensure the privacy safety of all agents in the system. Moreover, the forementioned difference Newton algorithm in this study avoid the behavior of Zeno, greatly accelerating the speed of iteration and finding the best energy market price,. At the same time, the privacy safety of all agentsin the distributed energy system are ensured. Finally, a distributed integrated energy system based on the algorithm proposed by this study has went through theoretical proof and simulation experiment, whose result shows the validity of the algorithm.

KEYWORDS

difference Newton method, integrated energy system, energy scheduling, optimization, distributed algorithm

1 Introduction

Recent years have seen the need to bring a major shift of energy source from coal to and electricity in an attempt to ensure power supply Therefore, renewable energy is connected to the power system, which can ensure sustainable and reliable power supply. Despite unprecedented challenge and change, the traditional power system gradually transformed into new power system generating clean energy. However, as the new energy power systemincreasing in scale, it still faces numerous challenges, such as new balance system and complex security mechanism. The introduction of the integrated energy system can meet the regional energy demand and the multi-source strategy development is of great significance, that said, the key still lies in safeguarding regional energy safety and stable operation of energy system.

For the traditional electric power system, renewable energy is introduced into too little, therefore, most of the scholars at home and abroad research contains only a single power network (YANG and WANG, 2021), and for the centralized algorithm. These algorithms included multi-objective optimization scheduling (Zhang et al., 2020), mixed nonlinear programming (Marty et al., 2017), (Hemamalini and Simon, 2009) Newton method, and traditional iterative methods (Lin and Viviani, 1984) (Hemamalini and Simon, 2009) to solve the non-convex participant energy management problem in centralized energy systems. The literature suggests that centralized algorithms can more accurately obtain optimal values (Hemamalini and Simon, 2009), and are fast and easy to design. However, using centralized algorithms requires significant computational resources and communication costs, and damage to the central agent can be difficult to recover, such as (Yin et al., 2018). To address the aforementioned challenges, a distributed algorithm has been proposed by relevant scholars, which effectively overcomes the issue of handling large volumes of data and prevents problems such as information processing. The distributed algorithm encompasses the following aspects: Chow initially proposed a numerical method for consistency that was utilized by foreign scholars to solve the problem of distributed energy scheduling (Zhang and Chow, 2012). For a single distribution power grid, the primary consideration is the impact of electricity prices on power consumption (Xie et al., 2022a). Moreover, the robustness and control of the micro grid must be taken into account (Xie et al., 2022b), while optimization of parallel distribution in weak power grids is achieved through the application of the method of group economical ICA and the NSGA-II (Nie et al., 2023), (Zhong et al., 2022), which aims to identify the optimal operating point for the micro grid. The optimization of the micro grid mainly includes approaches such as neural network-based methods (Zhang et al., 2023), alternating direction multiplier methods (Gao et al., 2022) (Zhu et al., 2022), and dynamic programming (Yang and Yang, 2022). Scholars, such as Yang Ping, have proposed the GPS model in light of the relationship between information flow and energy flow, and have also developed optimal control strategies to explore the micro grid (Yang and Yang, 2022). The aforementioned research effectively addresses the challenges associated with communication and computing stress in traditional micro grid control centers. In addition, due to the use of distributed methods, the absence of a control center ensures that local damage has minimal impact on the entire system. However, the research only focuses on electricity and does not consider other forms of energy. With the constant improvement of the proportion of new energy power system, balance system, the security mechanism of the new type of power system problems such as challenged, in this case, the collaborative optimization of a variety of energy for the stability and security of the power system is obviously much better than a single grid. In this context, some scholars have proposed the concept of an integrated energy system that differs from single energy networks. Considering multiple energy networks together can enhance the effect of energy optimization, but it also increases the complexity of the transformation mechanisms across various forms of energy, such as electricity, gas, and heat, in both time and space scales (Lv, 2022). Consequently, the comprehensive optimization of an integrated energy system is more challenging than optimizing a single grid (Schfer et al., 2018). To address these issues, scholars have developed distributed computing methods for finding optimal values in integrated energy systems. Many studies by domestic and foreign scholars have proposed distributed non-iterative algorithms for multi-agent coordination optimization problems (Tan et al., 2019; Tan et al., 2021). For instance, one study (Munshi and Mohamed, 2019) proposed an unsupervised algorithm that uses electric meter data to determine electrical load parameters, while another study (Zhang et al., 2017) introduced the mixed alternating direction multiplier method to solve the coupling relationship between various forms of energy in the integrated energy system. Scholars such as Zhang have applied the integrated energy unit and alternating direction multiplier method to address the multivariate coupling between electric and heat energy systems and solve coordination problems between the energy networks (Zhang et al., 2017). On the basis of previous research, scholars both at home and abroad have mainly focused on the optimization of distributed optimization methods in integrated energy systems with regards to convergence speed. This has been done by addressing issues such as information attacks (Zhao et al., 2016; Duan and Chow, 2019), non-convexity of energy systems (Chen and Zhao, 2019; Huang et al., 2019; Li et al., 2019), and so on.

Although about the optimal management of traditional integrated energy system research have been studied from many aspects, can meet the balance between supply and demand, energy scheduling and achievements, but the traditional studies in distributed energy system, between the iterative speed and privacy protection problems still exist, Literature (Zhang et al., 2017; Li et al., 2020) has shown that when the iteration speed is slow, it is possible to ignore the kink behavior, which can lead to a loss in wireless loop. The traditional energy management approach is thus faced with the challenge of being too slow for a long period of time, resulting in delayed energy supply during emergencies and inevitable loss. Pressure is too large and integrated energy systems of communication, iterative speed too slow, resulting in the high cost problem. Based on the above analysis, this paper combined with the ring to algorithm design difference Newton's method, Newton method and greatly accelerate the iteration speed, reduce the number of iterations, delay to solve energy, reduce communication and computing pressure, privacy protection and integrated energy systems between adjacent agent. The main contributions of this paper are as follows.

1) The difference Newton's method is proposed based on the Newton's method. In comparison with the traditional approach, this method is characterized by a faster rate of iteration and a reduced number of iterations. Consequently, in the context of an integrated energy system, it can significantly reduce communication and computational overhead and mitigate energy latency.
2) The ring-based distributed algorithm is employed in the integrated energy system to ensure privacy protection among its participants. Conventional algorithms rely on participants to protect their privacy, but they require the exchange of adjacent information such as energy input/output power and energy price. In this regard, the use of the ring-based distributed algorithm effectively addresses this issue by providing complete privacy protection for all participants.

3) To avoid the divergence of Newton's method during the downhill, a kino line may occur where the algorithm iterates indefinitely within a limited time, leading to an infinite loop. To prevent this behavior, the proposed algorithm in this paper is designed to avoid kino behavior.

The paper is structured as follows: In the first section, the integrated energy system established in this study is introduced, along with the function and constraint conditions for each participant's cost in the system. The second section describes the Difference Newton's method employed in this paper (DNEA) and how it addresses the energy coupling issue. The third section provides a proof of DNEA's speed, convergence, optimality, and avoidance of kino behavior. The fourth section presents a simulation validation of the proposed DNEA algorithm in the established integrated energy system. Finally, the fifth section offers concluding remarks.

2 Models of IES

The composition of body, specifically its internal structure, comprises various energy devices that serve distinct functions. 1) The power generation device includes distributed coal-fired generators, gas generators, solar generators, wind turbines, and energy storage systems. 2) The heating device comprises distributed coal-fired heat production devices, distributed combustion gas heat production equipment, photovoltaic production engines, and distributed storage devices. 3) The thermal electric power plant machine. 4) The distributed gas suppliers constitute the remaining energy equipment. Each of these energy bodies accommodates three energy types, namely, electricity, gas, and heat, which need to be considered while accounting for electricity price fluctuations, load-side random scheduling, and demand response for electricity, gas, and heat. Because in traditional power system load is not adjustable, so you need to increase the "adjustable load", such as: conversion of electricity and heat, electricity and hydrogen between mutual conversion, energy storage device, etc.,. This paper is suitable for small energy network connected to the electricity grid if there are toning, can from the grid to compensate.

The figure illustrates the encryption of data to safeguard the privacy of each pluripotent micro power grid in the integrated energy system. During each iteration process, the control center establishes encrypted data to ensure secure communication.

2.1 Models of renewable energy devices

This article considers five energy bodies and takes into account the changing demands and environmental factors affecting the energy efficiency of each equipment within these bodies. Based on this, the following constraints have been established.

1) Distributed energy physical quantity balance constraints

$$P_{i,T}^{ex} = \left\{ \begin{array}{l} \sum\limits_{i\in K_i^{pg}} P_{ij,T}^{g} + \sum\limits_{i\in K_i^{pc}} P_{ij,T}^{c} + \sum\limits_{i\in K_i^{pes}} P_{ij,T}^{es} + \sum\limits_{i\in K_i^{pchp}} P_{ij,T}^{chp} + \sum\limits_{i\in K_i^{pp}} P_{ij,T}^{p} \\ + \sum\limits_{i\in K_i^{pw}} P_{ij,T}^{w} - \sum\limits_{i\in K_i^{\Lambda}} \left(\Lambda P_{ij,T}^{r} + \Lambda P_{ij,T}^{cl} \right) \end{array} \right\} \tag{1}$$

Type: $P_{i,T}^{ex}$ for the ith a total electricity energy body; $\sum\limits_{i\in K_i^{pg}} P_{ijT}^{g}$ for gas supplier by air to turn electric power. $\sum\limits_{i\in K_i^{pc}} P_{ij,T}^{c}$ as the coal to produce electricity, $\sum\limits_{i\in K_i^{pes}} P_{ij,T}^{es}$ as the energy storage equipment to produce electricity. $\sum\limits_{i\in K_i^{pchp}} P_{ij,T}^{chp}$ for cogeneration plant producing; $\sum\limits_{i\in K_i^{pp}} P_{ij,T}^{p}$ for photovoltaic generation; $\sum\limits_{i\in K_i^{pw}} P_{ij,T}^{w}$ for wind power generation; $\Lambda P_{ij,T}^{r}$ for the necessary power to the load side, $\Lambda P_{ij,T}^{cl}$ for electric power loss when converted into heat. This paper only considers the electric load that is converted to heat load, and not the heat load converted to electricity load case. K_i^{pg}, K_i^{pc}, K_i^{pes}, K_i^{pchp}, K_i^{pp}, K_i^{pw}, K_i^{Λ} respectively represent the ith coal-fired generator set, energy storage device, gas supplier collection, cogeneration unit set, pv electricity production device set, load, and fan electricity production device under given energy body scenarios.

$$H_{i,T}^{ex} = \left\{ \begin{array}{l} \sum\limits_{i\in K_i^{pg}} H_{ij,T}^{g} + \sum\limits_{i\in K_i^{pc}} H_{ij,T}^{c} + \sum\limits_{i\in K_i^{pes}} H_{ij,T}^{es} \\ + \sum\limits_{i\in K_i^{pchp}} H_{ij,T}^{chp} + \sum\limits_{i\in K_i^{pp}} H_{ij,T}^{p} - \sum\limits_{i\in K_i^{\Lambda}} \left(\Lambda H_{ij,T}^{r} + \Lambda H_{ij,T}^{cl} \right) \end{array} \right\} \tag{2}$$

$$G_{i,T}^{ex} = \sum_{i\in K_i^{gas}} G_{ij,T}^{gas} - \sum_{i\in K_i^{\Lambda}} \left(H_{ij,T}^{g} + P_{ij,T}^{g} + \Lambda G_{ij,T}^{cl} \right) \tag{3}$$

For each CLP energy body, the production amount of equipment for gas and heat must remain equal to the difference between the total load and the exchange of energy on the load side during operation. In addition, the exchange of distributed energy should satisfy the following constraints:

Regarding the heat transfer in type 2) variables, the concrete form of electricity exchange is as follows: the same redundancy avoidance applies, and it is not presented here. 3), $G_{i,T}^{ex}$ indicates the remaining gas amount for the ith energy body; $G_{ij,T}^{gas}$ represents the gas quantity supplied by gas suppliers; $\Lambda G_{ij,T}^{cl}$ denotes the gas volume lost when converted into other energy forms. In this article, $P_{i,T}^{ex}$ and $H_{i,T}^{ex}$ are regulated as the timing for discharge or exothermic processes, while negative values indicate electricity or heat absorption. $P_{ij,T}^{es}$ and $H_{ij,T}^{es}$ represent timing for energy storage devices to emit or absorb electric heat; negative values indicate electricity and heat energy storage devices' absorption.

2) Considering the randomness, volatility, and renewable energy output fluctuation value limit conditions, the following expressions apply:

$$P_{ij,T}^{p,\min} \le P_{ij,T}^{p} \le P_{ij,T}^{p,\max} \tag{4}$$

$$P_{ij,T}^{w,\min} \le P_{ij,T}^{w} \le P_{ij,T}^{w,\max} \tag{5}$$

$$H_{ij,T}^{p,\min} \le H_{ij,T}^{p} \le H_{ij,T}^{p,\max} \tag{6}$$

Type: $P_{ij,T}^{p,\min}$, $P_{ij,T}^{w,\min}$, $H_{ij,T}^{p,\min}$ for renewable energy to produce power and thermal power limit, $P_{ij,T}^{p,\max}$, $P_{ij,T}^{w,\max}$, $H_{ij,T}^{p,\max}$ for renewable energy to produce power and thermal power limit. Renewable energy constraints are designed with consideration for the renewable energy capacity confidence interval and prediction error, expressing the randomness and volatility of renewable energy (Zhang et al., 2017).

As a renewable energy source, solar electricity is widely utilized currently; however, its volatility and randomness necessitate the inclusion of photovoltaic (pv) motor and solar heating into the following functions:

$$C\left(P_{ij,T}^{p}\right)=\alpha_{ij,T}^{p,p}P_{ij,T}^{p}+\beta_{ij,T}^{p,p}\exp\left(\varepsilon_{ij,T}^{p,p}\frac{P_{ij,T}^{p,\max}-P_{ij,T}^{p}}{P_{ij,T}^{p,\max}-P_{ij,T}^{p,\min}}\right)+\kappa_{ij,T}^{p,p} \quad (7)$$

$$C\left(H_{ij,T}^{p}\right)=\alpha_{ij,T}^{h,p}H_{ij,T}^{p}+\beta_{ij,T}^{h,p}\exp\left(\varepsilon_{ij,T}^{h,p}\frac{H_{ij,T}^{p,\max}-H_{ij,T}^{p}}{H_{ij,T}^{p,\max}-H_{ij,T}^{p,\min}}\right)+\kappa_{ij,T}^{h,p} \quad (8)$$

Type: $\alpha_{ij,T}^{p,p}$, $\beta_{ij,T}^{p,p}$, $\varepsilon_{ij,T}^{p,p}$, $\kappa_{ij,T}^{p,p}$, $\alpha_{ij,T}^{h,p}$, $\beta_{ij,T}^{h,p}$, $\varepsilon_{ij,T}^{h,p}$, and $\kappa_{ij,T}^{h,p}$ are the cost coefficients.

Fan electricity production cost function:

$$C\left(P_{ij,T}^{w}\right)=\alpha_{ij,T}^{p,w}P_{ij,T}^{w}+\beta_{ij,T}^{p,w}\exp\left(\varepsilon_{ij,T}^{p,w}\frac{P_{ij,T}^{w,\max}-P_{ij,T}^{w}}{P_{ij,T}^{w,\max}-P_{ij,T}^{w,\min}}\right)+\kappa_{ij,T}^{p,w} \quad (9)$$

Type: $\alpha_{ij,T}^{p,w}$、 $\beta_{ij,T}^{p,w}$、 $\varepsilon_{ij,T}^{p,w}$、 $\kappa_{ij,T}^{p,w}$ of cost coefficient.

Note: this article does not consider the relationships between kW and heat, electricity, and gas; therefore, the comprehensive energy kW should be applied to all energy units involved.

3) Considering coal heating device, coal thermal power plant and cogeneration plant output fluctuation value limit condition are:

$$P_{ij,T}^{c,\min}\le P_{ij,T}^{c}\le P_{ij,T}^{c,\max} \quad (10)$$

$$H_{ij,T}^{c,\min}\le H_{ij,T}^{c}\le H_{ij,T}^{c,\max} \quad (11)$$

$$P_{ij,T}^{chp,\min}\le P_{ij,T}^{chp}\le P_{ij,T}^{chp,\max} \quad (12)$$

$$H_{ij,T}^{chp,\min}\le H_{ij,T}^{chp}\le H_{ij,T}^{chp,\max} \quad (13)$$

Type: $P_{ij,T}^{c,\min}$, $H_{ij,T}^{c,\min}$, $P_{ij,T}^{chp,\min}$, and $H_{ij,T}^{chp,\min}$ represent the lower limits for the power supply of T moment coal-fired thermal power equipment, coal heating equipment, and cogeneration plant heating power, respectively; $P_{ij,T}^{c,\max}$, $H_{ij,T}^{c,\max}$, $P_{ij,T}^{chp,\max}$, and $H_{ij,T}^{chp,\max}$ respectively denote the upper limits for the power supply of T moment coal-fired thermal power equipment, coal heating equipment, and cogeneration plant heating power, respectively.

4) Coal-fired thermal power equipment, coal heating equipment, and combined heat and power output ramping restrictions are as follows:

$$-P_{ij,T}^{c,ccl}\le P_{ij,T}^{c}-P_{ij,T-1}^{c}\le P_{ij,T}^{c,ccl} \quad (14)$$

$$-H_{ij,T}^{c,ccl}\le H_{ij,T}^{c}-H_{ij,T-1}^{c}\le H_{ij,T}^{c,ccl} \quad (15)$$

$$-P_{ij,T}^{chp,ccl}\le P_{ij,T}^{chp}-P_{ij,T-1}^{chp}\le P_{ij,T}^{chp,ccl} \quad (16)$$

$$-H_{ij,T}^{chp,ccl}\le H_{ij,T}^{chp}-H_{ij,T-1}^{chp}\le H_{ij,T}^{chp,ccl} \quad (17)$$

Type: $H_{ij,T}^{c,ccl}$, $P_{ij,T}^{chp,ccl}$, and $H_{ij,T}^{chp,ccl}$ represent the maximum change in *T* moment coal-fired thermal power equipment compared to T-1 h, the maximum change in *T* moment coal-fired heat production equipment compared to *T-1* h, and the maximum change in T moment cogeneration equipment compared to *T-1* h for electricity and heat production, respectively. $P_{ij,T-1}^{c}$, $H_{ij,T-1}^{c}$, $P_{ij,T-1}^{chp}$, and $H_{ij,T-1}^{chp}$ denote the initial production of *T-1* coal-fired thermal power equipment, *T-1* coal-fired heat production equipment, and *T-1* cogeneration plant for electricity and heat, respectively.

Coal is commonly used in energy bodies to produce electricity and heat, and its consumption characteristics are determined by the energy size produced at time T. Although its stability is reliable, it causes a certain level of environmental pollution and is subject to ramping constraints. The cost functions for coal-fired generators and heat production engines are as follows:

$$C\left(P_{ij,T}^{c}\right)=\alpha_{ij,T}^{p,c}\left(P_{ij,T}^{c}\right)^{2}+\beta_{ij,T}^{p,c}P_{ij,T}^{c}+\varepsilon_{ij,T}^{p,c}e^{\kappa_{ij,T}^{p,c}P_{ij,T}^{c}}+\lambda_{ij,T}^{p,c} \quad (18)$$

$$C\left(H_{ij,T}^{c}\right)=\alpha_{ij,T}^{h,c}\left(H_{ij,T}^{c}\right)^{2}+\beta_{ij,T}^{h,c}H_{ij,T}^{c}+\varepsilon_{ij,T}^{h,c}e^{\kappa_{ij,T}^{h,c}H_{ij,T}^{c}}+\lambda_{ij,T}^{h,c} \quad (19)$$

Type: $\alpha_{ij,T}^{p,c}$, $\beta_{ij,T}^{p,c}$, $\varepsilon_{ij,T}^{p,c}$, $\kappa_{ij,T}^{p,c}$, $\lambda_{ij,T}^{p,c}$, $\alpha_{ij,T}^{h,c}$, $\beta_{ij,T}^{h,c}$, $\varepsilon_{ij,T}^{h,c}$, $\kappa_{ij,T}^{h,c}$, $\lambda_{ij,T}^{h,c}$ are cost coefficients, with R being positive.

As an energy body, the CLP cogeneration unit exhibits a thermal coupling relationship with its main equipment. The cost function is determined by the simultaneous production of electric and thermal energy, and its output falls within a specific range. The cogeneration unit cost function is as follows:

$$C\left(P_{ij,T}^{chp},H_{ij,T}^{chp}\right)=\alpha_{ij,T}^{p,chp}\left(P_{ij,T}^{chp}\right)^{2}+\beta_{ij,T}^{p,chp}P_{ij,T}^{chp}+\varepsilon_{ij,T}^{h,chp}\left(H_{ij,T}^{chp}\right)^{2}+\lambda_{ij,T}^{h,chp}H_{ij,T}^{chp}+\eta_{ij,T}^{chp} \quad (20)$$

Type: $\alpha_{ij,T}^{p,chp}$, $\beta_{ij,T}^{p,chp}$, $\varepsilon_{ij,T}^{h,chp}$, $\lambda_{ij,T}^{h,chp}$, $\eta_{ij,T}^{chp}$ represent the cost coefficients.

5) Distributed gas supplier supply constraints are given by the following expression:

$$0\le G_{ij,T}^{gas}\le G_{ij,T}^{gas,\max} \quad (21)$$

Type: $G_{ij,T}^{gas,\max}$ represents the maximum gas supply provided by gas suppliers at time T. Gas, gas electricity production, and gas used as fuel for electricity and heat production exhibit similar characteristics to coal-fired capacity. The size of energy produced at time T determines the real-time fuel consumption amount, with combustion gas suppliers supplying gas within a specific range.

6) Resistance and energy storage restrictions for energy storage devices and heat values are as follows:

$$P_{ij,T}^{es,\min}\le P_{ij,T-1}^{es,n}-\left|P_{ij,T}^{es}\right|\le P_{ij,T}^{es,\max} \quad (22)$$

$$H_{ij,T}^{es,\min}\le H_{ij,T-1}^{es,n}-\left|H_{ij,T}^{es}\right|\le H_{ij,T}^{es,\max} \quad (23)$$

$$G_{ij,T}^{es,\min}\le G_{ij,T-1}^{es,n}-\left|G_{ij,T}^{es}\right|\le G_{ij,T}^{es,\max} \quad (24)$$

Type: $P_{ij,T}^{es,\min}$, $H_{ij,T}^{es,\min}$, $G_{ij,T}^{es,\min}$ represent the lower limits of T moment heat storage equipment, storage equipment, and gas storage capacity, respectively. $P_{ij,T}^{es,n}$, $H_{ij,T}^{es,n}$, $G_{ij,T}^{es,n}$ denote the storage of heat, electricity, and gas for T-1 h heat storage, storage equipment, and gas equipment, respectively. $P_{ij,T}^{es,\max}$, $H_{ij,T}^{es,\max}$, $G_{ij,T}^{es,\max}$ represent the upper limits of storage capacity for electricity, heat, and gas at time T.

7) Electricity, heat, and energy storage device discharge and power change constraints are as follows:

$$P_{ij,T}^{es,\min} \le \left|P_{ij,T}^{es}\right| \le P_{ij,T}^{es,\max} \tag{25}$$

$$H_{ij,T}^{es,\min} \le \left|H_{ij,T}^{es}\right| \le H_{ij,T}^{es,\max} \tag{26}$$

$$G_{ij,T}^{es,\min} \le \left|G_{ij,T}^{es}\right| \le G_{ij,T}^{es,\max} \tag{27}$$

Type: $P_{ij,T}^{es,\min}$, $H_{ij,T}^{es,\min}$, $G_{ij,T}^{es,\min}$ represent the lower limits for discharge and energy absorption of storage, heat storage, and gas storage equipment, respectively. $P_{ij,T}^{es,\max}$, $H_{ij,T}^{es,\max}$, $G_{ij,T}^{es,\max}$ denote the upper limits for discharge and energy absorption of storage, heat storage, and gas storage equipment, respectively.

Energy storage devices store energy when electricity prices are low and release energy when prices are high, playing a regulatory role. Consequently, they are essential equipment within energy bodies. Due to varying factors across different types of energy storage devices, a unified storage device cost function is established as follows:

$$C\left(P_{ij,T}^{es}\right) = \alpha_{ij,T}^{p,es}\left(P_{ij,T}^{es} + \beta_{ij,T}^{p,es}\right)^2 + \lambda_{ij,T}^{p,es} \tag{28}$$

$$C\left(H_{ij,T}^{es}\right) = \alpha_{ij,T}^{p,es}\left(H_{ij,T}^{es} + \beta_{ij,T}^{p,es}\right)^2 + \lambda_{ij,T}^{p,es} \tag{29}$$

Type: $\alpha_{ij,T}^{p,es}$, $\beta_{ij,T}^{p,es}$, $\lambda_{ij,T}^{p,es}$, $\alpha_{ij,T}^{p,es}$, $\beta_{ij,T}^{p,es}$, $\lambda_{ij,T}^{p,es}$ represent cost coefficients.

8) Gas-to-electricity transfer and thermal conversion rates are as follows:

$$P_{ij,T}^{es} = \alpha G_{ij,T}^{pes} \tag{30}$$

$$H_{ij,T}^{es} = \beta G_{ij,T}^{hes} \tag{31}$$

Type: a and b represent the gas-to-electricity and heat conversion rates, respectively. $G_{ij,T}^{pes}$ and $G_{ij,T}^{hes}$ denote the capacity for electricity and heat conversion, respectively.

9) Lateral load consumption of electricity and heat cost functions are as follows:

$$C\left(P_{ij,T}^{lp}\right) = \alpha_{ij,T}^{p,lp}\left(P_{ij,T}^{lp}\right)^2 + \lambda_{ij,T}^{p,lp}P_{ij,T}^{lp} + \varepsilon_{ij,T}^{p,lp} \tag{32}$$

$$C\left(H_{ij,T}^{lh}\right) = \alpha_{ij,T}^{h,lh}\left(P_{ij,T}^{lh}\right)^2 + \lambda_{ij,T}^{h,lh}P_{ij,T}^{lh} + \varepsilon_{ij,T}^{h,lh} \tag{33}$$

Type: $P_{ij,T}^{lp}$, $H_{ij,T}^{lh}$ represent load side electricity and heat consumption, respectively. $\alpha_{ij,T}^{p,lp}$, $\lambda_{ij,T}^{p,lp}$, $\varepsilon_{ij,T}^{p,lp}$, $\alpha_{ij,T}^{h,lh}$, $\lambda_{ij,T}^{h,lh}$, and $\varepsilon_{ij,T}^{h,lh}$ are positive cost coefficients.

2.2 The interests of the function

The benefit of the energy body function revenue function and cost function are two parts, and the mathematical expression is as follows:

$$\Psi_{i,T} = \mathrm{O}_{i,T} - C_{i,T} \tag{34}$$

Type: $\Psi_{i,T}$ represents the ith a energy body in T time overall interests, $\mathrm{O}_{i,T}$ means the energy body in T moment ith total earnings, $C_{i,T}$ refers to the case of an energy body in T time ith the total cost. The specific expressions for the profit function and cost function in Eq. 34 are as follows:

$$\mathrm{O}_{i,T} = \mathrm{K}_{ij,T}^{use} + pr_T^p P_{i,T}^{ex} + pr_T^h H_{i,T}^{ex} + pr_T^g G_{i,T}^{ex} \tag{35}$$

$$C_{i,T} = C\left(P_{ij,T}^{p,s}\right) + C\left(P_{ij,T}^{h,s}\right) + C\left(P_{ij,T}^{chp}, H_{ij,T}^{chp}\right) \tag{36}$$

$$\mathrm{K}_{ij,T}^{use} = -\eta_{ij}^p\left(\Lambda P_{ij,T}^r\right)^2 + \nu_{ij}^p\Lambda P_{ij,T}^r - \eta_{ij}^h\left(\Lambda H_{ij,T}^r\right)^2 + \nu_{ij}^h\Lambda H_{ij,T}^r \tag{37}$$

$$C\left(P_{ij,T}^{p,s}\right) = C\left(P_{ij,T}^{p}\right) + C\left(P_{ij,T}^{w}\right) + C\left(P_{ij,T}^{c}\right) + C\left(P_{ij,T}^{g}\right) + C\left(P_{ij,T}^{es}\right) \tag{38}$$

$$C\left(P_{ij,T}^{h,s}\right) = C\left(H_{ij,T}^{p}\right) + C\left(H_{ij,T}^{c}\right) + C\left(H_{ij,T}^{g}\right) + C\left(H_{ij,T}^{es}\right) \tag{39}$$

Type: $\mathrm{K}_{ij,T}^{use}$ represents the energy utilization function for the energy system on the load side, η_{ij}^p, ν_{ij}^p, η_{ij}^h, ν_{ij}^h are cost coefficients. pr_T^p, pr_T^p, pr_T^p denote the electricity, heat, and gas prices at time T, respectively. $C\left(P_{ij,T}^{p,s}\right)$ and $C\left(P_{ij,T}^{h,s}\right)$ represent the cost of producing electricity and heat for all equipment except cogeneration units at time T.

2.3 The objective function

This study focuses on the optimization of an integrated energy system that aims to coordinate the use of different types of energy, such as electricity, gas, and heat, with the goal of reducing production costs and improving energy efficiency. Specifically, we investigate the collaborative optimization of three energy supply and demand types, namely, electricity, heat, and gas. The energy conversion model is employed to allow for price adjustments among the three types of energy (Yu-Shuai et al., 2020). We strive to achieve a globally optimal solution that takes full advantage of the complementary characteristics of various energy sources to obtain the most economic price, while ensuring the balance between energy supply and demand. The optimization problem is formulated as (34), using a modified version of Newton's method, known as the difference Newton's method, to speed up the algorithm iteration and reduce communication and computational pressure. The objective function is expressed as type (40), which represents the overall benefits of the entire energy system, while ensuring that the net energy value is zero, thus guaranteeing the balance between energy supply and demand. The function expression is presented below.

$$\max \ Object = \sum_{i=1}^{n}\Psi_{i,T} \tag{40}$$

$$\sum_{i=1}^{n}P_{i,T}^{ex} = 0, \sum_{i=1}^{n}H_{i,T}^{ex} = 0, \sum_{i=1}^{n}G_{i,T}^{ex} = 0 \tag{41}$$

3 The algorithm design

3.1 The traditional Newton iteration method

The traditional numerical method referred to as Newton's method is commonly utilized to solve nonlinear equations. Within integrated energy systems, collaborative optimization can utilize the traditional Newton's method to solve complex optimization models. The basic idea of this method is to iteratively solve equations of zero and determine the direction of the next iteration through the first-order approximation of the equation. In practical applications, the traditional Newton

method can achieve optimal cooperation among parties based on the integrated energy system states and parameters of continuous optimization. When addressing comprehensive power, heat, and gas optimization problems in energy systems, the traditional Newton method can be applied to solve conflicts and coordinate energy sources to realize optimal system synergy (Tan and Li, 2022).

3.2 DNEA algorithm design

In integrated energy systems, each energy entity is equipped with its own processor. Nonetheless, the absence of a centralized system causes a distributed structure which lacks significant communication and computing power. Consequently, the computing capability of each processor in the energy entity is limited. When faced with the high-speed and high utilization of renewable energy, the conventional algorithm struggles to compute the parameters in a distributed energy system. To tackle this challenge, this study introduces the difference Newton's method as a solution. This method is designed to resolve issues with slow calculation speed and communication and computing pressure. By applying the difference Newton's method to every energy entity during the calculation process, the computational speed is significantly enhanced, while maintaining a balance between supply and demand and maximizing profit. The following outlines the design of the difference Newton's method in the calculation process of the integrated energy system.

Due to the convex nature of the cost function designed in this paper, the derivative of the energy body's benefit function for all participants is the iterative price $pr_T^p\eta_{ij}^p$, pr_T^h, pr_T^g. To ensure the maximization of the overall interests objective function of the energy system, this study assumes that each participant achieves the same benefits for the same unit of electricity and heat, namely, $pr_T^p = pr_T^h$. The specific algorithm design process is as follows:

$$\frac{dC\left(P_{ij,T}^p\right)}{dP_{ij,T}^p} = \frac{dC\left(H_{ij,T}^p\right)}{dH_{ij,T}^p} = \ldots\ldots = pr_{T,1}^{p,h} \tag{42}$$

Type: Given the goal of finding the optimal balance between supply and demand conditions for the maximum overall energy interests, the price of electricity and heat is assumed to be the same. Hence, the price of electricity and heat are represented by $pr_{T,1}^{p,h}$. The derivative of the cost function for the remaining energy body participants equals $pr_{T,1}^{p,h}$, which is not elaborated upon further to avoid redundancy. The sum of electricity and heat provided by all participants in the energy body is calculated as $S(\Lambda_{T,1}^{p,h})$.

$$S\left(\Phi_{T,1}^r\right) = S\left(\Phi_{T,1}^{p,r}\right) + S\left(\Phi_{T,1}^{h,r}\right) \tag{43}$$

Type: $S(\Phi_{T,1}^{p,r})$, $S(\Phi_{T,1}^{h,r})$ denote the sum of electricity and heat required by the load side participants at the given prices, respectively. This study assumes a 1:1 conversion efficiency for electricity and heat, resulting in the need for electricity and heat by the participants. The difference between supply and demand balance values is calculated using the following formula:

The difference between the value of $\zeta_{T,1}^{sd}$ between the supply and demand balance values at this time is calculated using the following formula:

$$\zeta_{T,1}^{sd} = \left|S\left(\Lambda_{T,1}^{p,h}\right) - S\left(\Phi_{T,1}^r\right)\right| \tag{44}$$

$$\frac{dC\left(P_{ij,T}^p\right)}{dP_{ij,T}^p} = \frac{dC\left(H_{ij,T}^p\right)}{dH_{ij,T}^p} = \ldots\ldots = pr_{T,2}^p \tag{45}$$

Assuming that the second energy iteration price is $pr_{T,2}^{p,h}$, the total energy provided by the participants is $S(\Lambda_{T,2}^{p,h})$, the total energy required is $S(\Phi_{T,2}^r)$, the imbalance of supply and demand is $\zeta_{T,2}^{sd}$, and the second parameter is conceptually the same as the first parameter formula. The computation formula is as follows:

$$pr_{T,3}^{p,h} = pr_{T,2}^{p,h} - \zeta_{T,2}^{sd}\frac{pr_{T,1}^{p,h} - pr_{T,2}^{p,h}}{\zeta_{T,1}^{sd} - \zeta_{T,2}^{sd}} \tag{46}$$

Type: according to the relationship between price and the imbalance between supply and demand, if all functions are linear and the balance between supply and demand is guaranteed, the energy price is $pr_{T,3}^{p,h}$. Due to the linear overtaking convex function, the imbalance of supply and demand and the demand for $\zeta_{T,3}^{sd}$ and $S(\Phi_{T,3}^r)$ are met, respectively. Using $pr_{T,2}^{p,h}$ and $pr_{T,3}^{p,h}$ as the new iteration prices, the next iteration price is found by repeating the process until meeting $|\zeta_{T,i}^{sd}| < \upsilon_{T,i}^a$: type: $\zeta_{T,i}^{sd}$ is the ith iteration imbalance between supply and demand, and $\upsilon_{T,i}^a$ is the allowed error range. For all participants in the energy body, the changes in electricity, heat, and gas provision correspond to the price changes of each iteration $pr_{T,i}^{p,h}$.

3.3 Ring signature algorithm design

This paper ensures privacy among all participants in the integrated energy system by initializing the encrypted energy data as PH_T^{ed}. For the first integrated energy system, the energy body's privacy increases with each iteration, as each iteration process, PH_T^{ed} modifies the initial encrypted data. This prevents the encrypted data from being guessed with increasing iteration numbers, thus avoiding privacy leaks for all participants in the integrated energy system. The ring signature algorithm is used as the basis for data transmission in integrated energy systems, with the formula as follows:

$$PH_{ij,ki}^{ed} = PH_{ij,i-1}^{ed} + PH_T^{ed} \tag{47}$$

Type: In the first i-1 iterations, energy body information $PH_{ij,ki}^{ed}$ is introduced into the ith energy body, and $PH_{ij,i-1}^{ed}$ denotes the real information of the ith energy body. The information transfer direction is shown in Chart 1. This process strengthens privacy protection among energy bodies, ensuring each energy body's privacy and fully protecting the privacy of all agents in the system. This is an improvement compared to traditional privacy protection, which does not adequately protect privacy between integrated energy system energy bodies.

4 DNEA algorithm theory to prove

4.1 DNEA iteration speed

Setting parameters $\delta, \forall\delta \in R^+$, R^+ denotes all positive values. The traditional iterative method using Newton's method establishes an

adjustment volume of each time as $\zeta_{T,i}^{sd,tra}$, and meeting $\zeta_{T,i}^{sd,tra}$, and $\forall|\zeta_{T,i}^{sd,tra}|<\delta$. Therefore, the average adjustment volume for the traditional iteration method is:

$$\zeta_{T,i,ave}^{sd,tra}=\sum_{i=1}^{n}\zeta_{T,i}^{sd,tra}\Big/N \tag{48}$$

Type: The total number N for iteration, $\zeta_{T,i}^{sd,tra}$ $\forall|\zeta_{T,i}^{sd,tra}|<\delta$. Then, N is the number of iterations, with $\forall|N|>\delta$. An inequality exists such that $|\zeta_{T,i,ave}^{sd,tra}|\le\delta$, and the iterative algorithm designed in this paper is based on the traditional Newton iteration method, employing the Newton difference method. In the early stages of the iterative algorithm presented in this paper, the adjustment of the imbalance of supply and demand $\zeta_{T,i}^{sd,ea}$ $pr_{T,3}^{p,h,ea}$ does not satisfy the price inequality $\forall|\zeta_{T,i}^{sd,ea}|<\delta$, $\forall|pr_{T,3}^{p,h,ea}|<\delta$, and the iteration process is repeated. Later in the iteration, the imbalance of supply and demand approaches $\zeta_{T,i}^{sd,la}$, and the iterative prices approach $pr_{T,3}^{p,h,la}$, $\forall|\zeta_{T,i}^{sd,ea}|<\delta$, and $\forall|pr_{T,3}^{p,h,ea}|<\delta$. Gradually, the material difference satisfies Equation $\zeta_{T,i,ave}^{sd}=\sum_{i=1}^{n}\zeta_{T,i}^{sd}/N$, on average, it does not meet the equation for $\zeta_{T,i}^{sd}$ $\forall\sum_{i=1}^{n}\zeta_{T,i}^{sd}<\delta$, $\zeta_{T,i,ave}^{sd}$ does not meet the $\forall\zeta_{T,i,ave}^{sd}<\delta$. In summary, the iteration algorithm $\zeta_{T,i,ave}^{sd}>\zeta_{T,i,ave}^{sd,tra}$ designed in this paper improves upon the traditional Newton iteration method. This proof demonstrates that, within the same number of iterations, the difference Newton method achieves a smaller imbalance between supply and demand, significantly enhancing the iteration speed of the integrated energy system and reducing the amount of computation.

4.2 DNEA convergence is proved

Starting with the first iteration, $pr_{T,1}^{p,h}$, $pr_{T,2}^{p,h}$, are the calculated prices for the second iteration. Due to price changes, the imbalance of supply and demand alters the value of $\zeta_{T,1-2}^{sd}$. The corresponding relationship between price and the supply-demand imbalance assumes a linear characteristic between price and supply. The new iteration price $pr_{T,3}^{p,h}$ is determined when supply and demand are balanced. The first iteration point is connected to the second iteration point on the price and supply function, with a linear slope of $f'_{\dot{p}r_{T,12}^{p,h}}$ Lagrange's theorem indicates that there is a point ε_1 between the first and second iteration points with a slope satisfying $f'_{\varepsilon_1}=f'_{\dot{p}r_{T,12}^{p,h}}$ The second iteration point is connected to the third iteration point, with a linear slope of $f'_{\dot{p}r_{T,23}^{p,h}}$ Similarly, it can be found in the two point ε_2, $f'_{\varepsilon_2}=f'_{\dot{p}r_{T,23}^{p,h}}$, by the nature of the convex function, the inequality of $f'_{\varepsilon_1}>f'_{\varepsilon_2}$, therefore, inequality $f'_{pr_{T,12}^{p,h}}>f'_{\dot{p}r_{T,23}^{p,h}}$ It is also known that, ensuring that the units change with $\Delta pr_{T,i}^{p,h}$, $\Delta\zeta_{T,i}^{sd}$, the change in becomes progressively smaller. Thus, the iteration points for the balance between supply and demand, obtained by linear prediction, do not exceed the supply and demand balance formed by the convex function.

4.3 DNEA optimality

In the energy body, a balance between supply and demand for electricity and heat must be maintained. Electricity and heat conversion are employed to compensate for energy deficiencies. Assuming equal prices for electricity and heat, if the energy body lacks a heat quantity of $H_{ij,T}^{now}$, $H_{ij,T}^{lack}$, the surplus electricity and power are $P_{ij,T}^{now}$, $P_{ij,T}^{lack}$, respectively. If electricity is not used for heat conversion, an increase in price for this portion of heat is required $pr_T^{h,ch}$, $pr_T^{h,unit}=H_{ij,T}^{lack}/pr_T^{h,ch}$, with and satisfying the equation. As the cost function of all participants in the energy body is convex, thus the $pr_T^{h,unit}>pr_{T,i}^{p,h}$, and the energy and power for the excess production unit price are $pr_T^{p,unit}$. The convex function properties indicate that the energy cost function has a larger slope for a larger y, with the slope representing the energy unit price. Therefore, the inequality $pr_T^{h,unit}>pr_{T,i}^{p,h}>pr_T^{p,unit}$ is obtained, ensuring that equal prices for electricity and heat result in the largest gains for the energy body.

4.4 DNEA kinetic behavior analysis

This section provides mathematical proof that the difference Newton iterative algorithm designed in this paper effectively avoids kinetic behavior. Based on the convergence proof, the difference Newton designed in this paper gradually tends toward a supply and demand balance of 0. Setting parameter σ_T^{aisd} as the allowable maximum imbalance between supply and demand, the energy system is triggered from the beginning and iterates infinitely. The first time the supply and demand equilibrium is reached is at time T, and $|\zeta_{T,i}^{sd}|<\sigma_T^{aisd}$ satisfies the supply and demand imbalance $\zeta_{T,i}^{sd}$. It can be concluded that convergence has been achieved, eliminating the need for further triggering and avoiding infinite iterations within a limited time, thus preventing kinetic behavior.

5 DNEA algorithm simulation analysis

To verify the algorithm presented in this manuscript, a testing of a distributed algorithm based on differential points and Newton's method was performed on an energy system described in Appendix 5, wherein the fundamental parameters of the simulation device are exhibited. Figure 1 portrays the integrated energy system under consideration. A condition is stipulated in this paper, wherein the energy supply and demand must remain within 10 kW of each other to achieve a balance between energy production and consumption. The algorithm was designed to accomplish this goal, and it achieved the desired balance within five iterations. The simulation process is as follows.

5.1 DNEA simulation analysis iteration speed

A comparison between the iterative processes of the distributed algorithm based on differential points and Newton's method and the traditional finite difference algorithm was conducted on five energy systems with unbalanced supply and demand. The simulation results, depicted in Figure 2, demonstrate that the differential points Newton algorithm achieved a supply and demand balance of less than 10 kW within the fifth iteration without causing any disturbances. In contrast, the traditional algorithm failed to reach the optimal balance even after 50 iterations. Dichotomy optimization for the iterative error is small, the eight time but also known from the analysis of the simulation, the final results, not avoid kino, cannot ensure the final iteration for optimal

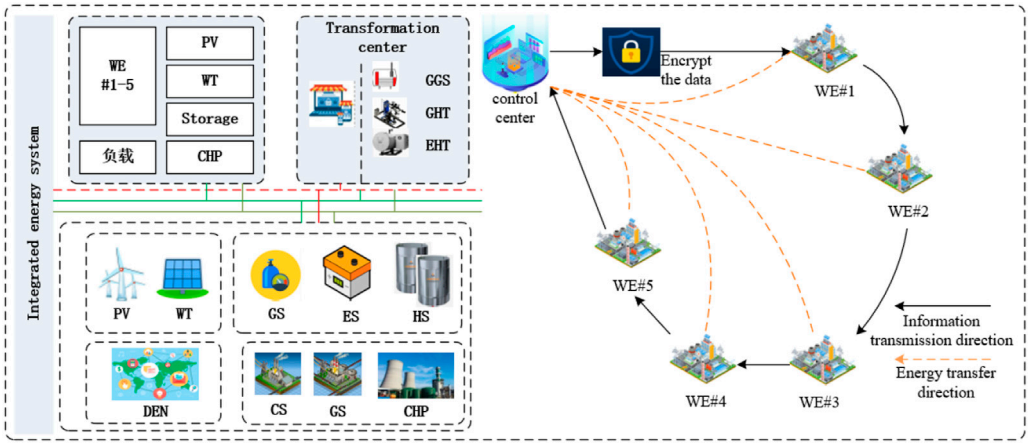

FIGURE 1
DNEA algorithmic trading structure.

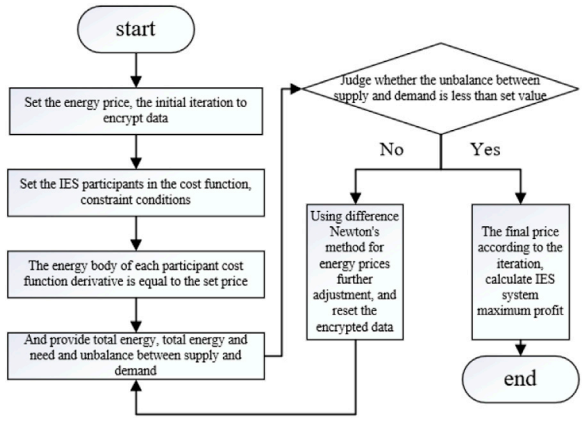

FIGURE 2
IES difference flow chart of Newton's method.

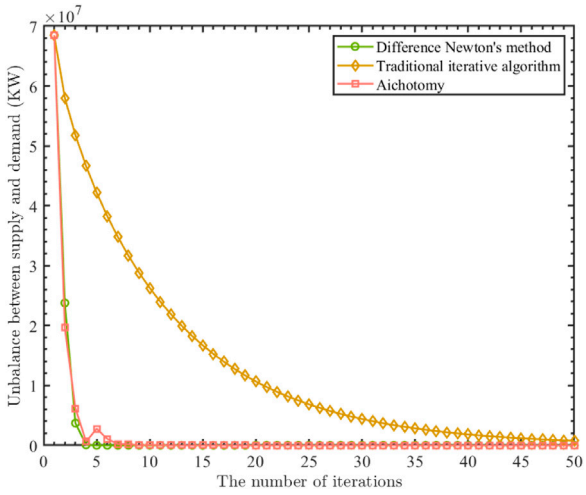

FIGURE 3
the balance between supply and demand iteration curve.

results. Simulation results depicted in Figure 2, Figure 3 indicate that all participants in the energy system, designed in this manuscript, achieved rapid convergence to the optimal forecast price point while ensuring a balance between supply and demand. These results verify the feasibility and effectiveness of the algorithm presented in this paper. The differential points Newton algorithm was employed to calculate the energy system under conditions of supply and demand balance, which yielded faster iteration speeds compared to traditional computing methods by several orders of magnitude. Consequently, energy losses, delays, and communication costs were considerably reduced, leading to more efficient energy systems.

5.2 DNEA simulation convergence analysis

In this paper, an integrated energy system has been designed. The simulation diagram presented in Figure 4, Figure 5, Figure 6 depicts the supply side, and reveals that the total electricity generated is 69828694.93 kW. The final values of heat and gas are 35815789.39 kW and 368579.09 kW, respectively. The relevant parameters, such as the change of price and the fast convergence to phase, contribute to achieving a stable state. As a result, the aforementioned values remain practically unchanged.

Furthermore, it is worth noting that Newton's method, when used in this study, yields highly accurate and reliable calculation results. Moreover, it significantly reduces the communication and computation workload associated with the distributed energy system, facilitating a fast scheduling process and ensuring a steady state energy system. As shown in Figure 7, the power supply amounts to 72907191.36 kW, and the heating load

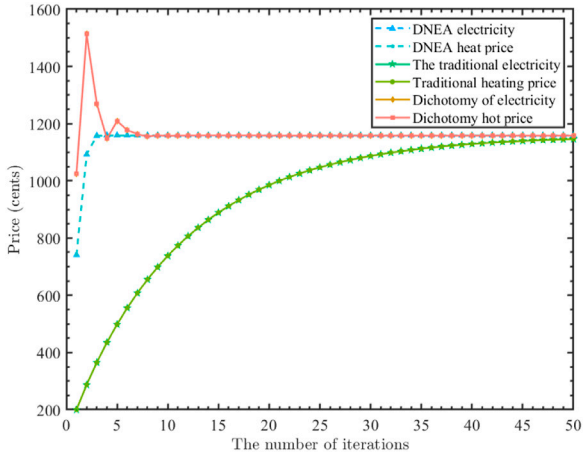

FIGURE 4
electricity price, heat price change curve.

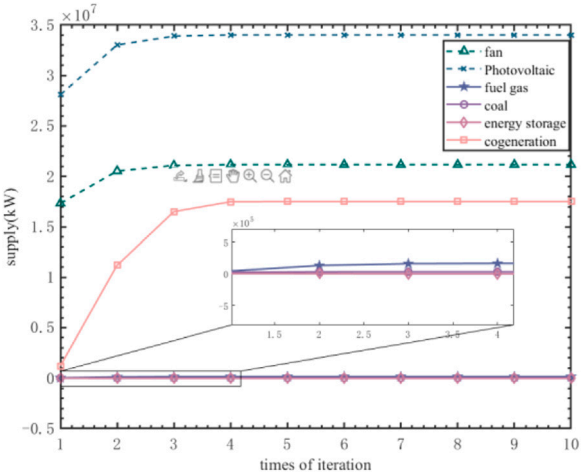

FIGURE 6
power supply curve to the participants.

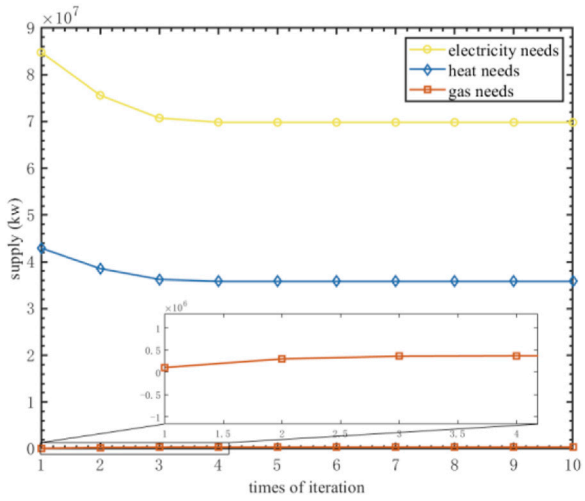

FIGURE 5
energy demand curve.

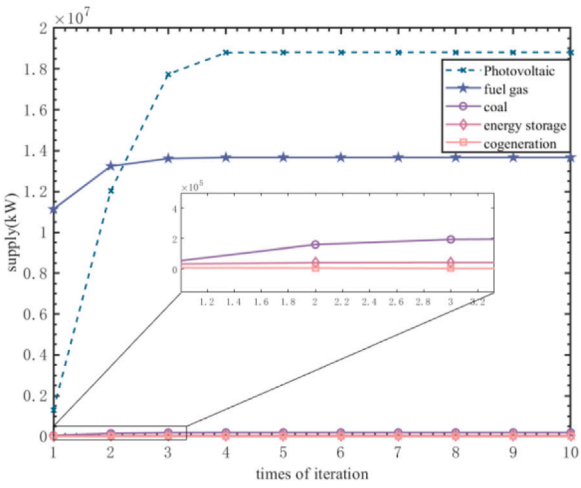

FIGURE 7
heating participants curves of heating load.

reaches 32737316.53 kW, thereby achieving a balance between supply and demand.

Combining the simulation results presented in Figure 4, Figure 5, Figure 6, Figure 7, Figure 8, it can be concluded without surprise that by utilizing the difference Newton's method, this study is capable of rapidly achieving a stable state, while simultaneously ensuring that the results remain stable post convergence.

5.3 Ring to privacy protection analysis

Traditional algorithm (Tan and Li, 2022) privacy often meet:

$$Mpl_T = \frac{Ac_T{}^{*}Na_T}{2} \tag{49}$$

Type: Mpl_T refers to privacy, and Ac_T, represents average connectivity, the term Na_T denotes an agent. Combined with the simulation Figure 9 shows in conventional privacy protection algorithms, an increase in the number of agents and average connectivity leads to a gradual enhancement in privacy levels. However, in this study, the researchers have designed a distinct Newton algorithm with a ring structure. In this approach, the growth in the number of agents and average connectivity does not result in elevated privacy levels, but rather maintains comprehensive privacy protection for the agents involved.

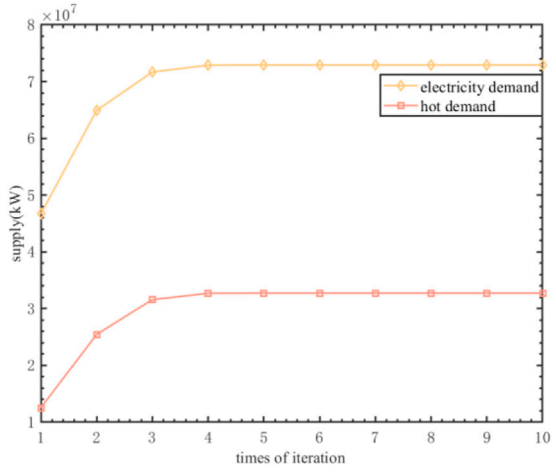

FIGURE 8
load side can use change curve.

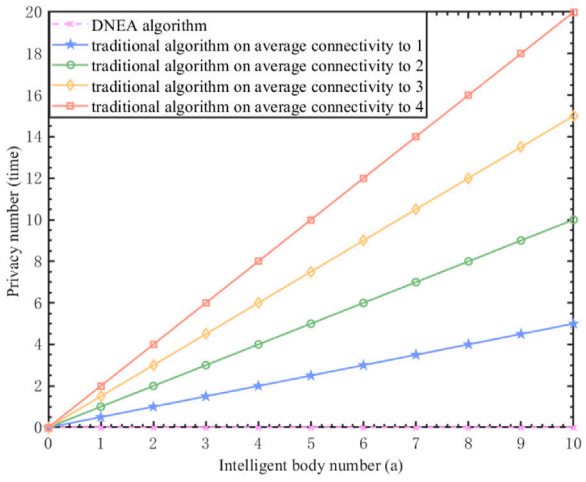

FIGURE 9
Privacy number and average number of connectivity and agent relationship diagram.

5.4 Usage scenarios and limit analysis of the algorithm

The utilization of the DNEA algorithmic approach is not applicable within the context of an integrated energy system, as the cost function follows a convex pattern. This system is characterized by interconnections, and it should not be employed in scenarios with high-quality energy standards, such as parks, intelligent buildings, hospitals, among others.

6 Conclusion

The calculation speed for the traditional iterative algorithm was evaluated multiple times, and each participant achieved the optimal convergence value. This confirmed the feasibility and stability of the proposed algorithm. However, it should be noted that this algorithm is not suitable for participants in the energy system with convex cost functions and constraints. Future scholars may explore non-convex cost functions and constraints to further develop the proposed algorithm. One limitation of this paper is that it did not address the non-convex cost function and constraints for the proposed algorithm.

Data availability statement

The original contributions presented in the study are included in the article/Supplementary Material, further inquiries can be directed to the corresponding author.

Author contributions

XC and XK has corrected the format and simulation prove. Other study is carried out by XL. All authors contributed to the article and approved the submitted version.

Conflict of interest

The authors declare that the research was conducted in the absence of any commercial or financial relationships that could be construed as a potential conflict of interest.

Publisher's note

All claims expressed in this article are solely those of the authors and do not necessarily represent those of their affiliated organizations, or those of the publisher, the editors and the reviewers. Any product that may be evaluated in this article, or claim that may be made by its manufacturer, is not guaranteed or endorsed by the publisher.

Supplementary material

The supplementary material for this article can be found online at: https://www.frontiersin.org/articles/10.3389/fenrg.2023.1215786/full#supplementary-material

References

Chen, G., and Zhao, Z. Y. (2019). Delay effects on consensus-based distributed economic dispatch algorithm in microgrid. *IEEE Trans. Power Syst.* 33 (1), 602–612. doi:10.1109/tpwrs.2017.2702179

Duan, J., and Chow, M. Y. (2019). A novel data integrity attack on consensus based distributed energy management algorithm using local information. *IEEE Trans. Industrial Inf.* 15 (3), 1544–1553. doi:10.1109/tii.2018.2851248

Gao, S., He, J., Yang, S., and Xiao, B. (2022). En ergy management of interconnected microgrid bas ed on alternating direction method of multipliers method [J]. *Grid Clean Energy* 38 (06), 1 13–120.

Hemamalini, S., and Simon, S. P. (2009). Maclaurin series-based Lagrangian method for economic dispatch with valve-point effect. *IET Generation, Transm. Distribution* 3 (9), 859–871. doi:10.1049/iet-gtd.2008.0499

Huang, B. N., Liu, L. N., Zhang, H. W., Li, Y. S., and Sun, Q. Y. (2019). Distributed optimal economic dispatch for microgrids considering communication delays. *IEEE Trans. Syst. Man, Cybern. Syst.* 49 (8), 1634–1642. doi:10.1109/tsmc.2019.2900722

Li, F. Y., Qin, J. H., and Kang, Y. (2019). Multi-agent system based distributed pattern search algorithm for non-convex economic load dispatch in smart grid. *IEEE Trans. Power Syst.* 34 (3), 2093–2102. doi:10.1109/tpwrs.2018.2889989

Li, Y., Gao, D. W., Gao, W., Zhang, H., and Zhou, J. (2020). Double-mode energy management for multi-energy system via distributed dynamic event-triggered Newton-raphson algorithm. *IEEE Trans. Smart Grid* 11 (6), 5339–5356. doi:10.1109/tsg.2020.3005179

Lin, C. E., and Viviani, G. L. (1984). Hierarchical economic dispatch for piece wise quadratic cost functions. *IEEE Trans. Power Apparatus Syst.* 6, 1170–1175. doi:10.1109/tpas.1984.318445

Lv, H. (2022). *Research on coordination method of multi-type demand response considering electrica l thermal coupling [D]*. Jinan, China: Shandong University.

Marty, F., Serra, S., Sochard, S., and Reneaume, J. M. (2017). Economic optimization of a combined heat and power plant: Heat vs electricity. *Energy Procedia* 116, 138–151. doi:10.1016/j.egypro.2017.05.062

Munshi, A. A., and Mohamed, Y. A. R. I. (2019). Unsupervised nonintrusive extraction of electrical vehicle charging load patterns. *IEEE Trans. Industrial Inf.* 15 (1), 266–279. doi:10.1109/tii.2018.2806936

Nie, Y., Peng, C., Hu, Y., He, Y., Ma, G., and Huang, C. (2023). Parallel distribute d optimal economic dispatch of high penetration microgrid based on edge computing [J/OL]. *So uthern Power Grid Technol.* 1-11. [2023-01-20]].

Schfer, B., Beck, C., Aihara, K., Witthaut, D., and Timme, M. (2018). Non-Gaussian power grid frequency fluctuations characterized by Lévy-stable laws and superstatistics. *Nat. Energy* 3, 119–126. doi:10.1038/s41560-017-0058-z

Tan, J., and Li, H. (2022). Annular directed distrib uted algorithm for energy internet. *Int. Trans. Electr. Energy Syst.* 2022. doi:10.1155/2022/7717605

Tan, Z., Zhong, H., Wang, J., Xia, Q., and Kang, C. (2019). Enforcing intra-regional constraints in tie-line scheduling: A projection based framework. *IEEE Trans. Power Syst.* 34 (6), 4751–4761. doi:10.1109/tpwrs.2019.2913876

Tan, Z., Zhong, H., Xia, Q., and Kang, C. (2021). Non-iterative multiarea coordinated dispatch via condensed system representation. *IEEE Trans. Power Syst.* 36, 1594–1604. doi:10.1109/tpwrs.2020.3019828

Xie, Z., Lu, C., Wang, X., Wen-tao, Y., and Qi, C. (2022a). Microgrid based on distribute d resource cooperative contro research and appl ication of bidding strategy [J]. *Electr. Age* 10, 37–42.

Xie, Z., Lu, C., wang, X., Wen-tao, Y., and Qi, C. (2022b). Microgrid based on distribute d resource cooperative contro research and appl ication of bidding strategy [J], the electrical age, 2022(10):37-42 control in dcmicrogrid based on linear matrix I nequalities [J], header-icon. *J. Sol. Energy* 43 (05), 45–52.

Yang, M., and Wang, J. (2021). Optimal scheduling of islanded microgrid considering uncertain output of renewable energy[J]. *Chin. J. Electri cal Eng.* 41 (03), 973–985.

Yang, Y., and Yang, P. (2022). The hierarchical modeling approach for centralized control microgrid cyber physical system [J]. *Chin. J. Electr. Eng.* 42 (19), 7088–7102.

Yin, S., Qian, A., Zeng, S. Q., Wu, Q., Ran, H., and Jiang, D. (2018). Challenges and prospects of multi-energy distributed optimization for energy internet. *Power Syst. Technol.* 42 (5), 1–10.

Yu-Shuai, L., Tian-yi, L., Gao, W., and Gao, W. (2020). Distributed collaborative optimization operati on approach for integrated energy system based on asynchronous and dynamic event-triggering C ommunication strategy [J]. *J. Automation* 46 (09), 1831–1843.

Zhang, H., Li, Y., Gao, D. W., and Zhou, J. (2017). Distributed optimal energy management for energy internet. *IEEE Trans. Industrial Inf.* 13 (6), 3081–3097. doi:10.1109/tii.2017.2714199

Zhang, N., Sun, Q., and Yang, L. (2020). A two-stage multi-objective optimal scheduling in the integrated energy system with we energy modeling. *Energy* 215, 119121. doi:10.1016/j.energy.2020.119121

Zhang, Y., Lin, Y., Huang, G., Yang, X., Weng, G., and Zhou, Z. (2023). Rev iew on applications of deep reinforcement learning in regulation of microgrid systems [J/OL]. *Power Grid Technol.* 1-15. [2023-01-20].

Zhang, Z., and Chow, M. Y. (2012). Convergence analysis of the incremental cost consensus algorithm under different communication net work topologies in a smart grid. *IEEE Trans. Power Syst.* 27 (4), 1761–1768. doi:10.1109/tpwrs.2012.2188912

Zhao, C. C., He, J. P., Cheng, P., and Chen, J. M. (2016). Analysis of consensus based distributed economic dispatch under stealthy attacks. *IEEE Trans. Industrial Electron.* 64 (6), 5107–5117. doi:10.1109/tie.2016.2638400

Zhong, Y., Zhou, Y., Gao, Z., Ton, J., and Yu, D. (2022). Optimal scheduling of micro grid based on ICA and NSGA-II compound algori thm [J]. *Appl. Electr.* 41 (11), 78–8 4.

Zhu, Y., Zhang, J., Cheng, Q., Deng, K. F., Ma, K. J., Zhang, J. H., et al. (2022). Research progress of automatic diatom test by artificial intelligence. *J. Mech. Inf. Technol. y* 38 (07), 14–19. doi:10.12116/j.issn.1004-5619.2021.410404

frontiers | Frontiers in Energy Research

TYPE Original Research
PUBLISHED 22 June 2023
DOI 10.3389/fenrg.2023.1204960

Check for updates

OPEN ACCESS

EDITED BY
Yushuai Li,
University of Oslo, Norway

REVIEWED BY
Zheng Qi,
North China Electric Power University, China
Jiawei Tang,
Cranfield University, United Kingdom
Dake Gu,
Northeast Electric Power University, China

*CORRESPONDENCE
Kun Zhang,
zhangkun@sut.edu.cn

RECEIVED 13 April 2023
ACCEPTED 09 June 2023
PUBLISHED 22 June 2023

CITATION
Qiu S, Zhang K, Chen Z, Zhang Y, Chen Z and Cheng S (2023), Identification model for weak areas of transient energy balance in EESs based on dynamic grid partitioning.
Front. Energy Res. 11:1204960.
doi: 10.3389/fenrg.2023.1204960

COPYRIGHT
© 2023 Qiu, Zhang, Chen, Zhang, Chen and Cheng. This is an open-access article distributed under the terms of the Creative Commons Attribution License (CC BY). The use, distribution or reproduction in other forums is permitted, provided the original author(s) and the copyright owner(s) are credited and that the original publication in this journal is cited, in accordance with accepted academic practice. No use, distribution or reproduction is permitted which does not comply with these terms.

Identification model for weak areas of transient energy balance in EESs based on dynamic grid partitioning

Shi Qiu[1], Kun Zhang[1]*, Zhuo Chen[1], Youming Zhang[2], Zhe Chen[1,3] and Songqing Cheng[1]

[1]Shenyang University of Technology, Shenyang, Liaoning, China, [2]State Grid Liaoning Electric Power Co., Ltd., Shenyang, Liaoning, China, [3]The Faculty of Engineering and Science, Aalborg University, Aalborg, Denmark

In response to the high uncertainty of large-scale new energy output in the electrical energy system (EES) and the weak controllability of energy output at multiple time scales, this paper proposes a weak grid identification model for transient energy balance in EESs based on grid partitioning, which has an increasingly complex impact on the weak areas of transient energy balance in the sending-end network. First, the accumulation of port energy during transient faults and the propagation mechanism of port energy in the sending-end system were studied, and an EES transient energy propagation mechanism model was established. Then, considering the energy balance support requirements of nodes, an EES grid partitioning model was established. Afterward, based on the characteristics of transient energy propagation and a grid partitioning model, an identification model for weak areas of transient energy balance in EESs was constructed. Finally, based on actual operating data, numerical simulations were conducted, and the results showed that the proposed weak grid identification model for transient energy balance can meet the requirements for transient stability analysis and transient energy balance characteristic analysis during actual operation of power grids.

KEYWORDS

EES, transient stability, dynamic grid partition, weak area identification, transient energy

1 Introduction

Under the guidance of the adjustment of the energy consumption structure and the strategic policy of "carbon peak and carbon neutrality," the construction of an EES connected to new energy (Li Y. et al., 2019; Li et al., 2020) with new energy as the main body is deepening. China is gradually forming a power grid pattern of large-scale cross-regional interconnected systems consisting of wind power and photovoltaic resource-rich sending-end power grids in the western and northwestern regions through long-distance UHV AC and DC channels, and eastern load-intensive regional power grids (Wu et al., 2018; Huang et al., 2019; Li and Liu, 2019; Li et al., 2021). At present, the development of new energy faces the following three problems. First, the total installed capacity of new energy is far beyond the load, and limited by the characteristics of conventional power supply and power grid structures (Da Cruz Sessa and Mariano Lessa Assis, 2018), the difficulty of new energy consumption is prominent. Second, a large amount of new energy power stations

leads to a reduction of conventional power supply in the system, the reduction of system inertia, frequency and voltage response characteristics, and a significant increase in the security risk of power grid operation (Li C. S. et al., 2019). Third, the new energy power station has no energy storage link, which is a disturbance source for the power grid and has no adjustment ability. Therefore, the stability circumstance of large-scale new energy connected to the power grid urgently needs to seek new means to assist traditional units to promote the ensemble regulation ability of the power grid (Bhui and Senroy, 2017; Zhang J. et al., 2022; Zhang DW. et al., 2022). The research and establishment of the transient energy stability criterion and weak area identification method of transient energy balance in new energy sending-end systems forms the theoretical and algorithm basis for further research on the robust control model of transient energy balance in sending-end systems based on battery energy storage coordination and can also provide the theoretical basis for the optimization of transient stability-related constraints for the optimal configuration of battery energy storage in sending-end systems (Heetal, 2020).

At present, researchers all around the world have already conducted in-depth studies on the DC transmission of EESs connected to new energy, power grid stability, and identification of weak areas of transient energy balance. In HAN et al. (2018), for solving the transient overvoltage problem of AC bus caused by DC blocking in the HVDC transmission system sending end, the emergency shutdown strategy of triggering DC blocking is improved to slow down the triggering process of DC blocking and ensure the stable operation of wind turbines. In order to maintain the safety and stability of the HVDC transmission system and avoid the outage of the HVDC transmission system caused by transient fault of the DC line (Xu et al., 2019; Ding et al., 2021), Muniappan (2021) added the fault restart function of the DC line in DC control protection. Scientific and reasonable division of the grid is the key to the continuous implementation of the target grid of the sending-end power grid.

The scientific and reasonable division of grids and the identification of weak areas are key to the sustainable implementation of the target grid structure of grid transformation. LIU et al. (2010) considered the uncertainty of changes in the location of fault points and proposed a method to determine the commutation fault-related area (CFCR), searching for weak areas. In FU et al. (2011) and CAI et al. (2017), active margin index, sensitivity index, and other parameters were chosen as indicators to identify weak areas in the grid region, or full network voltage scanning was used for identification. However, for more complex systems, the calculation of this identification method is more complex. XIAO et al. (2016) proposed a new method that combines an improved modal method and a P-V curve to identify weak areas, but the accuracy of identifying weak areas still needs to be improved.

In summary, there is relatively little research on EES partition based on the energy balance capability. Therefore, this paper studies the propagation mechanism of transient energy in an EES during fault occurrence and establishes a transient energy propagation mechanism model for EES fault ports. Considering the energy balance support requirements of nodes in EESs, we establish an EES grid partitioning model. The transient energy propagation characteristics and the identification method of the EES energy balance weak partition area were also studied. Finally, a simulation model for identifying the weak grid of transient energy balance in the EES was established. Based on the analysis results, it can be concluded that the proposed method for identifying the weak grid of transient energy balance can meet the analysis requirements of the power grid.

2 Transient energy propagation mechanism of fault ports in the EES

2.1 Unconstrained transient energy propagation model for fault ports in the EES

To study the propagation mechanism of transient energy at the fault port in the EES during the occurrence of a fault, this paper establishes an unconstrained propagation model for transient energy:

$$N(x)\ddot{x} + D(x,\dot{x})\dot{x} + H(x) + G(x,\dot{x}) = u \tag{1}$$

where $x \in R^n$, $\dot{x} \in R^n$, and $\ddot{x} \in R^n$ are the state phasors of each node, the derivative of state phasors, and the second derivative of the corresponding system in the transmission process of the fault port energy under the transient fault state, respectively; $N(x) \in R^{n\times n}$, $D(x,\dot{x})\dot{x}$, $H(x) \in R^n$, and $G(x,\dot{x}) \in R^n$ are the inertia influence relation matrix, forward energy propagation term, reverse energy propagation term, and energy loss term when the fault port energy is transmitted in the interconnected system network under the transient fault state, respectively; and $u \in R^n$ is the control variable of the influence of power supply and load connected to each node on the energy of the fault port in the transient fault state.

The energy action model of node s can be transformed into the following form:

$$\begin{cases} N_i(x_s)\ddot{x}_s + D_s(x_s,\dot{x}_s)\dot{x}_s + H_s(\dot{x}_s) + G_s(x_s,\dot{x}_s) + A_s(x_s,\dot{x}_s,\ddot{x}_s) = u_s \\ A_i(x_s,\dot{x}_s,\ddot{x}_s) = \left\{\sum_{r=1,r\neq s}^{n} N_{sr}(x_s)\ddot{x}_s + [N_{ss}(x_s) - N_s(x_s)]\ddot{x}_s\right\} \\ \quad + \left\{\sum_{r=1,r\neq s}^{n} D_{sr}(x_s,\dot{x}_r)x_s,\dot{x}_r + [D_{sr}(x_s,\dot{x}_s) - D_s(x_s,\dot{x}_s)]\dot{x}_s\right\} \\ \quad + [\overline{H_s}(x_s) - H_s(x_s)] \end{cases} \tag{2}$$

where $x_s, \dot{x}_s, \ddot{x}_s, \overline{H_s}(x_s), G_s(x_s,\dot{x}_s)$, and u_s represent the s-th component of vectors $x, \dot{x}, \ddot{x}, \bar{H}(x), G(x,\dot{x})$, and u, respectively; $N_{sr}(x)$ and $D_{sr}(x,\dot{x})$ are the s-th and r-th components of the matrix $N(x)$ and $D(x,\dot{x})$, respectively; and $A_s(x,\dot{x},\ddot{x}) \in R$ is the energy transfer subsystem cross-linking term of node s.

Setting $x_s = [x_{s1} \quad x_{s2}]^T = [x_s \quad \dot{x}_s]^T (s = 1, 2, \cdots, n)$, the port transient energy transitive relation network of the aforementioned formula can be transformed into the following form:

$$\begin{cases} \dot{x}_s = B_s x_s + C_s[f_s(x_s,\dot{x}_s) + g_s(x_s)u_s + h_s(x_s,\dot{x}_s,\ddot{x}_s)] \\ \dot{y}_s = D_s x_s \end{cases} \tag{3}$$

where x_s is the state phasor of node s, y_s is the output of node s, and

$$\begin{cases} B_s = \begin{bmatrix} 0 & 1 \\ 0 & 0 \end{bmatrix}; C_s = \begin{bmatrix} 0 \\ 1 \end{bmatrix}; D_s = \begin{bmatrix} 1 & 0 \\ 0 & 1 \end{bmatrix}; \\ f_s(x_s, \dot{x}_s) = N_s^{-1}(x_s)[-D_s(x_s, \dot{x}_s)\dot{x}_s - H_s(x_s) - G_s(x_s, \dot{x}_s)]; \\ g_s(x_s) = N_s^{-1}(x_s); \\ h_s(x_s, \dot{x}_s, \ddot{x}_s) = -N_s^{-1}(x_s)A_s(x_s, \dot{x}_s, \ddot{x}_s) \end{cases} \tag{4}$$

2.2 Transient energy transfer model for EES ports based on multiple constraints

During the transient energy balance control process of the EES fault port, when constrained by load fluctuations, wind and photovoltaic output fluctuations, transmission line capacity, and other constraints, each constraint condition is uniformly represented as follows:

$$\lambda(x, t) = 0 \tag{5}$$

where $x \in R^n$ represents the variables of each node in the EES; λ: $R^n \to R^m$ represents the state variable constraint function corresponding to each node; and m is the dimension of the constraint condition acting on the transient energy transmission of the port in the transient energy balance control process.

The derivative of the aforementioned equation is taken to obtain

$$\dot{\lambda}(x, t) = \frac{\partial \lambda(x, t)}{\partial x}\dot{x} + \frac{\partial \lambda(x, t)}{\partial t} \tag{6}$$

The definition is as follows:

$$\begin{cases} K_\lambda(x, t) = \dfrac{\partial \lambda(x, t)}{\partial x} = \dfrac{\partial \lambda}{\partial x} \\ \dot{Q}(t) = \dfrac{\partial \lambda(x, t)}{\partial t} \end{cases} \tag{7}$$

where $K_\lambda(x, t)$ is the $m \times n$-dimensional Jacobian matrix, $\dot{Q}(t)$ is the change vector of the state variable constraint condition, and its size depends on the change rate of the state variable. Eq. 6 is represented as follows:

$$\dot{\lambda}(x, t) = K_\lambda(x, t)\dot{x} + \dot{Q}(t) \tag{8}$$

The relationship between the effect of each state constraint on the transient energy transfer path and mode of the port p and its corresponding x in the spatial coordinate system composed of each node in the EES is as follows:

$$p = I(x) \tag{9}$$

Eq. 5 can be rewritten as follows:

$$\lambda(p, t) = \lambda(I(x), t) \tag{10}$$

At this time, the Jacobian matrix is as follows:

$$K = K_\lambda(x, t) = \frac{\partial \lambda}{\partial p}\frac{\partial I(x)}{\partial x} \tag{11}$$

Assuming $\delta\lambda(p)$ as the contribution of the constraint condition to the changes in the transient energy transfer joint path and mode of the fault port, the following can be obtained:

$$\delta\lambda = \frac{\delta\lambda}{\delta p}\delta p = 0 \tag{12}$$

Taking the Lagrange multiplier $f \in R^m$ into account, we can obtain the following:

$$\left(\frac{\delta\lambda}{\delta p}\delta p\right)^T f = 0 \tag{13}$$

Set

$$(\delta p)^T G_2 = 0 \tag{14}$$

where G_2 represents the action of multidimensional constraints on the change of the transient energy transfer path and mode at fault ports; δp is the variation of various parameters under the action of G_2 after the transient energy propagation of the fault port ends. From Eqs 13, 14, it can be concluded that

$$(\delta p)^T G_2 - \left(\frac{\delta\lambda}{\delta p}\delta p\right)^T f = 0 \tag{15}$$

Transforming the state constraint G_2 into the system state space of the transient energy balance control process at the fault port, we obtain the following:

$$G_1 = K^T f = K_\lambda^T(x, t) f \tag{16}$$

In summary, the system model for the transient energy balance control process of fault ports considering n state constraints is as follows:

$$N(x)\ddot{x} + D(x, \dot{x})\dot{x} + H(x) + G(x, \dot{x}) = u + K_\Phi^T(x, t) f \tag{17}$$

The variables of each node in the network defined in the aforementioned system are as follows:

$$x = \begin{bmatrix} x_1 \\ x_2 \end{bmatrix}, x_1 \in R^{n-m}, x_2 \in R^m \tag{18}$$

Eq. 18 is substituted into Eq. 5 to obtain

$$\Phi(x_1, \Omega(x, t), t) = 0 \tag{19}$$

where $x_2 = \Omega(x_1, t)$, and Eq. 18 can be expressed by variable x_1 as

$$x = \begin{bmatrix} x_1 \\ \Omega(x_1, t) \end{bmatrix} \tag{20}$$

From the derivation of Formula 20, we obtain

$$\begin{aligned} \dot{x} &= \begin{bmatrix} \dot{x}_1 \\ \dfrac{\partial \Omega(x_1, t)}{\partial x_1} + \dfrac{\partial \Omega(x_1, t)}{\partial t} \end{bmatrix} \\ &= \begin{bmatrix} J_{n-m} & 0 \\ \dfrac{\partial \Omega(x_1, t)}{\partial x_1} & J_m \end{bmatrix} \begin{bmatrix} \dot{x}_1 \\ 0 \end{bmatrix} + \begin{bmatrix} 0 \\ \dfrac{\partial \Omega(x_1, t)}{\partial t} \end{bmatrix} \\ &= U\dot{\theta} + I \end{aligned} \tag{21}$$

where $U = \begin{bmatrix} J_{n-m} & 0 \\ \dfrac{\partial \Omega(x_1,t)}{\partial x_1} & J_m \end{bmatrix} \in R^{n\times n}$, $\dot{\theta} = \begin{bmatrix} \dot{x}_1 \\ 0 \end{bmatrix} \in R^n$, and $I = \begin{bmatrix} 0 \\ \dfrac{\partial \Omega(x_1,t)}{\partial t} \end{bmatrix} \in R^n$.

Eq. 21 can be obtained by calculating the second derivative of x:

$$\ddot{x} = U\ddot{\theta} + \dot{U}\dot{\theta} + \dot{I}. \tag{22}$$

From Eqs 20–22, it can be concluded that

$$\begin{aligned} &N(x)\left(U\ddot{\theta} + \dot{U}\dot{\theta} + \dot{I}\right) + D(x,\dot{x})\left(U\dot{\theta} + \dot{I}\right) \\ &+H(x) + G(x,\dot{x}) = u + K_{\Phi}^{T}(x,t)f \end{aligned} \tag{23}$$

By separating the state constraint terms in the network node variable parameters, the node s model can be obtained as follows:

$$\begin{aligned} &N_s(x_s)\ddot{x}_s + D_s(x_s,\dot{x}_s)\dot{x}_s + H_s(x_s) + \\ &G_s(x_s,\dot{x}_s) + A_s(x_s,\dot{x}_s,\ddot{x}_s) - \tau_{\Phi s}^{*} = u_s \end{aligned} \tag{24}$$

where

$$\begin{aligned} A_s(x_s,\dot{x}_s,\ddot{x}_s) = &\sum_{\substack{r=1 \\ r\neq s}}^{n} N_{sr}(x)\left[(UE\ddot{x}_s)_r + \left(\dot{U}E\dot{x}_s\right)_r + \dot{I}_r\right] \\ &+N_{sr}(x)\left[(UE\ddot{x}_s)_r + \left(\dot{U}E\dot{x}_s\right)_r \quad +\dot{I}_s\right] - N_s(x_r)\ddot{x}_s \\ &+\sum_{\substack{r=1 \\ r\neq s}}^{n} D_{rs}(x_s,\dot{x}_r)\left((UE\dot{x}_s)_r + I_r\right) + D_{sr}(x,\dot{x}_s) \\ &\left((UE\dot{x}_s)_r + I_r\right) - D_s(x_s,\dot{x}_s)\dot{x}_s \\ &+\left(\overline{H_s}(x) - H_s(x_s)\right) + \left(\tau_{\Phi s}^{*} - \tau_{\Phi s}\right) \end{aligned} \tag{25}$$

3 Dynamic grid partitioning model of the EES

When considering the energy balance support requirements of nodes in the EES, the set of node state variables in the EES can be expressed as follows:

$$X = \{x_s \mid x_s \in \Omega,\ s \in S\} \tag{26}$$

where Ω can reflect the energy requirement of node s in the EES.

When the energy balance requirement of node s is Ω, the EES is divided into Λ grid regions, $\Lambda = \{0, 1, \cdots, L\}$, and the energy field matrix formed by injecting energy into each grid region is expressed as follows:

$$Y = \left\{y_s \mid y_s \in \Lambda,\ s \in S\right\} \tag{27}$$

where y_s is the injected energy of node s.

Under the given operating state variable X, the probability of each scheme for energy partition of energy field Y (this energy field is the Markov random field) is given as follows:

$$P(Y \mid X) = \frac{P(X \mid Y)P(Y)}{P(X)} \tag{28}$$

In the process of constantly changing the operating state variable X, the energy field matrix also changes accordingly. Therefore, the energy partitioning problem can be converted to solve the minimization of energy imbalance in the EES by calculating the global optimal estimation solution Y^{*}, that is, dynamically solving the minimization of energy imbalance in the EES:

$$\begin{aligned} Y^{*} &= \arg\max_{Y} P(Y \mid X) \sim \arg\min_{Y} E_g(X,Y) \\ &= \arg\min_{Y} \{E_d(X,Y) + E_s(Y)\} \end{aligned} \tag{29}$$

where $E_g(X,Y)$ represents the energy supply and demand balance condition in Y; $E_d(X,Y) = -\lg P(X \mid Y)$ represents the still present energy requirement after dividing the system; $E_s(Y) = \sum_{s,r\in N(s)} \delta(y_s, y_r)$ represents the battery energy that can be called within the dividing scope; and $N(s)$ refers to all neighboring nodes within the grid partition where node s is located.

4 Identification model of the weak partition area for transient energy balance in the EES

4.1 Identification model of the weak partition area

We establish an energy correlation model for adjacent nodes in the EES, namely, the degree of topological overlap $c_{sr}(x_s, x_r)$:

$$c_{sr}(x_s,x_r) = \frac{b_{sr}}{1-b_{sr}} \tag{30}$$

$$b_{sr} = \left|\exp\left\{\frac{-2\times\left(\|x_s - x_r\|_2\right)^2}{\left(\rho \max\limits_{r\in N_s}\|x_s - x_r\|_2\right)^2}\right\}\right|^{\gamma} \tag{31}$$

where x_s and x_r are the state variables of two adjacent nodes which provide direct energy exchange to each other, $s \neq r$; b_{sr} represents the energy exchange level; $\|x_s - x_r\|_2$ represents the Euclidean distance of adjacent nodes; ρ refers to the homogenization element of heterogeneous nodes connected to hybrid energy; and γ is the penalty element for the energy interaction exceeding limit.

Let w_s represent a set of nodes within the partition area where node s is located that has direct energy injection or cascading energy interaction, and $\vartheta_s(y_s)$ is the set of adjoining nodes that provide direct energy exchange with set w_s. Then, the energy interaction degree with high-order topological prior for nodes $c_{w_s}(x_s, x_{\vartheta_s})$ is as follows:

$$c_{w_s}(x_s,x_{\vartheta_s}) = c_{N1}(x_s,x_{N1}) + c_{N2}(x_s,x_{N2}) + \cdots + c_{Ni}(x_s,x_{Ni}), \tag{32}$$

where $c_{w_s}(x_s, x_{\vartheta_s})$ represents all energy correlation values c_{Ni} related to node s added together in the partition area where node s is located; $c_{N1}, c_{N2}, \ldots, c_{Ni}$ indicates the energy correlation between node s and all adjacent nodes that have an energy interaction.

In summary, we establish a high-order prior energy model for node energy correlation:

$$E_h(x_w|\Upsilon) = \sum_{s\in S, r\in N_s}\left[\frac{b_{sr} + \sum\limits_{u\neq s,r} b_{su}b_{ru}}{\min\left\{\sum\limits_{u\neq s} b_{su}\sum\limits_{u\neq r} b_{ru}\right\} + 1 - b_{sr}}\right], \tag{33}$$

where $E_h(x_w|\Upsilon)$ is the prior energy of higher-order topological structures in the grid region where node s is located; $\Upsilon = \{\rho, \gamma\}$ is the higher-order prior parameters for network partitioning.

Based on this, a Gaussian likelihood estimation model for the partition area is constructed to identify the degree of energy imbalance in each partition area:

$$\begin{cases} P(X|Y,\theta) = \prod_{s=1}^{N}\left[P\left(x_s|y_s,\theta\right)\prod_{r\in\vartheta_s}P\left(x_r|y_r,\theta\right)^{\frac{w(y_r)}{w_r}}\right] \\ w(y_r) = \sum_{s\in S}\sum_{r\in\vartheta_s}\|x_s - x_r\| = \sum_{s\in S}\sum_{r\in\vartheta_s}(x_s + x_r - 2x_s x_r) \end{cases} \tag{34}$$

where $x_r = \{x_r | r \in \vartheta_s\}$ is the neighborhood node state variable set of node s; $\theta = \{\mu_l, \sigma_l^2\}_{l\in\Lambda}$, where μ_l, and σ_l^2 are the probability distribution mean and variance of energy imbalance within a partition area; w_r is the probability calculation weight of energy imbalance within the partition area, and $w_r = \sum_{r\in N_s} w(y_r)$. The smaller the w_r, the larger the estimated value Y^* of the energy imbalance within its corresponding partition area, and the weaker the energy balance ability of the partition area.

4.2 Identification process of the weak partition area for transient energy balance in the EES

The specific steps for identifying EES energy balance weak grids based on a prior knowledge model are as follows:

Step 1: Initialize the parameter node set w_s, the homogenization element of heterogeneous nodes connected to hybrid energy ρ, and the penalty element for the energy interaction exceeding limit γ.

Step 2: Calculate the energy correlation between node s and all adjacent nodes with the energy interaction $c_{sr}(x_s, x_r)$ in the partition area where node s is located.

Step 3: Calculate the prior energy of the topological structure $\gamma E_h(x_{w_s}|\gamma)$ of the partition area where node s is located.

Step 4: Repeat steps 2 to 3 until $s = S$.

Step 5: Sort the estimated values Y^* of the energy imbalance within the partition area by adopting the Gaussian likelihood estimation model and identify the weaker energy balance ability partition area.

The flow chart for grid identification with weak energy balance capability is shown in Supplementary Figure S1.

5 Example analysis

Consulting the actual operating EES data, this article designs a simulation system, as shown in Supplementary Figure S2: the add-up load of the sending-end power grid at node 1 is 10,000 MW, the AC transmission is 2,000 MW, and the DC transmission is 3,000 MW. The total load of the node 2 receiving-end system is 60,000 MW, and the DC is 3,000 MW from the sending-end system. The total load of the node 3 receiving-end system is 50,000 MW, and the AC 2,000 MW is connected from the sending-end system.

The internal equivalent network structure of the new energy transmission terminal grid is shown in Supplementary Figure S3. G1, G5, and G8 are three photovoltaic converging power nodes with capacities of 3,000, 2,000, and 3,000 MW, respectively. G2 is the wind power-gathering power node with a capacity of 4,000 MW. G13 is a hydropower power node with a capacity of 6,000 MW; G11 is a thermal power node with a capacity of 2,000 MW; B1, B5, B6, B14, and B24 are battery energy storage units with capacities of 1,500, 1,000, 1,600, 1,100, and 900 MW·h, respectively.

We built a system transient stability simulation model based on MATLAB, with a limit cutoff time of 0.3 s set for simulation. Aiming at testing and verifying the effectiveness of the EES weak grid identification method for transient energy balance proposed in this paper, two simulation scenarios are set. Scenario 1 does not consider the energy support role of energy storage devices in the transient energy equilibration, and scenario 2 considers energy storage to adjust the energy balance.

5.1 Energy storage devices do not participate in energy balance

Supplementary Figure S4 shows the equivalent power angle instability curve and its corresponding transient stability margin index change curve at node 1 of the sending-end system shown in Supplementary Figure S3, without considering the participation of energy storage in regulation, when a fault occurs at node 1 with a three-phase short circuit, and this fault is not removed within the limit removal time.

As shown in Supplementary Figure S4, when the fault occurs along the output line of channel 1 of the sending-end system and the system becomes unstable, the power angle of the system at node 1 exceeds the power angle stability limit after the first swing and the sending-end system loses synchronization with the receiving-end system. During the instability process of the sending-end system, the equivalent power angle change curve of the system at node 1 is a continuously increasing oscillation process. Meanwhile, as shown in the variation curve of the stability margin index of the system in Supplementary Figure S4, the curve shows that the stability margin index of the sending-end changes significantly during the first swing of the power angle swing of node 1, indicating that the system will lose synchronization with the receiving-end system.

According to the EES dynamic grid partitioning model, as mentioned earlier, the grid partitioning of the sending-end power grid shown in Supplementary Figure S2 is carried out, and the partitioning results are shown in Supplementary Figure S5.

Supplementary Figure S5 is shows that when a transient fault happens in the output channel of the sending-end system, due to the large startup methods of new energy sources, such as photovoltaic and wind power in the system, and the lack of energy storage, when dividing the grid of the sending-end network, the new energy sources are all divided in the same grid as hydroelectric or thermal power units to ensure that the transient energy balance characteristics within the grid meet the system stability requirements as much as possible.

When the sending-end system loses stability under the scenario of the three-phase short circuit fault at node 1 in Supplementary Figure S3, the energy balance weak grid identification method put forward in this article is adopted to calculate the estimated energy imbalance of each grid. This article mainly calculates the estimated value of energy imbalance within the grid and ranks the calculation results of multiple grids in order to identify the grid with the largest energy imbalance and the weakest energy balance ability. The comparison between the calculation results and the maximum frequency deviation of each grid during the fault time period can be seen in Supplementary Table S1.

Supplementary Table S1 shows that except for partition area 1, where the fault point is located, the variation pattern of the estimated value of energy imbalance calculated using the method put forward in this article is mostly consistent with the variation pattern of the maximum grid frequency deviation during the fault time period, which verifies the effectiveness of the energy balance weak partition area identification method mentioned earlier. In addition, when the sending-end system becomes unstable, the frequency deviation of each partition area in the system is relatively large. This also indicates that when the energy storage system is not configured, the sending-end system will not only lose synchronization with the receiving-end system when facing large transient energy injection but also cause significant energy oscillations inside the sending-end system. If the startup mode of thermal and hydroelectric units existing in the power grid is small at this time and the response speed can hardly reach the requirement level of suppressing transient energy propagation within an effective time, the sending-end system is likely to undergo splitting or even collapse.

5.2 Energy storage devices participate in energy balance

Considering the involvement of multi-energy storage equipment involved in energy regulation, at the time the fault occurs at node 1 of channel 1 of the sending-end system in Supplementary Figure S2, the equivalent power angle instability curve and its corresponding transient stability margin index change curve at node 1 are shown in Supplementary Figure S6.

Supplementary Figure S6 shows that at the time of fault occurrence to channel 1 in the sending-end system, the system protection and safety control devices do not cut off the fault within the limit cutting time. The power angle of node 1 in the system exceeds the power angle stability limit after the first swing. However, due to the rapid absorption of transient energy by the energy storage device configured in the sending-end system after the system's transient energy exceeds the limit, the amplitude of the power angle swing in the system decreases rapidly during the second swing and makes the subsequent oscillation process converge quickly.

Meanwhile, the variation curve of the stability margin index in Supplementary Figure S6 shows that the stability margin index in the sending-end system quickly decreases to within the stability threshold after a jump in the first swing of the power angle swing at node 1. It can be seen that after configuring battery energy storage, the ability of the sending-end system to maintain transient stability has been significantly improved, but the system will still enter an unstable state, causing significant energy impacts on the synchronous power supply, new energy power supply, and load of the sending-end system.

The grid division results when considering the participation of energy storage devices in regulation are shown in Supplementary Figure S7.

Supplementary Figure S7 shows that compared to the grid division in Supplementary Figure S5, the transient energy balance grid division results shown in Supplementary Figure S7 not only consider the support role of traditional hydropower and thermal power units for new energy sources but also consider the support role of energy storage systems for new energy sources and loads.

The energy balance weak grid identification method proposed in this article is used to calculate the estimated energy imbalance values of each grid after re-partitioning. The comparison between the calculated results and the maximum frequency deviation of each grid during the fault time period is shown in Supplementary Table S2.

Supplementary Table S2 shows that compared with the estimated energy imbalance value in Supplementary Table S1, after considering the participation of energy storage devices, the estimated values of energy imbalance within each grid have been reduced, and the energy balance ability has been improved. This once again verifies the effectiveness of the energy balance weak grid identification method mentioned previously. Moreover, when the sending-end system is unstable due to the transient energy support effect of the energy storage system, the frequency deviation of each grid area of the sending-end system increases and decreases significantly. On the other hand, the simulation results also indicate that although the energy storage system could improve the transient energy balance ability of the system to a certain extent, relying on the energy absorption or release characteristics of a simple energy storage system still cannot effectively maintain the stability circumstance of the sending-end system during serious transient fault at the outlet of the sending channel.

6 Conclusion

To improve the stability of transient faults in EESs with battery energy storage, this paper proposes a weak partition area identification method for transient energy balance in an EES based on a high-order prior energy model with energy correlation.

(1) This article studies the transient energy propagation mechanism of ports during faults in EESs, establishes an unconstrained propagation model that reflects the transient energy propagation characteristics of ports, and adds actual multiple constraints to establish a system model that describes transient energy transfer.
(2) Considering the energy balance support requirements in EESs, this paper proposes an EES dynamic partitioning model and an energy balance weak partition area identification method based on a prior model of node energy correlation, achieving the identification of areas with weak energy balance capabilities in EES.
(3) This article is based on actual operating data and verifies the proposed method through numerical simulation. The simulation results verify the effectiveness of the proposed

transient energy balance weak grid identification method (QIN, 2015; Hu et al., 2021; Cheng et al., 2022).

Data availability statement

The original contributions presented in the study are included in the article/Supplementary Material; further inquiries can be directed to the corresponding author.

Author contributions

This article was written by SQ, who carried out the design and data analysis of the main research, KZ led the writing of the article, ZuC and SC proofread all the drafts, ZeC gave guidance to the paper, and YZ objectively proofread the article. All authors contributed to the article and approved the submitted version.

Funding

This research was funded by the National Key Research and Development Program of China (No. 2017YFB0902100).

Conflict of interest

Author YZ was employed by State Grid Liaoning Electric Power Co., Ltd.

The remaining authors declare that the research was conducted in the absence of any commercial or financial relationships that could be construed as a potential conflict of interest.

Publisher's note

All claims expressed in this article are solely those of the authors and do not necessarily represent those of their affiliated organizations, or those of the publisher, the editors, and the reviewers. Any product that may be evaluated in this article, or claim that may be made by its manufacturer, is not guaranteed or endorsed by the publisher.

Supplementary material

The Supplementary Material for this article can be found online at: https://www.frontiersin.org/articles/10.3389/fenrg.2023.1204960/full#supplementary-material

References

Bhui, P., and Senroy, N. (2017). Real-time prediction and control of transient stability using transient energy function. *IEEE Trans. Power Syst.* 32 (2), 923–934. doi:10.1109/TPWRS.2016.2564444

Cai, H., Zhang, W., and Wan, Z., (2017). Research on the voltage stability and counter-measures in suzhou southern power grid. *Power Capacitor React. Power Compens.* 38 (1), 110–116. doi:10.14044/j.1674-1757.pcrpc.2017.01.021

Cheng, S., Teng, Y., Zuo, H., and Chen, Z. (2022). Power balance partition control based on topology characteristics of multi-source energy storage nodes. *Front. Energy Res.* 10, 843536. doi:10.3389/fenrg.2022.843536

Da Cruz Sessa, B., and Mariano Lessa Assis, T. "Voltage stability assessment in multi-infeed HVDC systems: Application to the Brazilian grid," in Proceedings of 2018 IEEE Power & Energy Society General Meeting, Portland, OR, USA, August 2018, 1–5.

Ding, T., Zeng, Z., Qin, B., Zhao, J., Yang, Y., Blaabjerg, F., et al. (2021). Quantifying cyber attacks on industrial MMC-HVDC control system using structured pseudospectrum. *IEEE Trans. Power Electron.* 36 (5), 4915–4920. doi:10.1109/tpel.2020.3032883

Fu, W., Zhang, W., and Xing, Y. (2011). Study on weak buses of voltage stability based on StaticVoltage stability analysis. *Electr. Power Sci. Eng.* 27 (3), 41–46.

Han, P., Chen, L., and Hu, D., (2018). Impact of transient overvoltage caused by DC block on wind power transmission and its suppression measure. Power Syst. Prot. Control, *Xuchang* 46 (5), 99–105. doi:10.7667/PSPC170255

Heetal, J. (2020). Review of protection and fault handling for a flexible DC grid. *Prot. Control Mod. Power Syst.* 5 (2), 151–165. doi:10.1186/s41601-020-00157-9

Hu, S., Xiang, Y., Liu, J., Li, J., and Liu, C. (2021). A two-stage dispatching method for wind-hydropower pumped storage integrated power systems. *Front. Energy Res.* 9, 646975. doi:10.3389/fenrg.2021.646975

Huang, W., Zhang, N., Yang, J., Wang, Y., and Kang, C. (2019). Optimal configuration planning of multi-energy systems considering distributed renew-able energy. *IEEE Trans. Smart Grid* 10 (2), 1452–1464. doi:10.1109/tsg.2017.2767860

Li, C. S., Li, Y. K., He, P., Guo, J., Fang, Y., and Sheng, T. Y. (2019b). Considering reactive power coordinated control of hybrid multi-infeed HVDC system research into emergency DC power support. *IET Generation, Transm. Distribution* 13 (20), 4541–4550, Nov. doi:10.1049/iet-gtd.2019.0138

Li, P., and Liu, C. (2019). Modeling correlated power time series of multiple wind farms based on hidden Markov model. *Proc. CSEE* 39 (19), 5683–5691. doi:10.13334/j.0258-8013.pcsee.182412

Li, Y., Gao, D. W., Gao, W., Zhang, H., and Zhou, J. (2021). A distributed double-Newton descent algorithm for cooperative energy management of multiple energy bodies in energy internet. *IEEE Trans. Ind. Inf.* 17 (9), 5993–6003. doi:10.1109/tii.2020.3029974

Li, Y., Gao, D. W., Gao, W., Zhang, H., and Zhou, J. (2020). Double-mode energy management for multi-energy system via distributed dynamic event-triggered Newton-raphson algorithm. *IEEE Trans. Smart Grid* 11 (6), 5339–5356. doi:10.1109/tsg.2020.3005179

Li, Y., Zhang, H., Liang, X., and Huang, B. (2019a). Event-triggered based distributed cooperative energy management for multi-energy systems. *IEEE Trans. Ind. Inf.* 15 (14), 2008–2022. doi:10.1109/tii.2018.2862436

Liu, J.-S., Yan, F., Han, J.-T., and Zhong-jun, P. (2010). A method of determining the weak voltage region by static stability analysis. *Power Syst. Clean Energy* 26 (9), 20–24.

Muniappan, M. (2021). A comprehensive review of DC fault protection methods in HVDC transmission systems. *Prot. Control Mod. Power Syst.* 6 (1), 1–20. doi:10.1186/s41601-020-00173-9

Qin, W. (2015).Power system reliability assessment and weak bus identification based on voltage stability. Ph.D. dissertation. Taiyuan, China: Taiyuan University of Technology.

Wang, D., Liu, L., Jia, H. J., Wang, W. L., Zhi, Y. Q., Meng, Z. J., et al. (2018). Review of key problems related to integrated energy distribution systems. *CSEE J. Power Energy Syst.* 4 (2), 130–145. doi:10.17775/cseejpes.2018.00570

Wu, D., Wang, J., Li, H., Wang, Z., Zhang, N., and Kang, C. (2018). Research on capacity and delivery sequence of interconnected northwestern-southwestern power grid towards renewable energy accommodation. *Power Syst. Technol.* 42 (7), 2103–2110. doi:10.13335/j.1000-3673.pst.2018.0697

Xiao, H., Li, Y., and Yu, R., (2016). Rapid identification method of weak areas in power grid based on commutation failure analysis in multi-infeed HVDC systems. *Proc. CSEE* 36 (7), 1781–1789. doi:10.13334/j.0258-8013.pcsee.2016.07.003

Xu, J., Zhu, S., Li, C., and Zhao, C. (2019). The enhanced DC fault current calculation method of MMC-HVDC grid with FCLs. *IEEE J. Emerg. Sel. Top. Power Electron.* 7 (3), 1758–1767. doi:10.1109/jestpe.2018.2888931

Zhang, D. W., Fang, J., and Goetz, S. (2022b). Control and optimization algorithms for lattice power grids with multiple grid-forming converters. *Front. Energy Res.* 10, 878592. doi:10.3389/fenrg.2022.878592

Zhang, J., Hou, L., Diao, X., Yang, X., Tang, P., and Cao, X. (2022a). Power allocation method of battery energy storage system considering state balance in smoothing photovoltaic power fluctuations. *Front. Energy Res.* 10, 965812. doi:10.3389/fenrg.2022.965812

frontiers | Frontiers in Energy Research

TYPE Original Research
PUBLISHED 11 September 2023
DOI 10.3389/fenrg.2023.1212304

Check for updates

OPEN ACCESS

EDITED BY
Yushuai Li,
University of Oslo, Norway

REVIEWED BY
José Baptista,
University of Trás-os-Montes and Alto Douro, Portugal
Fei Teng,
Dalian Maritime University, China

*CORRESPONDENCE
Ghulam Hafeez,
ghulamhafeez393@gmail.com

RECEIVED 26 April 2023
ACCEPTED 08 August 2023
PUBLISHED 11 September 2023

CITATION
Ahmad SY, Hafeez G, Aurangzeb K, Rehman K, Khan TA and Alhussein M (2023), A sustainable approach for demand side management considering demand response and renewable energy in smart grids.
Front. Energy Res. 11:1212304.
doi: 10.3389/fenrg.2023.1212304

COPYRIGHT
© 2023 Ahmad, Hafeez, Aurangzeb, Rehman, Khan and Alhussein. This is an open-access article distributed under the terms of the Creative Commons Attribution License (CC BY). The use, distribution or reproduction in other forums is permitted, provided the original author(s) and the copyright owner(s) are credited and that the original publication in this journal is cited, in accordance with accepted academic practice. No use, distribution or reproduction is permitted which does not comply with these terms.

A sustainable approach for demand side management considering demand response and renewable energy in smart grids

Syed Yasir Ahmad[1], Ghulam Hafeez[2]*, Khursheed Aurangzeb[3], Khalid Rehman[1], Taimoor Ahmad Khan[4] and Musaed Alhussein[3]

[1]Department of Electrical Engineering, CECOS University of IT and Emerging Sciences, Peshawar, Pakistan, [2]Department of Electrical Engineering, University of Engineering and Technology, Mardan, Pakistan, [3]Department of Computer Engineering, College of Computer and Information Sciences, King Saud University, Riyadh, Saudi Arabia, [4]School of Engineering and the Built Environment, Edinburgh Napier University, Edinburgh, United Kingdom

The development of smart grids has revolutionized modern energy markets, enabling users to participate in demand response (DR) programs and maintain a balance between power generation and demand. However, users' decreased awareness poses a challenge in responding to signals from DR programs. To address this issue, energy management controllers (EMCs) have emerged as automated solutions for energy management problems using DR signals. This study introduces a novel hybrid algorithm called the hybrid genetic bacteria foraging optimization algorithm (HGBFOA), which combines the desirable features of the genetic algorithm (GA) and bacteria foraging optimization algorithm (BFOA) in its design and implementation. The proposed HGBFOA-based EMC effectively solves energy management problems for four categories of residential loads: time elastic, power elastic, critical, and hybrid. By leveraging the characteristics of GA and BFOA, the HGBFOA algorithm achieves an efficient appliance scheduling mechanism, reduced energy consumption, minimized peak-to-average ratio (PAR), cost optimization, and improved user comfort level. To evaluate the performance of HGBFOA, comparisons were made with other well-known algorithms, including the particle swarm optimization algorithm (PSO), GA, BFOA, and hybrid genetic particle optimization algorithm (HGPO). The results demonstrate that the HGBFOA algorithm outperforms existing algorithms in terms of scheduling, energy consumption, power costs, PAR, and user comfort.

KEYWORDS

smart grid, renewable energy sources, demand response, day-ahead scheduling, energy management controller, electric vehicles, energy storage system

1 Introduction

Over the last decade, the energy needs of consumers have risen at an exponential rate (Hafeez et al., 2019; Alzahrani et al., 2023). The development of technology, substantial use in industry, and introduction of electric vehicles on the road have led to an increased demand for electricity. It will continue to rise exponentially. Energy consumption from buildings accounts for approximately one-third of the energy that is generated worldwide (Gul and

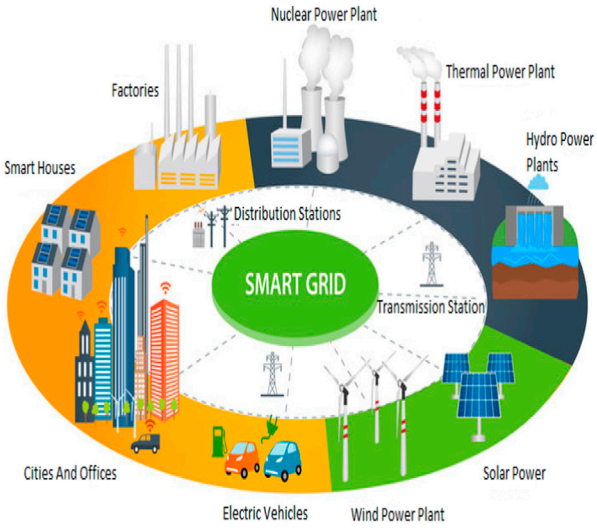

FIGURE 1
Smart grid overview.

Sandhya, 2015). The United States Department of Energy projects that energy use will increase by 56% in 2040 (United States Department of Energy, 1225). Traditional power grids cannot cope with the current world's needs because of the enormous increase in energy demand. The concept of smart grids has been developed as a result of reduced effectiveness, environmental concerns (Yu et al., 2023), distributed economic dispatch (Li et al., 2022), distributed grounding layout (Xiao et al., 2022), harmonic power flow (Xie and Sun, 2022), diverse maintenance needs, and reliability issues in the traditional power network (Li et al., 2022). Conventional networks have become a smart grid due to advances in communication technologies and their integration into the electricity infrastructure. Passive customers have become active consumers because of the smart grid. Due to the elastic nature of loads, the success of smart grids lies in the availability of resources like distributed generation (Ribeiro et al., 2020). Figure 1 represents a model of a smart grid.

Offering incentives in the form of prices revolutionized the traditional power grid and enabled utility companies to change the behavior of consumers in terms of energy consumption (Ma et al., 2016). With the emergence of liberality in the electricity market, efficiency is improved due to better economic solutions provided by the power companies (Ribeiro et al., 2018). Due to smart grids, electric utility companies (EUCs) are able to dispatch price signals to consumers using day-ahead pricing (DAP) signals, time of use (TOU), and real-time pricing (RTP) signals. Therefore, users can modify the load at their own pace. This increases the possibility for electricity consumers to alter their load patterns in accordance with tariffs. However, an intelligent optimization mechanism is extremely necessary in order to prevent peak formation during low hours of the day (Hafeez et al., 2020a). Thus, optimization methods are developed to address various aspects like distribution generation effective utilization (Chen et al., 2022; Sun et al., 2022), reliability improvement (Ma et al., 2021), energy consumption minimization (Min et al., 2023), and industrial applications (Lv et al., 2022). However, electricity theft is a challenge while implementing optimization methods (Yan and Wen, 2021). Load demand management can ensure that consumers' electricity needs are met. The mechanism for managing the demand mainly consists of demand response (DR) and demand side management (DSM) in particular. A DSM shall be designed with the primary aim of planning consumer load, taking into account the price information provided by the energy companies that use DR. The DSM is a key contributor to the development of various strategies for ensuring grid stability by scheduling electricity generation and the use of renewable resources during periods when peak loads occur in order to balance the load on smart grids. The DSM, through the flexible and diverse development of plans, plays an essential role in ensuring electricity grid stability. In order to reduce the load on the primary grid and prevent the collapse of the whole power system during maximum demand hours, DR encourages consumers to shift their load from peak to off-peak hours (Imran et al., 2020). The DSM's primary strategy is to move loads through a DR program. Consumers are encouraged to cut their energy consumption at peak times and move loads into cheaper periods of the day through the DSM strategy, which reduces electricity costs and PAR (Gelazanskas and KelumGamage, 2014; Hafeez et al., 2020b). It can be achieved only when bi-directional communication exists between the electricity grid and the energy consumer. Smart meters (SMs), advanced metering infrastructure (AMI), automatically operated appliances (AOAs), energy management controllers (EMC), and renewable energy sources are required for this. The AMI will assist in the exchange of data between a power grid and the consumer's SM (LiHui and Ho, 2014). Price signals along with time are shared with the consumers so that they can easily adjust their AOAs according to the time slot which suits them. The price changes according to the consumers' load curve (Barbato and Capone, 2014). DSM must serve many residential, commercial, and industrial consumers to cater to the energy crisis. Nonetheless, residential buildings consume a large amount of energy, so this is a highly preferred research area.

Several techniques and mathematical models have been developed for scheduling residential loads, which helped reduce energy costs and PAR. In order to solve energy problems, optimization techniques such as linear, nonlinear, and mixed-integer programming (MIP) are in use (Huang et al., 2019; Elazab et al., 2021). More efficient solutions for cost reduction are a number of developed mathematical models and other techniques. However, the mathematical model does not seem to be an effective way of scheduling appliances as it demonstrates poor efficiency in solving problems having multiple objectives. Furthermore, taking on a large number of devices that have to be scheduled increases computational time (Albogamy et al., 2022). For instance, to reduce PAR and solve appliance scheduling problems, game theoretic techniques, such as Nash and Stackelberg, are developed. Stackelberg's method helps smooth out the load curve and fulfill the energy needs of consumers by trading electricity among utility companies (Yu and Ho, 2016; Srinivasan et al., 2017). To address issues of gaming models, control techniques are developed (Wang et al., 2022). For example, an adaptive dynamic control with disturbance observers is developed by Zhang et al.

(2022) for energy balancing of a hybrid energy system. Likewise, model predictive control (Wang et al., 2022), distributed power sharing control (Zhao et al., 2022), and finite convergence control (Wang J. et al., 2022) are introduced to solve microgrids' energy balancing problems. However, battery life prediction, battery utilization for RES, battery charging/discharging scheduling, *etc.*, are ignored (Dang et al., 2023; Gu et al., 2023). Batteries are utilized in renewable energy systems (Cai et al., 2022) to smooth out renewable power generation, and storage technology is cascaded with an energy hub system (Jiang et al., 2022), storage technology-based photovoltaics (Zhang et al., 2022), and solar system development (Huang et al., 2023) for distribution network expansion. However, solar cell-based generation is uncertain and intermittent (Huang et al., 2023). In contrast, grid-connected inverters and composite circuits have power quality issues (Chung et al., 2022; Lin et al., 2022). A methodology for EV tour scheduling in a traffic environment is developed by Zhang et al. (2022). To address such limitations, heuristic algorithms, namely, particle swarm optimization (PSO) along with the genetic algorithm (GA) and bacteria foraging optimization algorithm (BFOA), emerged to resolve the issue of the single-objective optimization problem (Rehman et al., 2021). However, the multi-objective optimization aspect of the energy management problem is ignored (Cao et al., 2020a; Cao et al., 2020b). The authors developed a multi-objective optimization model to decide on the placement of PMU in the power grid (Cao et al., 2022). Likewise, a multi-objective optimization model is developed by Zhang et al. (2023) for a carbon-capturing facility in microgrids. A DSM model is solved using the BFA algorithm by Priya Esther et al. (2016). Similarly, the energy management problem is solved using GA for smart grid cost optimization. However, GA has the relevant characteristics of exploration but is limited only to the local best solution. On the other hand, BFA is more suited to exploitation but has drawbacks of obtaining a personal best solution. We used a hybrid bacteria foraging and genetic algorithm, the HGBFOA, which allows us to achieve a global best solution for multi-objective optimization problems by combining GA and BFA (Sarker et al., 2021).

So far, sufficient research has been carried out to improve energy efficiency in the smart grid. There are also some limits to most of the methods under discussion, which have certain prominent features. The authors were able to solve a lot of objectives with the help of mathematical models in many research works. However, in the case of loads that are spontaneous and have a non-linear effect, it is not possible to use mathematical techniques. Moreover, the techniques are, in essence, complicated and require a long period of time to arrive at an optimum solution. Compared to this, some of the algorithms have suffered from early convergence that leads to the loss of a number of algorithm features such as parameter substitution, population diversity, and ending criteria. However, the aforementioned techniques either cater to PAR, energy cost, user comfort maximization, or scheduling problems, but none of the aforementioned methods catered to all the objectives at the same time. In our research work, a hybrid algorithm (HGBFOA) that addresses all the aforementioned features simultaneously is considered.

The research work is setup in the following manner: Section 2 presents the related work, Section 3 shows the research methodology along with system modeling, and Section 4 presents details of the existing and suggested system models. Simulation and results are discussed in Section 5, while Section 6 provides an idea about future extensions.

2 Literature review

In the smart grid field, research is conducted to obtain better energy management by scheduling AOAs. In the study by Samadi et al. (2010), plug-in hybrid electric vehicles are introduced. The demand for energy from consumers is rising as a result of introduction of new and up-to-date electrical equipment with high power demand, leading to interruptions in the entire power system. Two easy ways of meeting users' requirements are present, i.e., the electricity generation companies must increase generation by building new plants or scheduling consumer appliances for efficient energy management. The foremost method is costlier because to increase generation, we have to construct new power plants along with the current power plants, which needs considerable funding. This will also lead to complexity in power transmission and distribution. In comparison, the second technique will have to manage the current requirement by introducing various pricing techniques for 24 h. A direct load control (DLC) method is presented by Abdollahi et al. (2011). Using the DLC method, the utility can manage the power consumption and demand by providing incentives to consumers for decreasing power usage during high-demand hours while shifting load to low-demand hours. However, an inclining block rate (IBR) with RPT and TOU is initiated to avoid a peak in off-peak hours (Zhao et al., 2013; Rastegar et al., 2016). The home energy management system (HEMS) algorithm is proposed by Abushnaf et al. (2016), which minimizes the electricity cost and power usage through appliance scheduling using TOU pricing criteria. The AOAs are monitored, controlled, and scheduled using HEMS (Zhou et al., 2016). In order to reduce PAR, HEMSs provide timeslots for each device. During these timeframes, automated equipment is scheduled according to various price signals from power companies. However, in many publications, the time allotted to each device is long enough, which some devices, such as kettles, juicers, and blenders, cannot achieve. Ma et al. (2016) considered the drawbacks of large timeframes, but user comfort is already compromised. User comfort is formulated by Zhou et al. (2016) by considering latency minimization and device energy consumption. In the study by Hafeez et al. (2020a), extensive research was conducted, and some exact algorithms were discussed. However, the issue of user convenience is also present if you want to reduce power consumption. One of the major drawbacks of this research is the lack of integration of renewable energy sources into the smart grid. There is no conceivable energy system that does not integrate renewable energy sources (Zafar et al., 2013). In the study by Adika and Wang (2014), MINLP is explained using RTP, which reduces energy consumption by scheduling thermal and electrical devices to minimize energy costs and maximize user comfort. Performance is very effective on different models. However, the computational complexity of this technique is a drawback. The authors addressed user-initiated changes in device scheduling (Jovanovic et al., 2016). However, the specified changes had to be fulfilled the next day, increasing consumer dissatisfaction. Hafeez

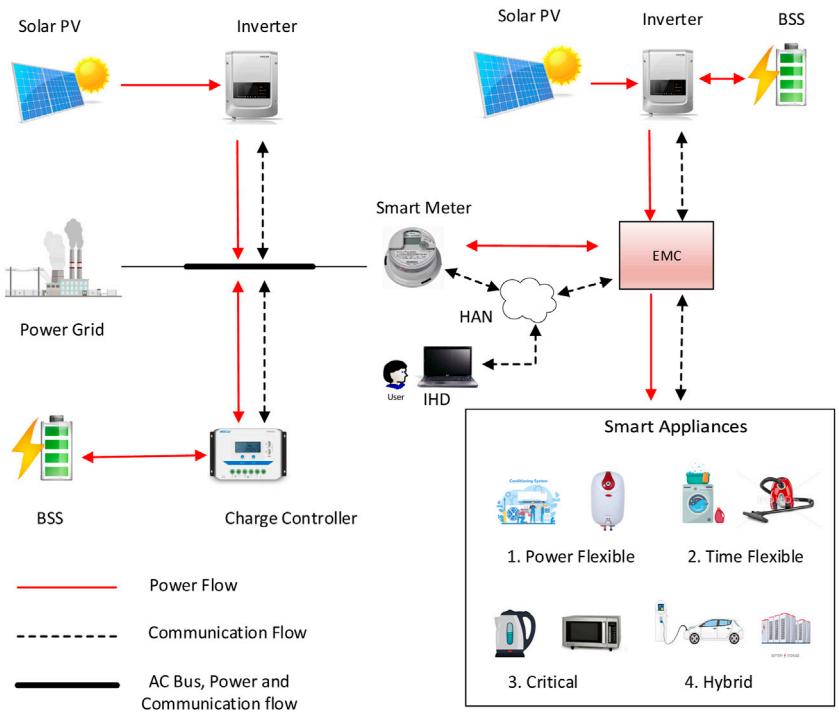

FIGURE 2
Proposed system model.

et al. (2019) solved this problem by allowing the consumer to turn off one device and turn on another at the user's request. Adika and Wang (2014) considered an energy storage system that reduces electricity costs and peak loads by almost a factor of five through scheduling through linear programming. The evolutionary algorithm (EA) in the study by Azar and Jacobsen (2016) was used to address the three goals of reducing power costs, maximizing power demand, and reducing carbon emissions. Elkazaz et al. (2016) used distributed generation (DG) to enable the bidirectional current flow, effectively reducing device latency and minimizing energy costs. However, installation, maintenance, and operating costs were completely ignored. Lokeshgupta and Sivasubramani (2019) and Muhsen et al. (2019) worked on reducing electricity costs and peak demand using linear programming (LP) and EA, respectively.

The aforementioned model is a valuable source of literature suitable for energy management. Few models are efficient for some specific goals and restraints. For example, one model considered PAR, another considered energy cost, whereas some techniques combined PAR and energy cost. However, other models took into consideration CO_2 emissions and user comfort in relation to price. The model described previously does not take advantage of the beneficial aspects of smart grids that simultaneously consider PAR, energy costs, user comfort, and energy consumption. Moreover, coordination between devices has been neglected in most studies, and adding renewable resources and other targets to already installed infrastructure has not been considered in the aforementioned literature. Therefore, we need a system model that integrates renewable energy sources and implements inter-device coordination to simultaneously consider PAR, energy costs, user comfort, and power consumption. With this motivation, an efficient and effective technique is proposed in our research paper. Renewable energy is added to the smart grids for energy management optimization and DR. Considering RES along with other goals of this study allows us to model efficient and cost-effective systems that can meet today's world's energy demands.

3 Proposed methodology

The suggested HGBFOA-based HEMS model consists of the main components discussed in the following sections. The functions and possible uses of all the components are described in following headings.

3.1 Proposed system model

The proposed residential energy management system is presented in this section. The energy management scheduling problem is solved with AMI. The EMS consists of the EMC, smart meter, intelligent devices, in-home display (IHD), home area network (HAN), and power company, along with the power station, as presented in Figure 2.

Smart energy meters collect device energy usage data from the energy management controller. Communication between smart meters and EMC is enabled by HAN. AMI can be considered the backbone of a smart grid. The AMI, present between the SM and the power company, can send price signals from the power company, and accordingly, the consumer can accordingly schedule their smart

devices. The consumers' demand data collected by the smart meter is sent to the power company via AMI (Shirazi and Jadid, 2015). In response, a real-time DR signal from the power company is sent to the smart meter. The IHD helps schedule appliances within EMC, according to the utility company's demand response signals. Our hybrid algorithm, i.e., HGBFOA, is implemented in EMC to schedule appliance operations according to the power rating and type. This EMC, based on HGBFOA, responds to energy price data, taking into account device operating time, device power rating, and user preferences for device operation.

3.2 Inputs for the system

The inputs to the presented EMS are grid power, the pattern of power consumption with a power rating of AOAs, and the demand response. However, sharing generation and consumption information in advance may create a security issue (Lv and Song, 2019; Lv et al., 2020a; Lv et al., 2020b; Cao et al., 2020c). Detailed description of the system input is as follows.

3.3 Smart appliances

The residential load is classified into four types, i.e., flexible power appliances, time flexible/elastic appliances, hybrid appliances, and critical appliances. The time of operation of various residential loads is given by Eq. 1.

$$O_i(t) = \left\{ \begin{matrix} 1 & if\ t \in \tau_i, i \in App \\ 0 & else \end{matrix} \right\}. \quad (1)$$

The time interval during which appliances are in operation is represented by τ_i. App shows the set of residential appliances. The explanation along with mathematical modeling of the aforementioned four categories of appliances is given in the following paragraphs:

3.3.1 Flexible power appliances

As the name suggests, devices that operate 24/7 and consume power between the maximum and minimum ranges are power-flexible appliances. For the user's comfort, delayed operation of these devices is not possible. Instead, these devices always work. Heating, ventilation, and air conditioning (HVAC), electric water heaters (EWHs), and refrigerators (Ref) are examples of energy-flexible appliances considered in this study. The following equations are used to model HVAC, EWHs, and Ref. Modeling of these loads is necessary because they consume power between the minimum and maximum values.

$$T_{\min} \le T_{req} \le T_{\max}, \quad \forall t \in \tau_i\, i \in \{AC, WH, \mathrm{Re}f\}. \quad (2)$$

Equation. 2 proves that the temperature of the power-flexible appliances is in the specified range.

$$O_i(1) = \left\{ \begin{matrix} 1, & if\ T_i(0) > T_i(i) & i \in \{AC, WH, \mathrm{Re}f\}, \\ 0, & if\ T_i(0) > T_i(i) & i \in \{AC, WH, \mathrm{Re}f\}. \end{matrix} \right. \quad (3)$$

To check whether the appliance should be turned on/off, the temperature is determined to see whether it exceeds the consumer's desired range of when the device will power on. If the temperature is below the required range, the appliance will power off for the initial interval described by Eq. 5. Mathematically, various energy flexible appliances are detailed in the following paragraphs.

HVAC: This equation takes into account the indoor–outdoor temperature differences, activity levels, and occupancy to provide a mathematical model for HVAC systems to maintain temperatures within specified limits.

$$T_{final}(t) = T_{ini}(t-1) + \mu(T_{out}(t) - T_{in}(t)) + \mu(\beta(t) + \zeta) + \mu O_i(t)\ \forall t = \tau\ \&\ i = AC. \quad (4)$$

Here, T_{ini} represents the initial temperature, whereas T_{out} and T_{in} show the outside and inside temperatures, respectively. The temperature variation effect, occupants' number, and the level of activity are denoted by μ. Cooling in the operation mode is given by β.

Electric water heater: Water heater is used at different times of the day. For maximum user comfort, the water temperature should be kept within certain limits. Usage patterns change depending on the weather and the weekdays. The EWH operating limits are given by Eq. 5.

$$T_{wh}(t) = T_{wh}(t-1) + v_{wh}(T_{cold} - T_{hot}) + [\phi O_i(i) - V_{cold}\omega_{wh}]. \quad (5)$$

The temperature of the water heater is expressed by the variation between the initial and hot water temperatures, water usage pattern, the room temperature, and the ON/OFF state of the EWH.

3.3.2 Time-flexible appliances or time elastic appliances

An appliance that is in operation only for certain time intervals is a time-stretchable or time elastic appliance. These appliances should be in operation during low demand or mid-peak hours. We can also slow down the operation of these devices to reduce the consumer's energy costs and PAR of the utility. Appliances that can be flexible with time are washing machines, dryers, and vacuum cleaners.

Dishwasher, washing machine, and dryer: The constraints of such appliances are shown in Eq. 6:

$$\sum_{t=\tau_i} O_i(t) = (OP_i)^{\max}, \quad \forall t \in \tau_i. \quad (6)$$

These are time-flexible devices and should be operated at the most reasonable time according to the user's demands. Unlike other household appliances, washers and dryers must operate in a specific order, i.e., the dryer should be run after the washing machine run stage. It shall not turn on before the washing machine run stage. Eqs 7, 8 represent the model equations as follows.

$$S_{dryer} + S_{washer} \le 1 \quad \forall t \in \tau_i, \quad (7)$$

$$F_{i1} \ge F_{i2} + \tau_i. \quad (8)$$

The first equation avoids running the washer and dryer in parallel. The second equation ensures that the functions of these devices remain in the correct order and that the dryer starts only after the washer time has expired.

3.3.3 Critical load/appliances

Critical equipment have a short run time and need to start as soon as the consumer wants them to start, so they cannot be delayed.

These devices are only used for short periods of time. Examples of this type of equipment include kettles, microwave ovens, juicers, and blenders.

Kettles, ovens, and blenders: These appliances cannot be interrupted during operation and have fixed power requirements. Eq. 9 expresses it.

$$C.L = \sum_{i=1}^{A} App^{i}_{P_{rate}} \times S_t. \tag{9}$$

Critical load is represented by $C.L$, and $App^{i}_{P_{rate}}$ is the appliance rated power. The appliance status is shown by S_t.

3.3.4 Hybrid load/appliances

Hybrid devices are a flexible device category in terms of both performance and time. Hybrid devices consume power between the maximum and minimum values, and their operation can also be delayed until a timeslot convenient for consumers and utilities. Examples of such devices are electric vehicles (EVs) and battery storage systems (BSS). Mathematically, these devices are represented as follows:

Electric vehicles and BSS: Due to technological advancement and user convenience, every home consumer has some kind of storage device (Mary and Rajarajeswari, 2014). To minimize the cost and flatten the load curve, such devices charge during low-price hours and discharge during high-demand hours. The batteries' required initial charge is required to extend the life of the storage system. Therefore, these storage devices must maintain a certain level of energy before being fully discharged. The generalized model for ESS is as follows:

$$E_{stor} = E_{stor}(t-1) + T[C_{ch}(t) - C_{dis}(t)] \quad \forall t \in \tau_i, \tag{10}$$

$$E_{\min} \le E_{stor} \le E_{\max} \quad \forall t \in \tau_i, \tag{11}$$

$$\sum_{t=\tau_i} O_i(t) = (OP_i)^{\max}, \quad \forall t \in \tau_i. \tag{12}$$

Equation 10 describes the energy stored in the battery and assumes a known charge–discharge interval. Equation 11 states that the stored energy should be within a certain interval to avoid overcharging or over discharging. This is necessary for the storage system life. The EV and BSS energy storage is given by Eq. 12 and relies on the initial charge or discharge in that particular timeslot.

DAP: DAP is a type of DR method. In this process, the electricity supplier, the energy company, and the consumer agree to buy or sell electricity prices 1 day in advance. Once an agreement is reached, whether the actual price is lower or higher than the agreed price, it cannot be changed for the day.

The EMC based on HGBFOA receives the DAP signal from the power company to schedule the operation of residential appliances, which is monitored using IHD.

3.4 Power-generating sources

Electricity is obtained from various resources, including conventional and non-conventional resources. However, non-conventional energy sources, such as solar PV, wind power, and tidal/wave, along with fuel cells, are readily available. Among the mentioned power sources, solar power is very important in today's world because it is free, widely available, and easy to install. Solar power reduces carbon emissions, minimizes PAR, and helps reduce overall energy costs. The energy produced from photovoltaics is given by Eq. 13 (Zhongming et al., 2019; Dang et al., 2023).

$$E_g^{Pv}(t) = \eta^{Pv} \times Area^{Pv} \times Irr(t) \times \left(1 - 5 \times 10^{-3}\left(Temp_{out}(t) - 25\right)\right). \tag{13}$$

E_g^{Pv} shows the solar power generated each hour. However, efficiency of solar PV is denoted by η^{Pv} and the area of a PV module in square meter is shown by $Area^{Pv}$. Irr shows the solar irradiation per hour, and $Temp_{out}$ shows the outdoor temperature. For temperature correction, a constant number *0.005* is multiplied with $Temp_{out}$. The HGBFOA helps in scheduling appliances while using power from solar PV during high-demand hours and charging batteries when demand is low.

3.5 Battery storage system

The main purpose of battery storage systems is to provide an alternative power source to minimize CO_2 emissions and maximize power reliability. The battery is installed together with the photovoltaic system. During the day, the battery is charged when the power generation is high and the consumption is low. During peak hours and nights, this stored energy powers the load. Powering loads during peak periods and charging during off-peak and mid-peak periods help minimize energy costs (Gu et al., 2023). It also helps maintain the grid stability by powering critical loads. Eq. 14 describes the battery charging and discharging mechanism.

$$ES(t) = ES(t-1) + \alpha.\mu^{ESS}.EE^{Ch}(t) - \frac{\left(\alpha.EE^{Dch}(t)\right)}{\mu^{ESS}} \quad \forall t. \tag{14}$$

Energy stored in KWH at time t is presented by ES, and the hourly duration is shown by α. μ^{ESS} denotes the battery efficiency. The battery charging rate is shown by EE^{Ch}, whereas the discharging rate is represented by EE^{Dch}, i.e., the power which turns on the load. In order to operate the battery in certain limits to avoid extreme charging and discharging, Eqs 15–17 represent the battery storage and operation limits, while the high and low limits can be denoted by EE^{Ch}_{UL} and EE^{Dch}_{LL}, respectively.

$$EE^{Ch}(t) \le EE^{Ch}_{UL}, \tag{15}$$

$$EE^{Dch}(t) \ge EE^{Dch}_{LL}, \tag{16}$$

$$ES(t) \ge ES^{Ch}_{UL}. \tag{17}$$

To optimize power usage, EMC receives the DAP signals from the utility companies, power signals from PV, and consumer priorities. Based on this, the efficient power usage pattern of the house is determined.

3.6 System outputs

The EMC receives input in the form of appliance patterns and generation sources. It processes this input and generates an output in the form of an optimal power consumption pattern for the devices.

Depending on the device's efficient power plan, the results achieved are lower energy costs, lower carbon emissions, minimized PAR, and maximized user comfort. This coordination between appliances helps maintain an optimized schedule for devices. The results are discussed in the following sections.

Energy cost is the bill that the consumers have to pay for electricity consumption. The power company will send the DAP signal to the user, and energy costs will be calculated based on the pricing signal. Research shows that users who followed DR signals and set their devices at different times of the day saw significant reductions in utility bills due to peak hours, mid-peak hours, and off-peak hours. The utility will calculate the DAP signal-related bill based on formula (18).

$$F_1 = \sum_{t=1}^{24}\left(\sum_{a=1}^{N} E_c^{App}(t) \times S_t \times \partial(t)\right). \tag{18}$$

Here, F_1 denotes the less costly bill of the users. Energy consumption of the appliance *App* is represented by E_c^{App}. S_t indicates the on/off status of appliance at that time, and N shows the number of appliances. This is obtained with the help of EMC based on HGBFOA.

In this study, we examined various types of devices and their energy consumption is mathematically represented in Eq. 19.

$$E_c^{T_F}(t) = P_r^{T_F} \times S_t. \tag{19}$$

Time-flexible appliance's energy consumption in each hour is shown by $E_c^{T_F}$, whereas $P_r^{T_F}$ denotes the highest power of that appliance. Total power consumed by mentioned appliances in 24 h is shown in Eq. 20. Time-flexible appliances are denoted by T_F.

$$E_T^{T_F} = \sum_{t=1}^{24}\left(\sum_{T_F=1}^{N} E_c^{T_F}(t) \quad \forall T_F \varepsilon\ App\right). \tag{20}$$

Equation 21 shows the energy consumption of power-flexible appliances for a timeslot.

$$E_c^{P_F}(t) = P_r^{P_F} \times S_t. \tag{21}$$

The energy consumed by power-flexible appliances in 24 h is given in Eq. 22.

$$E_T^{P_F} = \sum_{t=1}^{24}\left(\sum_{P_F=1}^{N} E_c^{P_F}(t) \quad \forall P_F \varepsilon\ App\right). \tag{22}$$

Here, P_F represents power-elastic devices, and the energy in KWH consumed by such appliances is denoted by $E_c^{P_F}$.

The power usage of critical appliances is presented in Eq. 23. The energy and power consumed by these appliances is denoted by E_c^{Cr} and P_r^{Cr}, respectively.

$$E_c^{Cr}(t) = P_r^{Cr} \times S_t. \tag{23}$$

The overall hours of consumption of critical appliances is shown in Eq. 24.

$$E_T^{Cr} = \sum_{t=1}^{24}\left(\sum_{C_r=1}^{N} E_c^{Cr}(t) \quad \forall Cr\ \varepsilon\ App\right). \tag{24}$$

Equation 25 gives the energy consumption of hybrid appliances, and energy consumption of these appliances is represented by E_c^H. P_r^H shows the highest power of hybrid appliances, while the status of appliance is shown by S_t.

$$E_c^H(t) = P_r^H \times S_t. \tag{25}$$

The 24 h energy consumption of hybrid appliances is shown in Eq. 26.

$$E_T^H = \sum_{t=1}^{24}\left(\sum_{H=1}^{N} E_c^H(t) \quad \forall H\varepsilon\ App\right). \tag{26}$$

The total 24 h consumption of all appliances is formulated in Eq. 27.

$$F_2 = E_T^{ta} = E_T^{T_F} + E_T^{P_F} + E_T^{Cr} + E_c^H. \tag{27}$$

Here, E_T^{ta} shows the overall energy consumption of appliances as a whole. Overall energy consumption by time-flexible/elastic appliances, power-flexible/elastic appliances, critical load, and hybrid devices is denoted by $E_T^{T_F}$, $E_T^{P_F}$, E_T^{Cr}, and E_c^H, respectively.

PAR means the peak to average energy consumption ratio over a specified period. DR shifts loads from peak to off-peak hours by encouraging consumer compliance. As a result, the energy supplier's load curve is smoothed and peak-free. For this reason, energy providers do not need additional power plants to operate during this time. This greatly reduces the user's electricity bill. Equation 28 shows the mathematical formula for PAR, where F_2 determines PAR, which is one of the goals of this research work, ensuring network stability and robustness. E_T denotes the overall power used by the consumer during the whole day.

$$F_3 = \left(\frac{\max\left(E_c^{T_F}(t), E_c^{P_F}(t), E_c^{Cr}(t)\right)}{E_T}\right) \times 24. \tag{28}$$

Consumer comfort is an objective that is computed by device operation delay, indoor/outdoor temperature variation, lighting, *etc.* (Cai et al., 2022). This work computes comfort using device latency and operation hours with/without scheduling. Correspondingly, if PAR reduction is desired, the load should be shifted to off-peak hours as it reduces user comfort. User comfort and energy costs are two competing goals. To reduce their electricity bills, consumers have to accept that their devices will run a little slower. At the same time, users have to pay higher electricity bills if they want to start using their devices immediately. User comfort, especially waiting time, is calculated by the formula shown in Eq. 29.

$$W_a = \frac{\sum_{t=1}^{T}\sum_{a=1}^{n}\left|\left(T_{a,t}^{0,unsch} - T_{a,t}^{0,sch}\right)\right|}{T_a^{op}}. \tag{29}$$

The waiting time of an appliance a due to scheduling is shown by 'W_a'. The pre- and post-scheduling status of an appliance is denoted by $T_{a,t}^{0,unsch}$ and $T_{a,t}^{0,sch}$, respectively. The operation time of such appliance is represented by T_a^{op}. EMC has the property of shifting a device to low-peak hours of a day with respect to the DAP signal. The maximum operational delay of a device can be formulated as follows:

$$W_a^d = T_a^t - T_a^{op}. \tag{30}$$

The maximum operational delay due to shifting of an appliance to low-demand hours can be represented by W_a^d, while T_a^t denotes the total time interval. The discomfort of the user can be calculated by the following formula in Eq. 31:

$$F3 = \frac{W_a}{W_a^d} \times 100. \tag{31}$$

3.7 Problem formulation

The aforementioned system outputs are the objective functions of this work, which are separately modeled in the previous subsection. Now, all these objectives are modeled combined in the optimization problem, which is modeled as the minimization problem as follows:

$$Min(F) = Min\left(\mathrm{F}_1\varphi_1 + \mathrm{F}_2\varphi_2 + \mathrm{F}_3\varphi_3 + \mathrm{F}_4\varphi_4\right), \tag{32}$$

$$\sum_{i \in App} p_i s_i(t) = P_{\lim}(t)\ \forall t \in \tau\ \&\ i \in App. \tag{33}$$

The objective functions in question, namely, energy cost, energy consumption, PAR, and user comfort, are represented by F1, F2, F3, and F4, respectively. The associated weighting factors for these functions are denoted as φ_1, φ_2, φ_3, and φ_4. These weights play a crucial role in determining which objective to prioritize, providing a sense of interest and motivation. The multi-objective function seeks to address multiple optimization problems simultaneously, taking into account user priorities and preferences. Eq. 33 shows the allowable power range for device operation so that the power limit must not be exceeded for a period of time. This helps avoid spikes, which are very important to utility company operations. Based on this, EMC designs the best power plan for the operation of the device. Devices are classified into four main categories based on uptime, power consumption, and schedule.

4 Proposed hybrid algorithm

Heuristic algorithms have been proposed to solve the energy management problem. Existing techniques for solving the scheduling problem cannot achieve effective energy management. Most of these algorithms require a computationally intensive solution for the scheduling problem of appliances, and the algorithms' efficiency decreases as the number of devices increases. In order to obtain efficient energy management when resolving scheduling problems, HGBFOA is proposed, which addresses the limitations explained previously.

4.1 A hybrid genetic bacteria foraging optimization algorithm

Genetic algorithm and bacteria foraging algorithm are good optimization methods and have efficient exploration ability. The search steps of the aforementioned optimization methods are divided into two parts: local and global searching ability.

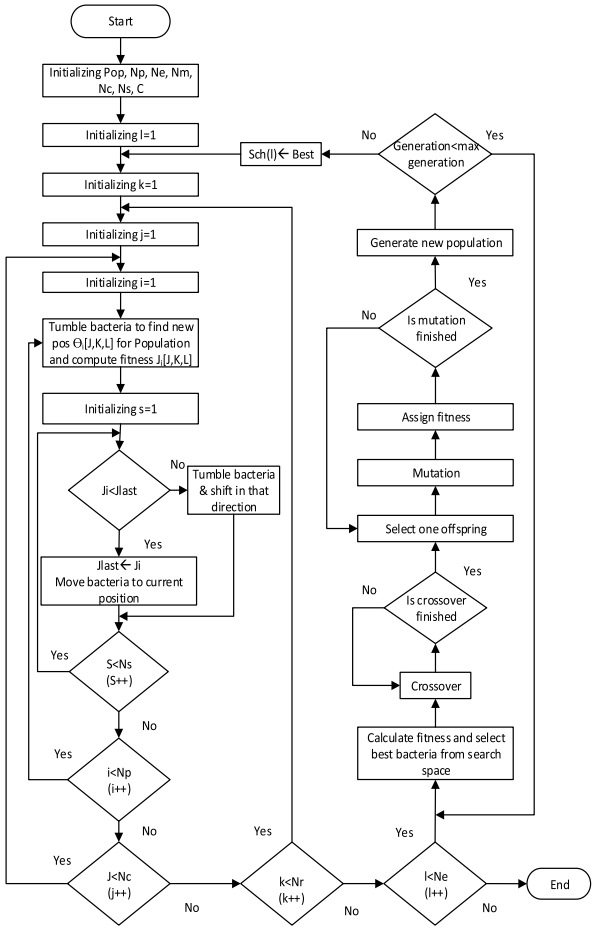

FIGURE 3
Flowchart diagram of HGBFOA.

BFOA focuses on local scope searches, whereas genetic algorithms have better global search capabilities. In addition to the benefits of these two techniques, they also have some drawbacks. For example, convergence problems exist in GA due to the maximum number of iterations and large search space requirements. At the same time, the BFOA elimination and dispersal steps may hinder the search for optimal solutions. The HGBFOA, with qualities of both GA and BFOA, is proposed to overcome the aforementioned limitations.

The flowchart of HGBFOA is shown in Figure 3 and explained step-by-step. First, the required parameters are initialized. HGBFOA performs BFOA step-by-step, as described in the flowchart. Furthermore, there is a difference between dispersal and elimination. The BFOA's elimination and dispersal steps have changed for HGBFOA. BFOA randomly removes and distributes the remaining bacteria after the reproductive stage. In HGBFOA, the elimination and propagation steps are performed through crossover and mutation. Then, GA is started up to a maximum number of iterations. Ultimately, an optimized schedule for devices is achieved by minimizing energy consumption, reducing costs, and lowering PAR values.

TABLE 1 Different appliances with their power ratings.

Appliance	Power rating	Appliance	Power rating
Air conditioner	70–130 W	Electric vehicles	200 W
Washing machine	100 W	Battery storage	50–120 W
Cloth dryer	100 W	Iron	250 W

5 Simulations and discussions

The simulation of the given model was conducted considering three different scenarios. In Scenario I, the simulation was performed using power solely from the grid. In Scenario II, the simulation incorporated both power from the grid and PV power. Finally, Scenario III involved simulations with the combination of the grid, PV power, and ESS. All simulations are performed in MATLAB, and results are obtained with comparisons to other methods, i.e., PSO, GA, HGPO, mixed PSO and GA, BFO algorithms, and HGBFOA and GA and BFO hybrid algorithms. We used these algorithms because they are similar. Comparisons are made between existing and proposed algorithms in terms of cost savings, power consumption, better peak reduction (PAR), and time delay.

Table 1 gives us an idea of six appliances with their power ratings used in this research, (taken from the work of Jiang et al., 2022).

The following diagram contains details of the basic data required to initialize the result. Figure 4A shows the day-ahead price signal (DAP) (from the study by Li et al., 2022).

Time in hours is measured horizontally, and the vertical value gives the energy price per unit in cents. In day-ahead pricing, an hourly energy price is agreed between the energy supplier and the consumer 1 day in advance. There are no additional costs for such pricing. Unit prices are cheaper at night due to off-peak hours and higher during peak hours. Therefore, the consumers schedule time flexibly and set up their hybrid devices at times when costs are lower.

Figure 4B shows the daily solar irradiance. The times shown on the graph start at 1:00 a.m., and there is no Sun until 6:00 a.m. As the Sun rises after 6 a.m., solar radiation increases exponentially, reaching a peak by 3 p.m. Therefore, PV power generation is currently at its maximum and starts to decrease after this time period as solar radiation decreases. Solar radiation continues to decrease sharply, reaching zero after 7 p.m. After that, no generations occur until the next day and the operation continues. The load consumes the maximum amount of power produced during maximum demand hours of the day. At present, green energy is being produced and used, resulting in lower carbon emissions from fossil fuel power plants.

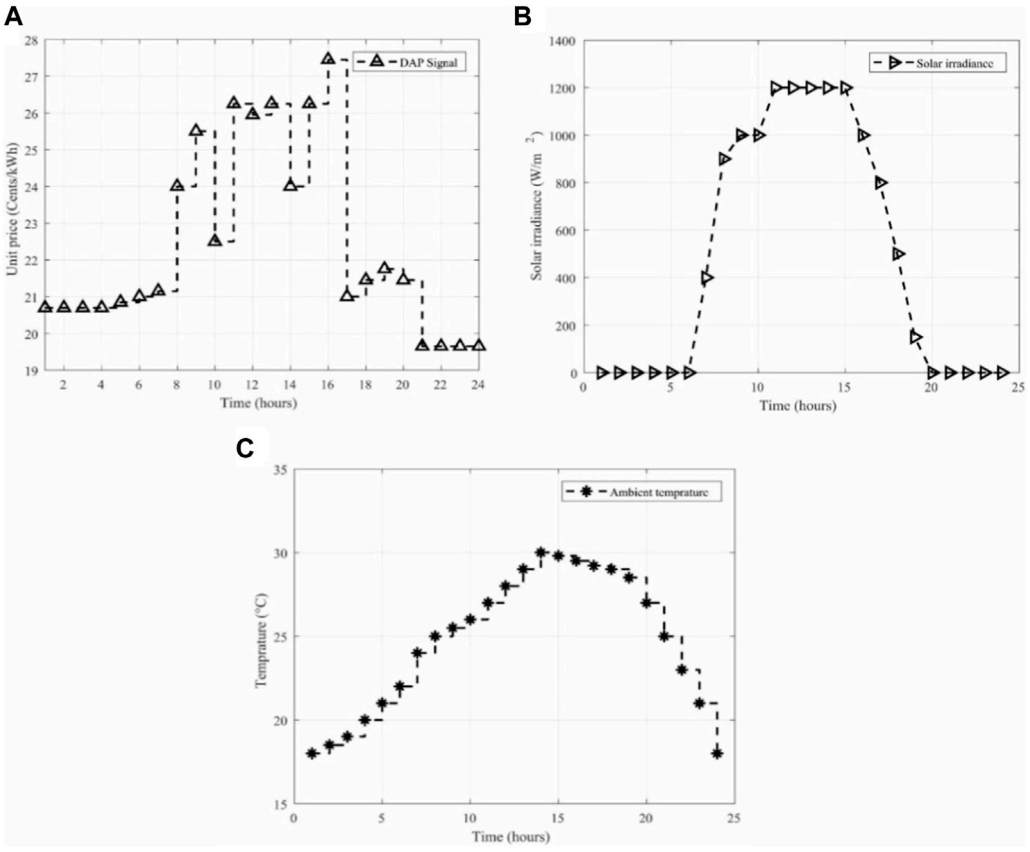

FIGURE 4
Day-ahead pricing signal is presented in **(A).** Solar irradiance **(B)** and ambient temperature **(C)**.

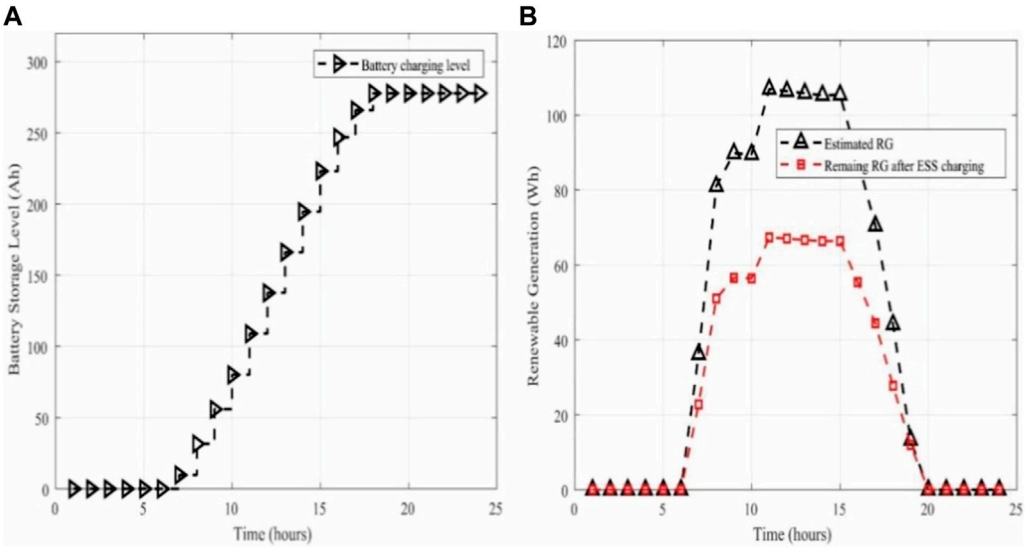

FIGURE 5
(A) Battery charging level is shown, and renewal generation along with remaining RG after charging is presented by **(B)**.

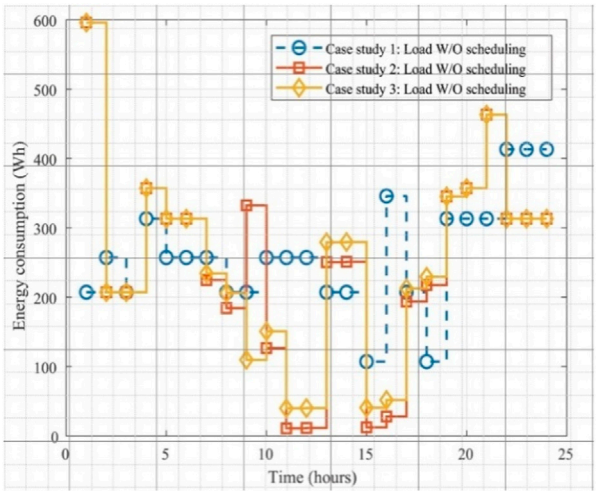

FIGURE 6
Load curve without scheduling.

Figure 4C shows ambient temperature over 24 h, and the temperature has a negative impact on the solar panel efficacy. Environmental temperature and photovoltaic efficiency are inversely proportional. The higher the temperature, the lower the PV yield. The efficiency of solar modules is maximized under STC, i.e., 25°C and 1,000 W/m^2. According to the graph, the temperature initially cools down at night and warms up again as the Sun rises. Temperatures are highest between 1:00 and 3:00 p.m. and decrease in the evening.

Figure 5A shows the battery charge status. The battery is initially assumed to be zero and starts charging during the day when solar power begins. The battery level increases hourly and is finally fully charged in the afternoon. According to the figure, the maximum storage capacity is 280 Ah, reaching around 7 p.m. The battery stays in this state until morning and starts charging again when PV starts generation. The battery status is displayed in Ampere hours (Ah). This graph is only for battery charging and does not show the battery discharge status.

Estimated renewable energy production and the excess renewable energy production after charging the ESS are given in Figure 5B. The *Y*-axis shows renewable energy production in Watt-hours, and the *X*-axis shows timeframes in hours. Renewable power generation is estimated to be up to 107 Wh after the 11th timeslot and continues to increase until 3:00 p.m. After that, renewable energy production decreases and approaches zero upon reaching 7:00 p.m. The red graph shows the leftover renewable energy production after charging the ESS. Excess generated power is dispatched directly to the appliances, thus reducing power consumption from the power grid. The battery starts charging after 6:00 a.m. and is fully charged after 7:00 p.m.

The original load curves for all three unplanned cases are shown in Figure 6. This curve shows that the load is unevenly distributed before optimization. In some cases, load power consumption is higher during peak hours, making it more costly than during off-peak hours.

5.1 Scenario I: Appliance scheduling while using grid power only

In this case, we have considered only power from the grid, while other sources like PV and ESS have not been used. Scheduling is obtained for appliances in such a manner that there is minimum load during peak hours, while the maximum load is shifted to off-peak hours of the day, during which the energy price is lower. The existing and HGBFOA algorithms are simulated in MATLAB. The result of our hybrid algorithm is

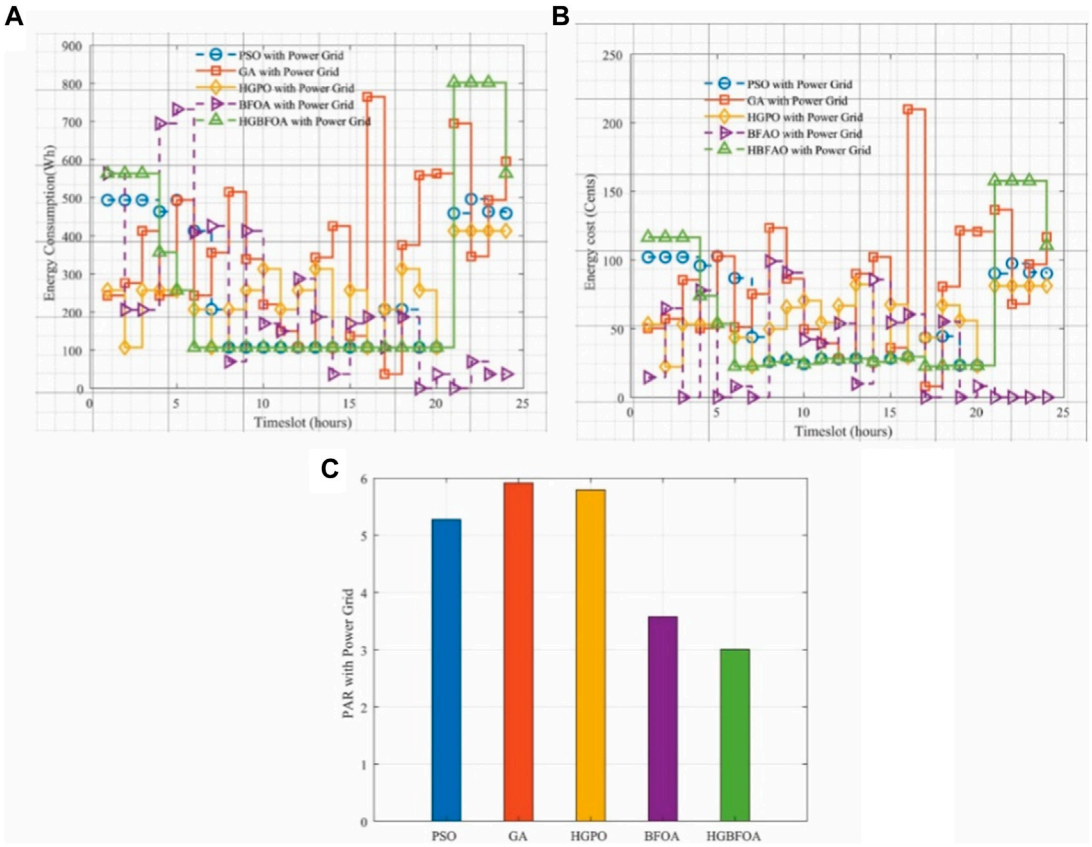

FIGURE 7
Energy consumption, energy cost, and PAR using power from the grid are shown in **(A–C),** respectively.

presented in a graph against the existing algorithms. The main goal of our research, i.e., energy consumption, energy cost, PAR, and scheduling, is compared with existing algorithms and our hybrid algorithm for grid power.

5.1.1 Energy usage

Figure 7A represents the energy consumption patterns of different devices at arbitrary times of the day. Comparisons are made between different algorithms. The graph shows that PSO has a maximum energy consumption of 500 Wh, while GA and BFOA have a maximum energy consumption of 760 Wh and 740 Wh, respectively. HGPO has a maximum power of 415 Wh, and HGBFOA has a maximum power of 800 Wh, which is the off-peak time with the lowest energy rates. However, on average, the energy utilization of HGBFOA is more efficient than that of the existing algorithms. From the graph, it can be seen that for 15 h, i.e., 6 a.m. to 9 p.m., the energy consumption is kept below 100 Wh by our proposed algorithm. This shows the efficacy of HGBFOA. These algorithms have gained an optimized power schedule for different kinds of appliances, and power is held within its specified limits (maximum during off-peak and minimum during peak hours).

5.1.2 Analysis of energy cost

As price per unit is very important for the consumers, our objective is to reduce the energy consumption during the high-price hours of the day. The energy cost for all existing algorithms and our proposed algorithm has been compared in Figure 7B. Only a nominal load is turned on during peak hours. The maximum energy cost during 24 h for PSO, GA, HGPO, and BFOA in cents is 105 cents, 215 cents, 83 cents, and 100 cents, respectively. In contrast, the maximum energy consumption of HGBFOA is 165 cents. These 165 cents are only for 3 h during low-demand hours, where the price signal is low, so we have turned on max appliances during these hours. For almost 16 h, the energy price is under 30 cents, and the average energy cost for HGBFOA during 24 h is less than 40 cents, which is lower than that of the other existing algorithms.

5.1.3 Analysis of PAR

Figure 7C shows the PAR of PSO, GA, HGPO, BFOA, and HGBFOA. If PAR is lower, then the peaks will be lower, which means that the power is consumed efficiently. The PAR is the maximum for GA and HGPO, which is 5.9 and 5.8, respectively. A comparison between HGBFOA and other existing algorithms is shown in Table 2. In the first two columns, algorithms are taken along with their PAR value. The third column shows the difference in the existing algorithms from our hybrid algorithm. The last column presents the percentage difference between HGBFOA and the other algorithms. In terms of percentage,

TABLE 2 PAR comparison for the grid.

Scheduling algorithm	PAR	Variation from HGBFOA	Difference from HGBFOA (%)
PSO	5.3	2.3	43.18
GA	5.9	2.9	49.15
HGPO	5.8	2.8	48.27
BFOA	3.6	0.3	16.66
HGBFOA	3	*Note: for other algorithms, HGBFOA is taken as the reference.*	

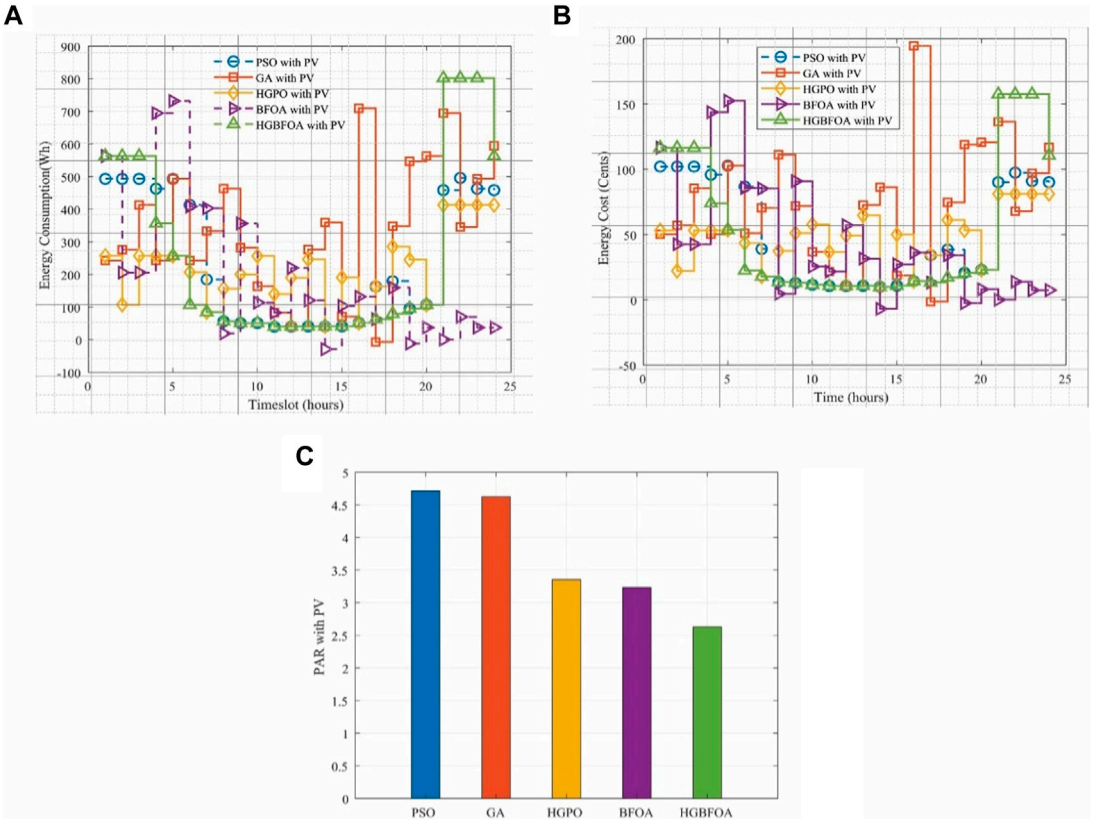

FIGURE 8
Energy consumption, energy cost, and PAR considering power from PV and the grid are shown in **(A–C),** respectively.

HGBFOA shows better performance and is 43.18% more efficient than PSO, 49.15% more efficient than GA, 48.27% more effective than HGPO, and 16.66% better than BFOA.

5.2 Scenario II: Appliance operation scheduling utilizing power from both PV and the grid

For scenario II, we considered two power sources, i.e., power from the grid and solar PV. During daytime, the renewable energy from PV is used to operate load or in combination with the grid when PV generation is insufficient. During nighttime, only grid power is in use. In this study, simulations are conducted to analyze the reduction of PAR, minimization of energy bills, and power consumption using the proposed HGBFOA and other algorithms. The results of these simulations and their comparison are described in the following paragraphs.

5.2.1 Power consumption and utility bill analysis

Figure 8 shows the power consumption, usage time, energy cost, and PAR of the existing algorithms and HGBFOA. The scheduling is designed to reduce overall power consumption and energy costs, especially during maximum-demand hours. During peak hours, HGBFOA showed better performance than other algorithms in terms of energy consumption and price. From Figure 8A, it is clear that minimum energy consumption is maintained during peak hours, i.e., during daytime. For comparison, we have

TABLE 3 PAR evaluation with PV and the grid.

Technique	PAR	Variation from HGBFOA	Variance from HGBFOA (%)
PSO	4.74	2.09	44.1
GA	4.7	2.05	43.6
HGPO	3.4	0.75	22.05
BFOA	3.24	0.59	18.2
HGBFOA	2.65	*Note: for other algorithms, HGBFOA is taken as the reference.*	

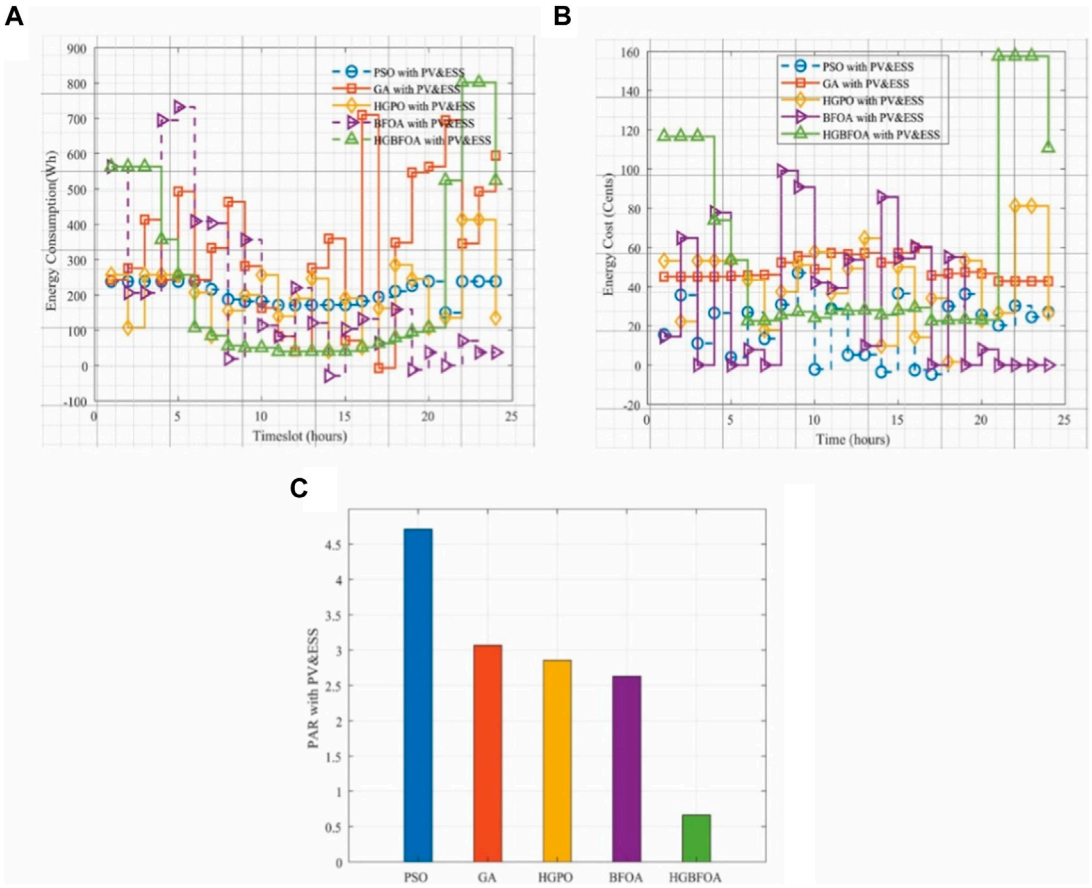

FIGURE 9
Energy consumption, energy cost, and PAR considering power from PV, the grid, and ESS are shown in **(A–C),** respectively.

considered 6 to 21 timeslots. The energy consumption of different appliances can be seen, which is below 100 Wh, which results in a lower average energy cost of only 15 cents for HGBFOA. The reason for the energy cost reduction is renewable power from PV during the daytime and the load being operated on this source along with the grid.

In Figure 8A, energy consumption (Watt-hours) is plotted on the *Y*-axis, and time in hours is plotted on the *X*-axis. In the sixth slot, the appliance with PSO consumes 406 Wh, that with GA consumes 495 Wh, that with BFOA consumes 406 Wh, and those with HGPO and HGBFOA consume 203 Wh and 105 Wh, respectively. Comparing the power costs in Figure 8B for the same sixth-hour slot, we get the following prices: energy cost for PSO is 85 cents, and the cost for GA and BFOA is 50 and 83 cents, respectively. Nevertheless, the utility bills for HGBFOA and HGPO are 20 cents and 45 cents, respectively. Thus, HGBFOA results in lower peak energy consumption, leading to a lower net utility bill compared to the existing techniques. Energy consumption and costs have been effectively reduced, specifically during peak time, i.e., timeslots from 6 to 20. In addition, EMC's HGBFOA-based energy consumption follows a regular pattern, mostly keeping energy costs at a low level.

TABLE 4 PAR evaluation utilizing PV, ESS, and the power grid.

Technique	PAR	Variance from HGBFOA	Difference from HGBFOA (%)
PSO	4.74	4.04	85
GA	3.07	2.37	77
HGPO	2.88	2.18	75.6
BFOA	2.65	1.95	73
HGBFOA	0.7	Note: for other algorithms, HGBFOA is taken as the reference.	

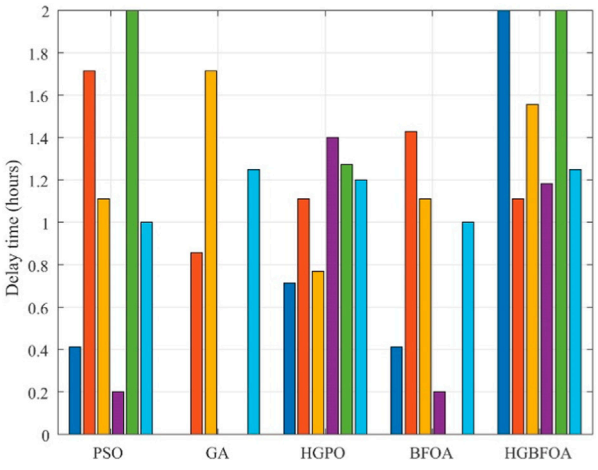

FIGURE 10
User comfort comparison of the algorithms.

5.2.2 Evaluation of PAR

A quick comparison between HGBFOA and other algorithms is shown in Figure 8C. The PAR scores for PSO, GA, HGPO, BFOA, and HGBFOA are 4.74, 4.7, 3.4, 3.24, and 2.65, respectively. As shown in Table 3, HGBFOA outperformed PSO by 44.1%, GA by 43.6%, HGPO by 22.05%, and BFOA by 18.2%. Effective scheduling reduced the peaks in different timeframes, and HGBFOA shows better performance than other algorithms regarding PAR minimization.

5.3 Scenario III: Appliance operation scheduling utilizing power from PV, ESS, and the power grid

In Scenario III, power is utilized from three different sources, namely, the grid, renewable energy systems, and energy storage systems. During daytime, PV and the grid together operate the load, and excess power from PV is used to charge the batteries. Our hybrid and other existing algorithms are applied. A comparison for power consumption, energy cost, PAR and user comfort is made. Further details are as follows.

5.3.1 Energy consumption and energy cost analysis

Figure 9 shows energy consumption, energy cost, and PAR using the algorithm described previously. Our main goal is to reduce energy consumption by scheduling devices during low energy-cost timeslots. This can be attained by lowering energy consumption during peak hours and shifting loads to low-peak hours. On average, the energy consumption of HGBFOA is relatively lower than the other aforementioned algorithms. For simplicity, we examine the energy consumption of the appliances during timeslot no. 10 using the algorithm described previously. The power consumption of the 10th slot for PSO, GA, and BFOA is 180 Wh, 170 Wh, and 110 Wh, respectively, whereas the power consumption while using HGPO is 260 Wh and that of HGBFOA is 50 Wh. This indicates a clear difference in the power consumption of the proposed algorithms.

Having determined the energy consumption during 10th hour, the energy cost for this timeslot is described in the next row. Energy costs for PSO, GA, and BFOA are −04 cents, 50 cents, and 42 cents, respectively. The energy cost for HGPO is 56 cents, whereas HGBFOA has an energy cost of 23 cents. HGBFOA's overall performance is better than the other existing algorithms.

5.3.2 PAR analysis with PV, grid, and ESS

Minimization of PAR is an important objective of this study. It is greatly facilitated by our proposed HGBFOA algorithm. PAR comparison with different algorithms is shown in Figure 9C. The PAR for PSO is 4.74, that of GA is 3.07, that of HGPO is 2.88, that of BFOA is 2.65, and that of HGBFOA is 0.7. HGBFOA is 85% more efficient than PSO, 77% better than GA, 75.6% better than HGPO, and 73% finer than BFOA. This is presented in Table 4. The table shows that the appliances are effectively shifted to low peak and mid-peak timeslots, resulting in a significant reduction in the PAR value.

5.4 User comfort

Figure 10 determines the user comfort, which is the operational delay of appliances, and the graph is explained in the following paragraph.

For PSO, the air conditioner has a 0.4-h delay, the refrigerator has a 1.72-h delay, the washing machine has a 1.1-h delay, the juicer blender has a 0.2-h delay, and the vacuum cleaner has a 2-h delay. There will be an hour delay in EV/ESS operations. Air conditioners, juicers, vacuum cleaners, and electric cars have no operational delays, while refrigerators and washing machines have delays of 0.85 and 1.72 h, respectively. HGPO lags by 0.72, 1.1, 0.78, 1.4, 1.28, and 1.2 h for air conditioners, refrigerators, washing machines, juicers, vacuum cleaners, and EV/ESS, respectively. When using BFOA, the devices such as air conditioners, refrigerators, washing machines, juicers, vacuum cleaners, and EV/ESS face delays of 0.4 h,

1.42 h, 1.1 h, 0.2 h, 0 h, and 1 h, respectively. In the end, the operating lags of air conditioners, refrigerators, washing machines, juicers, vacuum cleaners, and EV/ESS with HGBFOA are 2 h, 1.1 h, 1.55 h, 1.2 h, 2 h, and 1.24 h, respectively. There is a slight delay when operating devices with HGBFOA. However, the slight delay in operation is to reduce electricity bills, ensure efficient energy management, and maintain minimum PAR values.

5.5 Possible trade-off

User comfort is somewhat limited to achieve important goals such as optimal energy consumption, reduced energy costs, reduced CO_2 emissions, and minimum PAR values. Because this research is based on a multi-goal problem, the achievement of one goal depends on the achievement of another. Therefore, there is a trade-off among user comfort, energy costs, and PAR minimization. To avoid peaks, energy consumption costs, and PAR values, a compromise must be made on delays in the operation of some devices during peak hours. Appliances using HGBFOA, especially air conditioners and vacuum cleaners, have a slightly longer latency than those using other existing algorithms. Furthermore, the operational delay of these appliances resulted in lower power consumption, price, and PAR.

5.6 Conclusion

Although DR programs can obtain efficient energy utilization and optimal power consumption, but their implementation is complex because of insufficient user knowledge. To achieve this goal, HGBFOA, which combines the GA and BFOA algorithms, was developed. EMC has significantly improved the performance of the DR program. EMC based on HGBFOA schedules home appliances to operate automatically according to the DR signal, enabling energy-efficient, cost-saving, and lower PAR and CO_2 emission schemes. Simulations and results show that EMC based on HGBFOA outperforms other existing algorithms and can achieve ongoing goals such as minimizing energy consumption and cost, and reducing PAR while maximizing user comfort.

5.6.1 Future extension

This research work can be stretched in the following directions in the future.

- For optimal energy management in smart grids, a fog and cloud-based system can be used.
- Coordination of energy suppliers with consumers shall be introduced in load planning to lower energy waste.
- Two-way power trade-off between the utility company and the consumer shall be initiated, taking into account the "vehicle-to-grid" and "grid-to-vehicle" energy optimization.
- For online and real-time energy optimization, a Lyapunov optimization method can be established that considers field demands from both energy suppliers and consumers.

Data availability statement

The original contributions presented in the study are included in the article/Supplementary Material; further inquiries can be directed to the corresponding authors.

Author contributions

SYA: conceptualization, technical analysis, formal analysis, methodology, original draft writing, methodology, software. GH: supervision, original draft writing, editing and review, visualization, software, project administration, funding acquisition, formal analysis. MA: Methodology & implementation, Writing-review & editing, Formal analysis & acquisition, Data curation, Funding acquisition, and Resources. TAK: Conceptualization, Data curation, Interpretation, Acquisition, Formal analysis, Methodology, Software, Validation, and Writing-Review & editing; KR: supervision, formal analysis, project administration, methodology, software, review and editing. KA: Visualization, Investigation, Formal Analysis, interpretation, Funding Acquisition, Writing-review & Editing, review. All authors contributed to the article and approved the submitted version.

Funding

This research is funded by Researchers Supporting Project Number (RSPD2023R947), King Saud University, Riyadh, Saudi Arabia.

Conflict of interest

The authors declare that the research was conducted in the absence of any commercial or financial relationships that could be construed as a potential conflict of interest.

Publisher's note

All claims expressed in this article are solely those of the authors and do not necessarily represent those of their affiliated organizations, or those of the publisher, the editors, and the reviewers. Any product that may be evaluated in this article, or claim that may be made by its manufacturer, is not guaranteed or endorsed by the publisher.

References

Abdollahi, A., Parsa Moghaddam, M., Rashidinejad, M., and Sheikh-El-Eslami, M. K. (2011). Investigation of economic and environmental-driven demand response measures incorporating UC. *IEEE Trans. smart grid* 3 (1), 12–25. doi:10.1109/tsg.2011.2172996

Abushnaf, J., Alexander, R., and Górnisiewicz, W. (2016). Impact on electricity use of introducing time-of-use pricing to a multi-user home energy management system. *Int. Trans. Electr. Energy Syst.* 26 (5), 993–1005. doi:10.1002/etep.2118

Adika, C. O., and Wang., L. (2014). Smart charging and appliance scheduling approaches to demand side management. *Int. J. Electr. Power & Energy Syst.* 57, 232–240. doi:10.1016/j.ijepes.2013.12.004

Albogamy, F. R., Khan, S. A., Hafeez, G., Murawwat, S., Khan, S., Haider, S. I., et al. (2022). Real-time energy management and load scheduling with renewable energy integration in smart grid. *Sustainability* 14 (3), 1792–1828. doi:10.3390/su14031792

Alzahrani, A., Hafeez, G., Rukh, G., Murawwat, S., Iftikhar, F., Ali, S., et al. (2023). Demand response for optimal power usage scheduling considering time and power flexibility of load in smart grid. *IEEE Access* 11 (2023), 33640–33651. doi:10.1109/access.2023.3263849

Azar, A. G., and Jacobsen, R. H. (2016). Appliance scheduling optimization for demand response. *Int. J. Adv. Intelligent Syst.* 9 (1&2), 50–64.

Barbato, A., and Capone, A. (2014). Optimization models and methods for demand-side management of residential users: a survey. *Energies* 7 (9), 5787–5824. doi:10.3390/en7095787

Cai, T., Dong, M., Chen, K., and Gong, T. (2022). Methods of participating power spot market bidding and settlement for renewable energy systems. *Energy Rep.* 8, 7764–7772. doi:10.1016/j.egyr.2022.05.291

Cao, B., Wang, X., Zhang, W., Song, H., and Lv, Z. (2020a). A many-objective optimization model of industrial internet of things based on private blockchain. *IEEE Netw.* 34 (5), 78–83. doi:10.1109/MNET.011.1900536

Cao, B., Yan, Y., Wang, Y., Liu, X., Lin, J. C., Sangaiah, A. K., et al. (2022). A multiobjective intelligent decision-making method for multistage placement of PMU in power grid enterprises. *IEEE Trans. Industrial Inf.* 19, 7636–7644. doi:10.1109/TII.2022.3215787

Cao, B., Zhao, J., Gu, Y., Fan, S., and Yang, P. (2020c). Security-aware industrial wireless sensor network deployment optimization. *IEEE Trans. Industrial Inf.* 16 (8), 5309–5316. doi:10.1109/TII.2019.2961340

Cao, B., Zhao, J., Yang, P., Gu, Y., Muhammad, K., Rodrigues, J. J. P. C., et al. (2020b). Multiobjective 3-D topology optimization of next-generation wireless data center network. *IEEE Trans. Industrial Inf.* 16 (5), 3597–3605. doi:10.1109/TII.2019.2952565

Chen, J., Sun, B., Li, Y., Jing, R., Zeng, Y., and Li, M. (2022). Credible capacity calculation method of distributed generation based on equal power supply reliability criterion. *Renew. Energy* 201, 534–547. doi:10.1016/j.renene.2022.10.129

Chung, K. L., Tian, H., Wang, S., Feng, B., and Lai, G. (2022). Miniaturization of microwave planar circuits using composite microstrip/coplanar-waveguide transmission lines. *Alexandria Eng. J.* 61 (11), 8933–8942. doi:10.1016/j.aej.2022.02.027

Dang, W., Liao, S., Yang, B., Yin, Z., Liu, M., Yin, L., et al. (2023). An encoder-decoder fusion battery life prediction method based on Gaussian process regression and improvement. *J. Energy Storage* 59, 106469. doi:10.1016/j.est.2022.106469

Elazab, R., Saif, O., Metwally, A. M. A., and Daowd, M. (2021). Mixed integer smart off-grid home energy management system. *Energy Rep.* 7 (2021), 9094–9107. doi:10.1016/j.egyr.2021.11.227

Elkazaz, M. H., Hoballah, A., and Azmy, A. M. (2016). Artificial intelligent-based optimization of automated home energy management systems. *Int. Trans. Electr. Energy Syst.* 26 (9), 2038–2056. doi:10.1002/etep.2195

Gelazanskas, L., and KelumGamage, A. A. (2014). Demand side management in smart grid: A review and proposals for future direction. *Sustain. Cities Soc.* 11, 22–30. doi:10.1016/j.scs.2013.11.001

Gu, Q., Tian, J., Yang, B., Liu, M., Gu, B., Yin, Z., et al. (2023). A novel architecture of a six degrees of freedom parallel platform. *Electronics* 12 (8), 1774. doi:10.3390/electronics12081774

Gul, Mehreen S., and Sandhya, Patidar. (2015). Understanding the energy consumption and occupancy of a multi-purpose academic building. *Energy Build.* 87, 155–165. doi:10.1016/j.enbuild.2014.11.027

Hafeez, G., Islam, N., Ali, A., Ahmad, S., Usman, M., and Khurram Saleem, A. (2019). A modular framework for optimal load scheduling under price-based demand response scheme in smart grid. *Processes* 7 (8), 499. doi:10.3390/pr7080499

Hafeez, G., Khurram Saleem, A., Wadud, Z., Khan, I., Usman, M., Abdul Baseer, Q., et al. (2020b). An innovative optimization strategy for efficient energy management with day-ahead demand response signal and energy consumption forecasting in smart grid using artificial neural network. *IEEE Access* 8, 84415–84433. doi:10.1109/access.2020.2989316

Hafeez, G., Wadud, Z., Ullah Khan, I., Khan, I., Shafiq, Z., Usman, M., et al. (2020a). Efficient energy management of IoT-enabled smart homes under price-based demand response program in smart grid. *Sensors* 20 (11), 3155. doi:10.3390/s20113155

Huang, N., Zhao, X., Guo, Y., Cai, G., and Wang, R. (2023a). Distribution network expansion planning considering a distributed hydrogen-thermal storage system based on photovoltaic development of the Whole County of China. *Energy* 278, 127761. doi:10.1016/j.energy.2023.127761

Huang, X., Chen, N., Ye, D., Zhong, A., Liu, H., Li, Z., et al. (2023b). Structurally complementary star-shaped unfused ring electron acceptors with simultaneously enhanced device parameters for ternary organic solar cells. *Sol. RRL* 7, 2300143. doi:10.1002/solr.202300143

Huang, Y., Wang, W., and Hou, B. (2019). A hybrid algorithm for mixed integer nonlinear programming in residential energy management. *J. Clean. Prod.* 226, 940–948. doi:10.1016/j.jclepro.2019.04.062

Imran, A., Hafeez, G., Khan, I., Usman, M., Shafiq, Z., Baseer Qazi, A., et al. (2020). Heuristic-based programable controller for efficient energy management under renewable energy sources and energy storage system in smart grid. *IEEE Access* 8, 139587–139608. doi:10.1109/access.2020.3012735

Jiang, J., Zhang, L., Wen, X., Valipour, E., and Nojavan, S. (2022). Risk-based performance of power-to-gas storage technology integrated with energy hub system regarding downside risk constrained approach. *Int. J. Hydrogen Energy* 47 (93), 39429–39442. doi:10.1016/j.ijhydene.2022.09.115

Jovanovic, R., Bousselham, A., and Islam Safak, B. (2016). Residential demand response scheduling with consideration of consumer preferences. *Appl. Sci.* 6 (1), 16. doi:10.3390/app6010016

Li, J., Deng, Y., Sun, W., Li, W., Li, R., Li, Q., et al. (2022b). Resource orchestration of cloud-edge–based smart grid fault detection. *ACM Trans. Sen. Netw.* 18 (3), 1–26. doi:10.1145/3529509

Li, P., Hu, J., Qiu, L., Zhao, Y., and Ghosh, B. K. (2022a). A distributed economic dispatch strategy for power–water networks. *IEEE Trans. Control Netw. Syst.* 9 (1), 356–366. doi:10.1109/TCNS.2021.3104103

LiHui, X., and Ho, S. (2014). User-expected price-based demand response algorithm for a home-to-grid system. *Energy* 64, 437–449. doi:10.1016/j.energy.2013.11.049

Lin, X., Liu, Y., Yu, J., Yu, R., Zhang, J., and Wen, H. (2022). Stability analysis of Three-phase Grid-Connected inverter under the weak grids with asymmetrical grid impedance by LTP theory in time domain. *Int. J. Electr. Power & Energy Syst.* 142, 108244. doi:10.1016/j.ijepes.2022.108244

Lokeshgupta, B., and Sivasubramani, S. (2019). Multi-objective home energy management with battery energy storage systems. *Sustain. Cities Soc.* 47, 101458. doi:10.1016/j.scs.2019.101458

Lv, Z., Chen, D., Lou, R., and Song, H. (2020a). Industrial security solution for virtual reality. *IEEE Internet Things J.* 8 (8), 6273–6281. doi:10.1109/JIOT.2020.3004469

Lv, Z., Qiao, L., Li, J., and Song, H. (2020b). Deep-learning-enabled security issues in the internet of things. *IEEE Internet Things J.* 8 (12), 9531–9538. doi:10.1109/JIOT.2020.3007130

Lv, Z., and Song, H. (2019). Mobile internet of things under data physical fusion technology. *IEEE Internet Things J.* 7 (5), 4616–4624. doi:10.1109/JIOT.2019.2954588

Lv, Z., Wu, J., Li, Y., and Song, H. (2022). Cross-layer optimization for industrial internet of things in real scene digital twins. *IEEE Internet Things J.* 9 (17), 15618–15629. doi:10.1109/JIOT.2022.3152634

Ma, K., Yao, T., Yang, J., and Guan, X. (2016). Residential power scheduling for demand response in smart grid. *Int. J. Electr. Power & Energy Syst.* 78, 320–325. doi:10.1016/j.ijepes.2015.11.099

Ma, K., Li, Z., Liu, P., Yang, J., Geng, Y., Yang, B., et al. (2021). Reliability-Constrained throughput optimization of industrial wireless sensor networks with energy harvesting relay. *IEEE Internet Things J.* 8 (17), 13343–13354. doi:10.1109/JIOT.2021.3065966

Mary, G. A., and Rajarajeswari, R. (2014). Smart grid cost optimization using genetic algorithm. *Int. J. Res. Eng. Technol.* 3 (07), 282–287. doi:10.15623/ijret.2014.0319051

Min, C., Pan, Y., Dai, W., Kawsar, I., Li, Z., and Wang, G. (2023). Trajectory optimization of an electric vehicle with minimum energy consumption using inverse dynamics model and servo constraints. *Mech. Mach. Theory* 181, 105185. doi:10.1016/j.mechmachtheory.2022.105185

Muhsen, D. H., Haider, H. T., Al-Nidawi, Y., and Khatib, T. (2019). Optimal home energy demand management based multi-criteria decision making methods. *Electronics* 8 (5), 524. doi:10.3390/electronics8050524

Priya Esther, B., Shivarama Krishna, K., Sathish Kumar, K., and Ravi, K. (2016). "Demand side management using bacterial foraging optimization algorithm," in Proceedings of the Information Systems Design and Intelligent Applications Proceedings of Third International Conference INDIA, Berlin, Germany, February 2016 (Springer India), 657–666.

Rastegar, M., Fotuhi-Firuzabad, M., and Zareipour, H. (2016). Home energy management incorporating operational priority of appliances. *Int. J. Electr. Power & Energy Syst.* 74, 286–292. doi:10.1016/j.ijepes.2015.07.035

Rehman, A. U., Wadud, Z., Elavarasan, R. M., Hafeez, G., Khan, I., Shafiq, Z., et al. (2021). An optimal power usage scheduling in smart grid integrated with renewable energy sources for energy management. *IEEE Access* 9 (2021), 84619–84638. doi:10.1109/access.2021.3087321

Ribeiro, C., Pinto, T., Vale, Z., and Baptista, J. (2018). "Data mining for prosumers aggregation considering the self-generation," in *Distributed computing and artificial intelligence, 14th international conference* (Berlin, Germany: Springer International Publishing), 96–103.

Ribeiro, C., Pinto, T., Vale, Z., and Baptista, J. (2020). "Data mining for remuneration of consumers demand response participation," in *Highlights in practical applications of agents, multi-agent systems, and trust-worthiness. The PAAMS collection: International workshops of PAAMS 2020* (L'Aquila, Italy: Springer International Publishing), 326–338.

Samadi, P., Amir-Hamed, M. R., Robert, S., Wong, V. W. S., and Juri, J. (2010). "Optimal real-time pricing algorithm based on utility maximization for smart grid," in Proceedings of the 2010 First IEEE International Conference on Smart Grid Communications, Gaithersburg, MD, USA, October 2010 (IEEE).

Sarker, E., Halder, P., Seyedmahmoudian, M., Jamei, E., Horan, B., Mekhilef, S., et al. (2021). Progress on the demand side management in smart grid and optimization approaches. *Int. J. Energy Res.* 45 (1), 36–64. doi:10.1002/er.5631

Shirazi, E., and Jadid, S. (2015). Optimal residential appliance scheduling under dynamic pricing scheme via HEMDAS. *Energy Build.* 93, 40–49. doi:10.1016/j.enbuild.2015.01.061

Srinivasan, D., Rajgarhia, S., Radhakrishnan, B. M., Sharma, A., and Khincha, H. (2017). Game-Theory based dynamic pricing strategies for demand side management in smart grids. *Energy* 126, 132–143. doi:10.1016/j.energy.2016.11.142

Sun, B., Li, Y., Zeng, Y., Chen, J., and Shi, J. (2022). Optimization planning method of distributed generation based on steady-state security region of distribution network. *Energy Rep.* 8, 4209–4222. doi:10.1016/j.egyr.2022.03.078

United States Department of Energy *Energy information administration*. Washington: Government agency. Available at: https://www.eia.gov/todayinenergy/detail.cfm?id=12251 (Accessed December 17, 2015).

Wang, B., Zhang, Y., and Zhang, W. (2022a). A composite adaptive fault-tolerant attitude control for a quadrotor UAV with multiple uncertainties. *J. Syst. Sci. Complex.* 35 (1), 81–104. doi:10.1007/s11424-022-1030-y

Wang, H., Zheng, X., Yuan, X., and Wu, X. (2022b). Low-complexity model predictive control for a nine-phase open-end winding PMSM with dead-time compensation. *IEEE Trans. power Electron.* 1, 8895–8908. doi:10.1109/TPEL.2022.3146644

Wang, J., Tian, J., Zhang, X., Yang, B., Liu, S., Yin, L., et al. (2022c). Control of time delay force feedback teleoperation system with finite time convergence. *Front. NEUROROBOTICS* 16, 877069. doi:10.3389/fnbot.2022.877069

Xiao, S., Cao, Y., Wu, G., Guo, Y., Gao, G., Chen, S., et al. (2022). Influence of the distributed grounding layout for intercity trains on the 'train-rail' circumflux. *IEEE Trans. Circuits Syst. II Express Briefs* 70, 1194–1198. doi:10.1109/TCSII.2022.3223984

Xie, X., and Sun, Y. (2022). A piecewise probabilistic harmonic power flow approach in unbalanced residential distribution systems. *Int. J. Electr. Power & Energy Syst.* 141, 108114. doi:10.1016/j.ijepes.2022.108114

Yan, Z., and Wen, H. (2021). Electricity theft detection base on extreme gradient boosting in AMI. *IEEE Trans. Instrum. Meas.* 70, 1–9. doi:10.1109/TIM.2020.3048784

Yu, D., Duan, C., and Gu, B. (2023). Design and evaluation of a novel plan for thermochemical cycles and PEM fuel cells to produce hydrogen and power: application of environmental perspective. *Chemosphere* 334, 138935. doi:10.1016/j.chemosphere.2023.138935

Yu, M., and Ho, S. (2016). Supply–demand balancing for power management in smart grid: a Stackelberg game approach. *Appl. energy* 164, 702–710. doi:10.1016/j.apenergy.2015.12.039

Zafar, S., Nawaz, K., Naqvi, S. A. R., and Malik, T. N. (2013). Integration of renewable energy sources in smart grid: A review. *Nucl.* 50 (4), 311–327.

Zhang, S., Zhou, Z., Luo, R., Zhao, R., Xiao, Y., and Xu, Y. (2022c). A low-carbon, fixed-tour scheduling problem with time windows in a time-dependent traffic environment. *Int. J. Prod. Res.* 61, 6177–6196. doi:10.1080/00207543.2022.2153940

Zhang, W., Zheng, Z., Liu, H., Yang, P., Wang, J., Chen, Y., et al. (2022b). Global characterization of megakaryocytes in bone marrow, peripheral blood, and cord blood by single-cell RNA sequencing. *CSEE J. Power Energy Syst.* 8 (6), 1636–1647. doi:10.1038/s41417-022-00476-z

Zhang, X., Wang, Y., Yuan, X., Shen, Y., Lu, Z., and Wang, Z. (2022a). Adaptive dynamic surface control with disturbance Observers for battery/supercapacitor-based hybrid energy sources in electric vehicles. *IEEE Trans. Transp. Electrification*, 1. doi:10.1109/TTE.2022.3194034

Zhang, Z., Altalbawy, F. M. A., Al-Bahrani, M., and Riadi, Y. (2023). Regret-based multi-objective optimization of carbon capture facility in CHP-based microgrid with carbon dioxide cycling. *J. Clean. Prod.* 384, 135632. doi:10.1016/j.jclepro.2022.135632

Zhao, P., Ma, K., Yang, J., Yang, B., Guerrero, J. M., Dou, C., et al. (2022). Distributed power sharing control based on adaptive virtual impedance in seaport microgrids with cold ironing. *IEEE Trans. Transp. Electrification* 9, 2472–2485. doi:10.1109/TTE.2022.3211204

Zhao, Z., WonLee, C., Shin, Y., and Song, K. B. (2013). An optimal power scheduling method for demand response in home energy management system. *IEEE Trans. smart grid* 4 (3), 1391–1400. doi:10.1109/tsg.2013.2251018

Zhongming, Z., et al. (2019). *Climate central solutions brief: Battery energy storage*.

Zhou, B., Li, W., Chan, K. W., Cao, Y., Kuang, Y., Liu, X., et al. (2016). Smart home energy management systems: concept, configurations, and scheduling strategies. *Renew. Sustain. Energy Rev.* 61, 30–40. doi:10.1016/j.rser.2016.03.047

Nomenclature

Abbreviation	Definition
AMI	Advanced metering infrastructure
DSM	Demand side management
DR	Demand response
EMC	Energy management controller
EUC	Electricity utility company
DAP	Day-ahead pricing
SM	Smart meter
TOU	Time of use
RTP	Real-time pricing
PAR	Peak-to-average ratio
AOA	Automatically operated appliances
GA	Genetic algorithm
PSO	Particle swarm optimization
BFO	Bacteria foraging optimization
HGBFOA	Hybrid genetic bacteria foraging optimization algorithm
HEMS	Home energy management system
IHD	In-home display
HAN	Home area network
EWH	Electric water heater
Ref	Refrigerator
BPSO	Binary particle swarm optimization
HGPO	Hybrid genetic particle optimization
RG	Renewable generation
DLC	Direct load control
IBR	Inclining block rate
ESS	Energy storage system

Symbol	Definition
T_a^t	Time of operation of residential appliances
$F3 = \frac{W_a}{W_a^{td}} \times 100$	Appliance operational interval
App	Appliance
$Min(F) = Min(F_1\varphi_1+F_2\varphi_2+F_3\varphi_3+F_4\varphi_4)$	Required temperature
$\sum_{i\in App} p_i s_i(t) = P_{\lim}(t) \forall t \in \tau \,\&\, i \in App$	Initial temperature
φ_1	Cooling due to on status
φ_2	Rated power of the appliance
φ_3	Appliance status
φ_4	Stored energy
$O_i(t)$	Solar PV generation
τ_i	Solar PV efficiency
T_{req}	Solar irradiance
T_{ini}	Efficiency of the battery
β	Charging upper limit
$App^i_{P_{rate}}$	Discharging lower limit
S_t	Charging rate
E_{stor}	Discharging rate
E_g^{Pv}	Number of appliances
η^{Pv}	Energy consumed by time-flexible appliances
Irr	Energy consumed by critical appliances
μ^{ESS}	Energy consumed by hybrid appliances
EE_{UL}^{Ch}	Energy consumed by power-flexible appliances
EE_{LL}^{Dsh}	Appliance waiting time
EE^{Ch}	Pre-scheduled status of appliances
EE^{Dch}	Appliance status after scheduling
N	Maximum delay in appliance operation

frontiers | Frontiers in Energy Research

TYPE Original Research
PUBLISHED 29 September 2023
DOI 10.3389/fenrg.2023.1278305

Check for updates

OPEN ACCESS

EDITED BY
Yushuai Li,
University of Oslo, Norway

REVIEWED BY
Yajuan Guan,
Aalborg University, Denmark
Guoliang Wang,
Liaoning Shihua University, China
Wenlong Liao,
Swiss Federal Institute of Technology Lausanne, Switzerland

*CORRESPONDENCE
Yan Zhao,
zhaoyan@sie.edu.cn

RECEIVED 16 August 2023
ACCEPTED 18 September 2023
PUBLISHED 29 September 2023

CITATION
Zhang X, Zhao Y, Jiang H and Wei M (2023), Design of integral sliding mode control and fuzzy adaptive PI control for voltage stability in DC microgrid. *Front. Energy Res.* 11:1278305. doi: 10.3389/fenrg.2023.1278305

COPYRIGHT
© 2023 Zhang, Zhao, Jiang and Wei. This is an open-access article distributed under the terms of the Creative Commons Attribution License (CC BY). The use, distribution or reproduction in other forums is permitted, provided the original author(s) and the copyright owner(s) are credited and that the original publication in this journal is cited, in accordance with accepted academic practice. No use, distribution or reproduction is permitted which does not comply with these terms.

Design of integral sliding mode control and fuzzy adaptive PI control for voltage stability in DC microgrid

Xinyu Zhang[1,2], Yan Zhao[1,2]*, He Jiang[1,2] and Mofan Wei[3]

[1]School of Renewable Energy, Shenyang Institute of Engineering, Shenyang, China, [2]Liaoning Key Laboratory of Regional Multi-Energy System Integration and Control, Shenyang, China, [3]School of Electrical Engineering, Shenyang University of Technology, Shenyang, China

This paper introduces a novel control strategy that merges integral sliding mode control with fuzzy adaptive PI control. This hybrid approach maximizes the benefits of both techniques to ensure voltage stability in DC microgrid. Firstly, a mathematical model characterizes the DC–DC boost converter. Subsequently, a sliding surface, incorporating an integral term, is employed to regulate the converter's output voltage and current errors. To address uncertainties stemming from factors like input inductance and output capacitance, a dynamic sliding mode controller is formulated. The proposed sliding mode control scheme significantly reduces the time required for voltage stability, curbs system oscillations, and showcases robustness. Furthermore, the inclusion of fuzzy adaptive PI control aids in refining the voltage deviation signal and droop resistance. This enhancement improves the precision of the error tracking system. Finally, the effectiveness of this strategy is demonstrated through MATLAB simulations, supported by experimental validation and analysis. The findings reveal that this control strategy efficiently accelerates the convergence of DC microgrid voltage to a stable state.

KEYWORDS

sliding mode control, fuzzy control, adaptive PI control, DC microgrid, voltage stability

1 Introduction

A microgrid can be conceptualized as an integrated power system that encompasses distributed generation systems, loads, and energy storage devices (Ullah et al., 2022). The growing adoption of microgrids is attributed to their heightened reliability, improved economic considerations and reduced global warming impact. The DC microgrid, in particular, has garnered significant attention and research interest in the realm of power engineering owing to its distinct advantages and potential. When contrasted with AC microgrids, DC microgrids offer enhanced reliability, efficiency, and reduced power conversion losses. Additionally, a majority of loads in modern residential and industrial applications are powered by DC sources (Gui et al., 2021; Saafan et al., 2023). Consequently, DC microgrids hold appeal as integral components within contemporary intelligent power systems (Prabhakaran and Agarwal, 2020).

In the current context, with the focal point on sustainable energy and energy efficiency, the significance of DC–DC converters in electrical engineering and microgrid design has gained further prominence (Wang et al., 2020). These converters play a pivotal role in connecting the DC output of renewable energy sources to the distribution system, owing to their

cost-effectiveness, straightforward structure, and efficient power conversion performance. This aspect holds vital importance in optimizing energy utilization and enhancing energy efficiency at the user end (Haroun et al., 2015; Tiwary et al., 2023). The fundamental control objectives of a DC microgrid encompass skillful power distribution management and meticulous bus voltage regulation (Li et al., 2021). Prolonged substantial deviations in output voltage can precipitate system instability, necessitating the introduction of stabilizing control methodologies.

Regarding the stability quandary of boost converters, an array of advanced control strategies have been proposed, including proportional resonant (PR) control, proportional integral derivative (PID) control, fuzzy logic-based control, and repetitive control (Zheng et al., 2018). Among these control strategies mentioned above, sliding mode control is considered to be a very efficient nonlinear robust control method due to its large stabilization range, rapid dynamic response, and strong disturbance immunity (Wang et al., 2021; Linares-Flores et al., 2022). In (Liu et al., 2011), the authors designed two control loops containing different converters which involve variable charging and discharging modes to enhance the productivity of a hybrid power system. The designed method, although it has improved the efficiency of the system, employs electrical components such as bi-directional converters and inductors that are too idealized and do not take into account the presence of uncertainties at the same time, which does not achieve a fast tracking of the errors. Literature (Mao et al., 2022) tries to solve this problem by incorporating T-S fuzzy control when dealing with nonlinear state variables, so as to improve the utilization of PV cells connected to the microgrid while maintaining the stability of the bus voltage, but the procedure is relatively time consuming. The maintenance of system stability is an important task in control theory. In traditional discontinuous control theory, the generation of control rates usually relies on sign functions or hysteresis modulators and in this way ensures the stability of the system. These generated control laws must satisfy certain specific inequality conditions (Biricik and Komurcugil, 2016; Merabet et al., 2017) to ensure their validity. However, a noteworthy issue is that this control strategy still suffers from output chattering. This may negatively affect the system performance, especially in applications with high precision control or high dynamic response. To address this issue, researchers have started to consider the use of smoothing control law to eliminate the vibration problem of discrete-time sliding mode control. This is an effective strategy, which can suppress the chattering to a certain extent and thus improve the system performance. However, the smoothing control law is not without problems. The primary problem is that this control method may limit the regulation capability and dynamic response of the converter. Literature (Inomoto et al., 2022) provides a solution to the above problem by designing two control loops in the sliding mode controller. The first is an input voltage control loop for computing the inductive current, guided by the MPPT algorithm. The second circuit controls the current, which is related to the duty cycle of the switches. These two loops enhance the performance of the converter. The proposed technique uses a smooth switching function to avoid chattering, resulting in a substantial shortening of the time to reach a steady state. However, the literature selects high-order sliding surfaces, which leads to the drawback of overly complex algorithmic calculations.

The means for treating system uncertainties and variations are not only sliding mode control, the adaptive PI control and fuzzy control are also often in the priority list. Literature (Mi et al., 2019) incorporates a T-S fuzzy model in a sliding mode controller designed for the DC microgrid. Since the relationship between the output voltage and power of distributed power sources is nonlinear, the T-S fuzzy model is introduced for processing. The sliding mode droop control is used to improve the vibration resistance of the system due to parameter uncertainties and variations in operating conditions. This combination enables the system to be more accurate when allocating power according to the load. In the literature (Ahmed et al., 2018), the author addresses the occurrence of phenomena such as short-circuits or abrupt changes in load during the operation of power electronic devices. A fuzzy logic control was integrated into the coefficients of traditional PI controllers, enabling the controller to rapidly respond to these changes. Taking power electronic distribution transformer as an example, the voltage and current errors are transferred to the improved PI controller and the performance of the controller in its application under different operating conditions is considered. The experiment demonstrates that the proposed controller is capable of meeting the desired requirements, but suffers from the problem of slow response time. The authors in (Mokhtar et al., 2019) employed a sliding mode controller to control the tracking error, and then added an adaptive PI controller to adjust the error-related voltage and current more accurately, but the sliding mode control portion of it was not sufficiently stable for voltage error control. Different from the previous work that only considered different control methods combined together, in the literature (Jan et al., 2020), the authors emphasized on the improvement of the parameters while applying two control methods, in which the parameters are inferred by using the affiliation function and fuzzy rule table, and genetic algorithms are also involved. Ultimately, the output power of the renewable energy source can be maximized, while these measures assure the frequency stabilization in the system. However, with this control method, unknown system parameters need to be estimated through the use of multiple adaptive laws, which leads to the over-parameterization problem. Literature (Kuppusamy and Joo, 2021) designed a memory-integrated sliding mode control based on perturbation observer using T-S fuzzy approach, which defines an integral fuzzy switching surface function containing both input matrix and implicit parameters related to the state variables, and utilizes the disturbance estimation generated by the perturbation observer to offset the mismatched disturbance error. This strategy has a T-S fuzzy modeling of the sliding mode motion, which operates according to the control model in the initial state and maintains this state continuously under the limitations of the memory sliding mode. This method is guaranteed for the fast response of the system while preserving its continuous stability.

Addressing the challenge posed by the complex and uncertain operational environment, which impedes the maintenance of a sustained steady state, this study introduces a novel sliding mode control (SMC) scheme. To secure the stable operation of the DC microgrid, an integral sliding surface is constructed, subsequently refining the traditional SMC approach. The stability of the improved SMC method is substantiated through an appropriate Lyapunov function.

The main contributions of this paper are as follows.

1) The proposed SMC effectively mitigates system chattering by incorporating an integral sliding surface design, markedly enhancing tracking performance and ensuring voltage stability;

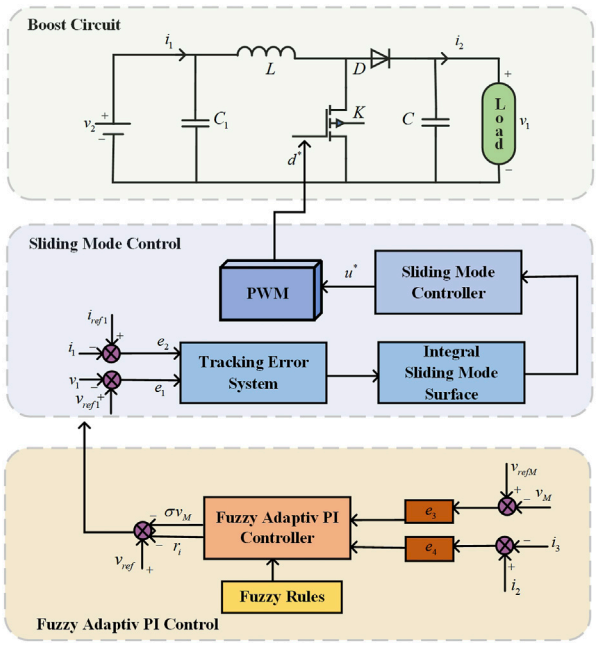

FIGURE 1
The general framework of the proposal control strategy in the DC microgrid.

2) An adaptive PI controller is combined to govern the error between the DC bus voltage and its reference value and the droop resistance to optimize voltage regulation. This combination yields a more precise converter output voltage;
3) Parameter tuning for the adaptive PI controller leverages fuzzy rules, allowing adaptation to varying internal and external parameters.

The rest of this paper is organized as follows. Section 2 shows the system model of the DC–DC converter. Section 3 introduces the designed sliding mode controller. Section 4 describes the fuzzy adaptive PI control. Section 5 presents the simulation results. The conclusion is illustrated in Section 6.

2 System model of the DC–DC converter

DC–DC converters are utilized in numerous applications in power systems. These converters manipulate the power electronics' on/off states to modulate current transmission paths for voltage augmentation. Notably, boost converters offer distinct advantages across diverse scenarios. Their short duty cycles translate to comparatively low energy losses, a crucial attribute for extended-operation devices like remote communication systems, computers, and office automation equipment. Moreover, boost converters find favor in precision-demanding sectors like military and aerospace owing to their stable output voltage traits (Lee et al., 2011). In essence, the realm of DC–DC converters is characterized by diversity and multifold applications, encompassing varied types. Boost converters, specifically, have seamlessly integrated into myriad domains owing to their distinctive attributes. Figure 1 illustrates the overarching framework of the described control strategy. The mathematical representation of a DC–DC converter is given by

$$\begin{cases} \dfrac{dv_1}{dt} = \dfrac{-i_2}{C} + \dfrac{-(u-1)i_1}{C} \\ \dfrac{di_1}{dt} = \dfrac{v_2}{L} + \dfrac{(u-1)v_1}{L} \end{cases} \tag{1}$$

where v_1 is the actual output voltage of the converter, v_2 is the input supply voltage of the converter, i_1 is the inductor current, i_2 is the actual output current, and u is the switching state, $u \in [0, 1]$.

3 Proposed sliding mode control

In microgrids, whether the voltage is stable or not is of especially significance for improving the performance of control accuracy and response speed, including ensuring the stable operation of microgrids. For this reason, the control approach used in this paper is the sliding mode control, where the object of control is chosen to be a tracking error system consisting of errors in output voltage and inductive current with their reference values, we introduce the following definitions:

$$e_1 = v_{ref1} - v_1 \tag{2}$$

where v_{ref1} is the reference value of the converter output voltage, and e_1 is the error between the output voltage and the reference value of the output voltage.

$$e_2 = i_{ref1} - i_1 \tag{3}$$

where i_{ref1} is the reference value of the converter output current, e_2 is the error between the converter output current and the current reference value. e_1 and e_2 are the tracking error state variables. From this, the dynamic equation for the tracking error of the system could be given in the following formulation:

$$\dot{e} = Ae + Bx(t)u + D(t) \tag{4}$$

In Eq. 4, the system state matrices e, A, B, $x(t)$ and $D(t)$ can be express by

$$e = \begin{bmatrix} e_1 & e_2 \end{bmatrix}^T$$
$$A = \begin{bmatrix} 0 & \frac{1}{C} \\ \frac{-1}{L} & 0 \end{bmatrix}$$
$$B = \begin{bmatrix} \frac{1}{C} & 0 \\ 0 & \frac{-1}{L} \end{bmatrix}$$
$$x(t) = \begin{bmatrix} i_1 & v_1 \end{bmatrix}^T$$
$$D(t) = \begin{bmatrix} \frac{i_2 - i_{ref1}}{C} & \frac{v_{ref1} - v_2}{L} \end{bmatrix}^T$$

The design of the sliding surface is crucial and it directly determines the dynamic properties of the system under sliding mode motion. After the system state reaches the sliding surface, the behavior will be governed by the nature of the sliding surface. This means that the system is robust to parameter variations and external perturbations. However, the traditional sliding mode control can lead to a large chattering in the

system due to the high frequency switching characteristics of the sliding surface. Hence, during the refinement of the algorithm, a consideration of how to balance the robustness in the system with the need to suppress chattering is warranted to gain an optimization of the control capability of the converter. The introduction of an integral term into the sliding surface is a mean to attenuate the high-frequency switching and consequently reduce the system vibration to a certain extent. The integral sliding surface can ensure more stable system operation. Therefore, the following sliding surface containing integral term is selected.

$$s = g_1 e + g_2 \int_0^t e dt \tag{5}$$

where g_1 and g_2 are constant matrices, $g_1 = [\, g_{11} \;\; g_{12} \,]$, $g_2 = [\, g_{21} \;\; g_{22} \,]$, g_{11}, g_{12}, g_{21} and g_{22} are constants, respectively.

Substituting Eq. 4 into the derivative of the integral sliding surface (5) yields

$$\dot{s} = g_1 \left(Ae + Bx(t)u + D(t) \right) + g_2 e \tag{6}$$

The equivalent control law can be obtained by setting Eq. 6 to be zero

$$u_{eq} = -\left(g_1 Bx(t) \right)^{-1} \left[\left(g_1 A + g_2 \right) e + g_1 D(t) \right] \tag{7}$$

Taking parameter uncertainty and resistance to perturbations into account as well, the hyperbolic tangent function is adopted and the final design of the sliding mode controller is expressed as follows:

$$\begin{aligned} u^* = & -\left(g_1 Bx(t) \right)^{-1} \left[\left(g_1 A + g_2 \right) e + g_1 D(t) \right] \\ & + \left(g_1 Bx(t) \right)^{-1} \left(-\eta \sqrt{|s|}\, sgn(s) - \int_0^t \tau sgn(s) dt \right. \\ & \left. -\lambda tanh(s) - \theta sgn(s) \right) \end{aligned} \tag{8}$$

where η, τ and θ are normal numbers, λ is a negative real number, and $|\lambda| \le \theta$, $sgn(s)$ are sign functions.

In this improved sliding mode controller, $\eta \sqrt{|s|} sgn(s)$, $\int_0^t \tau sgn(s) dt$ and $\theta sgn(s)$ are used to resist disturbances and reduce chattering. The purpose of adding $\lambda tanh(s)$ is to speed up the convergence of the system. The condition $|\lambda| \le \theta$ is to ensure system stability.

In order to analyze the stability of the proposed sliding mode control, the following Lyapunov function is selected.

$$V = \frac{1}{2} s^2 \tag{9}$$

Differentiating the Lyapunov function and combining with Eq. 8, it yields

$$\begin{aligned} \dot{V} &= s\dot{s} \\ &= s\left[g_1 A \left(e + Bx(t)u + D(t) \right) + g_2 e \right] \\ &= s\{ g_1 [Ae + Bx(t) \left(-\left(g_1 Bx(t) \right)^{-1} \left[\left(g_1 A + g_2 \right) e + g_1 D(t) \right] \right. \\ &\quad + \left(g_1 Bx(t) \right)^{-1} \left(-\eta \sqrt{|s|} sgn(s) - \int_0^t \tau sgn(s) dt \right. \\ &\quad \left. \left. -\lambda tanh(s) - \theta sgn(s) \right) \right) + D(t)] + g_2 e \} \\ &= s\left(-\eta \sqrt{|s|}\, sgn(s) - \int_0^t \tau sgn(s) dt - \lambda tanh(s) - \theta sgn(s) \right) \\ &= -\eta \sqrt{|s|} |s| - \tau s \int_0^t sgn(s) dt - \lambda s tanh(s) - \theta |s| \le 0 \end{aligned} \tag{10}$$

The above-mentioned verification indicates that the derivative of the Lyapunov function $\dot{V} \le 0$, affirming the stability of the controller devised in this study.

In a high switching frequency environment, the duty cycle can be interpreted as a smooth analytic function of the discrete pulses in a pulse width modulation (PWM) control system. The duty cycle of the DC–DC boost converter is a key parameter that determines the adjustment range and stability of the output voltage. The average control motion of the sliding mode control system can theoretically be viewed as the average dynamic response of a PWM control system. However, regardless of the output of the SMC system, the actual physical meaning has a limitation on the value of the duty cycle, which must be in the region of [0, 1]. Therefore, we can design an actual duty cycle d^* for generating a PWM control signal to drive the controllable switches of the converter. In this study, we use PWM to generate pulse signals to control the converter switches by opening and closing them, thus realizing the precise regulation of the system. The actual duty cycle d^* is expressed as follows:

$$d^* = \begin{cases} 1 & d \ge 1 \\ -\left(g_1 Bx(t) \right)^{-1} \left[\left(g_1 A + g_2 \right) e + g_1 D(t) \right] & \\ + \left(g_1 Bx(t) \right)^{-1} \left(-\eta \sqrt{|s|}\, sgn(s) - \int_0^t \tau sgn(s) dt \right. & 0 < d < 1 \\ \left. -\lambda tanh(s) - \theta sgn(s) \right) & \\ 0 & d \le 0 \end{cases} \tag{11}$$

4 Fuzzy adaptive PI control

To make the voltage error more accurate and ensure enhanced stability in the output voltage of the converter, two fuzzy adaptive PI controllers are added to the treatment of the voltage tracking error. These controllers serve to enhance precision in managing the DC bus voltage and the droop resistance, respectively. The inputs of adaptive PI controllers are the DC bus voltage error and the current distribution error. By manipulating the droop control parameters, precise control over the current allocation for each distributed generation system within the microgrid is achieved, leading to elevated power quality and microgrid reliability. The following equation presents an adaptive droop system expression:

$$v_{ref1} = v_{ref} + \sigma v_M - r_d i_2 \tag{12}$$

where σv_M is the voltage deviation signal to regulate the DC bus voltage v_M and its reference value v_{ref}, r_d is the droop resistance of the converter. The voltage deviation signal can be expressed by

$$\sigma v_M = -q_1 q_{2p}(t) e_3(t) + q_1 \int_0^t q_{3i}(t) e_3(t) dt \tag{13}$$

$$e_3(t) = v_{refM} - v_M \tag{14}$$

where $e_3(t)$ is the difference between the DC bus voltage v_M and its reference value v_{refM}, q_1 is a positive constant, $q_{2p}(t)$ is a proportional gain coefficient, and $q_{3i}(t)$ is an integral gain coefficient. The proportional and integral gains are expressed as follows:

$$q_{2p}(t) = {e_3}^2(t) + \rho_1 \int_0^t {e_3}^2(t) dt \tag{15}$$

$$q_{3i}(t) = \rho_2 \int_0^t {e_3}^2(t) dt \tag{16}$$

where ρ_1 and ρ_2 are normal numbers.

In the practical operation of microgrids, due to the occurrence of sudden changes in loads, etc., the currents are not immune to additional errors, which can have an effect on the droop resistance in the droop system. We have to cope with this situation and the new droop resistance can be written by

$$r_i = -q_4 q_{5p}(t) e_4(t) + q_4 \int_0^t q_{6i}(t) e_4(t) dt + r_d \tag{17}$$

$$q_{5p}(t) = {e_4}^2(t) + \rho_3 \int_0^t {e_4}^2(t) dt \tag{18}$$

$$q_{6i}(t) = \rho_4 \int_0^t {e_4}^2(t) dt \tag{19}$$

$$e_4(t) = i_2 - i_3 \tag{20}$$

where r_i is the new droop resistance, $e_4(t)$ is the current distribution error between actual output current and expected current, i_3 is the current expected value, q_4 is a constant, $q_{5p}(t)$ and $q_{6i}(t)$ are the proportional and integral gain coefficients in the current distribution loop, respectively, ρ_3 and ρ_4 are normal numbers.

While the conventional PI control approach enjoys widespread application, it exhibits poor robustness, susceptibility to voltage overshoot and current surges, and sensitivity to alterations in system parameters and nonlinear traits. Fuzzy control, in contrast, is an adaptable method not contingent upon an accurate system model. It showcases robustness, particularly when handling nonlinear systems. Nonetheless, despite the merits of fuzzy control, its performance might lag behind that of conventional PI control in certain instances. To synergize the advantages of both approaches and surmount their individual limitations, this paper combines fuzzy control with an adaptive PI controller. This combination enables online self-adjustment of PI parameters through fuzzy rules to make the parameters more accurate and flexible. The method seamlessly combines the robustness of fuzzy logic and the intuition of PI control, enabling the controller to flexibly adapt to diverse load variations and voltage fluctuations. Specifically, the engineered fuzzy adaptive PI controller initially acquires system error and error variation rate data. Subsequently, it employs a fuzzy logic system to conduct reasoning based on this information, adjusting parameters based on the outcomes. This design empowers the controller to dynamically fine-tune its performance to accommodate shifts in the system state.

The fuzzy domains of the fuzzy input variables e_3 and Δe_3 are set to [−6, +6], and the fuzzy domains of the fuzzy controller outputs $\Delta q_{2p}(t)$ and $\Delta q_{3i}(t)$ are set to [−6, +6] respectively. The membership functions are defined as NB (Negative Big), NM (Negative Medium), NS (Negative Small), ZE (Zero), PS (Positive Small), PM (Positive Medium), PB (Positive Big). Based on the experience of previous engineers and repeated experiments, fuzzy rule control tables are shown in Table 1 and Table 2. Subsequently, the membership function is determined, considering the degree of coverage of the domain and robustness, stability and sensitivity, the linguistic values of the fuzzy linguistic variables in this paper are using the triangular membership function, as shown in Figure 2.

TABLE 1 Fuzzy rule control table of $\Delta q_{2p}(t)$ and $\Delta q_{5p}(t)$

e	Δe						
	NB	NM	NS	ZE	PS	PM	PB
NB	PB	PB	NB	PM	PS	PS	ZE
NM	PB	PB	NM	PM	PS	ZE	ZE
NS	PB	PM	NS	PS	ZE	NS	NM
ZE	PM	PM	ZE	ZE	NS	NM	NM
PS	PM	PS	ZE	NS	NS	NM	NM
PM	PS	ZE	NM	NM	NM	NB	NB
PB	ZE	NM	NS	NM	NB	NB	NB

TABLE 2 Fuzzy rule control table of $\Delta q_{3i}(t)$ and $\Delta q_{6i}(t)$

e	Δe						
	NB	NM	NS	ZE	PS	PM	PB
NB	ZE	ZE	NB	NM	NM	PS	PS
NM	ZE	ZE	NM	NM	NS	ZE	ZE
NS	ZE	ZE	NS	NS	ZE	ZE	ZE
ZE	ZE	ZE	NS	NM	PS	ZE	ZE
PS	ZE	ZE	ZE	PS	PS	ZE	ZE
PM	ZE	ZE	PS	PM	PM	ZE	ZE
PB	NS	NS	NS	PM	PB	ZE	ZE

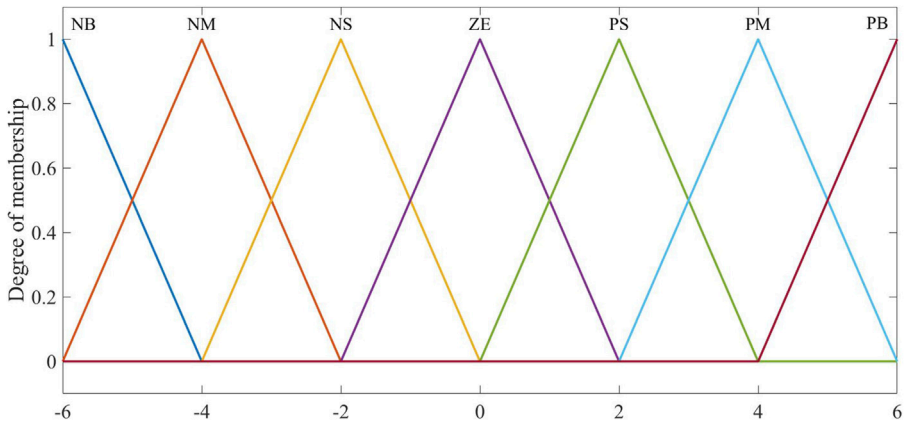

FIGURE 2
The membership function.

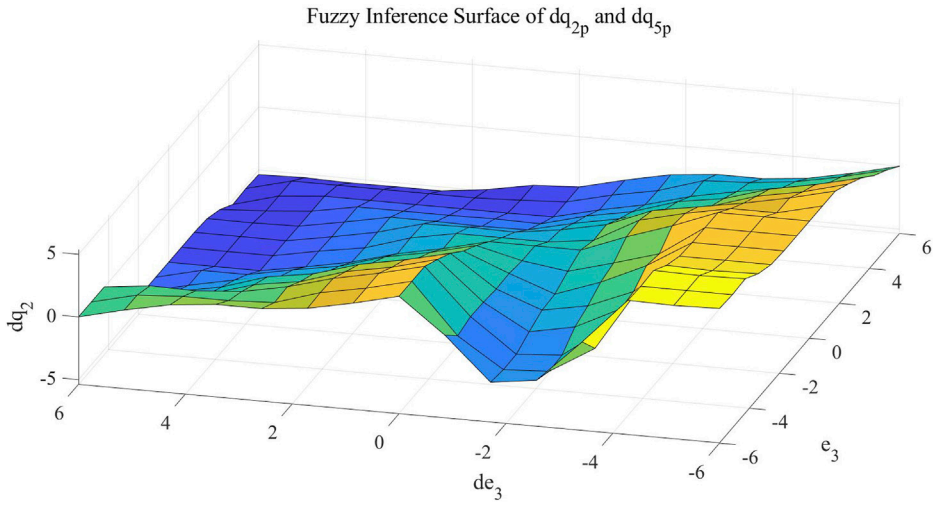

FIGURE 3
Fuzzy inference surface of $\Delta q_{2p}(t)$ and $\Delta q_{5p}(t)$.

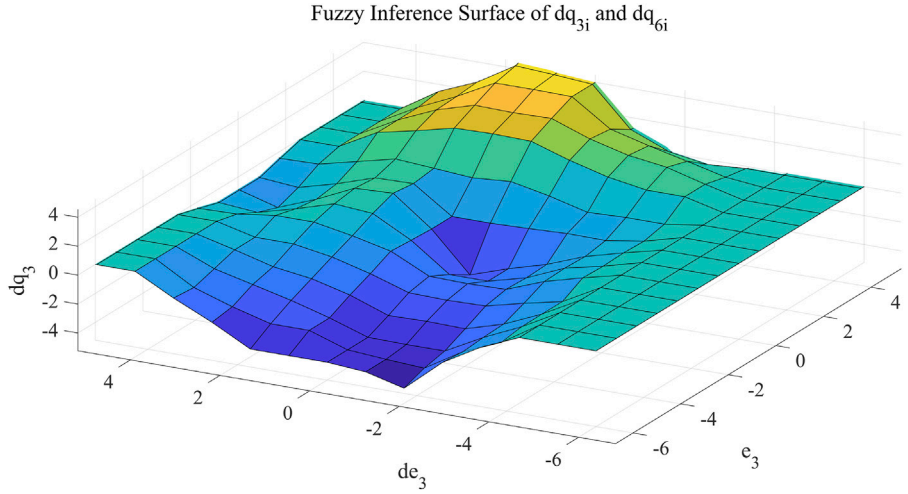

FIGURE 4
Fuzzy inference surface of $\Delta q_{3i}(t)$ and $\Delta q_{6i}(t)$.

Finally, the new scale and integration coefficients are obtained. Figure 3 and Figure 4 illustrate the fuzzy inference surface after the fuzzy rule.

The improved adaptive parameters are expressed as follows:

$$\begin{cases} q_{2p}^{*}(t) = q_{2p}(t) + \Delta q_{2p}(t) \\ q_{3i}^{*}(t) = q_{3i}(t) + \Delta q_{3i}(t) \end{cases} \tag{21}$$

where $q_{2p}{}^{*}(t)$ and $q_{3i}{}^{*}(t)$ are the new proportional and integral gain coefficients, $\Delta q_{2p}(t)$ and $\Delta q_{3i}(t)$ are the fuzzy controller output values respectively.

According to the same principle, the coefficients of the second fuzzy adaptive PI controller can be obtained as follows:

$$\begin{cases} q_{5p}^{*}(t) = q_{5p}(t) + \Delta q_{5p}(t) \\ q_{6i}^{*}(t) = q_{6i}(t) + \Delta q_{6i}(t) \end{cases} \tag{22}$$

where $q_{5p}^{*}(t)$ and $q_{6i}^{*}(t)$ are the new proportional and integral gain coefficients, $\Delta q_{5p}(t)$ and $\Delta q_{6i}(t)$ are the fuzzy controller output values respectively.

TABLE 3 System parameters.

Parameters	Value	Parameters	Value
L	100μH	τ	0.3
C	100μF	λ	−0.35
r_d	1Ω	θ	0.4
v_{ref1}	48V	q_1	4.5
i_{ref1}	1A	ρ_1	0.01
g_{11}	0.1	ρ_2	0.1
g_{12}, g_{22}	0.15	q_4	10
g_{21}	8	ρ_3	10
η	1.45	ρ_4	9

5 Simulation results

This subsection aims to substantiate the efficacy of the proposed algorithm through simulation examples. The parameters involved in the simulation are shown in Table 3.

Initially, we excluded the influence of external disturbances and solely evaluated the control performance of the proposed method under ideal circumstances. A comparison with the traditional SMC approach yielded the subsequent simulation outcomes. Referring to Figure 5 and Figure 6, we deduce that, within the confines of the control strategy, the system rapidly and effectively attains the desired target value. Notably, the proposed method exhibits a briefer regulation duration and significantly reduced chattering compared to the conventional method. In addition, the traditional SMC cannot accurately achieve the reference value of voltage. Upon examining Figure 5 and

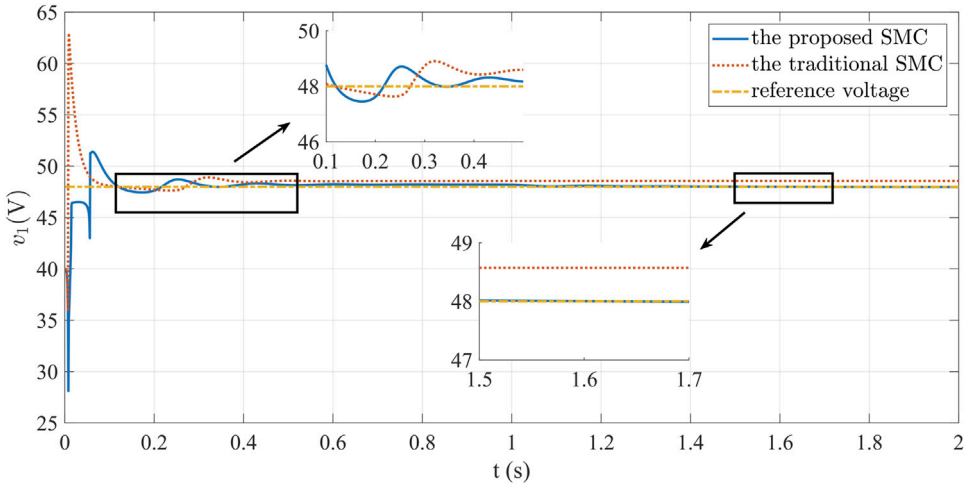

FIGURE 5
Curves of converter output voltage under ideal circumstances.

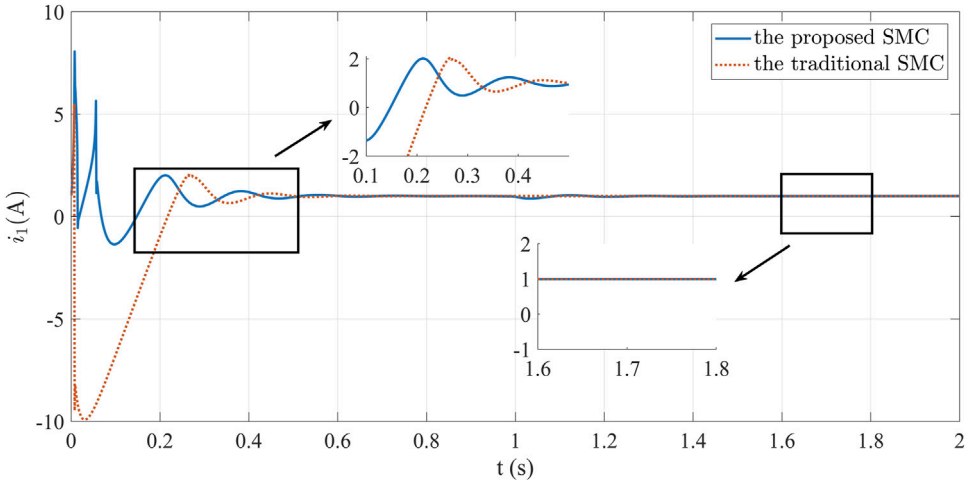

FIGURE 6
Curves of converter inductive current under ideal circumstances.

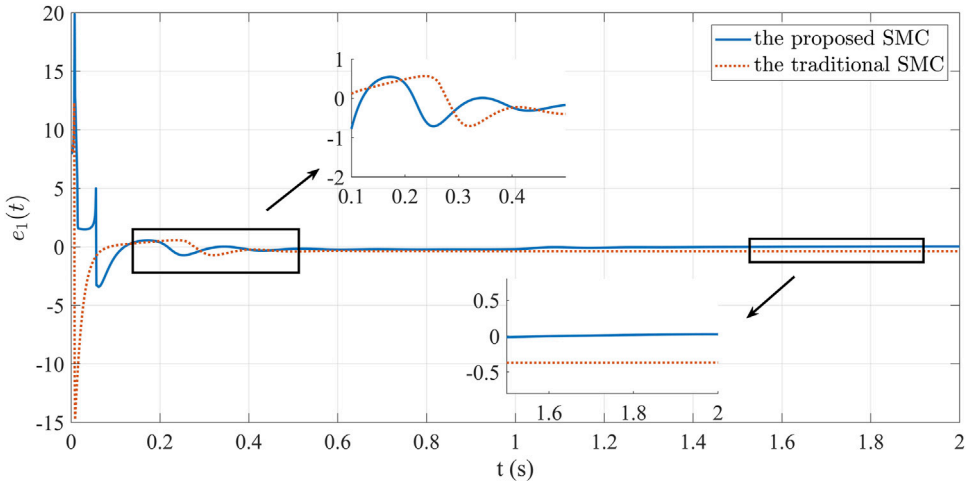

FIGURE 7
Curves of voltage error in the DC–DC converter under ideal circumstances.

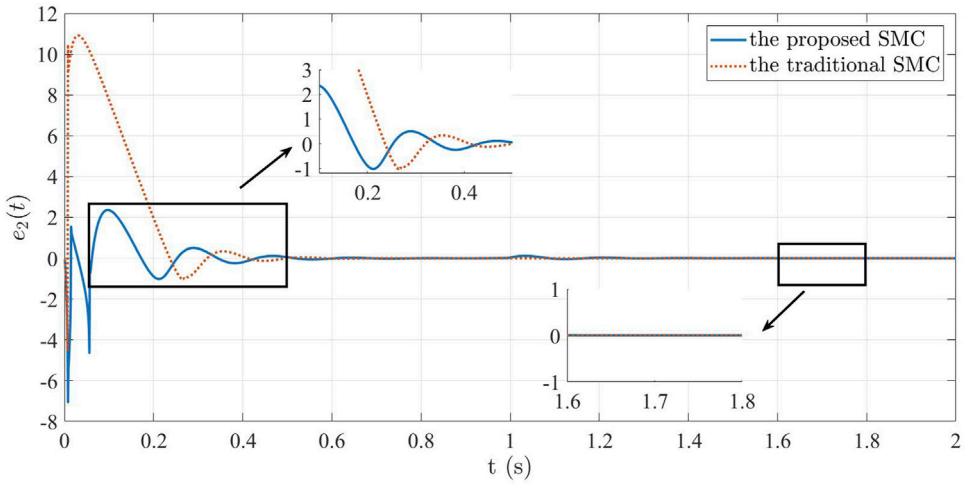

FIGURE 8
Curves of current error in the DC–DC converter under ideal circumstances.

Figure 7 concurrently, it becomes evident that the traditional method fails to achieve the desired voltage value, perpetuating an enduring error. The data in Figure 8 highlights the exceptional current control capability of the strategy developed in this paper. The current error swiftly converges to be zero within a brief span, and the oscillation amplitude remains notably smaller in comparison to the traditional method. Under ideal conditions, the advanced controller advocated in this study vividly showcases its prowess in dynamic performance enhancement.

To emulate real power system conditions, scenarios involving external disturbances were examined. Load variations were tested and discussed across different cases, with a comparison made to the performance of the traditional SMC method in these conditions. The ensuing simulation findings are presented as follows. Analyzing Figure 9, we infer that when external interference is present, the system tracks the predefined reference value quickly and effectively after changing the load, achieving regulation within 0.1 s. Figure 9 highlights that sizeable external disturbances induce more pronounced voltage fluctuations and changes under traditional SMC. This observation underscores the traditional method's inferior robustness and diminished anti-interference capacity. In contrast, the control strategy proposed herein swiftly stabilizes the system's output voltage, rapidly restoring equilibrium post-referential attainment. This exemplifies the strategy's enhanced robustness and its capacity to suppress the influence of external

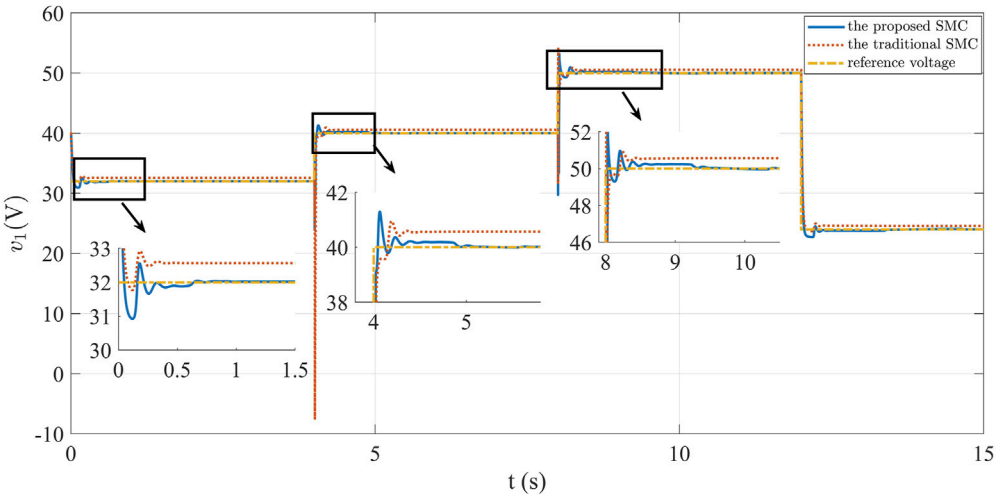

FIGURE 9
Dynamic curves of converter output voltage.

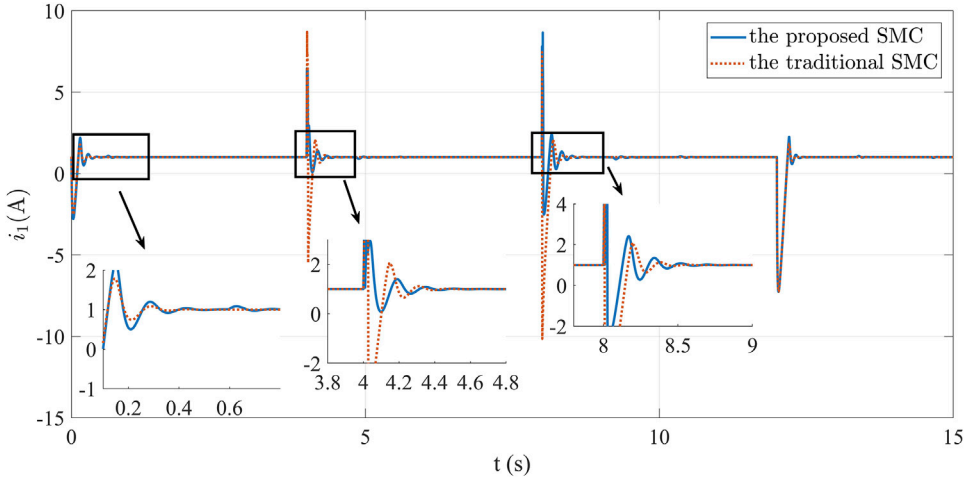

FIGURE 10
Dynamic curves of converter inductive current.

disturbances, thereby effectually advancing system control. Figure 10 presents the current variation. Although both methods can achieve the set reference value, the proposed method restrains the chattering. Figure 11 visually illustrates the voltage error, manifesting the error's eventual convergence to be zero under the controller's influence. This outcome underscores the effective asymptotic tracking capability of the current control strategy. In contrast, traditional SMC fail to converge the voltage error to be zero. Figure 12 illustrates current tracking error evolution. Notably, the traditional SMC method exhibits substantial performance deviations when faced with external disturbances. The proposed SMC enables the current error to reach the convergence state more quickly and steadily.

The simulation outcomes decisively showcase the proposed controller's pronounced improvements in both response time and precision, when juxtaposed with the conventional sliding mode controller. This method streamlines the algorithm, enhances voltage stability control, and optimizes overall system performance. These results affirm the effectiveness and superiority inherent in combining SMC and fuzzy adaptive PI control within DC–DC boost converter control.

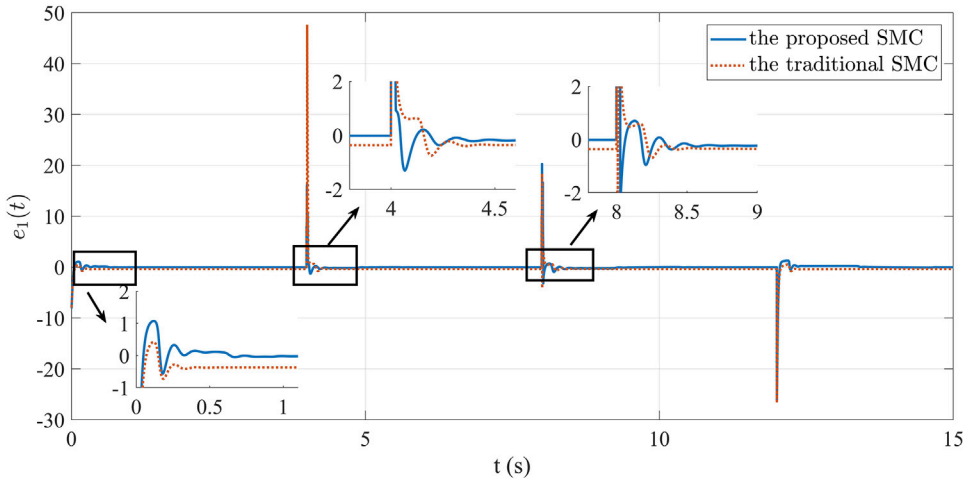

FIGURE 11
Curves of voltage error in the DC–DC converter.

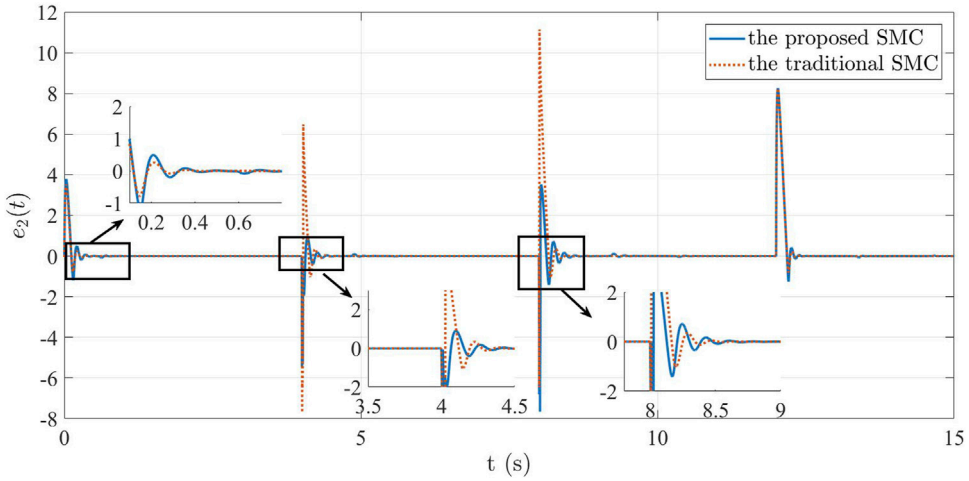

FIGURE 12
Curves of current error in the DC–DC converter.

6 Conclusion

This study proposes a voltage stabilization control strategy for DC–DC converters within DC microgrids, employing integral SMC and fuzzy adaptive PI control. The strategy effectively addresses the challenge of achieving rapid and steady output voltage states. The primary aim is to enhance dynamic performance and attain exceptional tracking error control, thereby elevating converter efficiency. The proposed SMC scheme demonstrates robust performance in countering external disturbances and voltage fluctuations. Incorporating fuzzy adaptive PI control bolsters system adaptability. The controller's capacity to dynamically adjust PI controller gains equips the system to respond adeptly to sudden parameter changes. The strategy was validated through MATLAB simulations, confirming its ability to swiftly stabilize voltage and attenuate oscillations. In conclusion, this paper presents an innovative and effective control approach for DC–DC converters in DC microgrids. The proposed method can be widely used in voltage stabilization control in DC microgrids. Future exploration of applying this strategy to more complex power electronic devices holds promise.

Data availability statement

The raw data supporting the conclusion of this article will be made available by the authors, without undue reservation.

Author contributions

XZ: Resources, Software, Writing–original draft. YZ: Investigation, Writing–original draft. HJ: Methodology, Validation, Writing–review and editing. MW: Formal Analysis, Validation, Writing–review and editing.

Funding

The author(s) declare financial support was received for the research, authorship, and/or publication of this article. Applied Foundational Research Plan Project of Liaoning Province (2022JH2/101300218).

Acknowledgments

The authors acknowledge the technical support from 2023 Innovation and Entrepreneurship Training Program for College Students (202311632004).

Conflict of interest

The authors declare that the research was conducted in the absence of any commercial or financial relationships that could be construed as a potential conflict of interest.

Publisher's note

All claims expressed in this article are solely those of the authors and do not necessarily represent those of their affiliated organizations, or those of the publisher, the editors and the reviewers. Any product that may be evaluated in this article, or claim that may be made by its manufacturer, is not guaranteed or endorsed by the publisher.

References

Ahmed, K. Y., Yahaya, N. Z. B., Asirvadam, V. S., Saad, N., Kannan, R., and Ibrahim, O. (2018). Development of power electronic distribution transformer based on adaptive PI controller. *IEEE Access* 6, 44970–44980. doi:10.1109/ACCESS.2018.2861420

Biricik, S., and Komurcugil, H. (2016). Optimized sliding mode control to maximize existence region for single-phase dynamic voltage restorers. *IEEE Trans. Industrial Inf.* 12, 1486–1497. doi:10.1109/TII.2016.2587769

Gui, Y., Han, R., Guerrero, J. M., Vasquez, J. C., Wei, B., and Kim, W. (2021). Large-signal stability improvement of DC–DC converters in DC microgrid. *IEEE Trans. Energy Convers.* 36, 2534–2544. doi:10.1109/TEC.2021.3057130

Haroun, R., Aroudi, A. E., Cid-Pastor, A., Garcia, G., Olalla, C., and Martínez-Salamero, L. (2015). Impedance matching in photovoltaic systems using cascaded boost converters and sliding-mode control. *IEEE Trans. Power Electron.* 30, 3185–3199. doi:10.1109/TPEL.2014.2339134

Inomoto, R. S., Monteiro, J. R. B. D. A., and Filho, A. J. S. (2022). Boost converter control of PV system using sliding mode control with integrative sliding surface. *IEEE J. Emerg. Sel. Top. Power Electron.* 10, 5522–5530. doi:10.1109/JESTPE.2022.3158247

Jan, M. U., Xin, A., Abdelbaky, M. A., Rehman, H. U., and Iqbal, S. (2020). Adaptive and fuzzy PI controllers design for frequency regulation of isolated microgrid integrated with electric vehicles. *IEEE Access* 8, 87621–87632. doi:10.1109/ACCESS.2020.2993178

Kuppusamy, S., and Joo, Y. H. (2021). Memory-based integral sliding-mode control for T–S fuzzy systems with PMSM via disturbance observer. *IEEE Trans. Cybern.* 51, 2457–2465. doi:10.1109/TCYB.2019.2953567

Li, X., Jiang, W., Wang, J., Wang, P., and Wu, X. (2021). An autonomous control scheme of global smooth transitions for bidirectional DC–DC converter in DC microgrid. *IEEE Trans. Energy Convers.* 36, 950–960. doi:10.1109/TEC.2020.3020127

Lee, J. Y., Jeong, Y. S., and Han, B. M. (2011). An isolated DC/DC converter using high-frequency unregulated LLC resonant converter for fuel cell applications. *IEEE Trans. Industrial Electron.* 58, 2926–2934. doi:10.1109/TIE.2010.2076311

Linares-Flores, J., Juárez-Abad, J. A., Hernandez-Mendez, A., Castro-Heredia, O., Guerrero-Castellanos, J. F., Heredia-Barba, R., et al. (2022). Sliding mode control based on linear extended state observer for DC-to-DC buck-boost power converter system with mismatched disturbances. *IEEE Trans. Industry Appl.* 58, 940–950. doi:10.1109/TIA.2021.3130017

Liu, W. S., Chen, J. F., Liang, T. J., and Lin, R. L. (2011). Multicascoded sources for a high-efficiency fuel-cell hybrid power system in high-voltage application. *IEEE Trans. Power Electron.* 26, 931–942. doi:10.1109/TPEL.2010.2089642

Mao, J., Zhang, X., Yin, C., Wu, A., and Zhang, X. (2022). Multivariable coordinated nonlinear gain droop control for PV-battery hybrid DC microgrid access system via a T-S fuzzy decision approach. *IEEE Access* 10, 89414–89427. doi:10.1109/ACCESS.2022.3201149

Merabet, A., Labib, L., Ghias, A. M. Y. M., Ghenai, C., and Salameh, T. (2017). Robust feedback linearizing control with sliding mode compensation for a grid-connected photovoltaic inverter system under unbalanced grid voltages. *IEEE J. Photovoltaics* 7, 828–838. doi:10.1109/JPHOTOV.2017.2667724

Mi, Y., Zhang, H., Fu, Y., Wang, C., Loh, P. C., and Wang, P. (2019). Intelligent power sharing of DC isolated microgrid based on fuzzy sliding mode droop control. *IEEE Trans. Smart Grid* 10, 2396–2406. doi:10.1109/TSG.2018.2797127

Mokhtar, M., Marei, M. I., and El-Sattar, A. A. (2019). An adaptive droop control scheme for DC microgrids integrating sliding mode voltage and current controlled boost converters. *IEEE Trans. Smart Grid* 10, 1685–1693. doi:10.1109/TSG.2017.2776281

Prabhakaran, P., and Agarwal, V. (2020). Novel boost-SEPIC type interleaved DC–DC converter for mitigation of voltage imbalance in a low-voltage bipolar DC microgrid. *IEEE Trans. Industrial Electron.* 67, 6494–6504. doi:10.1109/TIE.2019.2939991

Saafan, A. A., Khadkikar, V., Moursi, M. S. E., and Zeineldin, H. H. (2023). A new multiport DC–DC converter for DC microgrid applications. *IEEE Trans. Industry Appl.* 59, 601–611. doi:10.1109/TIA.2022.3213235

Tiwary, N., N, V. N., Panda, A. K., Narendra, A., and Lenka, R. K. (2023). A robust voltage control of DAB converter with super-twisting sliding mode approach. *IEEE J. Emerg. Sel. Top. Industrial Electron.* 4, 288–298. doi:10.1109/JESTIE.2022.3227007

Ullah, S., Khan, L., Sami, I., and Ro, J. S. (2022). Voltage/frequency regulation with optimal load dispatch in microgrids using SMC based distributed cooperative control. *IEEE Access* 10, 64873–64889. doi:10.1109/ACCESS.2022.3183635

Wang, J., Luo, W., Liu, J., and Wu, L. (2021). Adaptive type-2 FNN-based dynamic sliding mode control of DC–DC boost converters. *IEEE Trans. Syst. Man, Cybern. Syst.* 51, 2246–2257. doi:10.1109/TSMC.2019.2911721

Wang, Z., Li, S., and Li, Q. (2020). Continuous nonsingular terminal sliding mode control of DC–DC boost converters subject to time-varying disturbances. *IEEE Trans. Circuits Syst. II Express Briefs* 67, 2552–2556. doi:10.1109/TCSII.2019.2955711

Zheng, L., Jiang, F., Song, J., Gao, Y., and Tian, M. (2018). A discrete-time repetitive sliding mode control for voltage source inverters. *IEEE J. Emerg. Sel. Top. Power Electron.* 6, 1553–1566. doi:10.1109/JESTPE.2017.2781701

frontiers | Frontiers in Energy Research

TYPE Original Research
PUBLISHED 12 October 2023
DOI 10.3389/fenrg.2023.1258292

Check for updates

OPEN ACCESS

EDITED BY
Yushuai Li,
University of Oslo, Norway

REVIEWED BY
Xueqian Fu,
China Agricultural University, China
Yunyun Xie,
Nanjing University of Science and Technology, China
Hao Yu,
Tianjin University, China

*CORRESPONDENCE
Junjie Hu,
junjiehu@ncepu.edu.cn

RECEIVED 13 July 2023
ACCEPTED 27 September 2023
PUBLISHED 12 October 2023

CITATION
Ai X, Hu H, Hu J, Wang Z and Wang K (2023), Network-constrained flexible ramping product provision of prosumer aggregator: a data-driven stochastic bi-level optimization.
Front. Energy Res. 11:1258292.
doi: 10.3389/fenrg.2023.1258292

COPYRIGHT
© 2023 Ai, Hu, Hu, Wang and Wang. This is an open-access article distributed under the terms of the Creative Commons Attribution License (CC BY). The use, distribution or reproduction in other forums is permitted, provided the original author(s) and the copyright owner(s) are credited and that the original publication in this journal is cited, in accordance with accepted academic practice. No use, distribution or reproduction is permitted which does not comply with these terms.

Network-constrained flexible ramping product provision of prosumer aggregator: a data-driven stochastic bi-level optimization

Xin Ai, Huanyu Hu, Junjie Hu*, Zhe Wang and Kunyu Wang

School of Electrical and Electronic Engineering, North China Electric Power University, Beijing, China

Prosumers are expected to provide the flexible ramping product (FRP) in the power system. However, voltage violations and line congestion may arise in the distribution network, when FRP delivered by prosumers. Hence, this paper proposes a data-driven stochastic bi-level optimization model to coordinate the prosumer aggregator to decide FRP-offering while ensuring distribution network security under FRP delivery. In the proposed bi-level model, the upper-level is a min-max problem, representing the minimum expected cost under the worst-case scenario probability distribution for the prosumer aggregator. The lower-level is the operation cost minimization within the distribution network security for distribution network operator. The proposed model is converted into a single-level model using the Karush-Kuhn-Tucker condition and strong duality theory, and applied to the modified IEEE 33-bus network with three prosumers. The results demonstrate the effectiveness of the proposed model.

KEYWORDS

prosumer, flexible ramping product, distribution network, stochastic optimization, data-driven

1 Introduction

The expansion of renewable energy integration into the power grid has led to the de-committed of conventional units, exacerbating the scarcity of ramping resources in the power system (Wang and Hodge, 2017). According to the CAISO daily report dated 23 June 2023, the requirement of FRP during the 3 hours following 6 a.m. accounted for 40.4% of the peak load for that day (California Independent System Operator, 2023). Addressing this pressing issue requires urgent exploration of demand-side ramping capability (Yamujala et al., 2022). With the implementation of low-carbon policies and smart control technologies in distribution system, an increasing number of passive low-voltage consumers with distributed resources are being transformed into active prosumers, resulting in unprecedented improvements of flexibility in distribution system (Kubli et al., 2018). While significant improvements have been made in enhancing flexibility, its value cannot be fully realized without proper organization and coordination. As a crucial link between decentralized flexibility and economically scalable electricity services, research on prosumer aggregator has rapidly gained momentum (Olivella-Rosell et al., 2018). However, the deliverability and availability challenges associated with FRP (Fang et al., 2020), coupled

with the voltage violations and line congestion in prosumer active responses, pose additional challenges for prosumer aggregator in providing FRP. Therefore, this paper investigate how prosumer aggregator can provide FRP while ensuring the security of the distribution network.

The current definition of prosumer is broad, encompassing subjects such as electric vehicle aggregators, smart buildings, and grid-connected microgrids, which are also considered as prosumers (Gonzalez-Romera et al., 2019; Hu et al., 2019; Huang et al., 2020; Nizami et al., 2020). In order to comprehensively analyze the current state of research, this paper also considers the provision of FRP by this broad category of prosumer. Studies on the provision of FRP by prosumer aggregators can be categorized into two group.

The first group focuses solely on the economic strategy developed based on the portfolio model without considering distribution system security. For instance, the author in the literature (Kim et al., 2021) proposes a FRP offering strategy for electric vehicles considering travel chain uncertainty. Similarly, The literature (Wang et al., 2017; Hu et al., 2018) propose a FRP offering strategy for microgrid and battery energy storage aggregator, respectively. The literature (Zhang et al., 2022) develops a method to allocate ramping capacity in electric-gas systems. The literature (Zhu et al., 2020) proposes a decision framework for residential-level energy hubs considering the provision of FRP for arbitrage. The literature (Khoshjahan et al., 2020) develops a stochastic FRP offering strategy for energy storage systems. Likewise, The literature (Khoshjahan et al., 2022) presents a robust optimal strategy for prosumer aggregators to provide FRP in the real-time market. In summary, the studies have explored the prosumers that encompass various types of flexible resources based on the optimal offering model within forecast market clearing prices. This group of bidding decision models focuses only on the optimal power allocation of resources within the prosumer and ignores the interaction relationship with the market clearing price, which can lead to an underestimation of the prosumer's flexibility. Moreover, strategies formulated using predicted market clearing prices resemble passive time-of-use tariff demand response strategies. Such approaches do not fully showcase the proactive advantages inherent to the prosumer.

The second group considers the security of the distribution network when submitting an offering strategy but ignores the potential security issues when FRP is activated. For example, the literature (Zhang et al., 2020) proposes an extended ACOPF model that integrates electric vehicles and calculates the marginal benefit value of FRP. The literature (Bahramara et al., 2022) presents a method for considering distribution network line congestion when microgrids provide services to system-independent operators. The literature (Ghaemi et al., 2021a) proposes a bi-level model for DNO purchasing microgrid's FRP in the distribution network, while the literature (Allahmoradi et al., 2021) suggests a stochastic optimal strategy for reducing the net load ramping rate of active distribution networks. The literature (Ghasemi et al., 2021) introduces a bi-level optimal approach to incorporate distributed resources for providing FRP. Although the bi-level model described above effectively captures the interaction between the distribution network and prosumer aggregators, the upper models are not aggregator which are not suitable for bidding decisions. Although all of the work mentioned above considers distribution system security when the prosumer aggregator submit FRP, they only consider the energy strategy to satisfy distribution network security when the FRP is not activated. The power flow in the distribution network will change when the distribution network operator activates the FRP of the prosumer, which may cause distribution network security issues such as voltage violations and line congestions. In addition, the value of flexibility for each prosumer cannot be accounted for correctly because of the ignorance of the network security constraints during FRP delivery.

Moreover, the volatility of distributed renewable energy (DRE) indirectly affects the bidding/offering decision of prosumer aggregators. The optimization strategies developed in the aforementioned literature, based on stochastic optimization (Wang et al., 2017; Khoshjahan et al., 2020; Allahmoradi et al., 2021; Bahramara et al., 2022) and robust optimization (Zhu et al., 2020; Ghasemi et al., 2021b; Khoshjahan et al., 2022; Zhang et al., 2022) for uncertainty modeling in the DRE output and market clearing prices. Robust optimization does not rely on probability distribution characteristics and makes decisions based only on worst-case uncertainty scenarios. In optimal scheduling problems where uncertainty extreme scenarios have a low probability of occurring, robust models tend to result in overly conservative strategies. It is a characteristic more suited to the study of stable control and planning problems (Ma et al., 2023). Stochastic optimization assumes that the decision-making has a comprehensive understanding of uncertainty through known probability distributions, and often empirical or data-driven approaches are used to construct probability distributions (Fu et al., 2023a). However, due to the finiteness of the sample, the constructed probability distribution may be far from the true probability distribution, which can lead to an under-conservative strategy. Selecting representative discrete scenarios to characterize the probability distribution is also an issue, which a large set of scenarios will greatly increase the computational burden. The literature (Fu et al., 2023b) proposes an approach to select the representative scenarios by neural networks to reduce the size of scenarios. Distributionally robust methods have attracted much attention in recent years, which combine the advantages of stochastic optimization and robust optimization by formulating expected optimal decisions under robust probability distributions, and have been applied to power system optimal scheduling (Shi et al., 2023) and control (Xu et al., 2023) issues. Among them, a stochastic optimization method based on a mixed-norm model was firstly proposed in the literature (Zhao and Guan, 2016), which can achieve expectation-optimal decision-making under robust probability distribution. The method can adjust the conservativeness of uncertainty modeling and is particularly applicable to the formulation of bid-offer strategy. The prosumer aggregator can improve its response to the future development of the complex distribution grid market by employing external data and adopting a risk-averse willingness to dynamically adjust its bidding and offering strategy. Therefore, embedding this model into the problem of FRP decision-making by prosumer aggregators is also within the scope of research interest in this paper.

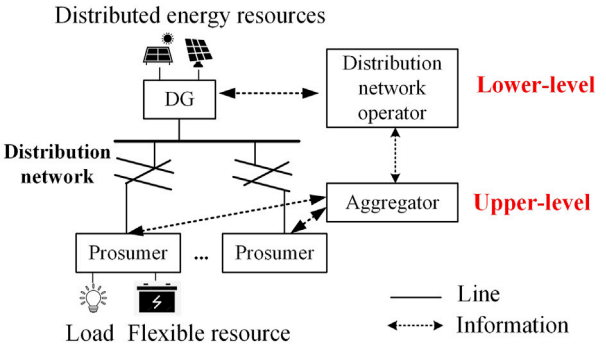

FIGURE 1
Coordinated operational framework for aggregator and DNO.

In this context, the paper proposes a bidding/offering model based on a data-driven stochastic bi-level optimization for prosumer aggregator. The major contributions of this paper are presented as follows.

1) Proposing a novel data-driven stochastic bi-level optimization framework for prosumer aggregator, which effectively incorporates the value of external data and proactively develops energy and FRP bidding/offering strategy that strike a better balance between economy and conservativeness.
2) Proposing an extended linearized ACOPF model that avoids technical violations of the distribution system after the delivery of FRP and enables the derivation of more detailed marginal prices of nodes. More importantly, the linearization greatly improves the model's applicability, especially in the construction of the bi-level programming.

The remainder of this paper is organized as follows. Section 2 presents the problem description. In Section 3, the proposed model and solution technique is formulated. The numerical results are analyzed in Section 4. Finally, Section 5 concludes the paper.

2 Problem description

2.1 Stochastic bi-level optimization structure for bid and offer strategy of prosumer aggregator

The proposed model presents a data-driven, stochastic bi-level optimization problem. This captures the interactive decision-making between the prosumer aggregator managing the prosumers and the DNO scheduling the DRE. The structure is illustrated in Figure 1. We assume that all prosumers within the distribution network can be managed by a single aggregator. The interactive decision-making of prosumer aggregator and DNO is a stochastic bi-level optimization problem that can be modeled based on the scenario approach. The upper-level problem represents the formulation of energy bidding and FRP offering at the distribution locational marginal price for prosumer aggregator, and the lower-level problem represents the energy and FRP clearing out locally for DNO receiving the upper-level decision, the structure of which is shown in Figure 2. In fact, the proposed model is also a Stackelberg Game problem, where the prosumer aggregator acts as the leader while the DNO acts as the follower. The proactive superiority of the prosumer aggregator is emphasized. DRE are common in distribution networks, and their energy management strategy affect the energy and FRP clearing of DNO, and subsequently the strategies of prosumers. The conservativeness of uncertainty modeling is corrected using a data-driven approach. The prosumer aggregator searches for the worst-case probability distribution in the optimization space of the scenario probability distribution, and ultimately achieves the minimum expected cost of the bidding/offering strategy under the worst probability distribution.

The KKT condition and strong dual theory are used to solve the model. The KKT condition can replace the lower-level optimization

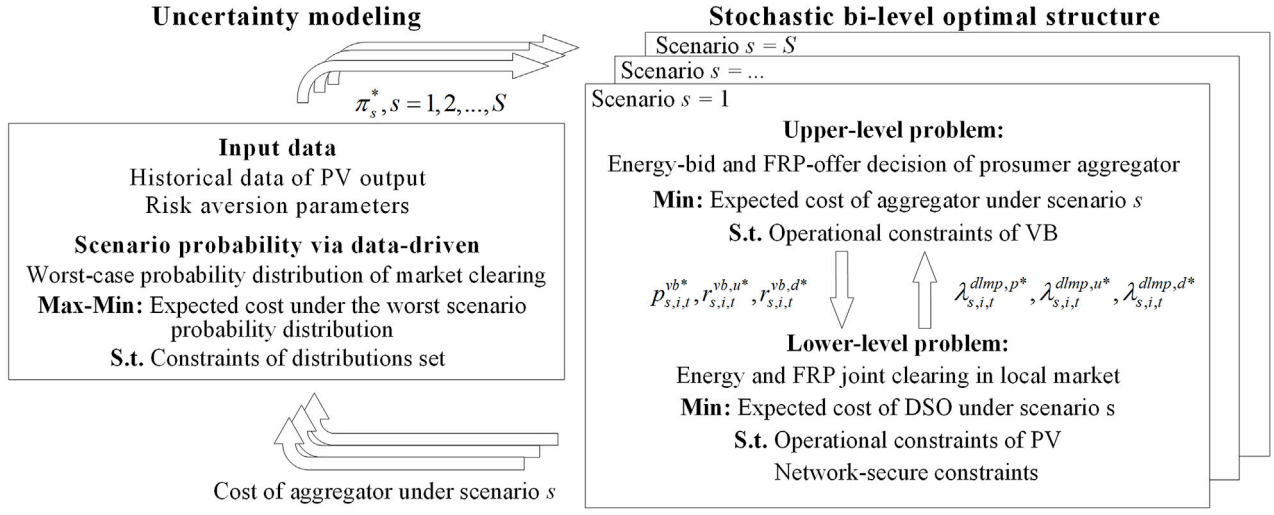

FIGURE 2
A data-driven stochastic bi-level optimization framework for prosumer aggregator decision bid-offer.

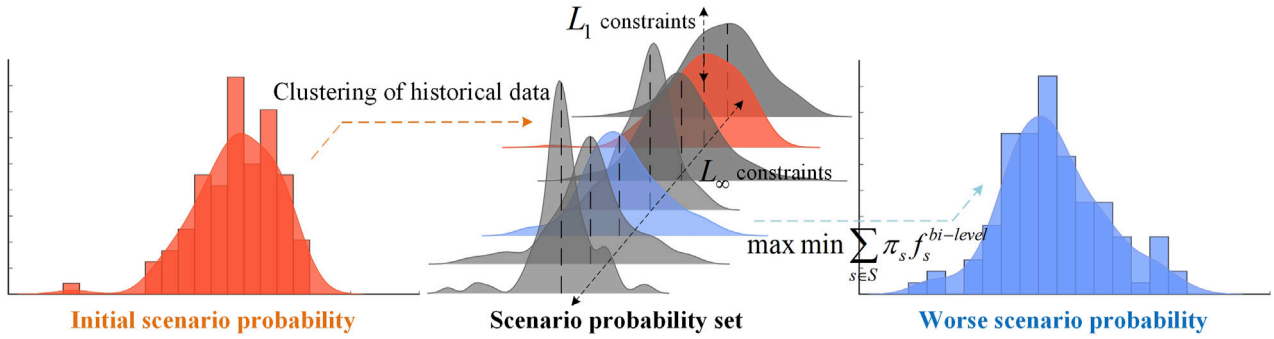

FIGURE 3
A data-driven framework for uncertainty modeling.

problem with an equilibrium constraint. The strong dual theory can replace the bi-linear term in the upper level objective. The linearization of the complementary relaxation constraints is done by the big-M method. The model can eventually be transformed into a mixed-integer linear programming problem that can be easily solved by commercial software.

2.2 Uncertainty modeling of DRE

DRE are widely deployed in distribution networks, and their stochastic output characteristics have a substantial influence on the energy and FRP locally clearing of DNO. The uncertainty model proposed in the literature (Zhao and Guan, 2016) is able to take into account the uncertainty of the probability distribution of random variables. In this paper, this model is integrated into the proposed stochastic bi-level programming problem.

The process of uncertainty modeling, as illustrated in Figure 3, comprises several steps. Firstly, historical data is clustered to obtain an initial probability distribution. Subsequently, the L_1 norm and L_∞ norm are utilized to construct the set of probability distributions. It is worth noting that the mix-norm captures the risk-averse of the prosumer aggregator, influencing the level of conservativeness within the ensemble. Lastly, a bi-level stochastic optimization model is employed to identify the worst-case distribution from the set, facilitating the formulation of an optimal decision that is both economically viable and conservative.

3 Method development of FRP provision by prosumer aggregator

3.1 Scenario probability distribution set

$$\sum_{s\in S}|\pi_s-\pi_0|\le\frac{S}{2N_s}ln\frac{2S}{1-\alpha_1} \tag{1}$$

$$max_{s=1,\ldots,S}|\pi_s-\pi_0|\le\frac{1}{2N_s}ln\frac{2S}{1-\alpha_s} \tag{2}$$

$$\sum_{s\in S}\pi_s=1 \tag{3}$$

$$\pi_s\ge 0, s=1,\ldots,S \tag{4}$$

Equation 1 sets the limits of the overall uncertainty of the probability distribution while Eq. 2 sets the limits on the maximum probability uncertainty (Zhao and Guan, 2016). Eqs. 3-4 denotes the basic properties of discrete probabilities.

3.2 Optimization model of prosumer aggregator

3.2.1 Objective function

The upper-level problem aims to minimize operating cost under the worst-case scenario probability distribution, which comprises two terms. The first term represents the cost of purchasing energy while the second term corresponds to the revenue from providing the FRP, encompassing both upward FPR and downward FRP, respectively.

$$minmax\Delta t\sum_{s\in S}\pi_s\sum_{i\in N}\sum_{t\in T}\lambda_{s,i,t}^{dlmp,p}p_{s,i,t}^{vb}-\left(\lambda_{s,i,t}^{dlmp,u}r_{s,i,t}^{vb,u}+\lambda_{s,i,t}^{dlmp,d}r_{s,i,t}^{vb,d}\right) \tag{5}$$

3.2.2 Operational constraints of prosumer

The energy management problem within the prosumer could be deal with the portfolio model previously reviewed, which is outside the scope of this paper. Therefore, the virtual battery model is used here to represent the prosumer flexibility, referring to the authors' previous work (Hou et al., 2019; Hu et al., 2019; Wu et al., 2019).

$$p_{s,i,t}^{vb}\le\bar{p}_{s,i,t}^{vb} \tag{6}$$

$$p_{s,i,t}^{vb}-r_{s,i,t}^{vb,u}\ge 0 \tag{7}$$

$$r_{s,i,t}^{vb,d}+p_{s,i,t}^{vb}\le\bar{p}_i^{vb} \tag{8}$$

$$p_{s,i,t}^{vb},r_{s,i,t}^{vb,u},r_{s,i,t}^{vb,d}\ge 0 \tag{9}$$

$$e_{s,i,t+1}^{vb}=e_{s,i,t}^{vb}+\eta^c p_{s,i,t}^{vb}\Delta t \tag{10}$$

$$\bar{e}_i^{vb}-e_{s,i,t+1}^{vb}\ge\eta^c r_{s,i,t}^{vb,d}\Delta t \tag{11}$$

$$e_{s,i,t}^{vb}\le\bar{e}_i^{vb} \tag{12}$$

$$e_i^{vb,ini}=e_{s,i,1}^{vb} \tag{13}$$

$$e_i^{vb,ex}=e_{s,i,T}^{vb} \tag{14}$$

The amount of energy and FRP of each prosumer is limited using Eqs.6–14. Eqs. 10–14 demonstrate the dynamic behavior of prosumer at each time step, which depends on the amount of stored energy in the previous time step.

3.3 Optimization model of DNO

3.3.1 Objective function

The lower-level problem aims to minimize the operating costs of the DNO and represents the energy and FRP clearing out within the distribution network, as described in Eq.15. The first term in Eq.15 represents the cost of energy purchased by the DNO from the retail market to maintain power balance within the distribution system. The second term corresponds to the revenue from providing FRP to the market by the DNO, which is determined by the quantities offered from DRE and the prosumers.

$$\min \Delta t \sum_{t\in T} \gamma_t^p p_{s,t}^{dso} - \left(\gamma_t^u r_{s,t}^{dso,u} + \gamma_t^d r_{s,t}^{dso,d}\right) \tag{15}$$

$$r_{s,t}^{dso,u} = \sum_{i\in N} r_{s,i,t}^{vb,u} + \sum_{j\in J} r_{s,j,t}^{pv,u} : \lambda_{s,t}^{u} \tag{16}$$

$$r_{s,t}^{dso,d} = \sum_{i\in N} r_{s,i,t}^{vb,d} + \sum_{j\in J} r_{s,j,t}^{pv,d} : \lambda_{s,t}^{d} \tag{17}$$

Where γ_t^p is the day-ahead energy price in the retail market, γ_t^u and γ_t^d are the upward and downward FRP price. The right-hand side of Eqs. 16, 17 denote the dual multiplier variables of the constraints. The expressions of the same form in the later section carry the same meaning as described here.

3.3.2 Operational constraints of PV

The selection of distributed PV as the representative DRE here is motivated by its widespread prevalence and common usage. Other DRE operational models can be extended on this basis easily.

$$p_{s,j,t}^{pv} \le p_{s,j,t}^{pv,fore} : \mu_{s,j,t}^{pv,p+} \tag{18}$$

$$r_{s,j,t}^{pv,d} \le p_{s,j,t}^{pv} : \mu_{s,j,t}^{pv,rd+} \tag{19}$$

$$p_{s,j,t}^{pv} + r_{s,j,t}^{pv,u} \le p_{s,j,t}^{pv,forr} : \mu_{s,j,t}^{pv,ru+} \tag{20}$$

$$p_{s,j,t}^{pv}, r_{s,j,t}^{pv,u}, r_{s,j,t}^{pv,d} \ge 0 : \mu_{s,j,t}^{pv,p-}, \mu_{s,j,t}^{pv,ru-}, \mu_{s,j,t}^{pv,rd-} \tag{21}$$

Eqs. 18–21 represent that the DRE providing energy and FRP within the forecasting power limits of the operating.

3.3.3 Network secure constraints

Inspired by the literature (Yuan et al., 2018), this paper proposes an extended linearized ACOPF model which can simultaneously optimize the system cost of providing energy and FRP.

$$p_{s,t}^{dso} + \sum_{j\in J} p_{s,j,t}^{pv} - \sum_{i\in N} p_{s,i,t}^{vb} - \sum_{b\in B} p_{b,t}^{load} - p_{s,t}^{loss} = 0 : \lambda_{s,t}^{p} \tag{22}$$

$$\underline{p}^{dso} \le p_{s,t}^{dso} \le \bar{p}^{dso} : \mu_{s,t}^{dso,p-}, \mu_{s,t}^{dso,p+} \tag{23}$$

$$p_{s,t}^{loss} \approx p_{s,t}^{loss\star} - \sum_{j\in J} z_j^d \left(p_{s,j,t}^{pv} - p_{s,j,t}^{pv\star}\right) + \sum_{i\in N} z_i^d \left(p_{s,i,t}^{vb} - p_{s,i,t}^{vb\star}\right) \tag{24}$$

Eq. 22 represents the energy balance at system-level. Eq. 23 shows the acceptable range of exchanging power between the DNO and grid. Eq. 24 represents the linearized expression of distribution network losses, where the matrix z^d is the partial derivatives of bus power of the distribution network with respect to the losses (Yuan et al., 2018).

$$p_{s,w,t}^{net} = p_{s,w,t}^{pv} - p_{s,w,t}^{vb} - p_{w,t}^{load} \tag{25}$$

$$v_{s,b,t} = v_1 + \sum_{w\in B} z_{b}^{p} p_{s,w,t}^{net} - \sum_{i\in B} z_{b,i}^{q} q_{s,i,t}^{load} \tag{26}$$

$$\underline{v} \le v_{s,b,t} \le \bar{v} : \mu_{s,b,t}^{v-}, \mu_{s,b,t}^{v+} \tag{27}$$

$$\underline{v} \le v_{s,b,t} + \sum_{w\in B} z_{b,w}^{p} \left(r_{s,w,t}^{pv,u} + r_{s,w,t}^{vb,u}\right) \le \bar{v} : \mu_{s,b,t}^{v,ru-}, \mu_{s,b,t}^{v,rd+} \tag{28}$$

$$\underline{v} \le v_{s,b,t} - \sum_{w\in B} z_{b,w}^{p} \left(r_{s,w,t}^{pv,d} + r_{s,w,t}^{vb,d}\right) \le \bar{v} : \mu_{s,b,t}^{v,rd-}, \mu_{s,b,t}^{v,rd+} \tag{29}$$

Eqs. 25–27 represent the maximum and the minimum permissible voltage magnitude of each bus. Eqs. 28, and 29 define the allowable operating range of voltage magnitude after the delivery of FRP, where the matrix z^p and z^q are the partial derivatives of active power and reactive power each bus respect to voltage magnitude respectively (Yuan et al., 2018).

$$p_{s,t}^{l_k} \approx p_{s,t}^{l_k\star} - \sum_{j\in J} z_j^{l_k} \left(p_{s,j,t}^{pv} - p_{s,j,t}^{pv\star}\right) + \sum_{i\in N} z_i^{l_k} \left(p_{s,i,t}^{vb} - p_{s,i,t}^{vb\star}\right) \tag{30}$$

$$\underline{p}^{l_k} \le p_{s,t}^{l_k} \le \bar{p}^{l_k} : \mu_{s,l_k,t}^{p-}, \mu_{s,l_k,t}^{p+} \tag{31}$$

$$\underline{p}^{l_k} \le p_{s,t}^{l_k} - \sum_{w\in B} z_{w}^{l_k} \left(r_{s,w,t}^{pv,u} + r_{s,w,t}^{vb,u}\right) \le \bar{p}^{l_k} : \mu_{s,l_k,t}^{ru-}, \mu_{s,l_k,t}^{ru+} \tag{32}$$

$$\underline{p}^{l_k} \le p_{s,t}^{l_k} + \sum_{w\in B} z_{w}^{l_k} \left(r_{s,w,t}^{pv,d} + r_{s,w,t}^{vb,d}\right) \le \underline{p}^{l_k} : \mu_{s,l_k,t}^{rd-}, \mu_{s,l_k,t}^{rd+} \tag{33}$$

Eqs. 30, and 31 represent the operating boundary of the branch power flow. Eqs. 32, and 33 define the allowable operating range of branch power flow after the delivery of FRP, where the matrix z^{l_k} is the partial derivatives of active power each bust respect to branch flow (Yuan et al., 2018).

3.4 Solution methodology

3.4.1 KKT conditions

The first-order optimality condition on the lower-level decision variable $p_{s,t}^{dso}, r_{s,t}^{dso,u}, r_{s,t}^{dso,d}, p_{s,t}^{pv}, r_{s,t}^{pv,u}, r_{s,t}^{dso,d}$ are sequentially presented in Eqs. 34–39.

$$\gamma_t^p + \lambda_{s,t}^{p} - \mu_{s,t}^{dsp,p-} + \mu_{s,t}^{dso,p+} = 0 \tag{34}$$

$$-\gamma_t^u + \lambda_{s,t}^{u} = 0 \tag{35}$$

$$-\gamma_t^d + \lambda_{s,t}^{d} = 0 \tag{36}$$

$$\begin{aligned} &\mu_{s,j,t}^{pv,p+} - \mu_{s,j,t}^{pv,rd+} + \mu_{s,j,t}^{pv,ru+} - \mu_{s,j,t}^{pv,p-} + \lambda_{s,t}^{p}\left(1 + z_j^p\right) \\ &+ \sum_{\epsilon} z_{b,j}^{p} \left(- \mu_{s,b,t}^{v-} + \mu_{s,b,t}^{v+} - \mu_{s,b,t}^{v,rd-} + \mu_{s,b,t}^{v,rd+} - \mu_{s,b,t}^{v,ru-} + \mu_{s,b,t}^{v,ru+} \right) \\ &+ \sum_{\epsilon} z_j^{l_k} \left(-\mu_{s,l_k,t}^{p-} + \mu_{s,l_k,t}^{p+} - \mu_{s,l_k,t}^{ru-} + \mu_{s,l_k,t}^{ru+} - \mu_{s,l_k,t}^{rd-} + \mu_{s,l_k,t}^{rd+}\right) = 0 \end{aligned} \tag{37}$$

$$\begin{aligned} &\mu_{s,b,t}^{pv,ru+} - \mu_{s,b,t}^{pv,ru-} - \lambda_{s,t}^{u} + \sum_{b\in B} z_{b,j}^{p} \left(- \mu_{s,b,t}^{v,ru-} + \mu_{s,b,t}^{v,ru+} \right) \\ &+ \sum_{k\in K} z_j^{l_k} \left(\mu_{s,l_k,t}^{ru-} - \mu_{s,l_k,t}^{ru+}\right) = 0 \end{aligned} \tag{38}$$

$$\begin{aligned} &\mu_{s,b,t}^{pv,rd+} - \mu_{s,b,t}^{pv,ru+} - \mu_{s,b,t}^{pv,rd-} - \lambda_{s,t}^{d} + \sum_{b\in B} z_{b,j}^{p} \left(\mu_{s,b,t}^{v,rd-} - \mu_{s,b,t}^{v,rd+}\right) \\ &+ \sum_{\epsilon} z_j^{l_k} \left(- \mu_{s,l_k,t}^{rd-} + \mu_{s,l_k,t}^{rd+}\right) = 0 \end{aligned} \tag{39}$$

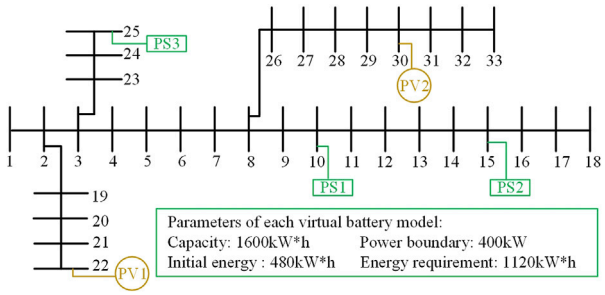

FIGURE 4
Topology of the modified IEEE 33 bus power system.

The resulting complementary conditions Eqs 40–59 are non-linear equations, but they can be linearized using the Big-M method.

$$0 \le \mu_{s,j,t}^{pv,p+} \perp p_{s,j,t}^{pv,fore} - p_{s,j,t}^{pv} \ge 0 \tag{40}$$

$$0 \le \mu_{s,j,t}^{pv,rd+} \perp p_{s,j,t}^{pv} - p_{s,j,t}^{pv,d} \ge 0 \tag{41}$$

$$0 \le \mu_{s,j,t}^{pv,ru+} \perp p_{s,j,t+1}^{pv,fore} - p_{s,j,t}^{pv} - r_{s,j,t}^{pv,u} + r_{s,j,t}^{pv,d} \ge 0 \tag{42}$$

$$0 \le \mu_{s,j,t}^{pv,p-} \perp p_{s,j,t}^{pv} \ge 0 \tag{43}$$

$$0 \ge \mu_{s,j,t}^{pv,ru-} \perp r_{s,j,t}^{pv,u} \le 0 \tag{44}$$

$$0 \le \mu_{s,j,t}^{pv,rd-} \perp r_{s,j,t}^{pv,d} \ge 0 \tag{45}$$

$$0 \le \mu_{s,t}^{dso,p-} \perp p_{s,t}^{dso} - \underline{p}^{dso} \ge 0 \tag{46}$$

$$0 \le \mu_{s,t}^{dso,p+} \perp \bar{p}^{dso} - p_{s,t}^{dso} \ge 0 \tag{47}$$

$$0 \le \mu_{s,b,t}^{v-} \perp v_{s,b,t} - \underline{v} \ge 0 \tag{48}$$

$$0 \le \mu_{s,b,t}^{v+} \perp \bar{v} - v_{s,b,t} \ge 0 \tag{49}$$

$$0 \le \mu_{s,b,t}^{v,ru-} \perp v_{s,b,t} + \sum_{\epsilon} z_{z,w}^{p}\left(r_{s,w,t}^{pv,u} + r_{s,w,t}^{vb,u}\right) - \underline{v} \ge 0 \tag{50}$$

$$0 \le \mu_{s,b,t}^{v,ru+} \perp \bar{v} - v_{s,b,t} - \sum_{\epsilon} z_{z,w}^{p}\left(r_{s,w,t}^{pv,u} + r_{s,w,t}^{vb,u}\right) \ge 0 \tag{51}$$

$$0 \le \mu_{s,b,t}^{v,rd-} \perp v_{s,b,t} - \sum_{\epsilon} z_{z,w}^{p}\left(r_{s,w,t}^{pv,d} + r_{s,w,t}^{vb,d}\right) - \underline{v} \ge 0 \tag{52}$$

$$0 \le \mu_{s,b,t}^{v,rd+} \perp \bar{v} - v_{s,b,t} + \sum_{\epsilon} z_{z,w}^{p}\left(r_{s,w,t}^{pv,d} + r_{s,w,t}^{vb,d}\right) \ge 0 \tag{53}$$

$$0 \le \mu_{s,l_k,t}^{p-} \perp p_{s,t}^{l_k} - \underline{p}^{l_k} \ge 0 \tag{54}$$

$$0 \le \mu_{s,l_k,t}^{p+} \perp \bar{p}^{l_k} - p_{s,t}^{l_k} \ge 0 \tag{55}$$

$$0 \le \mu_{s,l_k,t}^{ru-} \perp p_{s,t}^{l_k} - \sum_{w\in B} z_{w}^{l_k}\left(r_{s,w,t}^{pv,u} + r_{s,w,t}^{vb,u}\right) - \underline{p}^{l_k} \ge 0 \tag{56}$$

$$0 \le \mu_{s,l_k,t}^{ru+} \perp \bar{p}^{l_k} - p_{s,t}^{l_k} + \sum_{w\in B} z_{w}^{l_k}\left(r_{s,w,t}^{pv,u} + r_{s,w,t}^{vb,u}\right) \ge 0 \tag{57}$$

$$0 \le \mu_{s,l_k,t}^{rd-} \perp p_{s,t}^{l_k} + \sum_{w\in B} z_{w}^{l_k}\left(r_{s,w,t}^{pv,d} + r_{s,w,t}^{vb,d}\right) - \underline{p}^{l_k} \ge 0 \tag{58}$$

$$0 \le \mu_{s,l_k,t}^{rd+} \perp \bar{p}^{l_k} - p_{s,t}^{l_k} - \sum_{w\in B} z_{w}^{l_k}\left(r_{s,w,t}^{pv,d} + r_{s,w,t}^{vb,d}\right) \ge 0 \tag{59}$$

3.4.2 Strong duality property

The lower-level model is formulated as a linear programming problem thus exhibits strong duality property. Eqs. 60, 61 refers to the strong duality condition corresponding to lower-level problem under each scenario.

$$\begin{aligned}\sum_{t\in T} \gamma_t^p p_{s,t}^{dso} - \gamma_t^u r_{s,t}^{dso,u} - \gamma_t^d r_{s,t}^{dso,d} = \sum_{\epsilon}\Bigg[\sum_{\epsilon}\Big[-\lambda_{s,t}^{p} p_{s,i,t}^{v,b}\left(1 + z_i^d\right) - \sum_{\epsilon}\left(\lambda_{s,t}^{u} r_{s,t}^{vb,u} + \lambda_{s,t}^{d} r_{s,t}^{vb,d}\right)\Big] \\ + \sum_{i\in N} p_{s,i,t}^{v,b} \sum_{b\in B} z_{b,i}^{p}\left(\mu_{s,b,t}^{v-} - \mu_{s,b,t}^{v+} + \mu_{s,b,t}^{v,ru-} - \mu_{s,b,t}^{v,ru+} + \mu_{s,b,t}^{v,rd-} - \mu_{s,b,t}^{v,rd+}\right) \\ + \sum_{i\in N} p_{s,i,t}^{v,b} \sum_{b\in B} z_{i}^{l_k}\left(-\mu_{s,l_k,t}^{p-} + \mu_{s,l_k,t}^{p+} - \mu_{s,l_k,t}^{ru-} + \mu_{s,l_k,t}^{ru+} - \mu_{s,l_k,t}^{rd-} + \mu_{s,l_k,t}^{rd+}\right) \\ + \sum_{i\in N} r_{s,i,t}^{vb,u} \sum_{b\in B} z_{b,i}^{p}\left(-\mu_{s,b,t}^{v,ru-} + \mu_{s,b,t}^{v,ru+}\right) + r_{s,i,t}^{l_k} \sum_{b\in B} z_{i}^{l_k}\left(\mu_{s,l_k,t}^{ru-}\mu_{s,l_k,t}^{ru+}\right) \\ + \sum_{i\in N} r_{s,i,t}^{vb,d} \sum_{b\in B} z_{b,i}^{p}\left(\mu_{s,b,t}^{v,rd-} - \mu_{s,b,t}^{v,rd+}\right) + r_{s,i,t}^{l_k} \sum_{b\in B} z_{i}^{l_k}\left(\mu_{s,l_k,t}^{rd-}\mu_{s,l_k,t}^{rd+}\right)\Bigg] + X\end{aligned} \tag{60}$$

$$\begin{aligned}X = \sum_{t\in T}\Bigg[-\sum_{j\in J}\left(\mu_{s,j,t}^{pv,p+} p_{s,j,t}^{pv,fore} + \mu_{s,j,t}^{pv,ru+} p_{s,j,t}^{pv,fore}\right) + \lambda_{s,t}^{p}\Bigg(-\sum_{b\in B} p_{b,t}^{load} - p_{s,t}^{loss} \\ - \sum_{i\in N} z_i^d p_{s,i,t}^{vb} + \sum_{i\in N} z_i^d p_{s,j,t}^{vb}\Bigg) + \mu_{s,t}^{dso,p-}\left(\underline{p}^{dso} - \mu_{s,t}^{dso,p+}\bar{p}^{dso}\right) \\ + \sum_{b\in B}\left(\mu_{s,b,t}^{v-} + \mu_{s,b,t}^{v,ru-} + \mu_{s,b,t}^{v,rd-}\right)\left(\underline{v} - v_1 + \sum_{w\in B} z_{b,w}^{p} p_{w,t}^{load} + \sum_{w\in B} z_{b,w}^{q} p_{w,t}^{load}\right) \\ + \sum_{b\in B}\left(\mu_{s,b,t}^{v+} + \mu_{s,b,t}^{v,bu+} + \mu_{s,b,t}^{v,rd+}\right)\left(v_1 - \sum_{w\in B} z_{b,w}^{p} p_{w,t}^{load} - \sum_{w\in B} z_{b,w}^{q} p_{w,t}^{load} - \bar{v}\right) \\ + \sum_{k\in K}\left(\mu_{s,b,t}^{p-} + \mu_{s,b,t}^{ru-} + \mu_{s,b,t}^{rd-}\right)\left(\underline{p}^{l_k} - p_{s,t}^{l_k} - \sum_{j\in J} z_j^{l_k} p_{s,j,t}^{pv} + \sum_{i\in N} z_i^{l_k} p_{s,i,t}^{vb}\right) \\ + \sum_{k\in K}\left(\mu_{s,b,t}^{p+} + \mu_{s,b,t}^{ru+} + \mu_{s,b,t}^{rd+}\right)\left(p_{s,t}^{l_k} + \sum_{j\in J} z_j^{l_k} p_{s,j,t}^{pv} - \sum_{i\in N} z_i^{l_k} p_{s,i,t}^{vb} - \bar{p}^{l_k}\right)\Bigg]\end{aligned} \tag{61}$$

3.4.3 Linearized objective

The corresponding DLMP expressions can be obtained by taking partial derivatives of the Lagrangian function associated with the lower-level model, as shown by the following Eqs. 62–64.

$$\begin{aligned}\lambda_{s,i,t}^{dimp,p} = -\lambda_{s,t}^{p}\left(1 + z_i^d\right) \\ + \sum_{b\in B} z_{b,t}^{p}\left(\mu_{s,b,t}^{v-} - \mu_{s,b,t}^{v+} + \mu_{s,b,t}^{v,ru-} - \mu_{s,b,t}^{v,ru+} + \mu_{s,b,t}^{v,rd-} - \mu_{s,b,t}^{v,rd+}\right) \\ + \sum_{k\in K} z_i^{l_k}\left(-\mu_{s,l_k,t}^{p-} + \mu_{s,l_k,t}^{p+} - \mu_{s,l_k,t}^{ru-} + \mu_{s,l_k,t}^{ru+} - \mu_{s,l_k,t}^{rd-} + \mu_{s,l_k,t}^{rd+}\right)\end{aligned} \tag{62}$$

$$\lambda_{s,i,t}^{dlmp,u} = \lambda_{s,t}^{u} - \sum_{b\in B} z_{b,j}^{p}\left(\mu_{s,b,t}^{v,ru+} - \mu_{s,b,t}^{v,ru-}\right) - \sum_{k\in K} z_i^{l_k}\left(\mu_{s,l_k,t}^{ru-} - \mu_{s,l_k,t}^{ru+}\right) \tag{63}$$

$$\lambda_{s,i,t}^{dlmp,d} = \lambda_{s,t}^{d} - \sum_{b\in B} z_{b,j}^{p}\left(\mu_{s,b,t}^{v,rd-} - \mu_{s,b,t}^{v,rd+}\right) - \sum_{k\in K} z_i^{l_k}\left(\mu_{s,l_k,t}^{rd+} - \mu_{s,l_k,t}^{rd-}\right) \tag{64}$$

Finally, the linear equivalent expression of the objective function Eq. 5 can be driven from the strong duality condition Eq. 60 and the DLMP expressions Eqs. 62–64. The linear objective function can be substituted by Eq. 5 is stated below:

$$\boldsymbol{minmax} \sum_{s} \pi_s \triangle t \sum_{t} \gamma_t^p p_{s,t}^{dso} - \gamma_t^u r_{s,t}^{dso,u} - \gamma_t^d r_{s,t}^{dso,d} - X \tag{65}$$

4 Numerical studies

4.1 Input data

A modified IEEE-33 bus power system is employed to demonstrate the effectiveness of the proposed model. Figure 4 shows the specific access locations and capacities of the

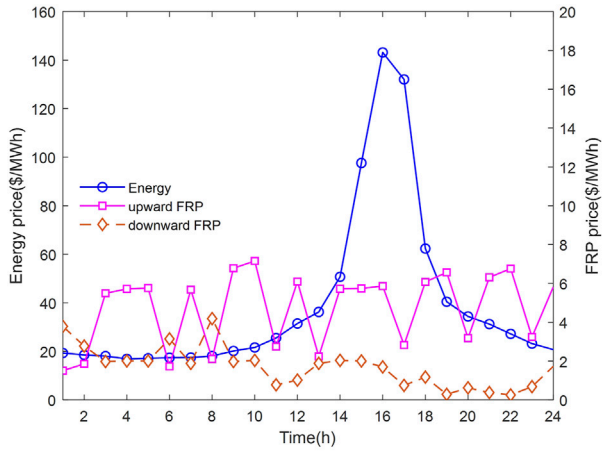

FIGURE 5
Energy, FRT market prices.

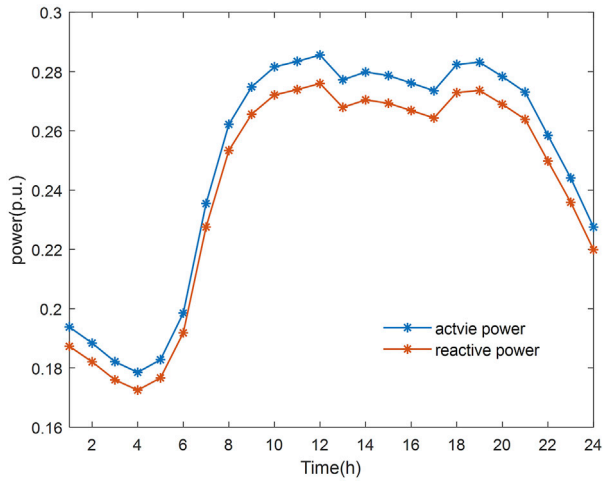

FIGURE 6
Load curve.

prosumers. The exchange power limit between the DNO and grid sets 5 MW. The simulation is presented in the form of per-unit value with a base value of 10 MW. The market prices for energy and FRP are displayed in Figure 5, derived from the case in the literature (Wang et al., 2017). The active and reactive loads demand of the distribution network is shown in Figure 6. All cases studies are performed on a PC with Inter Core 7 CPU (3.40 GHz) and 24.0 GB RAM with the commercial solver GUROBI 10.0.1 for MILP problems.

To demonstrate the effectiveness of the proposed model, two numerical case are designed here. In both cases, a total of 1,000 historical scenarios of PV's output are utilized, and the mix-norm constraint is applied with a confidence level of 90%.

1) Case 1: Aggregator provide FRP without considering the security of the distribution network after FRP delivery.
2) Case 2: The proposed model.

TABLE 1 Bid-offer decision of prosumer aggregator in case 1 and case 2.

Case	Energy cost/$	FRP revenue/$	Expected total cost/$
1	71.432	61.404	10.028
2	69.532	43.257	26.274

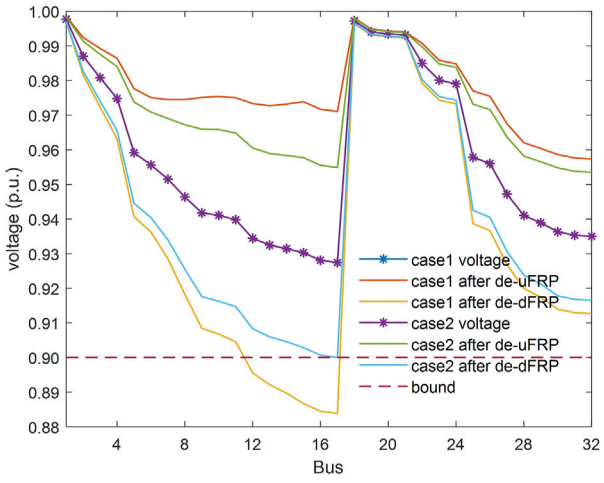

FIGURE 7
Cases results of voltage magnitudes.

To demonstrate the effectiveness of the data-driven model in adjusting offers conservativeness, two additional case are designed based on Case 2.

1) Case 3: The mix-norm constraint is applied with a confidence level of 80%.
2) Case 4: The mix-norm constraint is applied with a confidence level of 100%.

4.2 Distribution network security analysis

The energy-bidding and FRP-offering costs of the prosumer aggregator for different cases are shown in Table 1. Each type cost of Case 1 is better than that of Case 2. When comparing the energy costs of Case 1 and Case 2, it is clear that without considering the security constraint related to FRP delivery, the prosumer aggregator often prioritizes higher FRP benefit over energy costs. Obviously ignoring the security constraint related to FRP delivery will cause the prosumer flexibility value to be overestimated and affect the energy bidding decision.

The voltage magnitude of each bus for Case 1 and Case 2 at time slot 18:00 are shown in Figure 7. It can be seen that the voltage magnitude of bus 12–17 in case 1 violates the low bound after the delivery of the downward FRP. On the contrary, the voltage magnitude of each node in Case 2 remains within the safety boundary after the delivery of the downward FRP. In addition, it can be seen that the voltage magnitude boost is less in Case 2 than in

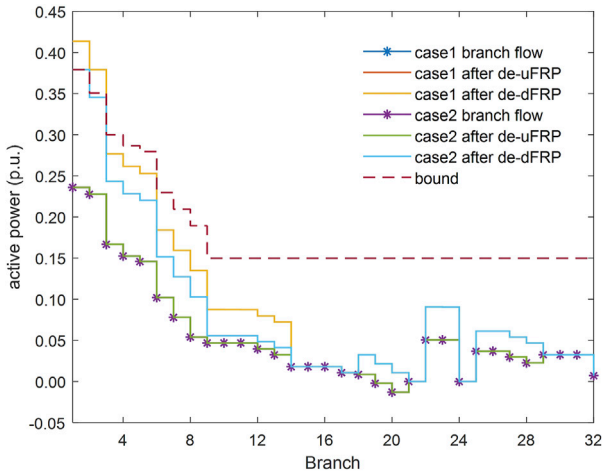

FIGURE 8
Case results of line congestion.

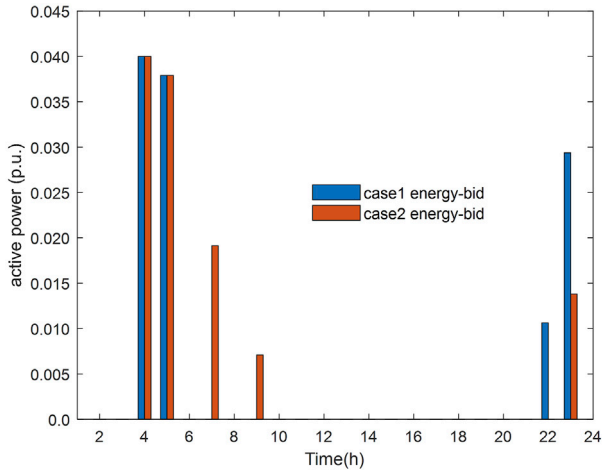

FIGURE 9
Case results of energy-bid od prosumer 2.

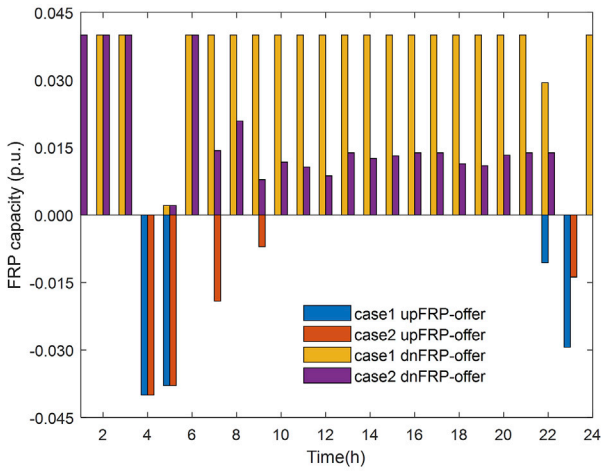

FIGURE 10
Cases results of FRP-offer of prosumer 2.

TABLE 2 Bid-offer decision of prosumer aggregator in cases 2–4.

Case	Energy cost/$	FRP revenue/$	Expected total cost/$
3	69.532	42.771	26.761
2	69.532	43.257	26.274
4	69.532	55.700	13.831

Case 1 after delivering the upward FRP, because the quantity of FRP in Case 2 is less than that of Case 1.

The power flow of each line of Case 1 and Case 2 in time slot 12:00 are shown in Figure 8. The congestion occurs in Case 1 after the delivery of downward FRP in line 1–3. On the contrary, there is no line occurring congestion after delivering the downward FRP. The power of each line does not change significantly in both cases after delivery of upward climbing because the quantity of upward FRP accounts for too small a proportion of the distribution network load demand.

The above analysis provides that the prosumer aggregator can offer FRP while enable distribution network security.

The full-time energy and FRP bidding/offering strategies of prosumer 2 in Case1 and Case2 are shown in Figure 9 and Figure 10, respectively. Comparing Figure 5 and Figure 6, it can be found that both energy and FRP cater better to the price and the peak-valley characteristics of the distribution grid load to minimize the operating cost. Case 2 purchases energy and offers downward FRP in periods 7 and 9, which differ significantly from Case1. Between the time periods 07:00–22:00, downward FRP of Case 2 is significantly less than that of Case 1, which is caused by the constraints related to post-delivery FRP.

4.3 Economic and conservative analysis

The costs of prosumer aggregator for Case3-4 are shown in Table 2. The expected total cost of the bidding/offering strategy increases with increasing confidence due to the consideration of greater distributional uncertainty, which makes the strategy more conservative and therefore less economical. It reflects the adjustment of the conservativeness of the strategy by the subjective risk-averse of the prosumer aggregator in the FRP-offer.

5 Conclusion

This paper addresses the problem of providing FRP by a prosumer aggregator within distribution network security. For this purpose, a data-driven bi-level stochastic optimization approach is proposed to model the process of active interaction between the prosumer and the DNO for decision making. The stochastic decision problem of adjustable conservativeness of the prosumer aggregator is solved by a data-driven scenario approach. The portfolio problem of the prosumer aggregator and the problem

of security-constrained economic dispatch of the distribution network are solved in the upper-level and lower-level model, respectively.

The simulation results show that through the optimal scheduling of aggregator, prosumers can actively purchase energy from DNO and provide the upward and downward FRP, and ensure that the distribution network does not occur voltage violations and line congestion. The prosumer aggregator is able to take advantage of the peak-valley characteristics of prices and adjust the conservativeness of its decisions based on confidence levels. The reduction in FRP available to the prosumer due to distribution network security constraints leads to higher costs for the prosumer.

Data availability statement

The original contributions presented in the study are included in the article/supplementary material, further inquiries can be directed to the corresponding author.

Author contributions

XA: Project administration, Supervision, Writing–review and editing. HH: Conceptualization, Data curation, Formal Analysis, Methodology, Software, Validation, Writing–original draft, Writing–review and editing. JH: Funding acquisition, Project administration, Supervision, Writing–review and editing. ZW: Formal Analysis, Investigation, Writing–review and editing. KW: Writing–review and editing.

Funding

The author(s) declare financial support was received for the research, authorship, and/or publication of this article. This work was supported by the National Natural Science Foundation of China (52177080, 2021YFB4000104).

Conflict of interest

The authors declare that the research was conducted in the absence of any commercial or financial relationships that could be construed as a potential conflict of interest.

Publisher's note

All claims expressed in this article are solely those of the authors and do not necessarily represent those of their affiliated organizations, or those of the publisher, the editors and the reviewers. Any product that may be evaluated in this article, or claim that may be made by its manufacturer, is not guaranteed or endorsed by the publisher.

References

Allahmoradi, S., Moghaddam, M., Bahramara, S., and Sheikhahmadi, P. (2021). Flexibility-constrained operation scheduling of active distribution networks. *Int. J. Electr. Power & Energy Syst.* 131, 107061. doi:10.1016/j.ijepes.2021.107061

Bahramara, S., Sheikhahmadi, P., Mazza, A., and Chicco, G. (2022). Day-ahead self-scheduling from risk-averse microgrid operators to provide reserves and flexible ramping ancillary services. *Int. J. Electr. Power & Energy Syst.* 142, 108381. doi:10.1016/j.ijepes.2022.108381

California Independent System Operator (2023). The net-demand trend. Available at: https://www.caiso.com/TodaysOutlook/Pages/default.aspx (Accessed June 23, 2023).

Fang, X., Sedzro, k., Yuan, H., Ye, H., and Hodge, B. (2020). Deliverable flexible ramping products considering spatiotemporal correlation of wind generation and demand uncertainties. *IEEE Trans. Power Syst.* 35 (4), 2561–2574. doi:10.1109/TPWRS.2019.2958531

Fu, X., Wu, X., Zhang, C., Fan, S., and Liu, N. (2023b). Planning of distributed renewable energy systems under uncertainty based on statistical machine learning. *Prot. Control Mod. Power Syst.* 7 (1), 41. doi:10.1186/s41601-022-00262-x

Fu, X., Zhou, Y., Wei, Z., and Wang, Y. (2023a). Optimal operation strategy for a rural microgrid considering greenhouse load control. *CSEE J. Power Energy Syst.*, 1–11. doi:10.17775/CSEEJPES.2022.06200

Ghaemi, S., Salehi, J., and Moeini-Aghtaie, M. (2021a). Developing a market-oriented approach for supplying flexibility ramping products in a multimicrogrid distribution system. *IEEE Trans. Industrial Inf.* 17 (10), 6765–6775. doi:10.1109/TII.2020.3047600

Ghaemi, S., Salehi, J., and Moeini-Aghtaie, M. (2021b). Estimating abilities of distributed energy resources in providing flexible ramp products for active distribution networks. *Sustain. Cities Soc.* 65, 102593. doi:10.1016/j.scs.2020.102593

Gonzalez-Romera, E., Ruiz-Cortes, M., Milanes-Montero, M., Barrero-Gonzalez, F., Barrero-Gonzalez, E., Lopes, R., et al. (2019). Advantages of minimizing energy exchange instead of energy cost in prosumer microgrids. *Energies* 12 (4), 719. doi:10.3390/en12040719

Hou, P., Hu, J., and Yang, G. (2019). Convex optimization of virtual storage system scheduling in market environment. *J. Mod. Power Syst. Clean Energy* 7 (6), 1744–1748. doi:10.1007/s40565-019-0548-z

Hu, J., Sarker, M., Wang, J., Wen, F., and Liu, W. (2018). Provision of flexible ramping product by battery energy storage in day-ahead energy and reserve markets. *IET Generation, Transm. Distribution* 12 (10), 2256–2264. doi:10.1049/iet-gtd.2017.1522

Hu, J., Yang, G., Ziras, C., and Kok, K. (2019). Aggregator operation in the balancing market through network-constrained transactive energy. *IEEE Trans. Power Syst.* 34 (5), 4071–4080. doi:10.1109/TPWRS.2018.2874255

Huang, Z., Fang, B., and Deng, J. (2020). Multi-objective optimization strategy for distribution network considering V2G-enabled electric vehicles in building integrated energy system. *Prot. Control Mod. Power Sysyem* 5 (1), 7. doi:10.1186/s41601-020-0154-0

Khoshjahan, M., and Kezunovic, M. (2022). Robust bidding strategy for aggregation of distributed prosumers in flexiramp market. *Electr. Power Syst. Res.* 209, 107994. doi:10.1016/j.epsr.2022.107994

Khoshjahan, M., Moeini-Aghtaie, M., Fotuhi-Firuzabad, M., Dehghanian, P., and Mazaheri, H. (2020). Advanced bidding strategy for participation of energy storage systems in joint energy and flexible ramping product market. *IET Generation, Transm. Distribution* 14 (22), 5202–5210. doi:10.1049/iet-gtd.2020.0224

Kim, D., Kwon, K., and Kim, M. (2021). Application of flexible ramping products with allocation rates in microgrid utilizing electric vehicles. *Int. J. Electr. Power & Energy Syst.* 133, 107340. doi:10.1016/j.ijepes.2021.107340

Kubli, M., Loock, M., and Wuestenhagen, R. (2018). The flexible prosumer: measuring the willingness to co-create distributed flexibility. *Energy Policy* 144, 540–548. doi:10.1016/j.enpol.2017.12.044

Ma, G., Li, J., and Zhang, X. (2023). Energy storage capacity optimization for improving the autonomy of grid-connected microgrid. *IEEE Trans. Smart Grid* 14 (4), 2921–2933. doi:10.1109/TSG.2022.3233910

Nizami, M., Hossain, M., Amin, B., and Fernandez, E. (2020). A residential energy management system with bi-level optimization-based bidding strategy for day-ahead bi-directional electricity trading. *Appl. Energy* 261, 114322. doi:10.1016/j.apenergy.2019.114322

Olivella-Rosell, P., Lloret-Gallego, P., Munne-Collado, I., Villafafila-Robles, R., Sumper, A., Ottessen, S., et al. (2018). Local flexibility market design for aggregators providing multiple flexibility services at distribution network level. *Energies* 11 (4), 822. doi:10.3390/en11040822

Shi, X., Xu, Y., Guo, Q., Sun, H., and Zhang, X. (2023). Day-Ahead Distributionally Robust Optimization-Based Scheduling for Distribution Systems With Electric Vehicles. *Electr. Veh.* 14 (4), 2837–2850. doi:10.1109/TSG.2022.3223332

Wang, J., Zhong, H., Tang, W., Rajagopal, R., Xia, Q., Kang, C., et al. (2017). Optimal bidding strategy for microgrids in joint energy and ancillary service markets considering flexible ramping products. *Appl. Energy* 205, 294–303. doi:10.1016/j.apenergy.2017.07.047

Wang, Q., and Hodge, B. (2017). Enhancing power system operational flexibility with flexible ramping products: A review. *IEEE Trans. Industrial Inf.* 13 (4), 1652–1664. doi:10.1109/TII.2016.2637879

Wu, J., Hu, J., Ai, X., Zhang, Z., and Hu, H. (2019). Multi-time scale energy management of electric vehicle model-based prosumers by using virtual battery model. *Appl. Energy* 251, 113312. doi:10.1016/j.apenergy.2019.113312

Xu, X., Li, Y., Ma, H., and Shahidehpour, M. (2023). Hierarchical Central-Local Inverter-Based Voltage Control in Distribution Networks Considering Stochastic PV Power Admissible Range. *Stoch. p. v. Power Admissible Range* 14 (3), 1868–1879. doi:10.1109/TSG.2022.3213776

Yamujala, S., Jain, A., Sreekumar, S., Bhakar, R., and Mathur, J. (2022). Enhancing power systems operational flexibility with ramp products from flexible resources. *Electr. Power Syst. Res.* 202, 107599. doi:10.1016/j.epsr.2021.107599

Yuan, H., Li, F., Wei, Y., and Zhu, J. (2018). Novel linearized power flow and linearized OPF models for active distribution networks with application in distribution LMP. *IEEE Trans. Smart Grid* 9 (1), 438–448. doi:10.1109/TSG.2016.2594814

Zhang, M., Zhou, M., Wu, Z., Yang, H., and Li, G. (2022). A ramp capability-aware scheduling strategy for integrated electricity-gas systems. *Energy* 241, 122813. doi:10.1016/j.energy.2021.122813

Zhang, X., Hu, J., Wang, H., Wang, G., Chan, K., and Qiu, J. (2020). Electric vehicle participated electricity market model considering flexible ramping product provisions. *IEEE Trans. Industry Appl.* 56 (5), 5868–5879. doi:10.1109/TIA.2020.2995560

Zhao, C., and Guan, Y. (2016). Data-driven stochastic unit commitment for integrating wind generation. *IEEE Trans. Power Syst.* 31 (4), 2587–2596. doi:10.1109/TPWRS.2015.2477311

Zhu, X., Zeng, B., Dong, H., and Liu, J. (2020). An interval-prediction based robust optimization approach for energy-hub operation scheduling considering flexible ramping products. *Energy* 194, 116821. doi:10.1016/j.energy.2019.116821

10.3389/fenrg.2023.1258292

Nomenclature

KKT	Karush-Kuhn-Tucker
CAISO	California Independent System Operator
FRP	flexible ramping product
ACOPF	alternative current optimal power flow
DNO	distribution network operator
PV	photovoltaic
Variables	
π_s	scenario probability
$p_{s,i,t}^{vb}$	energy bidding of prosumer
$r_{s,i,t}^{vb,u}$, $r_{s,i,t}^{vb,d}$	upward/downward FRP offering of prosumer
$e_{s,i,t}^{vb}$	state of energy of prosumer
$p_{s,t}^{dso}$	energy requirement of DNO
$r_{s,t}^{dso,u}$, $r_{s,t}^{dso,d}$	upward/downward FRP offering of DNO
$p_{s,j,t}^{pv}$	quantity of energy of DRE
$r_{s,j,t}^{pv,u}$, $r_{s,j,t}^{pv,d}$	quantity of upward/downward FRP offering of DRE
$\lambda_{s,i,t}^{dlmp,p}$, $\lambda_{s,i,t}^{dlmp,u}$, $\lambda_{s,i,t}^{dlmp,d}$	DLMP of energy, upward/downward FRP for prosumer
Parameters	
π_0	initial probability
η^c	energy conversion efficiency
γ_t^p, γ_t^u, γ_t^d	day-ahead energy price, upward/downward FRP price
$p_{s,j,t}^{pv,fore}$	forecast day-ahead generation
v_1	voltage magnitude of the reference bus
Indices and sets	
s, N_s	index/set of scenario
S	number of clustering scenarios
i, w, N	index/set of prosumer
t, T	index/set of time
j, J	index/set of DRE
B	set of nodes
b, w	index of node
k, K	index/set of branch

frontiers | Frontiers in Energy Research

TYPE Original Research
PUBLISHED 11 January 2024
DOI 10.3389/fenrg.2023.1341984

Check for updates

OPEN ACCESS

EDITED BY
Yushuai Li,
University of Oslo, Norway

REVIEWED BY
Bi Liu,
Anhui University, China
Yihuan Li,
North China Electric Power University, China
Xiao Wang,
The University of Manchester, United Kingdom

*CORRESPONDENCE
Jun Qi,
13898177452@163.com

RECEIVED 21 November 2023
ACCEPTED 26 December 2023
PUBLISHED 11 January 2024

CITATION
Li T, Sun F, Chen J, Wang L, Yang Z, Liu R and Qi J (2024), An attack-resilient distributed energy management strategy for integrated energy systems.
Front. Energy Res. 11:1341984.
doi: 10.3389/fenrg.2023.1341984

COPYRIGHT
© 2024 Li, Sun, Chen, Wang, Yang, Liu and Qi. This is an open-access article distributed under the terms of the Creative Commons Attribution License (CC BY). The use, distribution or reproduction in other forums is permitted, provided the original author(s) and the copyright owner(s) are credited and that the original publication in this journal is cited, in accordance with accepted academic practice. No use, distribution or reproduction is permitted which does not comply with these terms.

An attack-resilient distributed energy management strategy for integrated energy systems

Tong Li[1], Feng Sun[1], Jian Chen[1], Lei Wang[2], Zhibin Yang[1], Ruitong Liu[1] and Jun Qi[3]*

[1]Electric Power Research Institute of State Grid Liaoning Electric Power Co., Ltd., Shenyang, China, [2]State Grid Liaoning Electric Power Supply Co., Ltd., Shenyang, China, [3]School of Automation, Chengdu University of Information Technology, Chengdu, China

The increasing integration of various energy sources and the adoption of smart grid technologies have revolutionized the way we generate, distribute, and consume energy. While these advancements offer numerous benefits, they also introduce vulnerabilities to cyber–physical attacks. To this aim, this paper investigates a resilient energy management strategy for integrated energy systems. By adopting a switched control approach and incorporating a local estimation mechanism, we have developed a resilient distributed energy management strategy to tackle the energy management problem (EMP) in integrated energy systems (IESs). This methodology demonstrates strong robustness and resilience, successfully detecting data integrity attacks and denial-of-service (DoS) attacks. Finally, we provide a case study to demonstrate the effectiveness of our proposed strategy in a real-world scenario.

KEYWORDS

cyberattacks, energy management, integrated energy systems, smart grid, distributed optimization

1 Introduction

Integrated energy systems (IESs), encompassing various energy sources, storage systems, and smart grid technologies (Liu et al., 2023; Liu et al., 2022), have significantly improved the efficiency and sustainability of energy generation and distribution. The energy management problem (EMP) is the core research problem in IESs (Li et al., 2020; Li et al., 2020; Li et al., 2022). EMP can be conceptualized as an optimization challenge constrained by the goal of minimizing overall costs or maximizing societal benefit (Li et al., 2021; Zhang et al., 2023). This optimization aims to achieve these objectives while simultaneously ensuring a balance between energy supply and demand and adhering to operational constraints.

The algorithms designed for EMP can be broadly categorized as either centralized or distributed methods. Traditional centralized algorithms, such as the reinforcement learning algorithm (Yang et al., 2022) and cuckoo algorithm, have been extensively explored in previous research. However, a significant limitation of these algorithms lies in their centralized nature, demanding a central controller to collect and process all relevant information to compute optimal solutions. With the integration of distributed energy resources, there is a growing inclination to shift computationally intensive tasks toward the edge (Teng et al., 2023). Additionally, distributed participants are hesitant to divulge personal data to a centralized controller due to concerns regarding security and financial gain. To address this issue, distributed methods have been proposed, which attract

significant attention. The distributed algorithms possess several advantages: 1) Scalability: Distributed methods are highly scalable. They can efficiently handle large-scale problems by dividing the computational workload among multiple agents or nodes. 2) Flexibility: Distributed optimization can adapt to dynamic environments and changing conditions more effectively. Each node can respond to local changes independently, which is particularly useful in rapidly changing or unpredictable environments. 3) Privacy: In distributed optimization, each node or agent can keep its data local, which is beneficial for privacy-sensitive applications. The distributed methods primarily encompass the alternating direction method of multipliers (ADMM)-based approaches and consensus-based methods. As an illustration, a distributed energy management framework and model were introduced in Zhang et al. (2017), taking into account interrelated power, heat, and gas systems. In this context, an innovative distributed consensus-ADMM algorithm was devised to ascertain the global optimal operation for each participating entity. Utilizing a similar approach, the distributed consensus-ADMM algorithm was subsequently extended to address the multi-period energy management problem (EMP) for manufacturing execution systems (MESs), incorporating certain linearized network constraints (Xu et al., 2020). Building upon the foundation laid in Zhang et al. (2017), an asynchronous event-triggering-based distributed energy management algorithm was introduced in Li et al. (2019). This algorithm adeptly manages the distinctive timescales inherent in various energy network types. Furthermore, the concept of the We-Energy (WE) model, akin to the multi-energy prosumer concept, was unveiled in Sun et al. (2019). Concurrently, a distributed double-consensus (DDC) algorithm was introduced to facilitate cooperative energy management among multiple WE entities. Recently, various distributed optimization algorithms have been developed to cater to diverse application requirements. These include the adoption of a Newton-based method to expedite convergence (Li et al., 2021), a federated reinforcement learning algorithm (Lee and Choi, 2022), and a double-side coordinative method (Zhou et al., 2023).

The prior research mentioned above has effectively addressed EMP for IESs, yielding satisfactory results. However, it is worth noting that the efficacy of these methods relies on a fundamental assumption: the reliability of the communication network. The distributed algorithms are executed within a communication network that is susceptible to various malicious cyberattacks. In recent years, notable efforts have been undertaken to investigate the impact of different cyberattacks on distributed energy management algorithms. To elaborate, Zeng et al. (2017), Zhao et al. (2017), and Duan and Chow (2019) delved into the vulnerability of the distributed lambda iteration algorithm in the context of data integrity attacks. In such scenarios, the energy management system's operation may be compromised by the injection of false data into exchanged information or local utilization data. In contrast, denial-of-service (DoS) attacks are aimed at obstructing and disrupting information sharing among agents. These attacks can have severe consequences for IES security operations, as communication is disrupted during the DoS attack period, resulting in a fractured structure of the distributed communication network. In this scenario, agents cannot exchange real-time and accurate data with their neighbors, potentially causing a global supply and demand mismatch, leading to system failures and substantial economic losses. Developing effective dispatch strategies to withstand such attacks becomes imperative. In response, Zhang et al. (2019) introduced a DoS-attack-robust strategy that combats DoS attacks by implementing a mixed-integer linear programming method to allocate the load demand. Li et al. (2017) proposed a novel robust distributed economic dispatch strategy capable of identifying and isolating misbehaving distributed generators to safeguard the rest of the system. Most recently, Huang et al. (2022) introduced a privacy-preserving protocol-based distributed robust dispatch approach for MESs. This method proficiently addresses both colluding and non-colluding attacks. Additionally, Li et al. (2022) analyzed the impact of DoS attacks and proposed an effectively double-gradient-descent algorithm to resist the DoS attacks.

Although the existing research has investigated EMP under diverse cyberattacks, they still suffer from two key challenges: 1) the existing distributed and resilient energy management strategies are mainly designed to deal with a single type of cyberattack, such as data integrity or DoS attacks. It is highly needed to develop new algorithms that are compatible with integrity and DoS attacks simultaneously; 2) the existing distributed energy management strategies, considering cyberattacks, work on connected communication networks. However, in reality, the communication networks may not be two-way. It is necessary to design distributed algorithms that can handle directed graphs.

To tackle those challenges, we propose an attack-resilient distributed energy management strategy that is capable of handling integrity and DoS attacks and working under a directed communication network. The contributions of this paper are summarized as follows:

1) By introducing a switched control and local estimation mechanism, an attack-resilient distributed energy management strategy can be developed to solve EMP in IESs. The proposed method can well resist both integrity and DoS attacks, resulting in strong robustness and resilience.
2) The proposed energy management strategy fits well with the directed communication network. Compared with the existing distributed studies (Zeng et al., 2017; Zhao et al., 2017; Li et al., 2018; Duan and Chow, 2019; Zhang et al., 2019; Li et al., 2022; Huang et al., 2022), it possesses strong expansibility and universality.

2 Formulation of EMP in IES

An IES consists of numerous interconnected energy bodies (EBs) and principal networks. Each EB integrates a diverse array of energy generation and conversion devices. This includes renewable generators (RGs), renewable heating devices (RHDs), fuel generators (FGs), fuel heating devices (FHDs), combined heat and power (CHP) devices, electricity storage systems (ESSs), heat storage systems (HSs), and gas producers (GPs). Furthermore, every EB encompasses energy loads consisting of power, heat, and gas loads. These loads further comprise must-run and schedulable loads that are connected to their respective energy buses. The EMP of IES

is more complex than that of smart grids due to the following two parts. On the one hand, IES typically encompasses a wider array of energy resources compared to a smart grid. While smart grids primarily focus on electrical energy, integrating aspects like renewable energy sources, demand response, and storage, IES includes not only electricity but also other forms of energy, such as heat, gas, and sometimes cooling systems. Managing these diverse energy types, each with its own dynamics and constraints, adds complexity to EMP. On the other hand, the objectives of managing IES are more diverse and complex. In addition to ensuring the reliability and efficiency of each energy system, IES must optimize the overall system operation considering economic factors and the balance between different energy sources. This multifaceted objective set goes beyond the primary electrical focus of smart grids.

2.1 Model of EB

Considering the energy generation and consumption of single EB, electricity is produced from RG, FG, and CHP, represented as p^i_{re}, p^i_{fu}, and p^i_{chp}, respectively. Similarly, heat is generated from RHD, FHD, and CHP, symbolized as h^i_{re}, h^i_{fu}, and h^i_{chp}, respectively. Gas is supplied by GP, signified as g^i_{gas}. Regarding ES and HS, depending on their charge and discharge states, they can serve either as energy providers or users. The power and heat exchanges for ES and HS are designated as p^i_{st} and h^i_{st}, respectively. Positive values of p^i_{st} or h^i_{st} indicate discharging, while negative values signify charging. For energy demands, we use $l^i_{p,m}$ (or $l^i_{p,c}$), $l^i_{h,m}$ (or $l^i_{h,c}$), and $l^i_{g,m}$ (or $l^i_{g,c}$) to depict the essential (or adjustable) power, heat, and gas loads, respectively. Motivated by potential profit, each EB can act as both an energy supplier and a user by adeptly managing its internal elements. We define p^i_{im}, h^i_{im}, and g^i_{im} to illustrate the imbalance (either deficit or surplus) in power, heat, and gas, respectively. The energy-balancing conditions for the ith EB at instant T can be expressed as follows:

$$\begin{cases} p^{i,T}_{im} = p^{i,T}_{re} + p^{i,T}_{fu} + p^{i,T}_{chp} + p^{i,T}_{st} - l^{i,T}_{p,m} - l^{i,T}_{p,c}, \\ h^{i,T}_{im} = h^{i,T}_{re} + h^{i,T}_{fu} + h^{i,T}_{chp} + h^{i,T}_{st} - l^{i,T}_{h,m} - l^{i,T}_{h,c}, \\ g^{i,T}_{im} = g^{i,T}_{gas} - l^{i,T}_{g,m} - l^{i,T}_{g,c}. \end{cases} \tag{1}$$

Beyond the supply–demand balance constraints, each EB adheres to a series of localized operational constraints. Primarily, these constraints fall under six categories:

1) Capability constraints for FG, FHD, and GP are given by

$$\begin{cases} p^i_{fu,min} \le p^{i,T}_{fu} \le p^i_{fu,\max}, \\ h^i_{fu,min} \le h^{i,T}_{fu} \le h^i_{fu,\max}, \\ g^i_{gas,min} \le g^{i,T}_{gas} \le g^i_{gas,\max}, \end{cases} \tag{2}$$

where the superscripts "*min*" and "*max*" indicate the respective minimum and maximum permissible values.

2) Forecasting error-adjusted confidence constraints for RG and RHD are given by

$$\begin{cases} p^{i,T}_{re,\min} \le p^{i,T}_{re} \le p^{i,T}_{re,\max}, \\ h^{i,T}_{re,\min} \le h^{i,T}_{re} \le h^{i,T}_{re,\max}, \end{cases} \tag{3}$$

3) The operational feasibility region of CHO is composed of four linear inequality constraints defined as

$$\ell^1_{i,m} p^{i,T}_{chp} + \ell^2_{i,m} h^{i,T}_{chp} + \ell^3_{i,m} \ge 0, \ m = 1,2,3,4, \tag{4}$$

where $\ell^1_{i,m}$, $\ell^2_{i,m}$, and $\ell^3_{i,m}$ are the parameters.

4) Consideration of permissible charging/discharging processes and accumulated energy for ES and HS is given by

$$\begin{cases} -p^i_{ch,\max} \le p^{i,T}_{st} \le p^i_{ds,\max} \\ -h^i_{ch,\max} \le h^{i,T}_{st} \le h^i_{ds,\max} \\ SOC^{i,T}_p = SOC^{i,T-1}_p - p^{i,T-1}_{st}\Delta T \\ SOC^{i,T}_h = SOC^{i,T-1}_h - h^{i,T-1}_{st}\Delta T \\ SOC^{i,T}_{p,\min} \le SOC^{i,T}_p \le SOC^{i,T}_{p,\max} \\ SOC^{i,T}_{h,\min} \le SOC^{i,T}_h \le SOC^{i,T}_{h,\max} \end{cases}, \tag{5}$$

where $p^i_{ch,\max}$ and $p^i_{ds,\max}$ refer to the peak charging and discharging speeds of $p^{i,T}_{st}$. $h^i_{ch,\max}$ and $h^i_{ds,\max}$ refer to the peak charging and discharging speeds of $h^{i,T}_{st}$. $SOC^{i,T}_p$ and $SOC^{i,T}_h$ refer to the state of charge of ES and HS, respectively.

5) Restrictions on energy loads and associated proportions are given by

$$\begin{cases} 0 \le l^{i,T}_{p,c} + l^{i,T}_{p,m} \le l^{i,T}_{p,\max} \\ 0 \le l^{i,T}_{h,c} + l^{i,T}_{h,m} \le l^{i,T}_{h,\max} \\ 0 \le l^{i,T}_{g,c} + l^{i,T}_{g,m} \le l^{i,T}_{g,\max} \\ \Gamma^i_{g-p,\min} \le \dfrac{l^{i,T}_{p,c}}{l^{i,T}_{p,c} + \lambda l^{i,T}_{g,m}} \le \Gamma^i_{g-p,\max} \\ \Gamma^i_{g-h,\min} \le \dfrac{l^{i,T}_{h,c}}{l^{i,T}_{h,c} + \lambda l^{i,T}_{g,m}} \le \Gamma^i_{g-h,\max} \\ \Gamma^i_{h-p,\min} \le \dfrac{l^{i,T}_{p,c}}{l^{i,T}_{p,c} + l^{i,T}_{h,m}} \le \Gamma^i_{h-p,\max} \end{cases}, \tag{6}$$

where Γ^i_{g-p}, Γ^i_{g-h}, and Γ^i_{h-p} represent the respective fractions of electrical, thermal, and combined energy loads. The coefficient λ converts SCM/h to MW.

Next, the calculation of benefits for each individual EB, which directs optimal operational behavior, encompasses the following six components:

1) Derived from fuel costs, the FG and FHD cost functions, along with CHP, are expressed as

$$C\left(p^{i,T}_{fu}\right) = a^i_{p,fu}\left(p^{i,T}_{fu}\right)^2 + b^i_{p,fu}p^{i,T}_{fu} + c^i_{p,fu} + \varepsilon^i_{p,fu}\exp\left(\xi^i_{p,fu}p^{i,T}_{fu}\right), \tag{7}$$

$$C\left(h^{i,T}_{fu}\right) = a^i_{h,fu}\left(h^{i,T}_{fu}\right)^2 + b^i_{h,fu}h^{i,T}_{fu} + c^i_{h,fu} + \varepsilon^i_{h,fu}\exp\left(\xi^i_{h,fu}h^{i,T}_{fu}\right), \tag{8}$$

$$C\left(p^{i,T}_{chp}, h^{i,T}_{chp}\right) = a^i_{chp}\left(p^{i,T}_{chp}\right)^2 + b^i_{chp}p^{i,T}_{chp} + d^i_{chp}p^{i,T}_{chp}h^{i,T}_{chp} + e^i_{chp}\left(h^{i,T}_{chp}\right)^2 + f^i_{chp}h^{i,T}_{chp} + c^i_{chp}, \tag{9}$$

where $C(p^{i,T}_{fu})$, $C(h^{i,T}_{fu})$, and $C(p^{i,T}_{chp}, h^{i,T}_{chp})$ are the cost functions of FG, FHD, and CHP, respectively. $a^i_{p,fu}$, $b^i_{p,fu}$, $c^i_{p,fu}$, $\varepsilon^i_{p,fu}$, $\xi^i_{p,fu}$, $a^i_{h,fu}$, $b^i_{h,fu}$, $c^i_{h,fu}$, $\varepsilon^i_{h,fu}$, $\xi^i_{h,fu}$, a^i_{chp}, b^i_{chp}, c^i_{chp}, d^i_{chp}, e^i_{chp}, and f^i_{chp} are the positive cost coefficients.

2) When contemplating the balance between optimality and generative likelihood, the cost functions of RG and RHD are

$$C\left(p_{re}^{i,T}\right) = a_{p,re}^{i} p_{re}^{i,T} + b_{p,re}^{i} \exp\left(\xi_{p,re}^{i} \frac{P_{re,\max}^{i,T} - P_{re}^{i,T}}{P_{re,\max}^{i,T} - P_{re,\min}^{i,T}}\right), \tag{10}$$

$$C\left(h_{re}^{i,T}\right) = a_{h,re}^{i} h_{re}^{i,T} + b_{h,re}^{i} \exp\left(\xi_{h,re}^{i} \frac{h_{re,\max}^{i,T} - h_{re}^{i,T}}{h_{re,\max}^{i,T} - h_{re,\min}^{i,T}}\right), \tag{11}$$

where $C(p_{re}^{i,T})$ and $C(h_{re}^{i,T})$ are the cost functions of RG and RHD, respectively. $a_{p,re}^{i}$, $b_{p,re}^{i}$, $\xi_{p,re}^{i}$, $a_{h,re}^{i}$, $b_{h,re}^{i}$, and $\xi_{h,re}^{i}$ are the positive cost coefficients.

3) The cost functions of ES and HS can be represented as

$$C\left(p_{st}^{i,T}\right) = a_{p,st}^{i,T}\left(p_{st}^{i,T} + b_{p,st}^{i,T}\right)^2, \tag{12}$$

$$C\left(h_{st}^{i,T}\right) = a_{h,st}^{i,T}\left(h_{st}^{i,T} + b_{h,st}^{i,T}\right)^2, \tag{13}$$

where $C(p_{st}^{i,T})$ and $C(h_{st}^{i,T})$ are the cost functions ES and HS, respectively. $a_{p,st}^{i,T}$, $b_{p,st}^{i,T}$, $a_{h,st}^{i,T}$, and $b_{h,st}^{i,T}$ are the positive cost coefficients.

4) The expression of GP's cost function is

$$C\left(g_{gas}^{i,T}\right) = a_{g}^{i}\left(g_{gas}^{i,T}\right)^3 + b_{g}^{i}\left(g_{gas}^{i,T}\right)^2 + d_{g}^{i} g_{gas}^{i,T} + c_{g}^{i}, \tag{14}$$

where $C(g_{gas}^{i,T})$ is the cost function of GP. a_{g}^{i}, b_{g}^{i}, c_{g}^{i}, and d_{g}^{i} are the positive cost coefficients. Since the gas generation is non-native, Eq. 14 is convex within the operation region, where $g_{gas}^{i,T} \geq 0$.

5) With demand response in focus, the energy load's utility function is

$$\begin{aligned} U\left(l_{p,c}^{i,T}, l_{h,c}^{i,T}, l_{g,c}^{i,T}\right) = & -\alpha_{p}^{i}\left(l_{p,m}^{i,T} + l_{p,c}^{i,T}\right)^2 + \beta_{p}^{i}\left(l_{p,m}^{i,T} + l_{p,c}^{i,T}\right) \\ & -\alpha_{h}^{i}\left(l_{h,m}^{i,T} + l_{h,c}^{i,T}\right)^2 + \beta_{h}^{i}\left(l_{h,m}^{i,T} + l_{h,c}^{i,T}\right) \\ & -\alpha_{g}^{i}\left(l_{g,m}^{i,T} + l_{g,c}^{i,T}\right)^2 + \beta_{g}^{i}\left(l_{g,m}^{i,T} + l_{g,c}^{i,T}\right), \end{aligned} \tag{15}$$

where $U(l_{p,c}^{i,T}, l_{h,c}^{i,T}, l_{g,c}^{i,T})$ is the utility function. α_{p}^{i}, β_{p}^{i}, α_{h}^{i}, β_{h}^{i}, α_{g}^{i}, and β_{g}^{i} are the positive utility coefficients.

The reasons for why we chose the second-order form of the load utility function are as follows: first, the second-order utility function provides a more accurate representation of user satisfaction in scenarios where it is not just the service itself but the rate of change in service quality that impacts user perception. Second, the second-order utility function provides the flexibility needed to model various user behaviors and preferences under different conditions. Third, this form of utility function offers a good balance between complexity and analytical tractability. It allows us to derive meaningful insights and results without overly complicating the mathematical framework.

2.2 Model of EMP

The overall objective of EMP of IES is to maximize the social welfare. Its mathematical expression is given by

$$\begin{aligned} Max \quad W = & U\left(l_{p,c}^{i,T}, l_{h,c}^{i,T}, l_{g,c}^{i,T}\right) - C\left(p_{fu}^{i,T}\right) - C\left(h_{fu}^{i,T}\right) - C\left(p_{chp}^{i,T}, h_{chp}^{i,T}\right) - C\left(p_{re}^{i,T}\right) \\ & - C\left(h_{re}^{i,T}\right) - C\left(p_{st}^{i,T}\right) - C\left(h_{st}^{i,T}\right) - C\left(g_{gas}^{i,T}\right), \end{aligned} \tag{16}$$

$$s.t. \begin{cases} \sum_{i=1}^{n}\left(p_{re}^{i,T} + p_{fu}^{i,T} + p_{chp}^{i,T} + p_{st}^{i,T} - l_{p,m}^{i,T} - l_{p,c}^{i,T}\right) = 0 \\ \sum_{i=1}^{n}\left(h_{re}^{i,T} + h_{fu}^{i,T} + h_{chp}^{i,T} + h_{st}^{i,T} - l_{h,m}^{i,T} - l_{h,c}^{i,T}\right) = 0 \\ \sum_{i=1}^{n}\left(g_{gas}^{i,T} - l_{g,m}^{i,T} - l_{g,c}^{i,T}\right) = 0 \\ equations\ (2-6) \end{cases}. \tag{17}$$

For the sake of analysis, we stipulate that the three-dimensional vector x^{ij} represents the power, heat, and gas attributes of the ith member in the ith EB. It is pertinent to mention that based on the specific traits of the participant, some of these elements might be zero. Furthermore, we characterize l_{m}^{ij} as a tri-dimensional vector denoting the power, heat, and gas of the jth indispensable energy load in the ith EB. Each member can modify its variable to resemble x^{ij} by ensuring that the maximum and minimum constraints of any zero component are set to zero. Concurrently, any cost function linked with the zero component(s) can be designated as any type of robustly convex function. We then introduce $f(x^{ij})$ to symbolize the associated cost function or adverse utility function. Then, the studied problem Eqs 16, 17) can be equivalently written as

$$\min \quad f = \sum_{i=1}^{n}\sum_{j=1}^{m_i} f\left(x^{ij}\right), \tag{18}$$

$$s.t. \begin{cases} \sum_{i=1}^{n}\sum_{j=1}^{m_i}\left(B^{ij}x^{ij} - l_{m}^{ij}\right) = 0 \\ x^{ij} \in \Omega^{ij} \end{cases}, \tag{19}$$

where m_i refers to the number of participants in ith EB. $B^{ij} = -1$ when x^{ij} signifies the controllable energy load. In all other cases, $B^{ij} = 1$. Ω^{ij} refers to the closed convex sets defined by the intrinsic inequality constraints.

Note that the cost function for each component is the convex function within the corresponding local operation region. Meanwhile, the global supply and demand constraint shown in Eq. 19 is the affine function. Thus, our studied problem is a convex problem. According to the convex theory, there is only one optimal point. Thus, in our considered model, there exists only one equilibrium point, which is the optimal point.

3 Attack-resilient distributed energy management strategy

3.1 Attack models

This study delves into the utilization of a distributed algorithm to address EMP. As the operational framework of such algorithms is deeply rooted in a distributed communication network, it becomes inherently vulnerable to diverse cyberattacks. In this paper, we consider data integrity and DoS attacks. The major mechanisms affected by the two types of cyberattacks on EMP are as follows:

1) Data integrity attacks in energy management algorithms refer to cyberattacks where adversaries manipulate or tamper with the data being used by these algorithms, leading to faulty decision-making. Energy management systems rely on accurate data to efficiently control and distribute energy

resources. By compromising the integrity of these data, attackers can cause operational inefficiencies, financial losses, system instabilities, and even safety hazards.

2) DoS attacks, in the context of computer networks, refer to attempts to make a machine, service, or network resource unavailable to its intended users by flooding the targeted system with superfluous requests in an effort to overload systems and prevent some or all legitimate requests from being fulfilled. The potential disruption by multiple adversaries targeting the communication flow between EBs is recognized, which can lead to an enduring compromise of essential shared data.

In order to divide the attack and non-attack zones, we provide the following definitions: Starting at a reference point T_0, the cumulative time span $[T_0, T]$ is bifurcated into regular intervals and periods of assault. The duration representing the kth attack is denoted as $(T_k, T_k + \sigma_k]$, wherein T_k signifies the moment the attack is initiated and σ_k denotes its persistence. The fraction of the overall time occupied by attacks within the interval $[T_0, T]$ is represented by $\Phi_{ap}(T) = \sum_{\forall k} \sigma_k / (T - T_0)$. Following this, the classification of time spans into attack and non-attack segments is expressed as $\Pi_{ap}(T) = \sqcup (T_k, T_k + \sigma_k] \cap [T_0, T]$ and $\Pi_{np}(T) = \sqcup (T_k + \sigma_k, T_{k+1}] \cap [T_0, T]$, respectively. When a node i experiences a DoS attack or data integrity, it is classified as an attack node. Such nodes fall under the category represented by $\wp_s(T)$.

3.2 Directed communication network

We study a directional communication network, represented by $G = (V, \xi, A)$. In this context, $V = [1, 2, \ldots, n]$ signifies the group of agents, and ξ encompasses a subset of pairs in $V \times V$, indicating the edges or communication links. The graph G is assumed to be robustly interconnected without any self-linking edges. For an edge originating from node $i\bar{j}$ and terminating at ij, i is represented by $(ij, i\bar{j}) \in \xi$. The adjacency matrix is denoted by $A = [a_{ij,i\bar{j}}]$, where $a_{ij,i\bar{j}} = 1$ if $(ij, i\bar{j}) \in \xi$ is an edge; otherwise, $a_{ij,i\bar{j}} = 0$. The in-degree matrix is expressed as $D^{in} = diag[d_1^{in}, d_2^{in}, \ldots, d_n^{in}]$, where d_i^{in} is the sum of $a_{ij,i\bar{j}}$ over all $i\bar{j}$ except when $i\bar{j} = ij$. Similarly, the out-degree matrix is depicted as $D^{out} = diag[d_1^{out}, d_2^{out}, \ldots, d_n^{out}]$, with d_i^{out} being the sum of $a_{i\bar{j}}$ across all $i\bar{j}$ with the exception of $i\bar{j} = ij$. Moreover, we have $L' = D^{out} - A$ and $L = D - A$. The in-neighbor of ij is defined as N_{in}^{ij}. In this paper, we require that the communication network be strongly connected during the non-attack segment. In addition, there is no limitation on the communication network during the attack segment.

3.3 Main algorithm

In this section, we propose a discrete-time attack-resilient distributed energy management algorithm to solve EMP, considering data integrity and DoS attacks. First, we define the following switched control variables:

$$v_1^{ij}[t-1] = \begin{cases} z^{ij}[t-1], t \in \Pi_{np}(T) \\ z^{ij}[T_k], t \in \Pi_{np}(T) \& ij \in \wp_s(T) \\ z^{ij}[t-1], t \in \Pi_{np}(T) \& ij \notin \wp_s(T) \end{cases}, \tag{20}$$

$$v_2^{ij}[t-1] = \begin{cases} -\sum_{i\bar{j} \in N_{in}^{ij}} a_{ij,i\bar{j}} \left(z^{ij}[t-1] - z^{i\bar{j}}[t-1] \right), t \in \Pi_{np}(T) \\ -\sum_{i\bar{j} \in N_{in}^{ij}} a_{ij,i\bar{j}} \left(z^{ij}[T_k] - z^{i\bar{j}}[T_k] \right), t \in \Pi_{np}(T) \& ij \in \wp_s(T) \\ -\sum_{i\bar{j} \in N_{in}^{ij}} a_{ij,i\bar{j}} \left(z^{ij}[t-1] - z^{i\bar{j}}[t-1] \right), t \in \Pi_{np}(T) \& ij \notin \wp_s(T) \end{cases}, \tag{21}$$

$$v_3^{ij}[t-1] = \begin{cases} -\sum_{i\bar{j} \in N_{in}^{ij}} a_{ij,i\bar{j}} \left(w^{ij}[t-1] - w^{i\bar{j}}[t-1] \right), t \in \Pi_{np}(T) \\ -\sum_{i\bar{j} \in N_{in}^{ij}} a_{ij,i\bar{j}} \left(w^{ij}[T_k] - w^{i\bar{j}}[T_k] \right), t \in \Pi_{np}(T) \& ij \in \wp_s(T) \\ -\sum_{i\bar{j} \in N_{in}^{ij}} a_{ij,i\bar{j}} \left(w^{ij}[t-1] - w^{i\bar{j}}[t-1] \right), t \in \Pi_{np}(T) \& ij \notin \wp_s(T) \end{cases}, \tag{22}$$

where z^{ij} and w^{ij} are assistant variables. v_1^{ij}, v_2^{ij}, and v_3^{ij} are control variables. The physical meaning of z^{ij} is the energy price, while w^{ij} does not have specific physical meaning.

Next, the updating rules of the discrete-time attack-resilient distributed energy management algorithm are given by

$$x^{ij}[t] = diag[\nabla^2 f(x^{ij}[t-1])]^{-1} \Theta_{\Omega^{ij}} \left(x^{ij}[t-1], -\nabla f(x^{ij}[t-1]) + v_1^{ij}[t-1] \right), \tag{23}$$

$$z^{ij}[t] = v_2^{ij}[t-1] + v_3^{ij}[t-1] - x^{ij}[t-1] + l_m^{ij}, \tag{24}$$

$$w^{ij}[t] = -v_2^{ij}[t-1], \tag{25}$$

where $\Theta_{\Omega^{ij}}$ refers to the differential projection operation.

We elaborate the updating processes, including the following steps:

Step (1) Each agent tries to send the information of $z^{ij}[t-1]$ and $w^{ij}[t-1]$ to its out-neighbors and receive information of $z^{i\bar{j}}[t-1]$ and $w^{i\bar{j}}[t-1]$ from its neighbors.

Step (2) Each agent should identify whether it is subjected to data integrity attacks and DoS attacks based on the methods proposed in Li T. et al. (2022) and Huang et al. (2022), respectively. Then, each agent is able to identify the current categories for $t \in \Pi_{np}(T)$, $t \in \Pi_{np}(T) \& ij \in \wp_s(T)$, or $t \in \Pi_{np}(T) \& ij \notin \wp_s(T)$.

Step (3) Each agent updates $v_1^{ij}[t-1]$, $v_2^{ij}[t-1]$, and $v_3^{ij}[t-1]$ based on Eqs 20–22.

Step (4) Each agent updates $x^{ij}[t]$, $z^{ij}[t]$, and $w^{ij}[t]$ based on Eqs 23–25.

Step (5) Repeat Steps (1–4) until the algorithm converges to stable values.

Based on the aforementioned processes, it can be observed that each agent only needs to share the information of $z^{ij}[t-1]$ and $w^{ij}[t-1]$ with its neighbors. Thus, the proposed method is fully distributed. In addition, we employ the switched strategy, as shown in Eqs 20–22, to resist the cyberattacks.

In this paper, we design a discrete-time algorithm to solve EMP. The reasons are as follows: first, by using the discrete-time algorithm, agents are executed at discrete time steps, making it easier to synchronize information sharing across distributed agents. This is particularly useful in IES, where coordinating the timing of operations is crucial. Second, discrete-time algorithms can be more resource-efficient in certain contexts. They can be designed to operate only at specific intervals, reducing the need for continuous computation and potentially saving on energy and computational resources. Last but not least, discrete-time

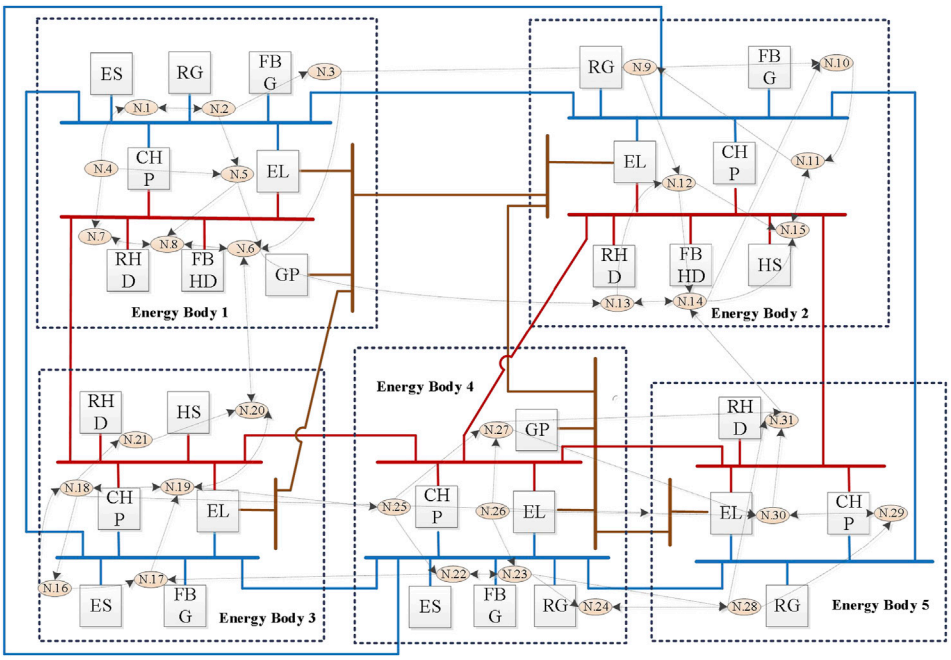

FIGURE 1
IES composed of five EBs.

algorithms offer flexibility in implementation, especially in digital systems where time is naturally discretized. This makes them well-suited for implementation in digital computers and microcontrollers.

4 Simulation analysis

4.1 Setting of the test system

The effectiveness of the proposed method will be tested in IES with five EBs. Its physical and communication structures are shown in Figure 1, as described previously in Zhang et al. (2017). We also follow Zhang et al. (2017) to set the parameters of each EB. The communication interval is 0.01 s. We consider that the system is subjected to data integrity attacks during [0.40 s, 0.66 s] and [2.3 s, 2.55 s] and is subjected to DoS attacks during [6.1 s, 6.2 s] and [11.1 s, 11.12 s]. The scales of energy and price are unified as 1 p.u. = 1 MW for power or heat, 1 p.u. = 84 SCM/h for gas, and 1 p.u. = 1 $/MWh for price.

4.2 Convergence analysis

In this section, the proposed attack-resilient distributed energy management algorithm is performed to solve EMP. The simulation outcomes are shown in Figures 2–7.

Specifically, Figures 2–4 exhibit the estimated calculations for power generation/demand, heat generation/demand, and gas generation/demand across all participating entities. Distinct colors within each graph are employed to differentiate between the various curves, each representing computational and

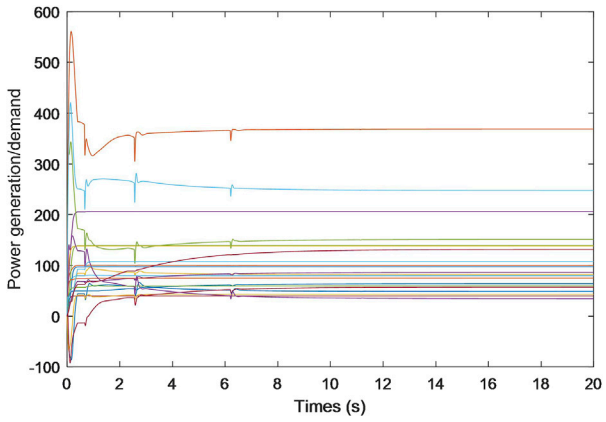

FIGURE 2
Power generation/demand.

convergence trajectory of each participant. These visual representations indicate that despite the data integrity and DoS attacks, the energy generation/demand (encompassing power, heat, and gas) for every participant is capable of stabilizing at a consistent value.

Additionally, the trajectories for the estimated prices of power, heat, and gas are shown in Figures 5–7, each progressively settling at three common values, ultimately representing the final market clearing prices for power, heat, and gas, respectively. This occurrence persists even in the face of data integrity and DoS attacks. The final settled values are marked at $32.6887 (p.u.) for the power price, $23.6611 (p.u.) for the heat price, and $15.2825 (p.u.) for the gas price. In addition, the final energy generation and

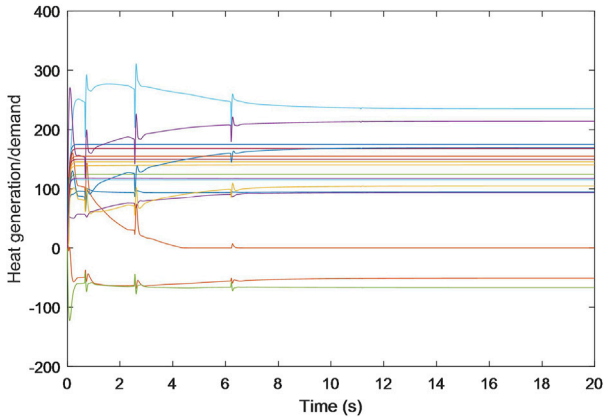

FIGURE 3
Heat generation/demand.

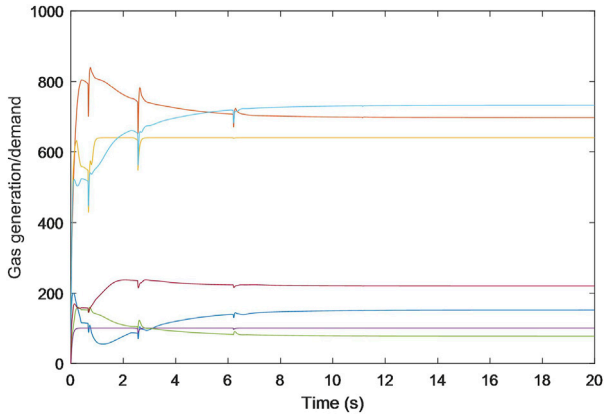

FIGURE 4
Gas generation/demand.

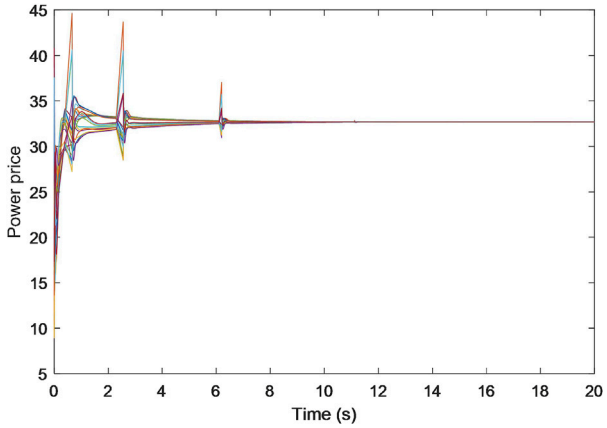

FIGURE 5
Power price.

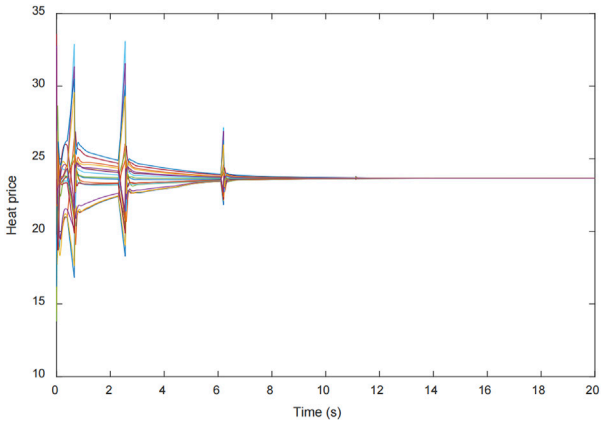

FIGURE 6
Heat price.

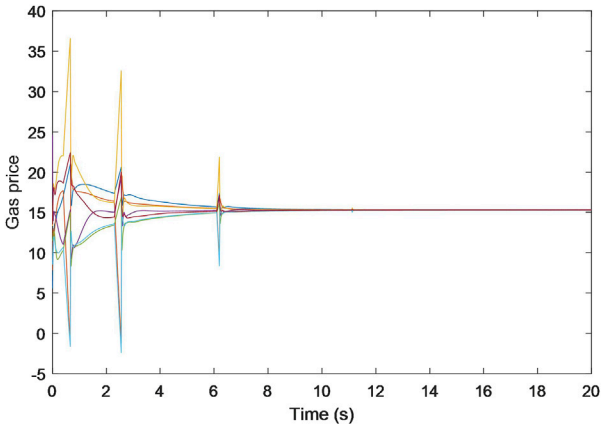

FIGURE 7
Gas price.

demands are listed in Table 1. These values are consistent with those derived in scenarios devoid of attacks, as referenced from Zhang et al. (2017).

These findings collectively underscore the resilience and robustness of the S-NRBDEM algorithm, affirming its capacity to empower each participant to persistently seek optimal operational states and market clearing prices for energy.

5 Discussion

This paper addresses the pressing need for resilient energy management in the context of IESs; this necessity has become even more urgent due to the ever increasing integration of diverse energy resources and the rapid adoption of IES technologies. Through rigorous investigation and analysis, we have introduced and validated an attack-resilient distributed energy management strategy, augmented by a local estimation

TABLE 1 Results of energy generation/demand.

	Number	Power	Heat	Gas
Energy body 1	N. 1	48.7268	0.0000	0.0000
	N. 2	99.9954	0.0000	0.0000
	N. 3	81.9283	0.0000	0.0000
	N. 4	205.9112	175.0624	0.0000
	N. 5	150.9604	0.0000	151.1224
	N. 6	0.0000	0.0000	697.1795
	N. 7	0.0000	140.4003	0.0000
	N. 8	0.0000	93.8493	0.0000
Energy body 2	N. 1	79.8125	0.0000	0.0000
	N. 2	40.0000	0.0000	0.0000
	N. 3	97.5581	124.7394	0.0000
	N. 4	368.7103	234.9918	640.0000
	N. 5	0.0000	149.9000	0.0000
	N. 6	0.0000	94.9337	0.0000
	N. 7	0.0000	−50.9576	0.0000
Energy body 3	N. 1	43.0000	0.0000	0.0000
	N. 2	86.3169	0.0000	0.0000
	N. 3	139.1635	145.6757	0.0000
	N. 4	247.9710	214.2603	100.0000
	N. 5	0.0000	−66.9455	0.0000
	N. 6	0.0000	115.3432	0.0000
Energy body 4	N. 1	57.3021	0.0000	0.0000
	N. 2	63.8647	0.0000	0.0000
	N. 3	74.8888	0.0000	0.0000
	N. 4	137.9980	168.0150	0.0000
	N. 5	34.6087	169.6301	77.3927
	N. 6	0.0000	0.0000	731.8678
Energy body 5	N. 1	59.7180	0.0000	0.0000
	N. 2	107.4698	155.1541	0.0000
	N. 3	131.4040	104.8088	220.5323
	N. 4	0.0000	117.5203	0.0000

mechanism and switched control. This strategy has been meticulously designed to address not only data integrity attacks but also DoS attacks. The simulations conducted in IES with five EBs show that our proposed method enables estimated energy prices and energy generation/demand to converge to the corresponding optimal solutions, although there are both data integrity attacks and DoS attacks. The findings and insights garnered from this case study underscore the potential of our proposed strategy to serve as a reliable safeguard against cyber–physical threats, ensuring uninterrupted and secure energy management.

Data availability statement

The original contributions presented in the study are included in the article/Supplementary Material; further inquiries can be directed to the corresponding author.

Author contributions

TL: methodology, validation, and writing–original draft. FS: conceptualization, investigation, and writing–original draft. JC: formal analysis, validation, and writing–original draft. LW: conceptualization, formal analysis, and writing–original draft. ZY: formal analysis, project administration, and writing–review and editing. RL: data curation and writing–review and editing. JQ: writing–original draft and writing–review and editing.

Funding

The author(s) declare that financial support was received for the research, authorship, and/or publication of this article. This work was supported by the Science and Technology Project of Electric Power Research Institute of State Grid Liaoning Electric Power Supply Co., Ltd. and Research on Network Security Risk Analysis and Attack Recovery Strategies for Integrated Energy Information Systems Facing the Distribution Network Side (2023YF-155).

Conflict of interest

Authors TL, FS, JC, ZY, and RL were employed by Electric Power Research Institute of State Grid Liaoning Electric Power Co., Ltd. Author LW was employed by State Grid Liaoning Electric Power Supply Co., Ltd.

The author declares that the research was conducted in the absence of any commercial or financial relationships that could be construed as a potential conflict of interest.

Publisher's note

All claims expressed in this article are solely those of the authors and do not necessarily represent those of their affiliated organizations, or those of the publisher, the editors, and the reviewers. Any product that may be evaluated in this article, or claim that may be made by its manufacturer, is not guaranteed or endorsed by the publisher.

References

Duan, J., and Chow, M. Y. (2019). A novel data integrity attack on consensus-based distributed energy management algorithm using local information. *IEEE Trans. Industrial Inf.* 15 (3), 1544–1553. doi:10.1109/TII.2018.2851248

Huang, B., Li, Y., Zhan, F., Sun, Q., and Zhang, H. (2022). A distributed robust economic dispatch strategy for integrated energy system considering cyber-attacks. *IEEE Trans. Industrial Inf.* 18 (2), 880–890. doi:10.1109/TII.2021.3077509

Lee, S., and Choi, D. H. (2022). Federated reinforcement learning for energy management of multiple smart homes with distributed energy resources. *IEEE Trans. Industrial Inf.* 18 (1), 488–497. doi:10.1109/TII.2020.3035451

Li, P., Liu, Y., Xin, H., and Jiang, X. (2018). A robust distributed economic dispatch strategy of virtual power plant under cyber-attacks. *IEEE Trans. Industrial Inf.* 14 (10), 4343–4352. doi:10.1109/TII.2017.2788868

Li, T., Chen, L., Jensen, C. S., and Pedersen, T. B. (2021a). TRACE: real-time compression of streaming trajectories in road networks. *Proc. VLDB Endow.* 14 (7), 1175–1187. doi:10.14778/3450980.3450987

Li, T., Chen, L., Jensen, C. S., Pedersen, T. B., Gao, Y., and Hu, J. (2022a). "Evolutionary clustering of moving objects," in 2022 IEEE 38th International Conference on Data Engineering, Kuala Lumpur, Malaysia, 09-12 May 2022, 2399–2411.

Li, T., Huang, R., Chen, L., Jensen, C. S., and Pedersen, T. B. (2020b). Compression of uncertain trajectories in road networks. *Proc. VLDB Endow.* 13 (7), 1050–1063. doi:10.14778/3384345.3384353

Li, Y., Gao, D. W., Gao, W., Zhang, H., and Zhou, J. (2020a). Double-mode energy management for multi-energy system via distributed dynamic event-triggered Newton-raphson algorithm. *IEEE Trans. Smart Grid* 11 (6), 5339–5356. doi:10.1109/TSG.2020.3005179

Li, Y., Gao, D. W., Gao, W., Zhang, H., and Zhou, J. (2021b). A distributed double-Newton descent algorithm for cooperative energy management of multiple energy bodies in energy internet. *IEEE Trans. Industrial Inf.* 17 (9), 5993–6003. doi:10.1109/TII.2020.3029974

Li, Y., Li, T., Zhang, H., Xie, X., and Sun, Q. (2022b). Distributed resilient double-gradient-descent based energy management strategy for multi-energy system under dos attacks. *IEEE Trans. Netw. Sci. Eng.* 9 (4), 2301–2316. doi:10.1109/TNSE.2022.3162669

Li, Y., Zhang, H., Liang, X., and Huang, B. (2019). Event-Triggered-based distributed cooperative energy management for multienergy systems. *IEEE Trans. Industrial Inf.* 15 (4), 2008–2022. doi:10.1109/TII.2018.2862436

Liu, Z., Huang, B., Hu, X., Du, P., and Sun, Q. (2023). Blockchain-based renewable energy trading using information entropy theory. *IEEE Trans. Netw. Sci. Eng.*, 1–12. doi:10.1109/TNSE.2023.3238110

Liu, Z., Xu, Y., Zhang, C., Elahi, H., and Zhou, X. (2022). A blockchain-based trustworthy collaborative power trading scheme for 5G-enabled social internet of vehicles. *Digital Commun. Netw.* 8 (6), 976–983. doi:10.1016/j.dcan.2022.10.014

Mellal, M. A., and Williams, E. J. (2020). Cuckoo optimization algorithm with penalty function and binary approach for combined heat and power economic dispatch problem. *Energy Rep.* 6, 2720–2723. doi:10.1016/j.egyr.2020.10.004

Sun, Q., Fan, R., Li, Y., Huang, B., and Ma, D. (2019). A distributed double-consensus algorithm for residential we-energy. *IEEE Trans. Industrial Inf.* 15 (8), 1–4842. doi:10.1109/TII.2019.2921431

Teng, F., Zhang, Y., Yang, T., Li, T., Xiao, Y., and Li, Y. (2023). Distributed optimal energy management for we-energy considering operation security. *IEEE Trans. Netw. Sci. Eng.*, 1–11. doi:10.1109/TNSE.2023.3295079

Xu, D., Wu, Q., Zhou, B., Li, C., Bai, L., and Huang, S. (2020). Distributed multi-energy operation of coupled electricity, heating, and natural gas networks. *IEEE Trans. Sustain. Energy* 11 (4), 2457–2469. doi:10.1109/TSTE.2019.2961432

Yang, L., Sun, Q., Zhang, N., and Li, Y. (2022). Indirect multi-energy transactions of energy internet with deep reinforcement learning approach. *IEEE Trans. Power Syst.* 37 (5), 4067–4077. doi:10.1109/TPWRS.2022.3142969

Zeng, W., Zhang, Y., and Chow, M. Y. (2017). Resilient distributed energy management subject to unexpected misbehaving generation units. *IEEE Trans. Industrial Inf.* 13 (1), 208–216. doi:10.1109/TII.2015.2496228

Zhang, H., Li, Y., Gao, D. W., and Zhou, J. (2017). Distributed optimal energy management for energy internet. *IEEE Trans. Industrial Inf.* 13 (6), 3081–3097. doi:10.1109/TII.2017.2714199

Zhang, X., Li, Y., Li, T., Gui, Y., Sun, Q., and Gao, D. W. (2023). Digital twin empowered PV power prediction. *J. Mod. Power Syst. Clean Energy*. doi:10.35833/MPCE.2023.000351

Zhang, Z., Yue, D., Dou, C., Cheng, Z., and Chen, L. (2019). A robust consensus-based economic dispatch strategy under dos attack. *IEEE Int. Conf. Industrial Cyber Phys. Syst. (ICPS)* 127–132. doi:10.1109/ICPHYS.2019.8780286

Zhao, C., He, J., Cheng, P., and Chen, J. (2017). Analysis of consensus-based distributed economic dispatch under stealthy attacks. *IEEE Trans. Industrial Electron.* 64 (6), 5107–5117. doi:10.1109/TIE.2016.2638400

Zhou, X., Ma, Z., Zou, S., Zhang, J., and Guo, Y. (2023). Distributed energy management of double-side multienergy systems via sub-gradient averaging consensus. *IEEE Trans. Smart Grid* 14 (2), 979–995. doi:10.1109/TSG.2022.3201814

frontiers | Frontiers in Energy Research

TYPE Original Research
PUBLISHED 28 March 2024
DOI 10.3389/fenrg.2024.1372612

Check for updates

OPEN ACCESS

EDITED BY
Bonan Huang,
Northeastern University, China

REVIEWED BY
Yuyang Zhou,
Edinburgh Napier University, United Kingdom
Zheng Qi,
North China Electric Power University, China
Junhui Li,
Northeast Electric Power University, China

*CORRESPONDENCE
Yun Teng,
tengyun@sut.edu.cn

RECEIVED 18 January 2024
ACCEPTED 28 February 2024
PUBLISHED 28 March 2024

CITATION
Liu S, Teng Y, Cheng S, Xu N, Sun P, Zhang K and Chen Z (2024), A cloud-edge cooperative scheduling model and its optimization method for regional multi-energy systems.
Front. Energy Res. 12:1372612.
doi: 10.3389/fenrg.2024.1372612

COPYRIGHT
© 2024 Liu, Teng, Cheng, Xu, Sun, Zhang and Chen. This is an open-access article distributed under the terms of the Creative Commons Attribution License (CC BY). The use, distribution or reproduction in other forums is permitted, provided the original author(s) and the copyright owner(s) are credited and that the original publication in this journal is cited, in accordance with accepted academic practice. No use, distribution or reproduction is permitted which does not comply with these terms.

A cloud-edge cooperative scheduling model and its optimization method for regional multi-energy systems

Shuo Liu[1], Yun Teng[1]*, SongQing Cheng[1], NingWei Xu[1], Peng Sun[1], Kun Zhang[1] and Zhe Chen[2]

[1]School of Electrical Engineering, Shenyang University of Technology, Shenyang, Liaoning, China, [2]The Faculty of Engineering and Science, Aalborg University, Aalborg, Denmark

In the process of multi-energy system optimal scheduling, due to the high data processing requirements of the multi-energy devices and loads and the complexity of the operating states of the multi-energy devices, the scheduling optimization of the system is to some extent more difficult. To address this problem, this paper proposes a regional multi-energy system optimal scheduling model based on the theory of cloud-edge collaboration. First, based on intelligent data sensors, a cloud-edge cooperative scheduling framework of the regional multi-energy system is constructed. Then, the physical model of operating state data of multi-energy system equipment and the allocation mechanism of system scheduling tasks are studied. With the cloud service application layer and the edge computing layer as the upper and lower optimization scheduling layers, the double-layer optimization scheduling model of the regional multi-energy system is established. The objectives of the model are optimal scheduling cost and minimum delay of scheduling data transmission. The multi-objective whale optimization algorithm is used to solve the model. Finally, a simulation model is built for verification. The simulation results show that the scheduling model established in this paper can effectively improve the scheduling data processing capability and improve the economy of regional multi-energy system scheduling.

KEYWORDS

regional multi-energy system, edge computing, cloud-edge collaboration, physical perception, optimized scheduling

1 Introduction

The development and operation of power grids are now focused on constructing an intelligent, informatized, and diversified new power system with new energy as the primary source, with the goal of achieving "Carbon peak and Carbon neutralization" (Teng et al., 2018). This requires higher standards for the operation, scheduling, and control of power grids, especially with the integration of a high proportion of new energy power generation resources (Teng et al., 2020). A regional multi-energy system is a complex system involving the input, conversion, and supply of electricity, heat, and gas energy. It contains various energy supply equipment. It can flexibly and reliably meet the consumption demands of users through the conversion and coordination between multiple types of energy (Zhang et al., 2017; Li et al., 2019). However, traditional centralized operation and control methods

have difficulty meeting the requirements of large-scale, high-capacity data and information processing of regional multi-energy systems (Lo and Ansari, 2013; Zhang et al., 2018). The rapid development of new intelligent control technologies, such as edge computing (Sulieman et al., 2022; Raeisi-Varzaneh et al., 2023) and IoT technologies (Abir et al., 2021; Gao et al., 2023), provides favorable conditions for promoting the coordinated and integrated development of regional multi-energy system data and information networks. This development forms new application scenarios of energy-information interaction and integration, including cloud-edge synergy, information-physical synergy, digital twins, and other new application technologies (Ren et al., 2019; Su et al., 2019). As a result, there is an urgent need to study optimized operation methods for regional multi-energy systems that can achieve flexibility, reliability and high data and information computation efficiency.

In view of the development and application prospects, some scholars have begun to research the optimization methods of intelligent and informative operation and control of regional multi-energy systems. In (Wang and Li, 2022), it focuses on the problem of short-term load forecasting of power grids. The study proposes a short-term forecasting method of power grid loads based on cloud edge collaboration. The model is trained with a large amount of historical data to provide accurate predictions. In (Luo et al., 2022), aiming at the scheduling deviation of distribution network in a long-time scale and considering the distribution characteristics of transformer equipment in the distribution network, a collaborative scheduling method of the distribution network based on cloud edge cooperation is proposed. The distribution network cooperative optimal scheduling is carried out by taking transformer equipment in different power supply areas of the distribution network as an edge layer, and the optimal scheduling cost of each transformer power supply area is targeted. This results in an improved dispatch economy for the distribution network. In (Xia et al., 2022), a hybrid model for power grid data recognition based on distributed compressed sensing and bidirectional long-short memory network is proposed to address the problem of low power quality data recognition accuracy in power grid. It optimizes the recognition parameters in the model by establishing a cloud-edge cooperative framework and using distributed compressed perception as the edge algorithm, and using a large amount of data to train the model. The improvement of grid power quality data recognition accuracy and anti-interference performance is realized. In (Liu et al., 2018), it analyzed the information architecture and optimization effect of edge computing technology when applied to the optimal scheduling of electric vehicles. The study focused on data processing and information security and proved the effectiveness of edge computing technology in meeting the real-time communication and arithmetic demands of the electric power network. In (Gooi et al., 2023), the advantages of edge computing technology in optimizing, allocating, and scheduling of smart grid resources are analyzed. Then, it explores the relationship between smart grid and artificial intelligence and proposes an optimization method for power grid cloud computing by applying edge intelligence technology. This reduces the pressure on cloud computing and improves the computing efficiency of power grid operation optimization tasks. As for the information and data security problems faced in the process of adopting intelligent technology for the optimal scheduling of power grids or energy systems, some scholars have also carried out research and discussion. In (Li et al., 2022; Li et al., 2023), it studied the collaborative energy management method of multi-energy system under DoS attack for the problems of cyber-attack faced during the energy optimization and scheduling process of multi-energy system. The information security capability for network optimization and energy management processes is enhanced, and its cyber defense resistance capability is improved. In (Huang et al., 2022), it focuses on the problem of the multi-energy system scheduling economy. The study employs a distributed robust optimization algorithm to develop a method for achieving this goal. Meanwhile, a data privacy protection protocol has been researched and designed to address network security issues encountered during the distributed optimal scheduling of the system. This protocol improves the reliability of information transmission during system scheduling and promotes the system's scheduling economy.

However, there is a lack of detailed modeling analysis and research on the integration of edge computing technology and cloud-edge collaboration technology into the optimization modeling of regional multi-energy system operation and scheduling. There is a lack of relevant research on how to better improve the efficiency of regional multi-energy system scheduling.

Based on the above analysis, this paper studies a cloud-edge cooperative optimal scheduling model of the regional multi-energy system based on edge computing. By utilizing sensors and controllers distributed at different nodes of the regional multi-energy system for collecting and sending energy equipment data and equipment operation control, a regional multi-energy system scheduling framework is established. A multi-node cloud-edge cooperative scheduling model of the regional multi-energy system is established by coordinating different edge computing scheduling layer base stations and by allocating scheduling tasks to multiple base stations. On this basis, a double-layer scheduling optimization model of the regional multi-energy system is established for optimization, and a scheduling model solution process based on multi-objective whale optimization algorithm is given. Thus, there are three main contributions to this research.

(1) A cloud-side coordinated scheduling framework of multi-node energy data information interaction for regional multi-energy systems is established in this paper. The scheduling process of the regional multi-energy system is optimized by dividing it into five service layers and configuring the corresponding computing servers in different scheduling service layers. This improves the data information processing capability of the scheduling calculation and optimization process of the system.
(2) The physical model of the regional multi-energy system is established. The operating parameters of the energy supply equipment have been preliminarily clarified, and a method for sensing the operating state data of the equipment of the multi-energy system has been studied. Further, the multi-node scheduling task allocation model of the regional multi-energy systems has been established to optimize scheduling results among the systems in the coverage area of different regional edge computing layer base stations.
(3) A double-layer optimization scheduling model of the regional multi-energy system is established, which aims at optimal

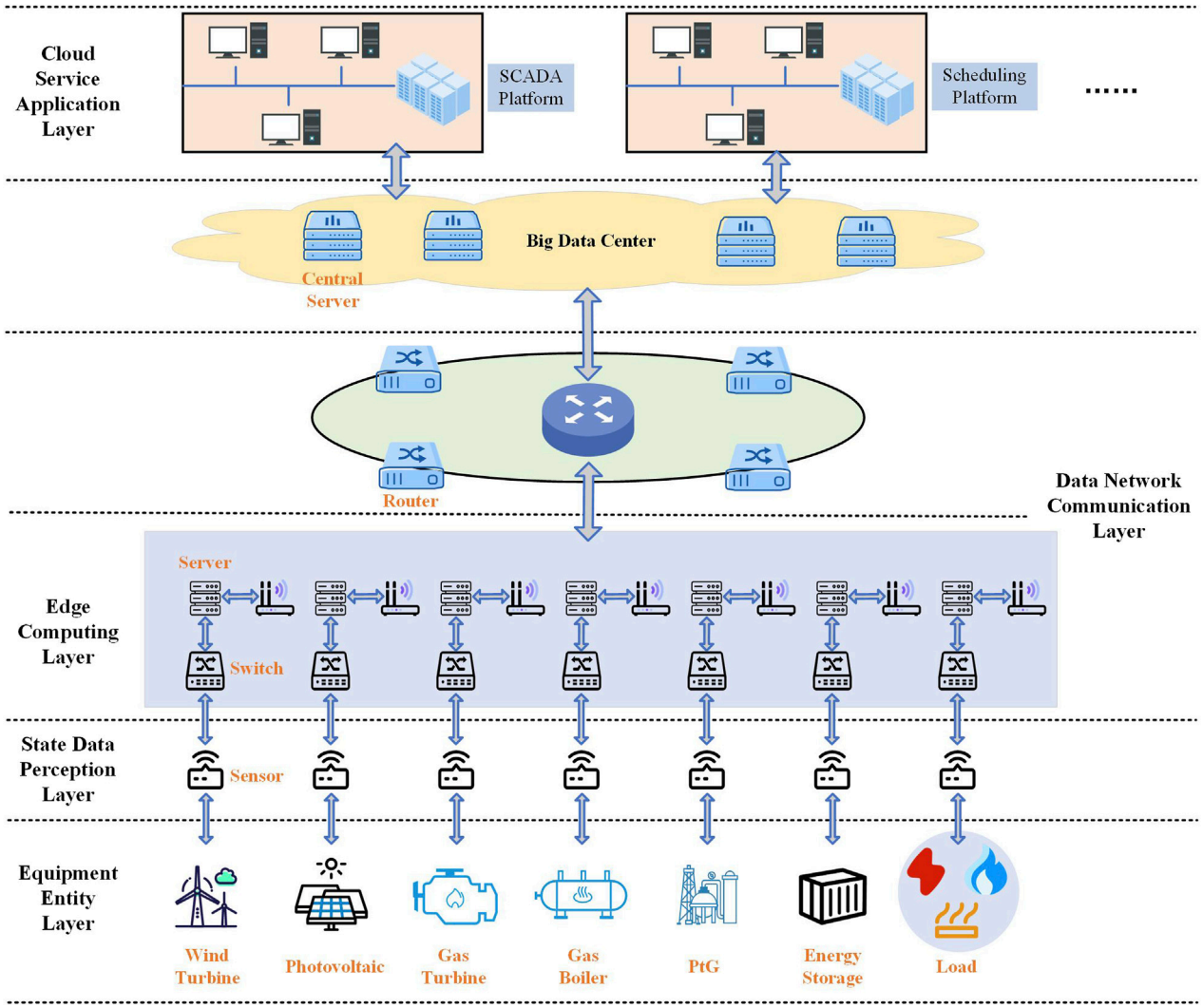

FIGURE 1
Scheduling framework of the regional multi-energy system.

operational scheduling costs and scheduling task transmission delays. The model is solved using the multi-objective whale optimization algorithm.

Finally, the feasibility and validity of the scheduling model established in this paper are analyzed and verified by obtaining the historical data of power grid operation in a region of Northeast China and building a simulation model.

2 Multi-node cloud-edge cooperative scheduling model of the regional multi-energy system

2.1 Scheduling framework of the regional multi-energy system

For the regional multi-energy system, the use of a centralized optimization scheduling method may result in increased energy consumption, scheduling costs, and network latency due to the centralized transmission, processing, computation, and distribution of distributed new energy power supply operation information and load demand information. To mitigate these issues, alternative scheduling methods should be considered. Edge computing technology makes use of various data sensors, data routing and other devices configured in the regional multi-energy system to analyze and process the collected operation information data on the side of each distributed power generation equipment. The calculation results are then transmitted to the cloud service data computing center for centralized coordination and scheduling. Based on this, this paper establishes a cloud-side coordinated scheduling framework of multi-node energy data information interaction for regional multi-energy systems, as shown in Figure 1.

The scheduling framework shown in Figure 1 is mainly composed of five scheduling service layers: equipment entity layer, state data perception layer, edge computing layer, data network communication layer, and cloud service application

layer (Ilic et al., 2010; Si et al., 2020). Computing servers are configured in the corresponding service layers to facilitate data processing, analysis, and storage.

(1) The equipment entity layer is composed of various energy equipment and equipment operation control module. The main task is to use each energy equipment to generate electricity, heat, gas and other energy supply to the consumer. Through the equipment operation control module, it controls and adjusts the operation status of energy equipment.
(2) The state data perception layer is composed of various intelligent energy data collection and measurement modules. Its main task is to assist the edge computing layer and cloud service application layer in perceiving the operating state of each energy equipment in the system.
(3) The edge computing layer is composed of edge computing modules and data storage. Its main task is to calculate the optimal operation scheme for each energy equipment in the regional energy system. This includes determining the optimal output of energy equipment, energy supply, and transaction prices.
(4) The data network communication layer is composed of data routing, wireless modules, etc., Its main task is to facilitate the communication and transmission of energy data, scheduling data, and control commands between the state data perception layer, edge computing layer, cloud service application layer, and other layers. Its goal is to ensure quick and lossless data transmission.
(5) The cloud service application layer serves as the energy management center for power generation, transmission, and supply in the regional multi-energy system. It is composed of servers and centralized scheduling centers, and its main task is to provide data storage, reading, computation, analysis, and dynamic display services for the centralized regulation and control of the regional multi-energy system. Through computation and analysis, the optimal supply scheme for a regional multi-energy system is calculated to realize the optimal scheduling of regional multi-energy system.

2.2 Physical model of the regional multi-energy system

As shown in Figure 1, the construction of the physical entity model of each energy supply equipment within the system is the basis for the optimal scheduling of the regional multi-energy system. To carry out this study, the network topology of the regional multi-energy system is established, as shown in Figure 2. The system is composed of photovoltaic cells, wind turbines, gas turbines, gas boilers, PtG equipment, and energy storage equipment. It provides electricity and heat energy to the system energy users by purchasing natural gas from the superior gas network. Part of the natural gas is directly supplied to the users through the gas network. The gas turbine and gas boiler are used to provide electricity and heat energy to the system energy users, respectively. The wind turbine and photovoltaic are used to provide electricity to users. The system

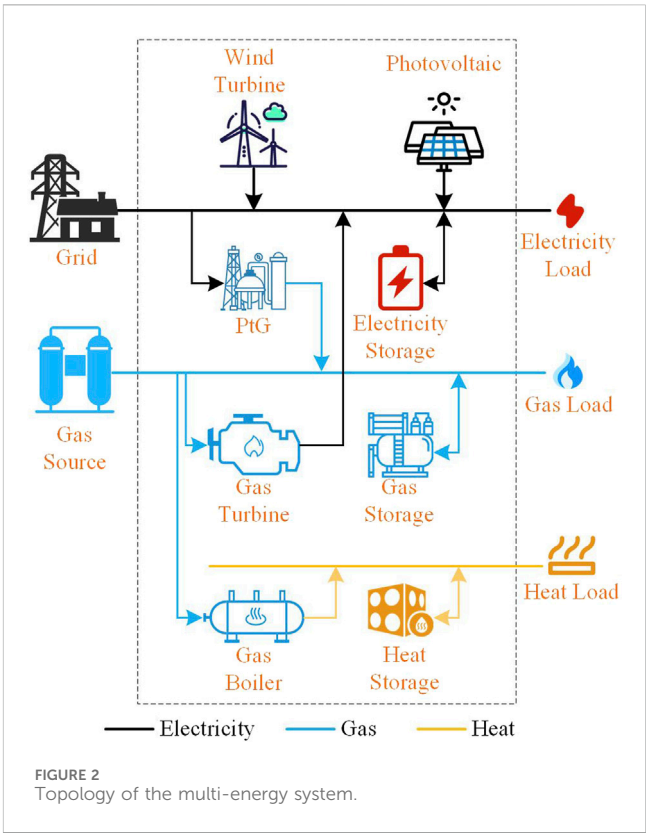

FIGURE 2
Topology of the multi-energy system.

is connected to the main power grid to compensate for any electricity shortages. The PtG equipment is used to output the gas energy to the energy users. The energy storage equipment is mainly used to regulate the input and output of various energy sources of the regional multi-energy system by charging and discharging energy.

2.2.1 Physical model of the wind turbine

Taking doubly-fed wind turbine as an example, the physical model of the wind turbine can be described by Eq. 1:

$$\begin{cases} J_{\mathrm{w}}\dot{\omega}_{\mathrm{w},t} = Q_{\mathrm{w,r}} - Q_{\mathrm{w,m}} \\ Q_{\mathrm{w,m}} = K_{\mathrm{m}}\left(\theta_{\mathrm{w,r}} - \dfrac{\theta_{\mathrm{w,g}}}{N_{\mathrm{w,g}}}\right) + B_{\mathrm{d}}\left(\omega_{\mathrm{w},t} - \dfrac{\omega_{\mathrm{w,g}}}{N_{\mathrm{w,g}}}\right) \\ Q_{\mathrm{w,r}} = 3\int_0^{R_{\mathrm{wind}}} \dfrac{1}{2}\pi\rho v_{\mathrm{w}}^3\left(C_{\mathrm{w}}^{\mathrm{u}}\sin\varphi - C_{\mathrm{w}}^{\mathrm{d}}\cos\varphi\right)R_{\mathrm{s}}r\mathrm{d}r \\ J_{\mathrm{w,g}}\dot{\omega}_{\mathrm{w,g}} = \dfrac{Q_{\mathrm{w,m}}}{N_{\mathrm{w,g}}} - Q_{\mathrm{w,e}} \\ P_{\mathrm{w},t} = Q_{\mathrm{w,r}}\omega_{\mathrm{w},t} \end{cases} \quad (1)$$

where $P_{\mathrm{w},t}$ is the output of the wind turbine at time t; $Q_{\mathrm{w,r}}$ is the torque corresponding to the force of the wind turbine blade in the rotation process; $Q_{\mathrm{w,m}}$ and $Q_{\mathrm{w,e}}$ are the input mechanical torque and the output electromagnetic torque of the unit, respectively; J_{w} is the rotational equivalent inertia of the blade; $J_{\mathrm{w,g}}$ is the rotational equivalent inertia of the wind turbine; $\omega_{\mathrm{w},t}$ and $\omega_{\mathrm{w,g}}$ are fan speed and wind turbine speed, respectively; K_{m} is the stiffness coefficient of the low-speed rotating shaft of the unit; B_{d} is the damping factor of the wind turbine; $\theta_{\mathrm{w},t}$ and $\theta_{\mathrm{w,g}}$ are the angular

velocity displacement of the wind wheel rotor and the rotational velocity displacement of the wind turbine rotor, respectively; $N_{w,g}$ is the gearbox ratio; C_w^u and C_w^d are the rising force factor and drag coefficient of fan blades when rotating, respectively; R_s is the chord length of the section at the radius r of the fan blade; ρ and v_w are the density and wind speed of the air in the operating environment, respectively; R_w is the length of the fan blade.

Therefore, there are 14 operational parameters needed to be sensed by the wind turbine, which can be expressed by Eq. 2:

$$P_{w,t} = \begin{bmatrix} v_w, \omega_{w,t}, \omega_{w,g}, \rho; C_w^u, C_w^d, \varphi; \\ K_m, B_d, \theta_{w,r}, \theta_{w,g}, N_{w,g}; R_w, R_s \end{bmatrix} \tag{2}$$

2.2.2 Physical model of the photovoltaic

The physical model of the photovoltaic cell can be described by Eq. 3:

$$\begin{cases} P_{PV,t} = \dfrac{U_{PV}^2}{R_{sh} + R_s} + I_{PV}^2 R_s \\ \begin{cases} I_{PV} = I_{ph} - I_0 \left[\exp\left(\dfrac{U_{PV} + I_{PV} R_s}{\beta k T_{PV}} \right) - 1 \right] - \dfrac{U_{PV} + I_{PV} R_s}{R_{sh}}, U_{PV} \geq 0 \\ I_{PV} = I_{ph} + I_0 - \dfrac{U_{PV} + I_{PV} R_s}{R_{sh}}, U_{br} < U_{PV} < 0 \end{cases} \end{cases} \tag{3}$$

where $P_{PV,t}$ is the output of the photovoltaic cells at time t; U_{PV} and I_{PV} are the voltage and current at both ends of the photovoltaic cells, respectively; U_{br} is the diode reverse breakdown voltage in the equivalent schematic diagram; R_s and R_{sh} are the equivalent series resistance and parallel resistance at both ends of the battery in the equivalent schematic diagram; I_{ph} is the photogenerated current of the photovoltaic cells when the illumination is Q_{PV} and the temperature is T_{PV}; I_0 is the diode equivalent reverse saturation current in the equivalent schematic diagram; $k = 1.38\ e^{-23}$ J/K; β is the fitting factor of the output characteristics of the diode inside the photovoltaic cell, which reflects the similarity between the output characteristics of the diode inside the photovoltaic cell and the output characteristics of the ideal diode.

Therefore, there are 10 physical parameters of the photovoltaic cell, which can be described by Eq. 4:

$$P_{PV,t} = \left[U_{PV}, I_{PV}, I_{ph}; U_{br}, I_0, R_s, R_{sh}; T_{PV}, \beta, Q_{PV} \right] \tag{4}$$

2.2.3 Physical model of the gas turbine

The operating status of the gas turbine is mainly limited by its operating efficiency and intake volume. The physical model of the gas turbine can be described by Eq. 5:

$$\begin{cases} P_{MGT,t} = (1+f) P_{MGT,g} - \left| P_{MGT,pa} \right| - \left| P_{MGT,gc} \right| \\ P_{MGT,g} = \eta_g c_g \left(T_{gin} - T_{gout} \right) V_{gas} \\ P_{MGT,pa} = \dfrac{c_{pa} \left(T_{pa,in} - T_{pa,out} \right)}{\eta_{pa}} V_{pa} \\ P_{MGT,gc} = \dfrac{c_g \left(T_{gc,in} - T_{gc,out} \right)}{\eta_{gc}} V'_{gas} \end{cases} \tag{5}$$

where $P_{MGT,t}$ is the output of the gas turbine at time t; $P_{MGT,g}$, $P_{MGT,pa}$, and $P_{MGT,gc}$ are the turbine output, compressed air consumption power, and compressed natural gas consumption power, respectively; f is the ratio coefficient of natural gas to air when natural gas is fed into the gas turbine; V_{gas} and V_{pa} are the gas intake and air volume of the gas turbine, respectively; V'_{gas} is the compression volume of the natural gas; c_g and c_{pa} are the specific heat capacity of natural gas and air, respectively; η_g, η_{pa}, and η_{gc} are the turbine efficiency, compressed air efficiency, and compressed natural gas efficiency of the gas turbine, respectively; T_{gin} and T_{gout} are the temperature of the gas entering the equipment and the temperature of the output equipment when the turbine is running, respectively; $T_{pa,in}$ and $T_{pa,out}$ are the inlet temperature and outlet temperature of the compressor, respectively; $T_{gc,in}$ and $T_{gc,out}$ are the inlet temperature and outlet temperature of the natural gas compressor in the gas turbine unit, respectively.

The physical parameters of the gas turbine can be described by Eq. 6:

$$P_{MGT,t} = \left[T_{gin}, T_{gout}, T_{pa,in}, T_{pa,out}, T_{gc,in}, T_{gc,out}; V_{gas}, V_{pa}, V'_{gas}; f, \eta_g, \eta_{pa}, \eta_{gc} \right] \tag{6}$$

2.2.4 Physical model of the gas boiler

The relationship between energy input-output of a gas boiler is described by Eq. 7:

$$P_{GB,t} = V_{GB,t} \eta_{GB} H_{CVNG} \tag{7}$$

where $P_{GB,t}$ is the heat output of the gas boiler at time t; $V_{GB,t}$ is the amount of natural gas intake at time t; η_{GB} is the heat production rate of the equipment; H_{CVNG} is the low calorific value of natural gas.

The physical parameters of the gas boiler can be described by Eq. 8:

$$P_{GB,t} = \left[V_{GB,t}, \eta_{GB} \right] \tag{8}$$

2.2.5 Physical model of the PtG equipment

The relationship between electrical energy consumption and natural gas output in the PtG equipment can be described by Eq. 9:

$$\begin{cases} P_{PtG,t} = \eta_{PtG,t} \left(P_{PtH,t} - \dfrac{P_{H2,t}}{\eta_{H2,t}} + P_{HtG,t} \eta_{HtG,t} \right) \\ Q_{H2,t+1} = Q_{H2,t} + P_{H2,t} \cdot \Delta t - P_{HtG,t} \cdot \Delta t \\ Q_{H2,t}^{sto} \in \left[Q_{H2}^{min}, Q_{H2}^{max} \right] \end{cases} \tag{9}$$

where $P_{PtG,t}$ is the natural gas output power of the PtG equipment at time t; $P_{PtH,t}$, $P_{H2,t}$, and $P_{HtG,t}$ are the electric-hydrogen conversion output power, hydrogen storage power and hydrogen-gas conversion output power inside the PtG equipment at time t, respectively; $\eta_{PtH,t}$, $\eta_{H2,t}$, and $\eta_{HtG,t}$ are the hydrogen methanation efficiency, hydrogen storage efficiency and hydrogen discharge efficiency of the PtG equipment at time t, respectively; $Q_{H2,t}$ is the hydrogen storage capacity in the PtG equipment at time t, and Q_{H2}^{min} and Q_{H2}^{max} are its minimum and maximum values, respectively.

The physical parameters of the gas turbine can be described by Eq. 10:

$$P_{MGT,t} = \left[P_{PtH,t}; P_{H2,t}; P_{HtG,t}; \eta_{PtG,t}, \eta_{H2,t}, \eta_{HtG,t}; Q_{H2,t}, Q_{H2}^{min}, Q_{H2}^{max} \right] \tag{10}$$

2.2.6 Physical model of the energy storage equipment

The regional multi-energy system utilizes electricity storage batteries, gas storage equipment, and heat storage equipment for charging and discharging, which serve to regulate the output of the regional multi-energy system. Therefore, it can be described by Eqs 11–13.

$$\begin{cases} Q_{e,t+1} = (1-\eta_{loss})Q_{e,t} + \left(\eta_{e,c}P^{c}_{e,t} - \dfrac{P^{d}_{e,t}}{\eta_{e,d}}\right)\Delta t \\ 0 \le P^{c}_{e,t} \le \gamma_c \cdot P^{cmax}_{e} \\ 0 \le P^{d}_{e,t} \le \gamma_d \cdot P^{dmax}_{e} \\ Q^{min}_{e} \le Q_{e,t} \le Q^{max}_{e} \end{cases} \tag{11}$$

where $P^{c}_{e,t}$ and $P^{d}_{e,t}$ are the charging and discharging power of the electricity storage battery at time t, respectively, and P^{cmax}_{e} and P^{dmax}_{e} are its upper limit, respectively; $\eta_{e,c}$ and $\eta_{e,d}$ are the charging and discharging efficiencies, respectively; η_{loss} is the proportion of the equipment's electricity loss; $Q_{e,t}$ is the capacity of the equipment, and Q^{min}_{e} and Q^{max}_{e} are its lower and upper limits, respectively; γ_c and γ_d denote that the battery is charged or discharged.

$$\begin{cases} Q_{g,t} = \int_{t_0}^{t} P_{g,t}\mathrm{d}t = Q_{g,t_0} + \eta_g\left(P^{in}_{g,t} - P^{out}_{g,t}\right)(t-t_0) \\ 0 \le Q_{g,t} \le Q^{max}_{g} \end{cases} \tag{12}$$

where $Q_{g,t}$ is the storage volume of gas storage equipment at time t; η_g is the storage efficiency; $Q_{g,t0}$ is the storage volume of natural gas at time t_0; $P^{in}_{g,t}$ and $P^{out}_{g,t}$ are the charging and discharging power of the gas storage equipment at time t, respectively.

$$\begin{cases} Q_{h,t} = \int_{t_0}^{t} P_{h,t}\mathrm{d}t = Q_{h,t_0} + \eta_h\left(P^{in}_{h,t} - P^{out}_{h,t}\right)(t-t_0) \\ 0 \le Q_{h,t} \le Q^{max}_{h} \end{cases} \tag{13}$$

where $Q_{h,t}$ is the heat energy storage of the equipment at time t; η_h is the heat efficiency; $Q_{h,t0}$ is the heat energy storage of the equipment at time t_0; $P^{in}_{h,t}$ and $P^{out}_{h,t}$ are the heat storage and heat release power of the heat storage equipment at time t, respectively.

2.3 Multi-node scheduling task allocation model

Assuming that the regional multi-energy system being studied includes m edge computing layer base stations (which handle the main tasks of the edge computing layer and the data network communication layer) and n energy-consuming users. These can be denoted as edge computing layer base station set $M = \{1, 2, \ldots, m\}$ and energy-consuming user set $N_{user} = \{1, 2, \ldots, n\}$, respectively. At this time, all energy-consuming users in the regional multi-energy system must satisfy the constraints of Eq. 14.

$$N_{user} = \bigcup_{k} N_{user,k\in M} \tag{14}$$

The edge computing layer base station provides data support and scheduling calculation services to energy consumption users and the cloud service layer. This is achieved according to the edge computing module, data storage and communication module, data routing and other equipment deployed in the system. At the same time, the base station can transmit the calculated data and collected data to the neighboring base station. Then, by allocating the computation tasks to be completed by its own base station, it realizes the cooperative computation of multiple edge computing base stations to better complete the edge node scheduling optimization in the regional multi-energy system. If the edge computing layer base station is responsible for a small amount of computation tasks, the current base station can be used to complete the scheduling tasks.

If all energy equipment and energy consumption users in the scheduling process of the regional multi-energy system perform system scheduling optimization at the same time, all the computation tasks of the edge computing layer base station are allocated according to Eq. 15.

$$\begin{cases} X = \{x_{n,i,m}\} \\ x_{n,i,m} = \begin{cases} 1, & \text{the computational task } i \text{ of the energy consumption user } n \text{ are assigned to the base station } m \\ 0, & \text{else} \end{cases} \end{cases} \tag{15}$$

where X is the system scheduling task allocation decision set; $x_{n,i,m}$ is the corresponding values taken in the set.

Meanwhile, at least one base station in the edge computing layer must perform all computational tasks while satisfying the constraint of Eq. 16.

$$\begin{cases} \sum\limits_{m\in M} x_{n,i,m} = 1, \forall n \in N, i \in Y_n \\ E^{cul}_{X,m} = \sum\limits_{n\in N}\sum\limits_{i\in Y_n} c_{n,i}x_{n,i,m} \le E\max^{cul}_{m}, m \in M \\ E^{sto}_{X,m} = \sum\limits_{n\in N}\sum\limits_{i\in Y_n} e_{n,i}x_{n,i,m} \le E\max^{sto}_{m}, m \in M \end{cases} \tag{16}$$

where the first term is the constraint on the computational tasks to be completed by the edge computing layer base station; the second and third terms are the constraints on the response of the computational and data storage capacity of the edge computing layer base station m; $E^{cul}_{X,m}$ and $E^{sto}_{X,m}$ are the amount of the response of the computational and data storage capacity of the edge computing layer base station m, and $E\max^{cul}_{m}$ and $E\max^{sto}_{m}$ are their corresponding upper limits; $c_{n,i}$ is the scheduling task computation demand; $e_{n,i}$ is the scheduling task data storage demand; Y_n is the optimized scheduling computation task n in the system.

When performing optimized scheduling computation tasks for the regional multi-energy system, each task requires energy for computation and data communication, as well as incurs transmission delays. Therefore, the cost and transmission delay consumed by the edge computing layer and the cloud service application layer can be expressed by Eq. 17:

$$\begin{cases} C_{coop,t} = Num_M C_{cul,m} \\ \bar{T}_{coop} = \dfrac{1}{Num_N}\sum\limits_{n\in N} T_{coop,i} \\ T_{coop,i} = \max\limits_{i\in Y_n}\left\{T^{send}_{n,i} + T^{cul}_{n,i} + T^{merge}_{n,i}\right\} + T^{return}_{n,i} \end{cases} \tag{17}$$

where $C_{coop,t}$ is the consumption cost of the optimized scheduling computation task performed by the regional multi-energy system; Num_M is the number of edge computing layer base stations executing the computation task at time t; $C_{cul,m}$ is the operation

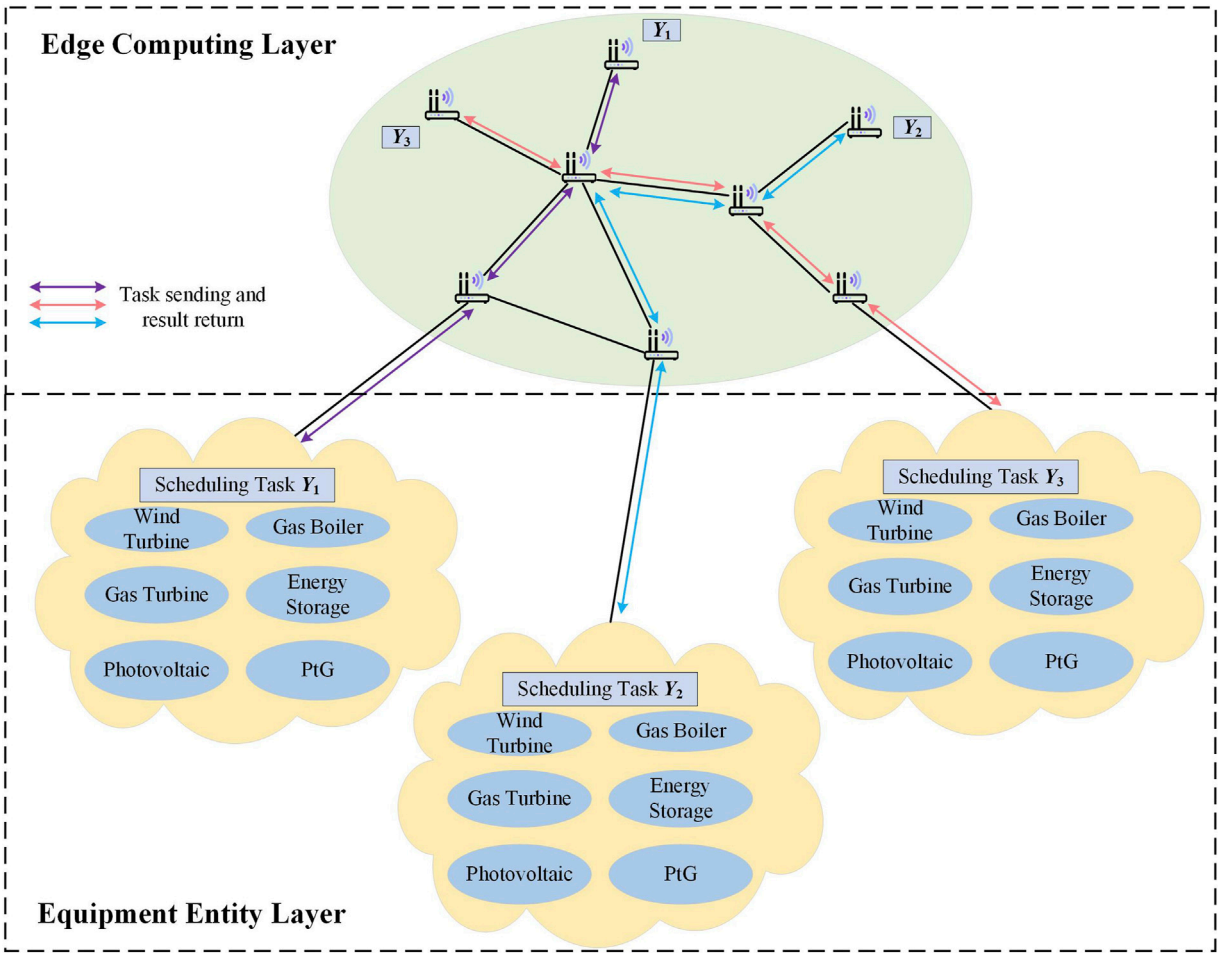

FIGURE 3
Multi-node cloud-edge collaborative scheduling computing process.

cost of the mth edge computing layer base station; $T_{\text{coop},i}$ is the transmission delay of the optimized scheduling computation task performed by the regional multi-energy system at time t, and $\bar{T}_{\text{coop}}$ is the average of its delay value; Num_N is the number of energy consuming users; $T_{n,i}^{\text{send}}$, $T_{n,i}^{\text{cul}}$, $T_{n,i}^{\text{merge}}$, and $T_{n,i}^{\text{return}}$ are the optimization scheduling task transmission delay, computation delay, computation result convergence delay, and computation result return delay, respectively.

In the actual optimization scheduling process, the computing process of multi-node cloud-edge cooperative scheduling in the regional multi-energy system is shown in Figure 3.

The state data sensing layer collects the operating state data and ledger data of each energy equipment in the equipment entity layer and stores them in the databases of the edge computing layer and the cloud service application layer. Then, the optimization scheduling task begins at each energy equipment and energy consumption user. It is then uploaded to the edge computing layer, where the computing task is allocated based on Eq. 15. The corresponding optimization computation is executed, and the operation scheduling commands are sent to the equipment entity layer based on the computational results to regulate the operation state of the energy equipment. At the same time, the computation results are summarized, merged, and sent to the cloud service application layer. Finally, the cloud service application layer performs the scheduling of region multi-energy systems covered by the edge computing layer base stations based on the received scheduling optimization data and the energy equipment operation data. The scheduling optimization calculation is unified and coordinated for the whole multi-energy system. The calculation results are also sent to the edge computing layer through the data network communication layer.

3 Cloud-edge cooperative optimization scheduling model of the regional multi-energy system

3.1 Scheduling model

To fully utilize the multi-node cloud-edge collaborative scheduling capability in the optimization and scheduling process of the regional multi-energy system, the double-layer optimization scheduling model of the regional multi-energy system is established as shown in Figure 4. The upper-layer optimization model in the cloud service application layer adopts an intelligent optimization algorithm to minimize the

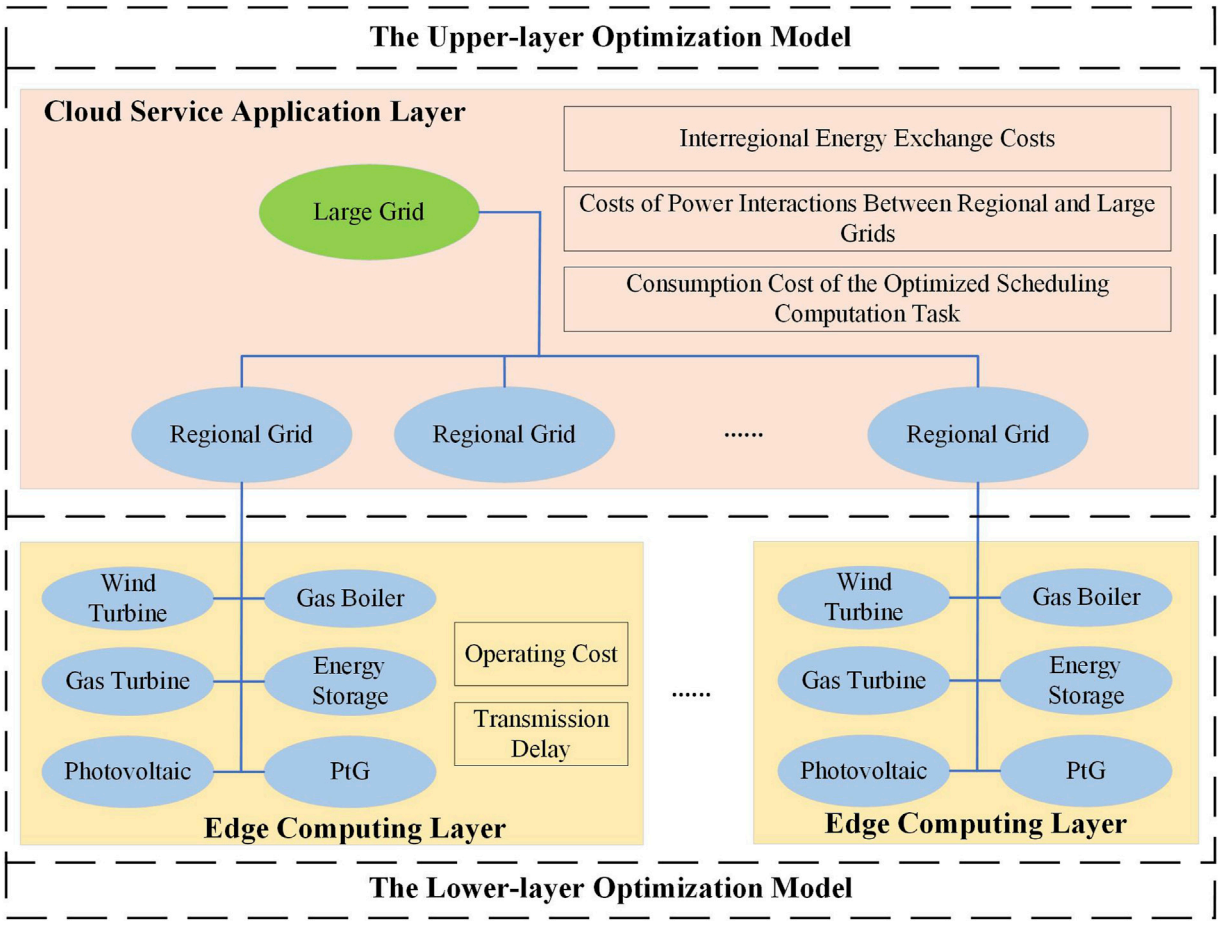

FIGURE 4
Double-layer optimization scheduling model of the regional multi-energy system.

overall operation and scheduling cost of the regional multi-energy system. It completes the scheduling optimization of the systems in the coverage area of the different regional edge computing layer base stations in the regional multi-energy system and obtains the optimal energy supply scheduling scheme, based on the received scheduling optimization data and energy equipment operation data. The lower-layer optimization model is that the edge computing layer calculates the optimal energy supply scheduling scheme based on the optimal energy supply scheduling scheme and control commands calculated by the cloud service application layer.

The objective function of the upper-layer scheduling optimization model for the cloud service application layer can be described by Eq. 18:

$$\min F_1 = \sum_{t=1}^{24}\left\{\sum_{i=1}^{Num_M} C_e P_{i,t} + \sum_{i=1}^{Num_M}\sum_{j=1}^{Num_M}\left(C^{e}_{exchange}\left|P^{e}_{i,j,t}\right| + C^{g}_{exchange}\left|P^{g}_{i,j,t}\right| + C^{h}_{exchange}\left|P^{h}_{i,j,t}\right|\right)\right\} + \sum_{i=1}^{Num_M}\alpha_i F_2 + \sum_{t=1}^{24} C_{coop,t} \quad (18)$$

where F_1 is the overall operation and scheduling cost of the regional multi-energy system; C_e is the unit electric energy interaction price between the regional multi-energy system covered by different regional edge computing layer base stations and the large power grid; $P_{i,t}$ is the interactive electric power between the regional multi-energy system covered by different regional edge computing layer base stations and the large power grid; $C^{e}_{exchange}$, $C^{g}_{exchange}$, and $C^{h}_{exchange}$ are the unit exchange cost of electricity, natural gas, and heat energy in the area covered by the ith and jth regional edge computing layer base stations, respectively; $P^{e}_{i,j,t}$, $P^{g}_{i,j,t}$, and $P^{h}_{i,j,t}$ are the exchange power of electricity, natural gas, and heat energy in the area covered by the ith and jth regional edge computing layer base stations, respectively; When the regional system covered by the ith regional edge computing layer base station exchanges electricity, natural gas and heat energy to the region covered by the jth regional edge computing layer base station, $P^{e}_{i,j,t}$, $P^{g}_{i,j,t}$, and $P^{h}_{i,j,t}$ are taken as a positive value, and the opposite are taken as a negative value; α_i is the scheduling optimization priority of the different regional edge computing layer base station, the larger the value of the priority level is, the higher the priority level of the computation order is in the calculation of the optimized scheduling task in this region; F_2 is the scheduling and operating cost of the regional multi-energy system covered by the regional edge computing layer base stations obtained by the edge computing layer calculation.

The objective function of the lower-layer scheduling optimization model for the edge computing layer can be described by Eq. 19:

$$\min F_2 = \sum_{t=1}^{24} \sum_{i=1}^{Num_M} \sum_{I} C_{i,I,t} P_{i,I,t} \tag{19}$$

where $C_{i,I,t}$ is the operating cost of the Ith energy equipment in the area covered by the ith regional edge computing layer base station at time t; $P_{i,I,t}$ is the electricity, heat energy or gas energy supply of the Ith energy equipment at time t.

In addition to the consideration of system operating costs, the regional multi-energy system to perform scheduling calculations is also required to consider the scheduling task transmission delay under the multi-node cloud-edge collaborative scheduling strategy, and minimize the data transmission delay of the scheduling optimization calculation process, which can be expressed by Eq. 20:

$$\min F_3 = \bar{T}_{\text{coop}} \tag{20}$$

3.2 Constraints

The supply balance constraints for electricity, gas, and heat in the regional multi-energy system can be described by Eq. 21

$$\begin{cases} \sum_{I_1} P_{i,I_1,t} - P^{\text{c}}_{i,\text{e},t} + P^{\text{d}}_{i,\text{e},t} + P_{i,t} + P^{\text{e}}_{i,j,t} = P_{i,\text{Le},t} \\ \sum_{I_2} P_{i,I_2,t} - P^{\text{in}}_{i,\text{g},t} + P^{\text{out}}_{i,\text{g},t} + P^{\text{g}}_{i,j,t} = P_{i,\text{Lg},t} \\ P_{i,\text{GB},t} - P^{\text{in}}_{i,\text{h},t} + P^{\text{out}}_{i,\text{h},t} + P^{\text{h}}_{i,j,t} = P_{i,\text{Lh},t} \end{cases} \tag{21}$$

where $P_{i,\text{Le},t}$, $P_{i,\text{Lg},t}$, and $P_{i,\text{Lh},t}$ are the electricity, heat and gas loads in the area covered by the ith regional edge computing layer base station, respectively; I_1 is the set of electricity energy equipment in the area covered by the ith regional edge computing layer base station, and I_1 = {wind turbine, photovoltaic, and PtG equipment}; I_2 is the set of natural gas energy equipment in the area covered by the ith regional edge computing layer base station, and I_2 = {gas turbine, PtG equipment, and gas boiler}; $P^{\text{e}}_{i,j,t}$, $P^{\text{g}}_{i,j,t}$, and $P^{\text{h}}_{i,j,t}$ are the exchange power of electricity, natural gas, and heat energy between the areas covered by the ith and jth edge computing layer base station, respectively; $P^{\text{c}}_{i,\text{e},t}$ and $P^{\text{d}}_{i,\text{e},t}$, $P^{\text{in}}_{i,\text{g},t}$ and $P^{\text{out}}_{i,\text{g},t}$, $P^{\text{in}}_{i,\text{h},t}$ and $P^{\text{out}}_{i,\text{h},t}$ are the charging and discharging power of the battery storage equipment, gas storage equipment and heat storage equipment at time t, respectively.

The operation constraints of multiple energy equipment in the regional multi-energy system can be described by Eq. 22

$$\begin{cases} P^{\min}_{i,\text{w},t} \le P_{i,\text{w},t} \le P^{\max}_{i,\text{w},t} \\ P^{\min}_{i,\text{PV},t} \le P_{i,\text{PV},t} \le P^{\max}_{i,\text{PV},t} \\ P^{\text{e,min}}_{i,\text{PtG},t} \le P^{\text{e}}_{i,\text{PtG},t} \le P^{\text{e,max}}_{i,\text{PtG},t} \\ P^{\min}_{i,\text{GT},t} \le P_{i,\text{GT},t} \le P^{\max}_{i,\text{GT},t} \\ P^{\min}_{i,\text{GB},t} \le P_{i,\text{GB},t} \le P^{\max}_{i,\text{GB},t} \\ P^{\text{g,min}}_{i,\text{PtG},t} \le P^{\text{g}}_{i,\text{PtG},t} \le P^{\text{g,min}}_{i,\text{PtG},t} \\ P^{\text{c,min}}_{i,\text{e},t} \le P^{\text{c}}_{i,\text{e},t} \le P^{\text{c,max}}_{i,\text{e},t} \\ P^{\text{d,min}}_{i,\text{e},t} \le P^{\text{d}}_{i,\text{e},t} \le P^{\text{d,max}}_{i,\text{e},t} \\ P^{\text{in,min}}_{i,\text{g},t} \le P^{\text{in}}_{i,\text{g},t} \le P^{\text{in,max}}_{i,\text{g},t} \\ P^{\text{out,min}}_{i,\text{g},t} \le P^{\text{out}}_{i,\text{g},t} \le P^{\text{out,max}}_{i,\text{g},t} \\ P^{\text{in,min}}_{i,\text{h},t} \le P^{\text{in}}_{i,\text{h},t} \le P^{\text{in,max}}_{i,\text{h},t} \\ P^{\text{out,min}}_{i,\text{h},t} \le P^{\text{out}}_{i,\text{h},t} \le P^{\text{out,max}}_{i,\text{h},t} \end{cases} \tag{22}$$

where $P^{\min}_{i,\text{w},t}$ and $P^{\max}_{i,\text{w},t}$, $P^{\min}_{i,\text{PV},t}$ and $P^{\max}_{i,\text{PV},t}$, $P^{\text{e,min}}_{i,\text{PtG},t}$ and $P^{\text{e,max}}_{i,\text{PtG},t}$ are the minimum and maximum output power of the wind turbine, photovoltaic and electricity power consumed by PtG equipment in the area covered by the ith regional edge computing layer base station, respectively; $P^{\min}_{i,\text{GT},t}$ and $P^{\max}_{i,\text{GT},t}$, $P^{\min}_{i,\text{GB},t}$ and $P^{\max}_{i,\text{GB},t}$, $P^{\text{g,min}}_{i,\text{PtG},t}$ and $P^{\text{g,min}}_{i,\text{PtG},t}$ are the minimum and maximum values of the gas power consumed by gas turbine, gas boiler, and gas output power of PtG equipment in the area covered by the ith regional edge computing layer base station, respectively; $P^{\text{c,min}}_{i,\text{e},t}$ and $P^{\text{c,max}}_{i,\text{e},t}$, $P^{\text{d,min}}_{i,\text{e},t}$ and $P^{\text{d,max}}_{i,\text{e},t}$ are the minimum and maximum values of the charging power and discharging power of the battery storage equipment at the time t, respectively; $P^{\text{in,min}}_{i,\text{g},t}$ and $P^{\text{in,max}}_{i,\text{g},t}$, $P^{\text{out,min}}_{i,\text{g},t}$ and $P^{\text{out,max}}_{i,\text{g},t}$ are the minimum and maximum values of the charging power and discharging power of the gas storage equipment at time t; $P^{\text{in,min}}_{i,\text{h},t}$ and $P^{\text{in,max}}_{i,\text{h},t}$, $P^{\text{out,min}}_{i,\text{h},t}$ and $P^{\text{out,max}}_{i,\text{h},t}$ are the minimum and maximum values of the charging power and discharging power of the heat storage equipment at time t, respectively.

Data transmission constraints in the multi-node cloud-edge cooperative scheduling framework. The relevant equations can be found in Eqs 15–17.

The regional grid operations flow constraints can be described by Eq. 23

$$\begin{cases} P_{i,\text{w},t} + P_{i,\text{PV},t} - P^{\text{e}}_{i,\text{PtG},t} - P^{\text{c}}_{i,\text{e},t} + P^{\text{d}}_{i,\text{e},t} + P_{i,t} + P^{\text{e}}_{i,j,t} - P_{i,\text{Le},t} = U_{i,x} \sum_{y=1} U_{i,y} \left(G_{xy} \cos\theta_{xy} + B_{xy} \sin\theta_{xy} \right) \\ Q_{i,\text{w},t} + Q_{i,\text{PV},t} + Q_{i,t} + Q^{\text{e}}_{i,j,t} - Q_{i,\text{Le},t} = U_{i,x} \sum_{y=1} U_{i,y} \left(G_{xy} \sin\theta_{xy} - B_{xy} \cos\theta_{xy} \right) \end{cases} \tag{23}$$

where $U_{i,x}$ and $U_{i,y}$ are the voltage at the node x and node y in the regional grid covered by the ith regional edge computing layer base station; $Q_{i,\text{w},t}$, $Q_{i,\text{PV},t}$, $Q_{i,t}$, and $Q^{\text{e}}_{i,j,t}$ are the output reactive power of wind turbine, output reactive power of photovoltaic, interaction reactive power with the larger grid, and reactive power exchange between regional grids, respectively; $Q_{i,\text{Le},t}$ is the reactive power of loads within the regional grid; G_{xy} and B_{xy} are the conductance and conductivity between the node x and node y in the regional grid, respectively.

4 Multi-objective whale optimization algorithm

To achieve optimal computation and control of regional multi-energy system scheduling under the framework of edge computing and cloud-edge collaborative scheduling, this paper proposes a multi-objective whale optimization algorithm, which is used to solve the optimal scheduling scheme of the regional multi-energy system.

4.1 Fundamentals of the algorithm

The whale optimization algorithm is a heuristic, single-objective optimization algorithm that simulates the feeding behavior of whale groups (Mirjalili and Lewis, 2016). It has the advantages of a simple algorithm structure, easy implementation, and high convergence speed and optimization accuracy. proposes a multi-objective whale optimization algorithm for solving regional multi-energy system scheduling

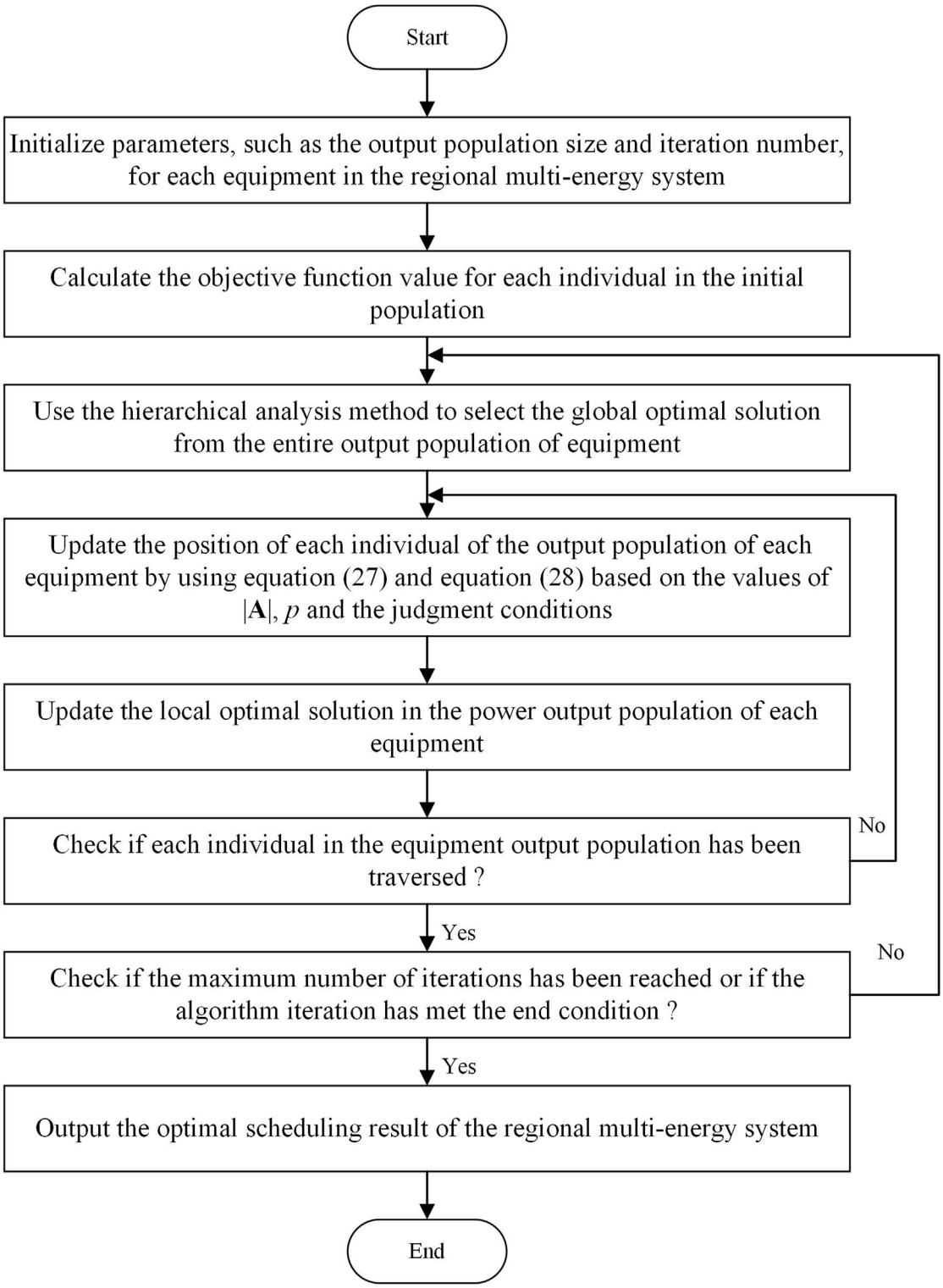

FIGURE 5
Solving algorithm.

schemes, based on a multi-objective algorithm framework with non-dominated as well as congestion ranking. The algorithm is divided into three phases: encircling prey, bubble net attack, and searching prey.

4.1.1 Encircling prey

In the first phase, the whale gradually approaches the prey through an encirclement approach. Assuming that the current optimal solution is the target prey, the positions of other

TABLE 1 Simulation parameters

Parameter	Value	Parameter	Value
Turbine efficiency of the gas turbine	0.8	Hydrogen storage efficiency	0.9
Compressed air efficiency of the gas turbine	1.3	Hydrogen discharge efficiency	0.85
Compressed natural gas efficiency of the gas turbine	1.3	Charging efficiency	0.85
Hydrogen methanation efficiency	0.75	Discharging efficiency	0.85
Gas turbine power generation costs/($/MWh)	74.14	Gas Storage Efficiency	0.85
Gas boiler heat production costs/($/MWh)	45.72	Heat Storage Efficiency	0.8
PtG Operating Costs/($/MWh)	78.57	Natural gas prices/($/m^3)	0.39

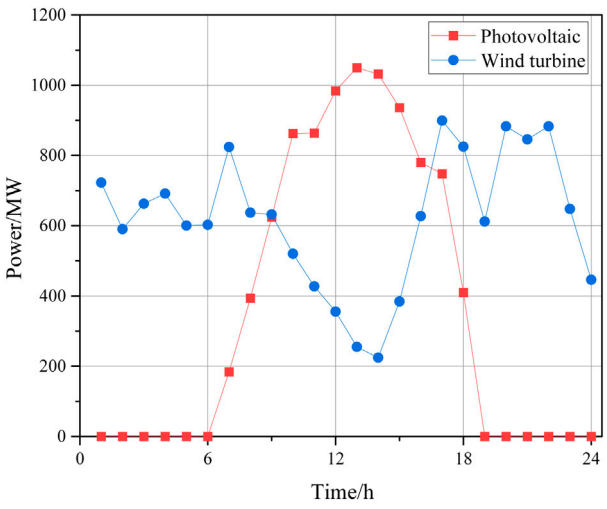

FIGURE 6
Photovoltaic and wind power output data.

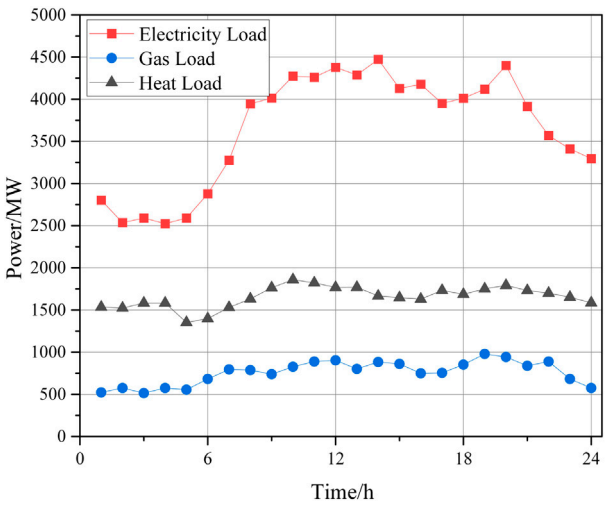

FIGURE 7
Load data.

individuals in the group are moved to the position of the optimal solution, and updated as Eq. 24:

$$\begin{cases} \mathbf{W} = |\mathbf{C} \cdot \mathbf{X}^*(t) - \mathbf{X}(t)| \\ \mathbf{X}(t+1) = \mathbf{X}^*(t) - \mathbf{A} \cdot \mathbf{W} \end{cases} \tag{24}$$

where $\mathbf{X}^*(t) = \{X_1^*, X_2^*, \ldots, X_N^*\}$ is the optimal solution solved by the algorithm, which is the position vector of the target prey hunted by the whale; t is the number of iterations; $\mathbf{X}(t)$ is the position vector of the solution; $\mathbf{A}\cdot\mathbf{W}$ is the encircling step size, which can be calculated according to the Eq. 26:

$$\begin{cases} \mathbf{A} = 2\mathbf{a} \cdot Rand - \mathbf{a} \\ \mathbf{C} = 2\mathbf{a} \cdot Rand \end{cases} \tag{25}$$

where *Rand* is a random number between [0,1]; a is the convergence factor, which decreases linearly from 2 to 0 as the number of iterations increases, and is denoted as Eq. 26:

$$a = \left(2 - \frac{2t}{T_{\max}}\right) \tag{26}$$

where $T_{\max}$ is the maximum number of iterations.

4.1.2 Bubble net attack

There are two ways to describe the feeding behavior of whales: the shrinking encirclement mechanism and the spiral updating position.

a) Shrinking encirclement mechanism: It is realized by constantly encircling the prey by the value of the convergence factor *a*.
b) Spiral updating position: The algorithm first calculates the distance between the current individual and the optimal solution position. Then, it approaches the optimal solution position in a spiral manner. The mathematical model can be expressed as Eq. 27:

$$\mathbf{X}(t+1) = \mathbf{W}^* \cdot e^{kl} \cos(2\pi l) + \mathbf{X}^*(t) \tag{27}$$

where $\mathbf{W}^*$ is the distance between the current individual and the current optimal position; k is a constant coefficient to qualify the logarithmic spiral form; l is a random number between [0,1].

Both above methods have a certain probability to appear in the actual whale hunting process. Therefore, the algorithm sets the selection probability coefficient p for performing the shrink-wrap mechanism and the spiral position update, denoted as Eq. 28:

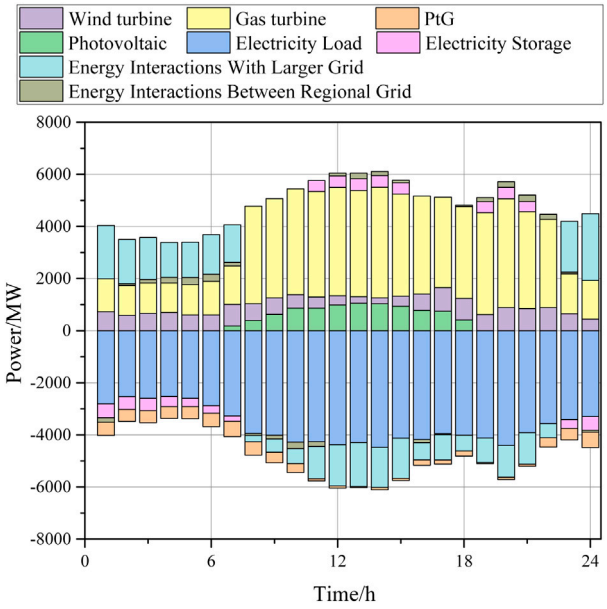

FIGURE 8
Electricity energy optimized scheduling results of Region 2.

$$\mathbf{X}(t+1)=\begin{cases}\mathbf{W}^{\star}\cdot e^{kl}\cos(2\pi l)+\mathbf{X}^{\star}(t), & p>0.5\\ \mathbf{X}^{\star}(t)-\mathbf{A}\cdot\mathbf{W}, & p\le 0.5\end{cases} \tag{28}$$

4.1.3 Searching prey

When $|\mathbf{A}|\geq 1$, the whale searches away from the reference target to find a superior prey, denoted as Eq. 29:

$$\begin{cases}\mathbf{W}=|\mathbf{C}\cdot\mathbf{X}_{\text{rand}}-\mathbf{X}(t)|\\ \mathbf{X}(t+1)=\mathbf{X}_{\text{rand}}-\mathbf{A}\cdot\mathbf{W}\end{cases} \tag{29}$$

where $\mathbf{X}_{\text{rand}}$ is the randomly selected position vector of the next prey.

4.2 Optimal solution selection mechanism of the algorithm

In a multi-objective optimization problem with n objective functions $F_i(x)$, $i = 1, 2, \ldots, n$, a decision variable Y_a is said to dominate Y_b if Eq. 30 is satisfied. If there is no other decision variable that can dominate a decision variable, it is considered a non-dominated solution.

$$\begin{cases}F_i(Y_a)\geq F_i(Y_b),\forall i\in 1,2,3,\cdots,n\\ F_i(Y_a)>F_i(Y_b),\exists i\in 1,2,3,\cdots,n\end{cases} \tag{30}$$

This paper proposes the idea of multi-objective particle swarm algorithm, which takes the global optimal solution as the target of bubble net attack, and the local optimal solution as the target of prey search. To achieve a local optimal solution, select the individual that dominates the current local optimal solution after moving positions. If the individual after moving position and the current local optimal solution do not dominate each other, randomly select both as the local optimal solution to ensure solution distribution and non-domination. The process of whale moving position fully uses the information obtained in the process of whale moving position, and the global optimal solution is selected according to the hierarchical analysis method, which ensures the effectiveness and objectivity of the global optimal solution selection process.

The distribution of the solution set of the algorithm uses the results of the crowding degree ranking in this paper as the standard for updating the solution set in the iterative process. The crowding degree is calculated using Eq. 31.

$$Y_d=Y_d+\frac{F_{i+1}-F_{i-1}}{F_{\max}-F_{\min}} \tag{31}$$

where $F_{\max}$ and $F_{\min}$ are the maximum and minimum values of the objective function, respectively; $F_{i\text{-}1}$ and F_{i+1} are the values of the objective function of the previous individual and the next individual after the descending order ranking, respectively.

The algorithm uses the crowding degree, which can visualize the distribution of solutions. A larger crowding degree indicates a better distribution of solutions, while a smaller crowding degree indicates a worse distribution. Therefore, during the iteration process of updating the solution set, larger solutions can be filtered based on the size of the crowding degree, and smaller solutions can be eliminated to maintain diversity and distribution of solutions.

4.3 Solution process of scheduling model based on multi-objective whale optimization algorithm

Figure 5 shows the solution process, and the specific steps are as follows:

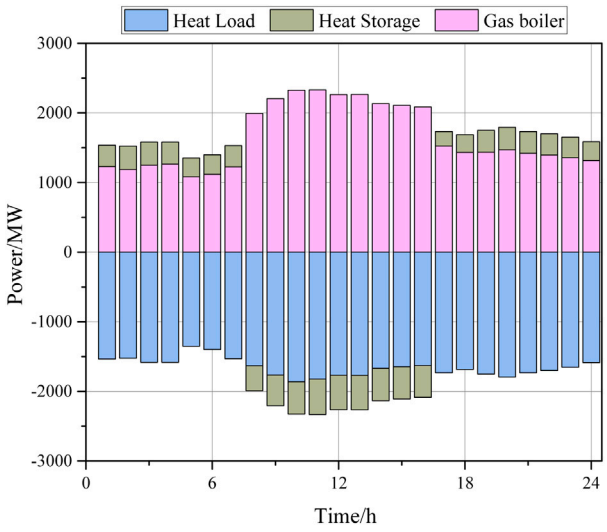

FIGURE 9
Heat energy optimized scheduling results of Region 2.

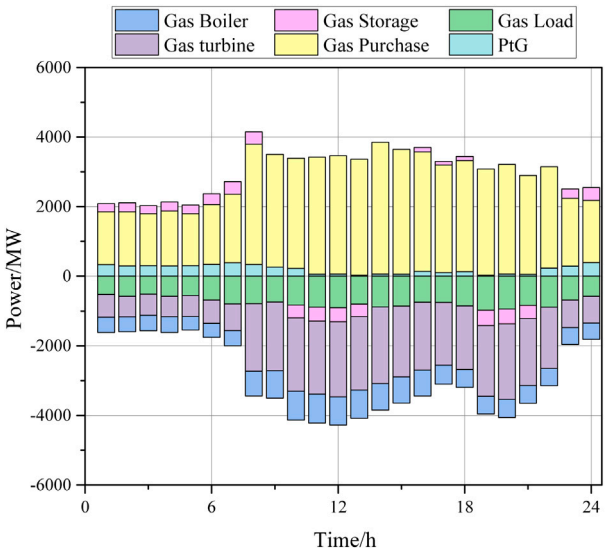

FIGURE 10
Gas energy optimized scheduling results of Region 2.

(1) Initialize parameters, such as the output population size and iteration number, for each equipment in the regional multi-energy system. Randomly initializing the position of each individual in the output population, and initializing the local optimal value of each equipment in the regional multi-energy system.
(2) Calculate the objective function value for each individual in the initial population, which represents the output power of each device in the regional multi-energy system.
(3) Use the hierarchical analysis method to select the global optimal solution from the entire output population of equipment and guide the position of the equipment power output population in the desired direction.
(4) To update the position of each individual of the output population of each equipment in the multi-energy system, use Eqs 27, 28 based on the values of $|\mathbf{A}|$, p and the judgment conditions.
(5) Update the local optimal solution in the power output population of each equipment in the multi-energy system using the optimal solution domination principle of Eqs 30, 31.
(6) Check if each individual in the equipment output population has been traversed. If not, go back to Step (4).
(7) Check if the maximum number of iterations has been reached or if the algorithm iteration has met the end condition. If yes, output the optimal scheduling result of the regional multi-energy system and end the algorithm. Otherwise, go back to Step (3).

5 Example analysis

Using the model established in this paper, the historical operation data of new energy units and the historical load data of a regional power grid in Northeast China on a typical operation day are selected. The topology shown in Figure 2 is used to build a regional multi-energy system multi-node cloud-edge cooperative scheduling simulation model to optimize the scheduling.

The parameters of the electricity/heat/gas multi-energy system are shown in Table 1. Figures 6, 7 show the PV and wind power output and load data during the simulation.

The regional power grid is divided into Num_M regions, and the equipment entity layer, state data perception layer, edge computing layer, data network communication layer, and cloud service application layer are set up according to the established multi-node cloud-edge collaborative scheduling model, respectively. In this paper, Num_M is set to 4. An AMD R7 5800H, 16 GB computer is used for scheduling optimization of the regional multi-energy system.

The scheduling optimization result of the edge computing layer of the region 2 multi-energy system are given in Figures 8–10.

According to Figures, the wind turbine and photovoltaic equipment output is consistently high throughout each time, resulting in a higher utilization of new energy in the region. Other power generation equipment is adjusted based on changes in load demand to better meet load requirements. During nighttime hours, electricity prices are low. As a result, the regional grid chooses to purchase electricity from the grid more frequently. Battery storage equipment is charged during these hours to discharge energy during times of high demand. This reduces the operation and dispatching costs of the regional multi-energy system. When demand is high, battery storage equipment will be charged and used to discharge energy when the load is high. This will reduce the operation and scheduling costs of the regional multi-energy system. To meet the heat and gas load demand in the regional multi-energy system, the edge computing layer calculates the optimal heat and gas energy supply arrangement scheme based on the acquired equipment data and load demand

TABLE 2 Operating costs

Cost	Before Optimization	After Optimization
Equipment operating cost /$	236.17	181.93
Natural gas cost /$	146.14	167.10
Power Purchase Cost /$	39.81	21.88
Power sales revenue /$	5.50	28.01
Total cost /$	427.62	398.92

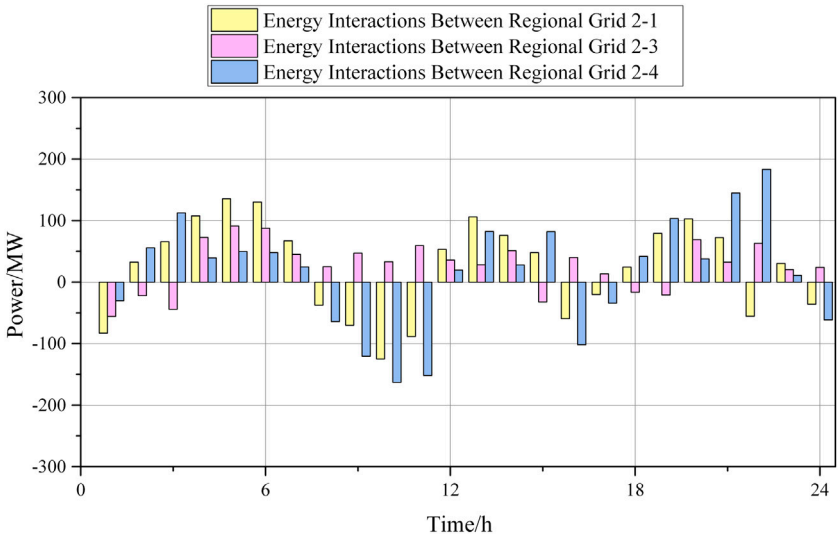

FIGURE 11
Optimized scheduling results of the electricity interaction.

data. It then adjusts the operation status of the corresponding energy equipment to meet the heat and gas load demand of users in the region when the load demand is high. Table 2 shows the results of the 24-h operation cost comparison for the regional multi-energy system.

Figure 11 gives the results of the electricity interaction between the region 2 multi-energy system and the other three regional multi-energy systems. The interaction of electric energy is mainly affected by changes in the output of new energy units and customer load demand.

This paper also explores the effectiveness of regional multi-energy system scheduling solution under two approaches: multi-node cloud-edge cooperative scheduling and centralized scheduling, and the results are shown in Table 3, Figure 12.

When the edge computing layer has not received the latest inter-regional energy interaction commands from the cloud service application layer, the edge computing layer can perform optimization calculations of energy equipment outputs within the regional multi-energy system by directly utilizing the operating state data and ledger data of each energy equipment in the equipment entity layer collected by the state data perception layer. At the same time, the amount of energy data and equipment operation data that need to be processed is smaller when each edge computing layer performs scheduling optimization calculation compared to centralized scheduling optimization. This reduction in data results in a decrease in the number of iterative calculations required for scheduling optimization solving using the multi-objective whale optimization algorithm. The corresponding results are shown in Table 3. Table 3 also shows the results of the number of iterations and average delay of scheduling optimization among regional multi-energy systems performed by the cloud service application layer. The number of iterations and delay are significantly lower than that of the centralized scheduling method.

The results of system operation data information processing and calculation time are shown in Figure 12. Compared to centralized scheduling method, cloud-edge cooperative scheduling technology improves the rate of data processing and calculation of the regional multi-energy system. The data processing time is reduced by 20.94%, and the optimization calculation time is reduced by 29.64%. This finding suggests that cloud-edge cooperative scheduling technology is a more efficient option for the regional multi-energy system.

TABLE 3 Operating Costs Solution comparison of scheduling optimization task

Number of regions	Cloud-Edge Cooperative Scheduling Method			Centralized Scheduling Method	
	Number of iterations of edge computing layer	Number of iterations of cloud service application layer	Average delay/s	Average delay/s	Number of iterations
2	106	84	2.03	3.69	373
4	232	167	2.97	6.27	583
8	536	241	4.12	8.95	1386
16	1272	501	7.62	13.28	2768

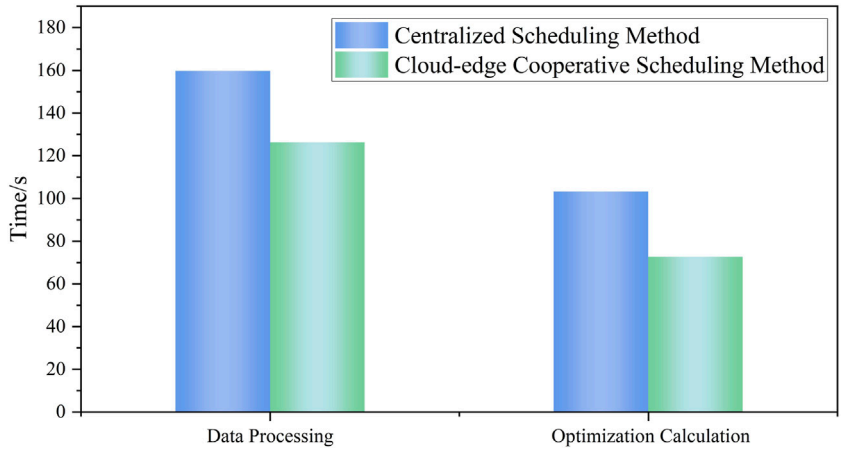

FIGURE 12
Comparison of data information processing and calculation time before and after optimization.

6 Conclusion

Based on edge computing technology and cloud-edge cooperative control framework, this paper proposes a multi-node cloud-edge cooperative optimal scheduling strategy of the regional multi-energy system coordinated with multiple edge service layer base stations. The paper establishes a two-layer optimal scheduling model for regional multi-energy systems. The method is simulated and verified through analysis, and the conclusions are presented as follows:

(1) The use of the cloud edge cooperative scheduling technology for the perception, monitoring, and optimization of the regional multi-energy system can effectively improve the ability of data information processing and calculation of the multi-energy system. The time of data information processing is reduced by 20.94%, and the time of optimization calculation is reduced by 29.64%.
(2) The efficiency of scheduling and optimization of the regional multi-energy system has been improved by allocating the scheduling and optimization tasks of the whole system to the edge computing service layer, and then performing cooperative computation among the multiple edge service layer base stations to reduce the amount of data computation and processing for the execution of the optimization and scheduling tasks of the regional multi-energy system;
(3) Through the analysis of the scheduling optimization results of the regional multi-energy system, the double-layer optimal scheduling model of the regional multi-energy system established in this paper can increase the flexible adjustment ability of the system, and realize the economic operation of the multi-energy system.

Data availability statement

The original contributions presented in the study are included in the article/Supplementary material, further inquiries can be directed to the corresponding author.

Author contributions

SL: Writing–original draft, Validation, Writing–review and editing. YT: Writing–original draft, Writing–review and editing. SC: Writing–original draft. NX: Writing–original draft. PS: Validation, Writing–original draft. KZ: Writing–review and editing. ZC: Writing–original draft, Writing–review and editing.

Funding

The author(s) declare that financial support was received for the research, authorship, and/or publication of this article. This work was supported by the National Key Research and Development Plan (No. 2017YFB0902100).

Conflict of interest

The authors declare that the research was conducted in the absence of any commercial or financial relationships that could be construed as a potential conflict of interest.

Publisher's note

All claims expressed in this article are solely those of the authors and do not necessarily represent those of their affiliated organizations, or those of the publisher, the editors and the reviewers. Any product that may be evaluated in this article, or claim that may be made by its manufacturer, is not guaranteed or endorsed by the publisher.

References

Abir, S. M. A., Anwar, A., Choi, J. H., and Kayes, A. S. M. (2021). IoT-enabled smart energy grid: applications and challenges. *IEEE ACCESS* 9, 50961–50981. doi:10.1109/ACCESS.2021.3067331

Gao, J., Chang, R., Yang, Z., Huang, Q., Zhao, Y., and Wu, Y. (2023). A task offloading algorithm for cloud-edge collaborative system based on Lyapunov optimization. *Clust. Computing-the J. Netw. Softw. Tools Appl.* 26 (1), 337–348. doi:10.1007/s10586-022-03563-w

Gooi, H., Wang, T., and Tang, Y. (2023). Edge intelligence for smart grid: a survey on application potentials. *CSEE J. Power Energy Syst.* 9 (5), 1623–1640. doi:10.17775/CSEEJPES.2022.02210

Huang, B., Li, Y., Zhan, F., Sun, Q., and Zhang, H. (2022). A distributed robust economic dispatch strategy for integrated energy system considering cyber-attacks. *IEEE Trans. Industrial Inf.* 18 (2), 880–890. doi:10.1109/TII.2021.3077509

Ilic, M. D., Xie, L., Khan, U. A., and Moura, J. M. F. (2010). Modeling of future cyber-physical energy systems for distributed sensing and control. *IEEE Trans. Syst. Man Cybern. - Part A Syst. Humans* 40 (4), 825–838. doi:10.1109/TSMCA.2010.2048026

Li, Y., Li, T., Zhang, H., Xie, X., and Sun, Q. (2022). Distributed resilient double-gradient-descent based energy management strategy for multi-energy system under DoS attacks. *IEEE Trans. Netw. Sci. Eng.* 9 (4), 2301–2316. doi:10.1109/TNSE.2022.3162669

Li, Y., Ren, R., Wang, R., Sun, Q., Gao, D. W., et al. (2023). Distributed hybrid-triggering-based secure dispatch approach for smart grid against DoS attacks. *IEEE Trans. Syst. Man, Cybern. Syst.* 53 (6), 3574–3587. doi:10.1109/TSMC.2022.3228780

Li, Y., Zhang, H., Liang, X., and Huang, B. (2019). Event-triggered based distributed cooperative energy management for multienergy systems. *IEEE Trans. Industrial Inf.* 15 (14), 2008–2022. doi:10.1109/TII.2018.2862436

Liu, H., Zhang, Y., and Yang, T. (2018). Blockchain-enabled security in electric vehicles cloud and edge computing. *IEEE Netw.* 32 (3), 78–83. doi:10.1109/MNET.2018.1700344

Lo, C. H., and Ansari, N. (2013). Decentralized controls and communications for autonomous distribution networks in smart grid. *IEEE Trans. Smart Grid* 4 (1), 66–77. doi:10.1109/TSG.2012.2228282

Luo, P., Liang, J., Fan, H., Zeng, S., Yang, G., and Lin, J. (2022). Real-time distributed dispatch strategy for distribution transformer supply zone cluster based on cloud-edge collaboration architecture. *Front. Energy Res.* 10, 1019349. doi:10.3389/fenrg.2022.1019349

Mirjalili, S., and Lewis, A. (2016). The whale optimization algorithm. *Adv. Eng. Softw.* 95, 51–67. doi:10.1016/j.advengsoft.2016.01.008

Raeisi-Varzaneh, M., Dakkak, O., Habbal, A., and Kim, B. S. (2023). Resource scheduling in edge computing: architecture, taxonomy, open issues and future research directions. *IEEE ACCESS* 11, 25329–25350. doi:10.1109/ACCESS.2023.3256522

Ren, J., Wang, H., Hou, T., Zheng, S., and Tang, C. (2019). Federated learning-based computation offloading optimization in edge computing-supported internet of things. *IEEE ACCESS* 7, 69194–69201. doi:10.1109/ACCESS.2019.2919736

Si, Y., Tan, Y., and Wang, F. (2020). Cloud-edge collaborative structure model for power internet of things. *Proc. Chin. Soc. Electr. Eng.* 40 (24), 7973–7979. doi:10.13334/j.0258-8013.pcsee.191532

Su, X., Sperlì, G., Moscato, V., Picariello, A., Esposito, C., and Choi, C. (2019). An edge intelligence empowered recommender system enabling cultural heritage applications. *IEEE Trans. Industrial Inf.* 15 (7), 4266–4275. doi:10.1109/TII.2019.2908056

Sulieman, N. A., Celsi, L. R., Li, W., Zomaya, A., and Villari, M. (2022). Edge-oriented computing: a survey on research and use cases. *ENERGIES* 15 (2), 452. doi:10.3390/en15020452

Teng, Y., Liu, S., and Hui, Q. (2020). Integrated demand side response model considering collaborative optimization of regional multi-energy system clusters. *Proc. Chin. Soc. Electr. Eng.* 40 (22), 7282–7295. doi:10.13334/j.0258-8013.pcsee.191715

Teng, Y., Zhang, T., and Chen, Z. (2018). Review of operation optimization and control of multi-energy interconnection system based on microgrid. *Renew. Energy* 36 (03), 467–474. doi:10.13941/j.cnki.21-1469/tk.2018.03.022

Wang, A., and Li, J. (2022). A novel cloud-edge collaboration based short-term load forecasting method for smart grid. *Front. Energy Res.* 10, 977026. doi:10.3389/fenrg.2022.977026

Xia, X., He, C., Lv, Y., Zhang, B., Wang, S., Chen, C., et al. (2022). Power quality data compression and disturbances recognition based on deep CS-BiLSTM algorithm with cloud-edge collaboration. *Front. Energy Res.* 10. doi:10.3389/fenrg.2022.874351

Zhang, H., Li, Y., Gao, D. W., and Zhou, J. (2017). Distributed optimal energy management for energy internet. *IEEE Trans. Industrial Inf.* 13 (6), 3081–3097. doi:10.1109/TII.2017.2714199

Zhang, W., Xu, Y., Li, S., Zhou, M., and Liu, W. (2018). A distributed dynamic programming-based solution for load management in smart grids. *IEEE Syst. J.* 12 (1), 402–413. doi:10.1109/JSYST.2016.2536141

frontiers | Frontiers in Energy Research

TYPE Original Research
PUBLISHED 23 May 2024
DOI 10.3389/fenrg.2024.1398655

Check for updates

OPEN ACCESS

EDITED BY
Yushuai Li,
Aalborg University, Denmark

REVIEWED BY
Dawei Gong,
University of Electronic Science and Technology of China, China
Cheng Zhang,
Hunan University, China
Ruizhuo Song,
University of Science and Technology Beijing, China

*CORRESPONDENCE
Jiantie Xu,
8275876@qq.com

RECEIVED 10 March 2024
ACCEPTED 08 April 2024
PUBLISHED 23 May 2024

CITATION
Wang Y, Xu J, Pei W, Wang H and Zhang Z (2024), Low-carbon economic scheduling of virtual power plant considering carbon emission flow and demand response. *Front. Energy Res.* 12:1398655. doi: 10.3389/fenrg.2024.1398655

COPYRIGHT
© 2024 Wang, Xu, Pei, Wang and Zhang. This is an open-access article distributed under the terms of the Creative Commons Attribution License (CC BY). The use, distribution or reproduction in other forums is permitted, provided the original author(s) and the copyright owner(s) are credited and that the original publication in this journal is cited, in accordance with accepted academic practice. No use, distribution or reproduction is permitted which does not comply with these terms.

Low-carbon economic scheduling of virtual power plant considering carbon emission flow and demand response

Yongchao Wang[1], Jiantie Xu[2]*, Wenhui Pei[2], Hanyang Wang[2] and Zhuang Zhang[2]

[1]College of Information Science and Engineering, Northeastern University, Shenyang, China, [2]State Grid Liaoning Electric Power Co., Ltd., Shenyang Power Supply Company, Shenyang, China

To fully explore the potential low-carbon and economic advantages of a virtual power plant (VPP) that aggregates multiple distributed resources, the paper proposes a VPP scheduling model that considers the carbon emission flow (CEF) and demand response (DR), which is characterized by electro-carbon coupling and source-load interaction. First, the electric-carbon characteristics of each distributed resource under VPP are modeled, and the source-load electric-carbon coupling characteristic model is modeled through the CEF theory. On this basis, a load-side multi-type DR model is established to achieve the purpose of source-load synergy to reduce carbon emissions from VPP. To this end, a two-stage scheduling model of VPP considering the source-load electro-carbon coupling relationship is established, and the implementation of the model can reduce power generation costs, carbon emissions and promote clean energy, and the simulation results of the improved IEEE-14 node system verify the effectiveness of the proposed model.

KEYWORDS

virtual power plant, electro-carbon coupling, carbon emission flow, demand response, low-carbon economic scheduling

1 Introduction

In the face of growing global awareness surrounding environmental preservation, the shift towards a low-carbon economy and sustainable development has emerged as a predominant global trend. Within the energy sector, conventional fossil energy sources like coal-fired and fuel oil have evolved into significant contributors to environmental pollution (Li et al., 2020). Therefore, in the context of low-carbon power, the increasing development of distributed resources has become an unavoidable trend, and the scale of development is expanding and the level of utilization is increasing (Li et al., 2019; Li et al., 2021). How to ensure the safe and stable operation of the power grid while realizing the access and optimal operation of distributed resources is a problem that needs to be solved at present (Huang et al., 2022). The virtual power plant (VPP) is a new type of energy supply model that can effectively aggregate multiple distributed resources with the advantages of low carbon, high efficiency and flexibility. Therefore, virtual power plants have received extensive attention in both theoretical and practical research areas in recent years.

The VPP achieves the synergy and complementarity of diverse energy types through the integration of multiple energy sources. This not only caters to the energy demands of

various load types but also significantly diminishes the carbon footprint of the system. The scheduling problem of the VPP is one of the keys and bases to realizing its efficient operation and optimal control, and its main purpose is to formulate a reasonable scheduling strategy to improve its operation efficiency and economic benefits (Liu et al., 2023). Extensive research efforts have been dedicated to this issue. For example, in (Naughton et al., 2021; Nguyen and Nguyen, 2021; Wang and Wu, 2021), a VPP scheduling model considering distributed resources aggregation such as distributed wind power (WT), photovoltaic (PV) and energy storage constructed, (Cao et al., 2016), established a VPP economic scheduling model, with the objective function being to minimize the cost of power generation. (Wang and Teng, 2023) established a VPP economic scheduling model incorporating the carbon trading mechanism. Based on this, (Sun et al., 2023; Tang et al., 2023) proposed a demand response (DR) taking into account the carbon trading mechanism and the low-carbon economic scheduling method for VPP, which improves the capacity of renewable energy consumption. It is worth noting that these references seldom analyze the electro-carbon coupling relationship of distributed resources, and there is a single means of carbon reduction and a lack of effective interaction between low-carbon means on both the source and load sides. As an effective analytical tool for the development of low-carbon electricity, the carbon flow emission (CEF) theory has been further developed and improved. (Zhou et al., 2012; Kang et al., 2015) elaborated on the concept of CEF theory, improving its theoretical framework and proposing corresponding calculation methods. (Cheng et al., 2019; Cheng et al., 2019; Cheng et al., 2020) applied the CEF theory to the integrated energy system, which significantly reduces the carbon emission of the system, and offers a fresh perspective and guiding principle for the virtual power plant to realize the low-carbon scheduling.

To further improve the low-carbon properties of VPPs, enhance the usage of clean energy sources and decrease energy expenses, research on load-side DR under VPPs has attracted increasing interest. For example, in (Li et al., 2022), flexible resources were designated as controllable units extensively situated on the distribution grid side. These units can be agilely controlled and regulated, facilitating a bidirectional and synergistic interaction between the main grid and the distribution grid. (Liu et al., 2022) conducted further research on electricity trading methods for electric vehicles. (Zahra et al., 2021) proposed an optimal VPP scheduling method taking DR into account, which coordinates the utilization of VPP storage and DR resources through a time-sharing tariff strategy to improve energy consumption while achieving peak-to-valley regulation. (Li et al., 2022) introduced a demand-side satisfaction coefficient, which significantly improves the motivation of users to participate in DR. (Li et al., 2020; Zhang et al., 2022) further classified loads into transferable loads and curtailable loads, and established a scheduling model for multiple types of loads to participate in DR. The above research works have achieved significant results in improving the motivation of users to participate in DR. However, the time period division of traditional time-sharing tariffs is relatively rigid and lacks sufficient flexibility, which has limited incentives for users. There are few tariff models that take into account the differences in carbon emissions of electricity consumption at different nodes, and few studies that classify loads according to their characteristics and develop DR models accordingly.

Addressing the issues above, this study centers on the electric-carbon coupling problem under VPP scheduling, proposes a source-load electric-carbon coupling relationship model founded on the principles of CEF theory, and subsequently establishes a two-stage VPP scheduling model incorporating participation in the carbon trading market and DR. Its main contributions and salient features are summarized below.

1) To comprehensively analyze the effect of electricity demand on carbon emissions, the CEF theory is utilized to track the carbon emissions from power generation measurement up to power consumption measurement. Additionally, investigate the potential low-carbon capacity of the load side to gain a better understanding of its contribution towards carbon reduction efforts.
2) To effectively integrate low-carbon means into both the supply and demand sides, and to promote the deep interaction and synergy between supply and demand, a multi-type load DR model that considers the relationship between load electricity consumption and carbon emissions is established.
3) A two-stage optimized scheduling model for VPP is established, based on a designed low-carbon dispatch strategy. The model takes into account both economic and low-carbon factors in making system operation decisions. The optimal scheduling results were obtained by iteratively optimizing the upper economic model and the lower low-carbon model.

The remaining portion of this paper is structured in the following manner. Section 2 introduces the structure of VPP and the CEF theory. In Section 3, the electric-carbon relation of distributed resources is modeled, and in Section 4, a multi-type DR model is based on the relationship between load electricity use and carbon emissions and develops a two-stage scheduling model for VPP. Section 5 presents a case study that illustrates the proposed model's effectiveness, while Section VI provides a concluding summary of the entire paper.

2 VPP basic structure and CEF theory

2.1 VPP physical structure

The structure of the VPP is illustrated in Figure 1 and it consolidates four resource types, controllable distributed power supply, new energy, energy storage, and load. Each resource type functions as a subsystem, allowing for optimal resource allocation across a broad spectrum through information transmission and energy interaction. This facilitates the reduction of carbon emissions, enhancing the system's new energy consumption capacity and increasing overall revenue (Kang et al., 2022).

2.2 Definition and calculation of CEF

Due to the consumption characteristics of power resources, the carbon emissions generated by the power system are

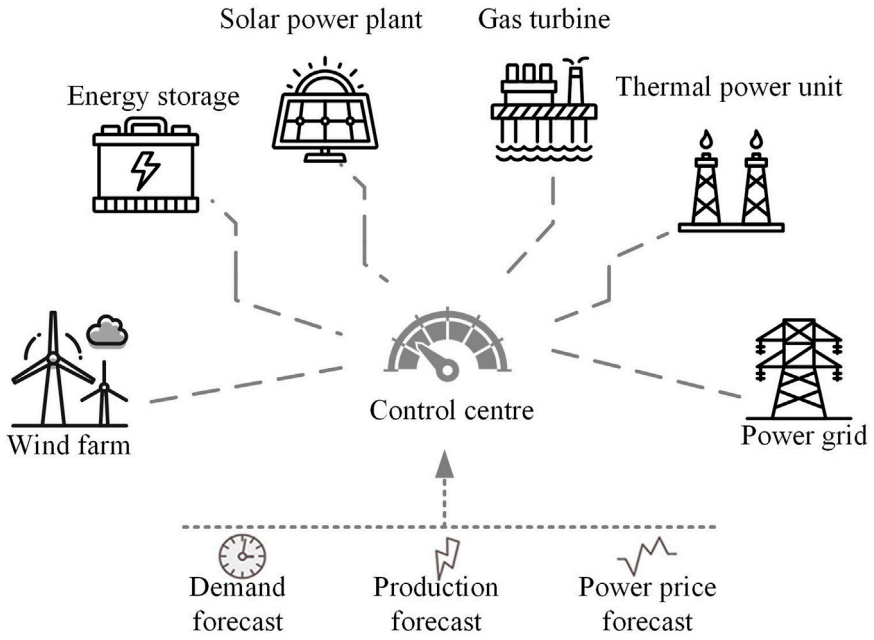

FIGURE 1
Physical structure diagram of VPP.

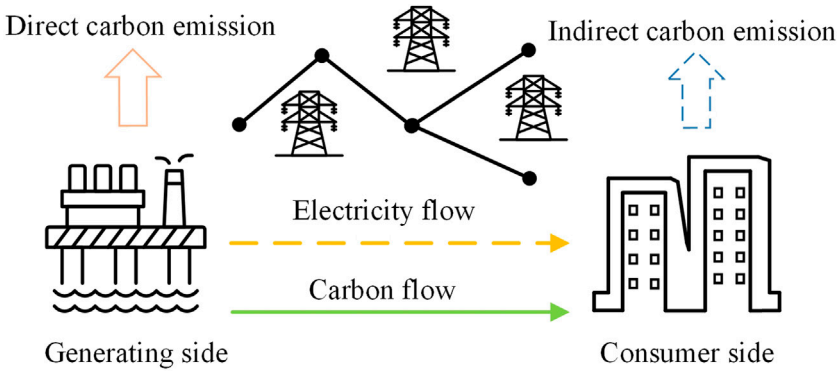

FIGURE 2
Schematic diagram of power system currents and CEF.

commonly referred to as off-site carbon emissions. Specifically, the loads themselves do not produce carbon emissions, electricity production is often accompanied by the release of carbon dioxide resulting from the utilization of non-renewable energy sources. To better track the carbon footprint of the load side and analyze the carbon characteristics of electricity from this perspective, it is necessary to introduce the concept of CEF. This allows for tracing the transfer of carbon emissions from power generation to the load side, providing a more accurate understanding of carbon emissions. As depicted in Figure 2, this model can calculate carbon flow indicators, such as emission flow rate and flow density, for each node and time period based on the existing distribution.

2.2.1 Carbon emission flow rate

Define the carbon emission resulting from the flow of energy through the network's nodes or branches per unit of time as the carbon flow emission rate R in $\bullet CO_2/h$, and the computational expression is Eq. (1).

$$R = \frac{dC}{dt} \tag{1}$$

Where C is the carbon flow emission rate of the network node or branch and t is the time.

2.2.2 Carbon density

Branch carbon density refers to the amount of carbon emissions produced by a single unit of electricity transmitted through a branch

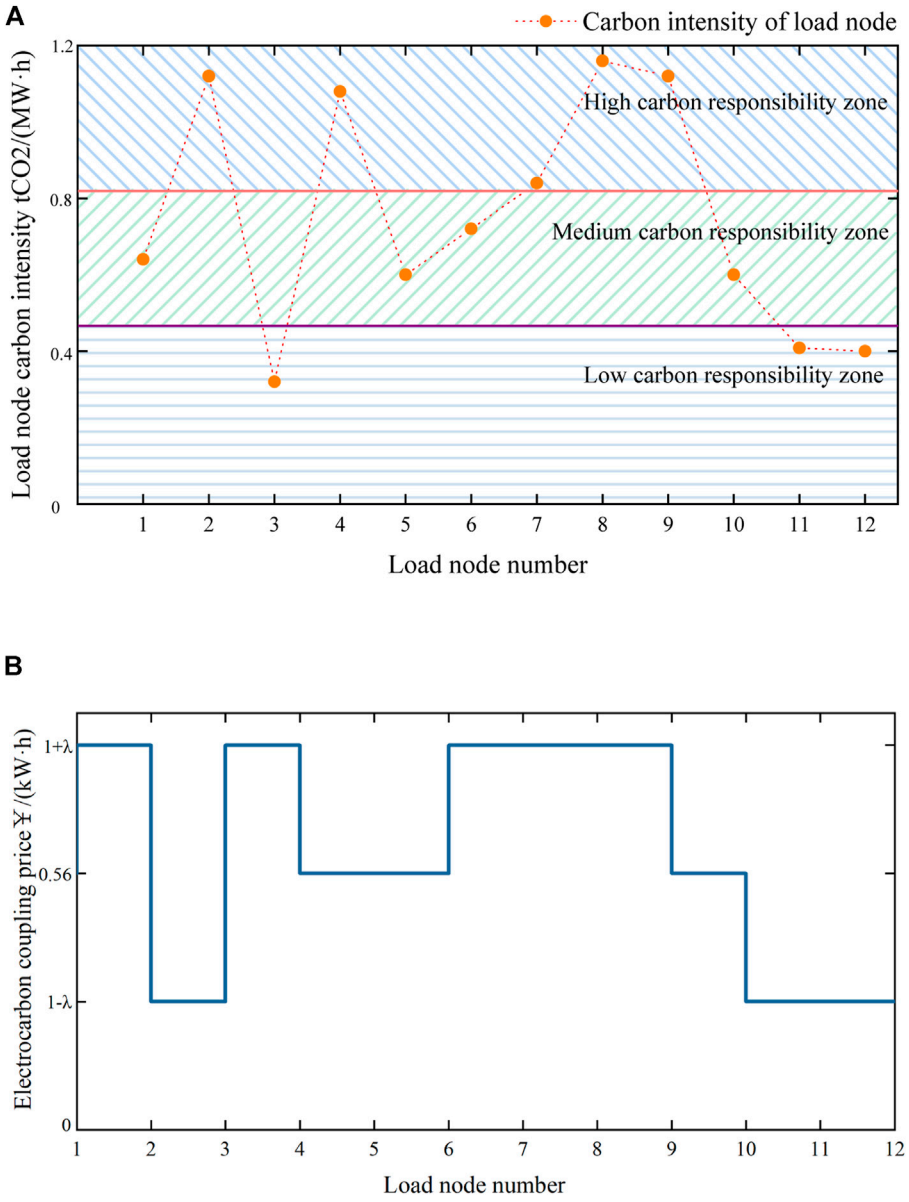

FIGURE 3
Schematic diagram of the steps in the coupled electro-carbon price modeling.

of a power system, i.e., it is the ratio of branch carbon flow emission rate to the active tidal current streaming through that branch and is denoted by ρ.

$$\rho = \frac{R}{P} \tag{2}$$

Where P donates the active current of the associated network.

2.2.3 Nodal carbon intensity

The nodal carbon flow density encompasses both the carbon flow density at generator nodes and the carbon flow density at load nodes. The generator node carbon flow density, referred to as carbon intensity, is denoted by E_G. Meanwhile, the load node carbon flow density, known as load node carbon intensity, describes the carbon emission associated with the load's consumption unit of electrical energy and is represented by e_n. Therefore, the carbon intensity at the node can be utilized for analyzing the relationship between electricity consumption and carbon emissions of the load side.

3 Modeling the electro-carbon characteristics of distributed resources

The "electric-carbon characteristic" is defined as the correlation between the net external power output and the net carbon emissions of a distributed generating unit. Presently, the prevailing approach in studies involves utilizing carbon intensity to articulate the electric-carbon characteristic of a unit. Carbon intensity quantifies the emissions produced per unit of electricity supplied to the grid by a unit.

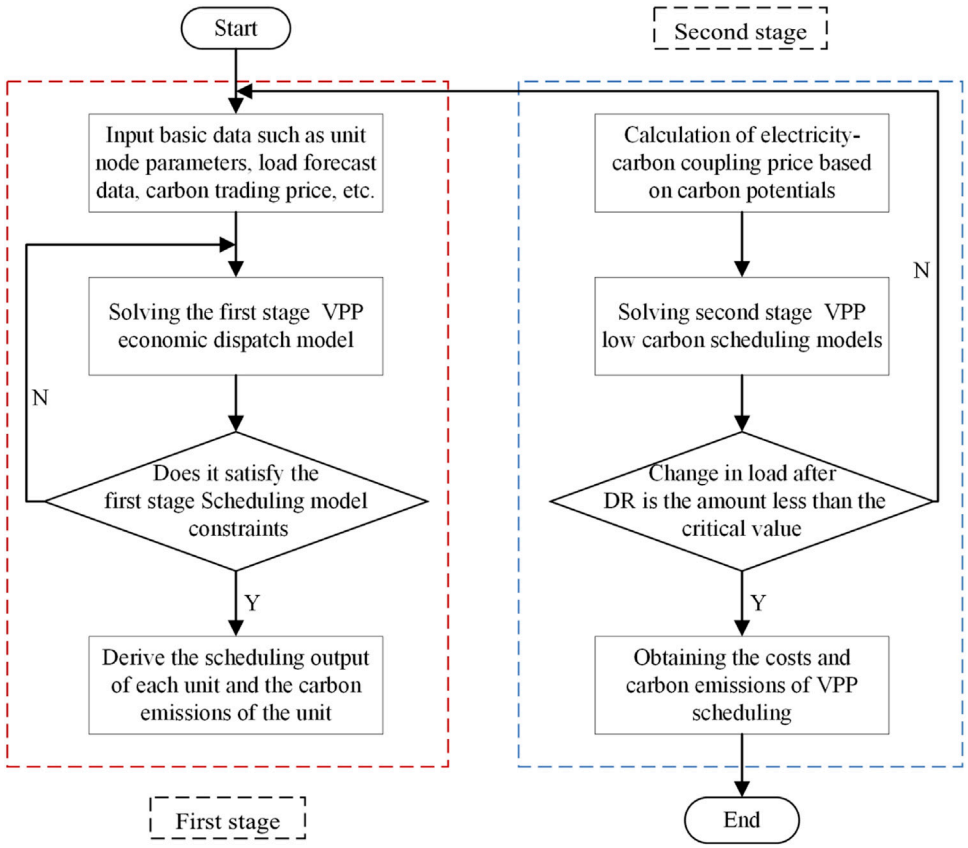

FIGURE 4
VPP two-stage optimized scheduling flowchart.

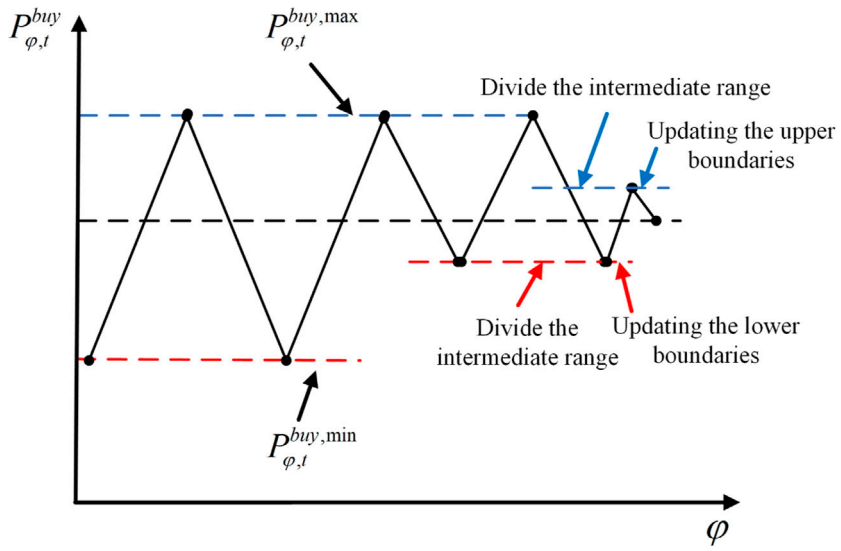

FIGURE 5
Schematic diagram of dichotomous iteration.

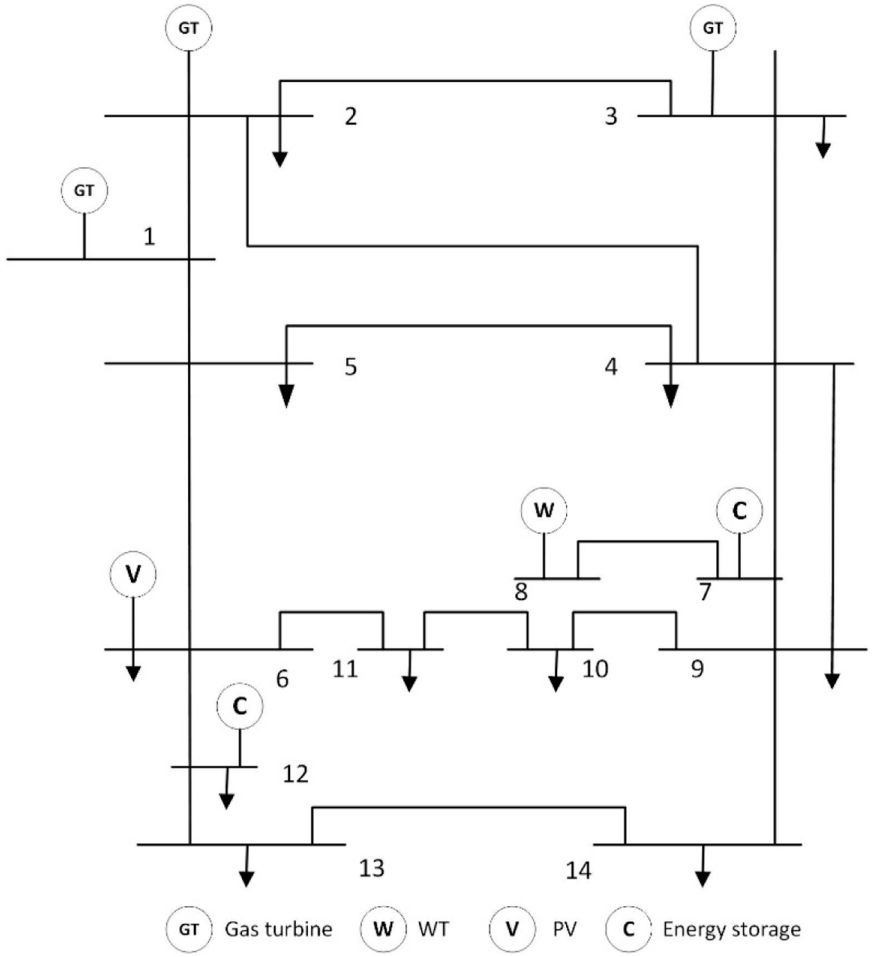

FIGURE 6
IEEE-14 system node diagram.

TABLE 1 Multi-type load distribution.

Form	Nodal load		
Type	Commercial load	Industrial load	Residential load
Nodal	6, 11–14	2–5	8–10

3.1 Unit electro-carbon characterization model

The fuel carbon emissions of fossil fuel producing units are the main source of carbon emissions from the VPP's power generation source. Carbon emissions from the operation and production processes of clean energy generating units, such WT and PV, are estimated to be zero. As such, in research investigations, their carbon intensity is usually set to 0.

$$E_{WT,PV} = 0 \tag{3}$$

Where $E_{WT,PV}$ is the carbon intensity of WT and PV.

The electrical carbon characteristics of a fuel unit are influenced by several factors, and its carbon intensity can usually be obtained from Eq. (4). Eq. (5).

$$\delta_i = \left(a_i P_{g,j}^2 + b_i P_{g,i} + c_i\right) h_i \Big/ P_{g,j} \times 10^3 \tag{4}$$

$$E_{G,i} = \eta_i k_i \frac{M_{CO_i}}{M_C} \frac{\delta_i}{10^3} \tag{5}$$

Where δ_i and a_i, b_i, c_i are the fuel consumption per unit of electrical energy and the characteristic parameters of the unit i, respectively, $E_{G,i}$ is the carbon intensity of the fuel unit, h_i is the correction factor, M_{CO_2}, M_C are the molar mass of carbon dioxide and carbon, η_i and k_i are the carbon content of the unit's fuel and carbon oxidation rate, respectively.

The above model applies to coal-fired, gas-fired, and other fuel-fired units, and the size of the parameters varies among different types of units.

3.2 Energy storage electro-carbon characterization model

The energy storage device operates in two concurrent states: charging and discharging. When in the charging state, it functions like a special load that can absorb a portion of carbon

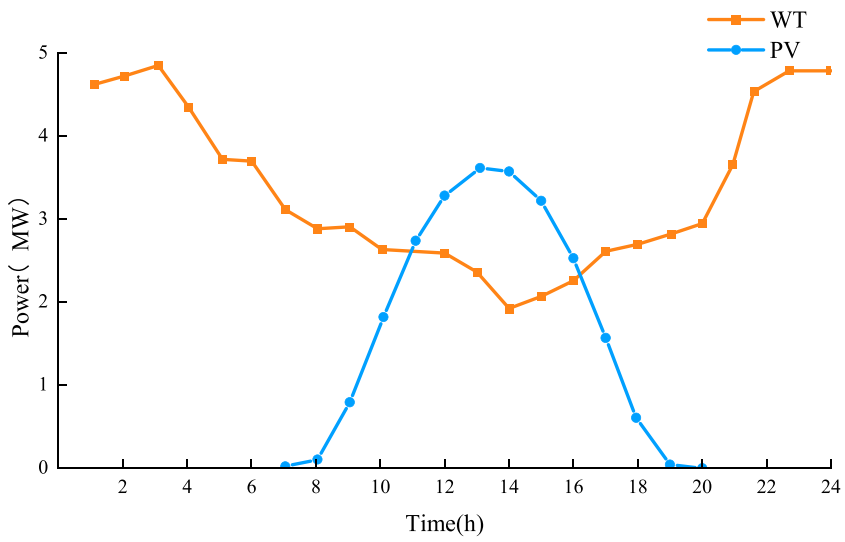

FIGURE 7
WT and PV forecast data.

emissions. On the other hand, when in the discharging state, it operates like special power generation equipment, resulting in the release of some carbon emissions. In conclusion, based on the CEF model, the electric-carbon characteristic model can be outlined as follows.

When the energy storage device is being charged, carbon emissions accompany the electrical energy charged into the energy storage device, at this time the energy storage charging carbon intensity is equivalent to the carbon intensity of the node where the element is located.

$$e_{cha} = e_j \tag{6}$$

When the energy storage device is in a discharged state, carbon emissions are released from the energy storage device along with electricity.

$$\begin{cases} Q_{e,t}^{cha} = P_{e,t}^{cha} e_{cha,t} \Delta t \\ Q_{e,t}^{\mathrm{dis}} = P_{e,t}^{dis} e_{j,t} \Delta t = \dfrac{P_{e,t}^{dis}}{\eta_e^{dis}} e_{dis,t-1} \Delta t \end{cases} \tag{7}$$

Where $Q_{e,t}^{cha}$, $Q_{e,t}^{dis}$ represents the amounts of carbon emission changes during the period of charging and discharging the energy storage device, $P_{e,t}^{cha}$, $P_{e,t}^{dis}$ represents the power associated with the charging and discharging, and η_e^{dis} is the discharging efficiency.

The carbon intensity of discharge emissions from energy storage devices is expressed as:

$$e_{dis} = \frac{e_{dis,t-1} SOC(t-1) + Q_{e,t}^{cha} - Q_{e,t}^{dis}}{SOC(t)} \tag{8}$$

Where $SOC(t)$ is the values of the capacity of the energy storage equipment at moment t.

3.3 Load electro-carbon characterization model

Carbon emissions from electricity consumption by power users are closely related to the quality and amount of the electricity they consume, where "quality" refers to the carbon content of the source of electricity, and "amount" as the name implies, pertains to the amount of electricity.

Reference (Da, 2016; Yang et al., 2023) demonstrates that the load node carbon intensity size is equivalent to the sum of all tributary carbon flow densities streaming into the node and the carbon intensity of the generators connected to the node concerning the tidal current weighted average. therefore, the load node CEF model is in Eq. (9).

$$e_j = \frac{\sum_{i=1, j \neq j}^{N} P_{i-j} \rho_{i-j} + P_{Gj} E_{Gj}}{\sum_{i=1, i \neq j}^{N} P_{i-j} + P_{Gj}} \tag{9}$$

where e_j represent the carbon intensity of load node j, P_{i-j} , ρ_{i-j} are the power and carbon flow density of the branches connected to node i and node j, respectively, P_{Gj} and E_{Gj} are the generating power and carbon intensity of the generators connected to the node j, respectively, and N is the number of network nodes.

The definition of load carbon intensity is the same as that of generating unit carbon intensity. Consequently, nodal carbon intensity can be used to express the electrical carbon properties of the load. As the load uses power per unit of time, the higher the carbon intensity of a load node, the more output the high carbon intensity unit produces relative to the load, increasing the value of carbon emissions. Users can independently participate in low-carbon DR by evaluating the variations in nodal carbon intensity throughout the day, as long as they stay within the

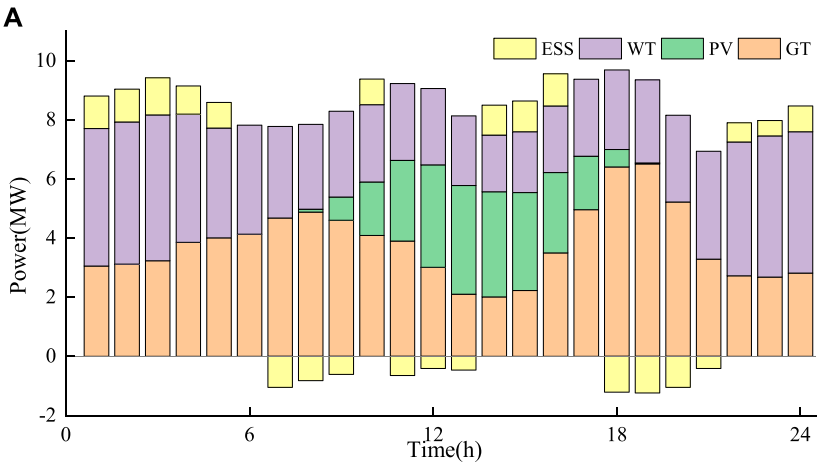

Scenario A scheduling result.

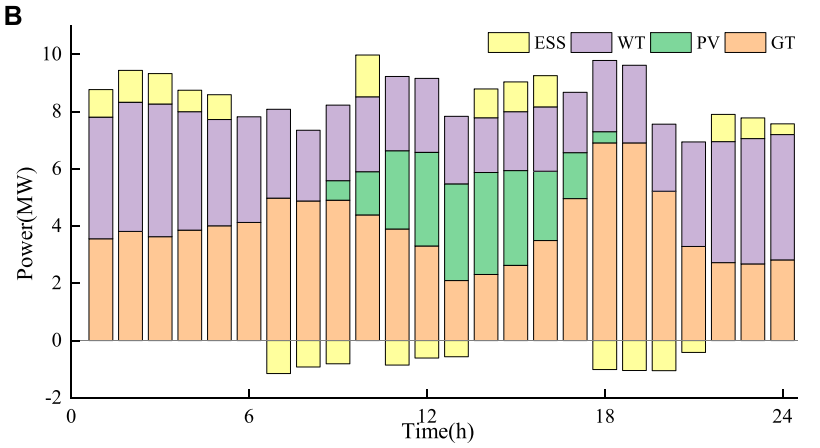

Scenario B scheduling result.

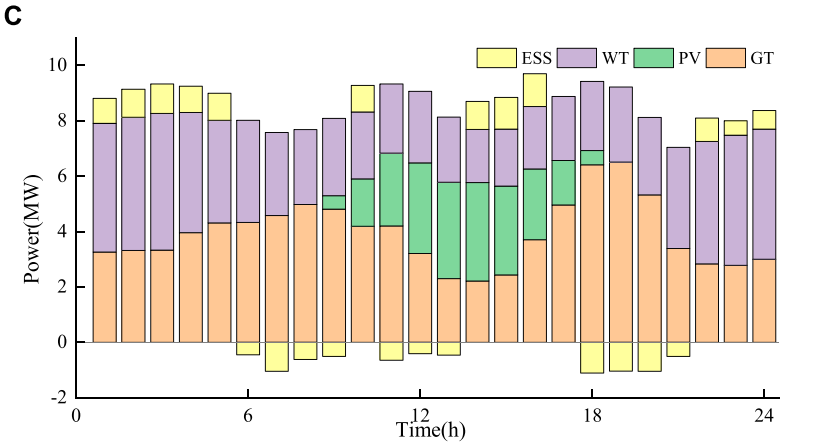

Scenario C scheduling result.

FIGURE 8
Scheduling results for different Scenarios. **(A)** Scenario A scheduling result. **(B)** Scenario B scheduling result. **(C)** Scenario C scheduling result.

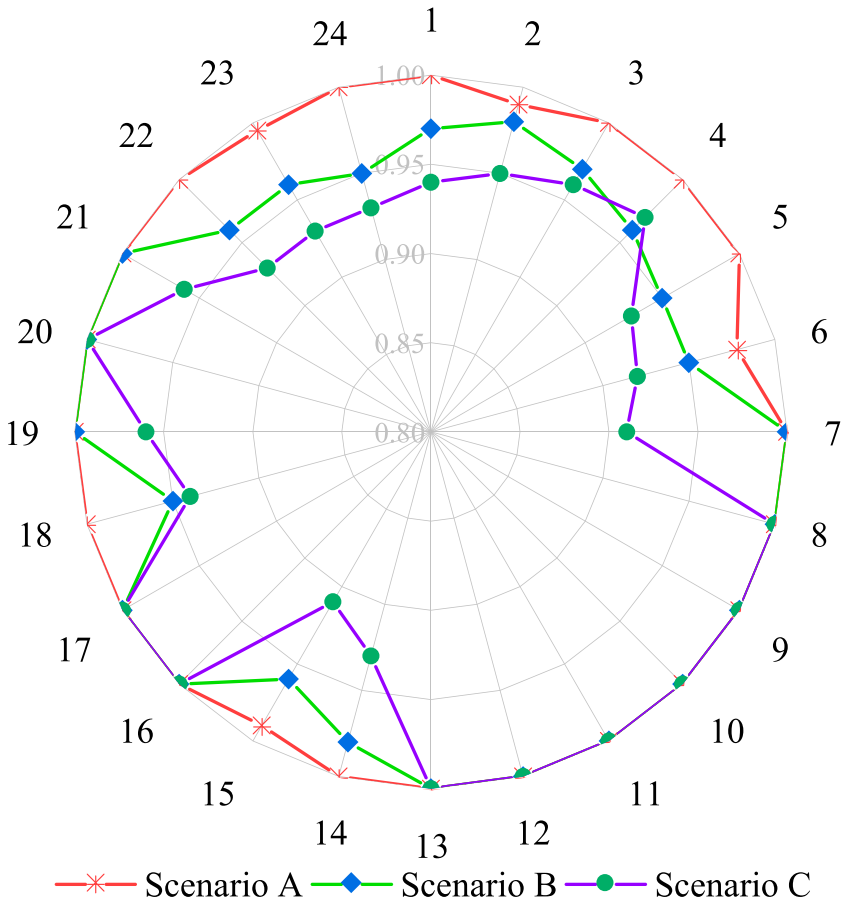

FIGURE 9
Clean energy consumption rates for different scenarios.

TABLE 2 Scheduling costs for each scenario.

Scheduling result	Generation cost/¥	Carbon trading cost/¥	Total cost/¥	Carbon emission/t
A	32,740	1,520	34,260	12.46
B	33,821	1,644	35,465	13.52
C	35,103	1912	37,015	15.23

parameters of load control capacity. They can then choose to individually increase or decrease loads and actively participate in low-carbon emission reduction activities, modifying their power consumption behaviors accordingly.

4 Low-carbon scheduling strategy considering source-load electro-carbon characteristics

4.1 Carbon market trading model

The carbon trading market system is currently the mainstream market mechanism to limit carbon emissions from the system at source by trading the carbon emission rights formulated. In the carbon trading market, it is necessary to determine the carbon trading volume of the VPP participating in the market based on the initial carbon emission amount, combined with the actual carbon emissions of the VPP (Lei et al., 2020). Among them, there are various ways to determine the initial carbon emission amount, such as the annual power generation method, baseline historical emissions and power generation intensity. For the output of the VPP units, the intensity of power generation is utilized to define the initial carbon quota of the VPP as in Eq. (10).

$$E_c = \eta_h P_{Gj,t} \tag{10}$$

Where E_c is the given unit carbon allowance, η_h is the carbon emission rights allocation factor.

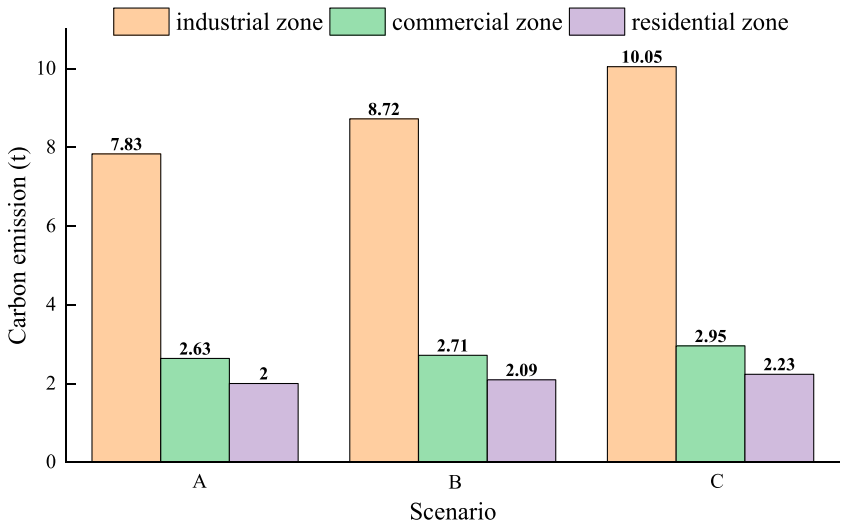

FIGURE 10
Comparison of carbon emissions by partition under different scenarios.

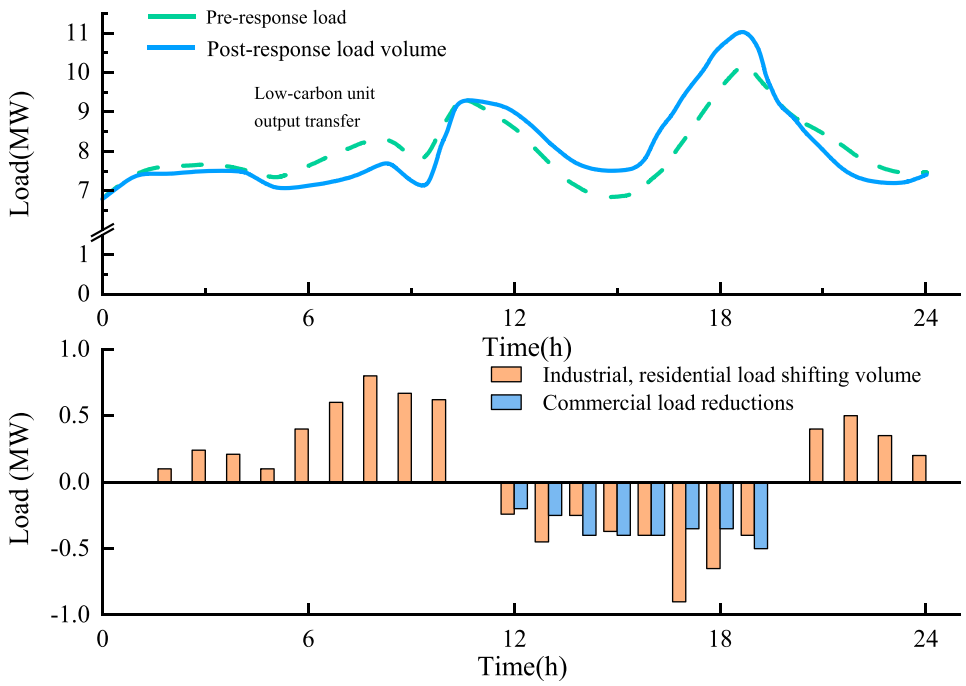

FIGURE 11
Scenario 1 load comparison before and after DR.

4.2 DR modeling based on load electro-carbon characteristics

As the carbon intensity of each load node increases, the value of carbon emissions associated with its unit of power consumption also increases. Leveraging this insight can optimize load scheduling to increase electricity consumption during low carbon intensity periods and decrease consumption during high carbon intensity periods. This strategic load scheduling can diminish the carbon emission value per unit of electricity over a cycle, resulting in energy savings and emission reduction.

According to the principle of consumer psychology, price-based DR guides users to carry out reasonable electricity consumption behavior through the change of electricity price (Liu et al., 2023), and China has achieved remarkable results in guiding users to peak shaving and valley filling through the establishment of DR model of peak-valley leveling time-sharing electricity price. However, the traditional electricity pricing strategy is usually based on

electricity supply and demand and cost considerations, and its pricing mechanism is relatively fixed, often without sufficient consideration of carbon emissions in the process of electricity production and use. Such strategies are usually simple and straightforward to implement, but may lack incentives for energy efficiency and environmental protection. In this paper, with reference to the time-sharing electricity pricing model, we analyze it from a low-carbon perspective, divide the low, medium and high carbon responsibility zones according to the carbon intensity, and establish the time-sharing electricity-carbon coupling price model for different carbon responsibility zones. The steps of the electricity-carbon coupling price model are shown in Figures 3A,B.

The specific steps are as follows:

1) As shown in Figure 3A, following the load node carbon intensity solution formula in Eq (9), the magnitude of carbon intensity at each load node at the current t time is calculated, and the low, medium and high carbon responsibility intervals are divided. The specific division method is shown in Eq. (11).

$$e_j(t) \in \begin{cases} e_{\min} \le e_j(t) \le \frac{1}{2}(e_{\min} + e_{ave}), \text{low carbon responsibility zone} \\ \frac{1}{2}(e_{\min} + e_{ave}) < e_j(t) \le \frac{1}{2}(e_{\max} + e_{ave}), \text{medium carbon responsibility zone} \\ \frac{1}{2}(e_{\max} + e_{ave}) < e_j(t) \le e_{\max}, \text{high carbon responsibility zone} \end{cases} \tag{11}$$

where $e_{\min}$ and $e_{\max}$ are the minimum and maximum load node carbon intensity at time t, e_{ave} is the average of all load node carbon intensity at time t, and e_j is the carbon intensity of load node j.

2) As shown in Figure 3B, the low, medium and high time-sharing carbon prices are set with reference to the peak, valley and level time-sharing prices, and the specific carbon price is shown in Eq. (12).

$$q_{j,c}(t) = \begin{cases} -\frac{1}{2}\lambda, e_j(t) \in \text{Low carbon responsibility zone} \\ 0, e_j(t) \in \text{Medium carbon responsibility zone} \\ \frac{1}{2}\lambda, e_j(t) \in \text{High carbon responsibility zone} \end{cases} \tag{12}$$

where λ is the carbon price difference between loads in the high and low responsibility zones, $q_{j,c}$ is the carbon value of load j.

$$q_j(t) = \begin{cases} q_0 - \frac{1}{2}\lambda, e_j(t) \in \text{Low carbon responsibility zone} \\ q_0, e_j(t) \in \text{Medium carbon responsibility zone} \\ q_0 + \frac{1}{2}\lambda, e_j(t) \in \text{High carbon responsibility zone} \end{cases} \tag{13}$$

where q_0 is the basic price.

4.3 Multi-type load DR modeling

Within a defined time frame, industrial and residential load users have the flexibility to shift a portion of their load without disrupting overall production plans and daily life demands. The primary aim is to execute load shedding during specific scheduling periods to mitigate demand peaks. To realize this goal, this paper introduces two forms of load-side DR through the electro-carbon coupling price acting as the pricing signal. This is achieved through the development of segmented prices, facilitating load transfer. Subsequent to implementation, the load of industrial and residential users for each time period can be represented using Eq. (14).

$$P_{tri,t} = P_{\exp,t} + P_{dr,t} \tag{14}$$

Where $P_{\exp,t}$ is the load value of the node before the response at the moment t, $P_{tri,t}$ is the load value of the node after the response at the moment t, $P_{dr,t}$ is the response value of the load.

During demand response implementation, the two load types previously mentioned need to adhere to the following restrictions: 1) the user's total electricity consumption stays constant during the entire scheduling cycle; 2) the user's load adjustment during each scheduling time period must fall within a predefined permissible range. The permitted range for demand response, given the context of this study, is [-12.5%, +7.5%] of the predicted load for the relevant time period.

$$\begin{cases} \sum_{t=1}^{24} P_{\exp,i,t} = \sum_{t=1}^{24} P_{\text{tri},i,t} \\ -0.125 P_{\exp,i,t} \le P_{\det,t} \le 0.075 P_{\exp,i,t} \end{cases} \tag{15}$$

Commercial loads including large shopping malls, schools and hospitals, are deemed rigid in this paper due to inherent industry limitations. These loads possess limited capacity for load transfer and face challenges in utilizing time-sharing prices for load shifting. In operational scenarios, users of such loads can receive instructions for load reduction, empowering them to voluntarily cut a portion of their load. In exchange for their responsive actions, users receive compensation. The load reduction model is depicted in Eqs. 16, 17.

$$P_{cut,t} \le P_{cut,t,\max}, t \in T_{out} \tag{16}$$

$$P_{cut,t,\max} \le 0.1 P_{\exp,j,t} \tag{17}$$

Where $P_{cut,t}$ is the commercial load reduction at the time t, $P_{cut,t,\max}$ is the maximum value of reduction at the time t, and T_{cut} is the time period that can be reduced, and during the time span that allows for reduction, the maximum value of reduction at time t is set to be no more than 10% of the load in that time period.

4.4 Two-stage VPP low-carbon economic scheduling model

4.4.1 First stage scheduling model

The primary objective of the first stage economic scheduling model is to reduce the generation cost of the VPP to its minimum. This objective function includes the power generation costs of thermal, WT and PV, along with the start-up (shut-down) cost of thermal units and the associated carbon trading costs. The detailed expression is depicted in Eq. (18).

$$f_1 = \min\left(f_g + f_w + f_v + f_k + f_s + f_c\right) \tag{18}$$

Where f_g denotes the fuel cost of thermal power units, f_w is the generation cost of WT, f_v is the generation cost of PV, f_k is the start-up (shut-down) cost of thermal power units, f_s refers to the operation and maintenance cost of energy storage equipment, and f_c is the cost of carbon trading.

$$\begin{cases} f_g = \sum_{t=0}^{T}\sum_{h=1}^{H}\left(a_h P_{G,h,t}^2 + b_h P_{G,h,t} + c_h\right) \\ f_w = \sum_{t=0}^{T}\sum_{k=0}^{K}\left(b_k P_{W,k,t}\right) \\ f_v = \sum_{t=0}^{T}\sum_{l=0}^{L}\left(b_v P_{V,l,t}\right) \\ f_k = \sum_{t=0}^{T}\sum_{h=1}^{H}\left(U_{h,t+1}\left(1-U_{h,t}\right) + U_{h,t}\left(1-U_{h,t+1}\right)C_{U,h}\right) \\ f_{soc} = \sum_{t=0}^{T}\omega_{soc}\left|P_{soc,t}\right| \\ f_c = \sum_{t=0}^{T}\varepsilon\left(E_{d,t} - E_{c,t}\right) \end{cases} \tag{19}$$

Where a_h, b_h, c_h signifies the cost coefficients of coal consumption for the unit, b_k, b_v are the cost coefficients of WT and PV, $P_{G,h,t}$, $P_{W,k,t}$, $P_{V,k,t}$ are the output power of thermal power, WT and PV in the time period t. $U_{h,t}$ is the start-up (shut-down) variable of the thermal power unit h in the time period t, which takes the values of 0 and 1, $C_{U,h}$ is the start-up (shut-down) cost of the unit h, H, K, L are the numbers of various types of units, ω_{SOC} is the cost coefficient of operation and maintenance of the storage equipment, $P_{SOC,t}$ is the power of the storage energy in time period t, and ε is the price of the carbon trade, $E_{d,t}$ is the carbon emission.

The constraints are as follows:

1) Thermal unit capacity and ramping constraints.

$$\begin{cases} P_{\mathrm{G,min}} \le P_{\mathrm{G},t} \le P_{\mathrm{G,max}} \\ R_{\mathrm{down}} \le P_{\mathrm{G},t} - P_{\mathrm{G},t-1} \le R_{\mathrm{up}}\ (t \ge 2) \end{cases} \tag{20}$$

Where $P_{G,\min}$, $P_{G,\max}$ are the maximum and minimum values of active output from thermal power units, R_{up} and R_{down} represent the maximum and minimum values of climbing power.

2) WT and PV capacity constraints.

$$\begin{cases} P_{\mathrm{W,min}} \le P_{\mathrm{W},t} \le P_{\mathrm{W,max}} \\ P_{V,\min} \le P_{V,t} \le P_{V,\max} \end{cases} \tag{21}$$

Where $P_{W,\max}$, $P_{V,\max}$ and $P_{W,\min}$, $P_{V,\min}$ represent the maximum and minimum values of the active output of WT and PV, respectively.

3) Energy storage capacity and charge/discharge state constraints.

$$SOC_{\min} \le SOC(t) \le SOC_{\max} \tag{22}$$

$$\begin{cases} X_{\mathrm{cha},t} + X_{\mathrm{dis},t} = 1, e_{\mathrm{cha}}(t) \ne e_{\mathrm{dis}}(t) \\ X_{\mathrm{cha},t} + X_{\mathrm{dis},t} = 0, e_{\mathrm{cha}}(t) = e_{\mathrm{dis}}(t) \end{cases} \tag{23}$$

Where $SOC_{\min}$ and $SOC_{\max}$ are the maximum and minimum values of the capacity of the energy storage equipment, suggest that the energy storage is undergoing a charging process, and similarly $X_{dis,t} = 1$ suggest that the energy storage is undergoing a discharging process.

4) Power balance constraints.

$$\sum_{\mathrm{h}=1}^{H} P_{G,t} + \sum_{k=1}^{K} P_{W,t} + \sum_{l=1}^{L} P_{V,t} = P_{L,\mathrm{t}} \tag{24}$$

Where $P_{L,t}$ denotes the load power.

4.4.2 Second stage scheduling model

This paper employs the first stage model to derive the start-up (shut-down) plan and unit output for generating units within the carbon trading market. The resulting data, encompassing both start-up (shut-down) plans and unit outputs, are subsequently transmitted to the second stage model. In the second stage, the load-side electricity and carbon coupling price function as the pricing signal, accounting for multiple load types in DR. The load amounts for responsive nodes are fed into the first stage scheduling model, and these steps are iteratively executed until the discrepancy in load-side DR changes falls below the critical value. The second stage low-carbon scheduling model is designed to minimize the combined cost of customer power purchases and DR, as depicted in Eq. (25).

$$f_2 = \min\left(f_{dr} + f_{cut} + f_q\right) \tag{25}$$

Where f_{dr} is the industrial and residential load node price DR cost, f_{cut} is the commercial load node load curtailment compensation cost, and f_q is the customer's power purchase cost.

$$\begin{cases} f_{\mathrm{dr}} = \sum_{t=1}^{24}\sum_{i=1}^{G_{IP}+G_{RP}} P_{\mathrm{dr},t} c_{\mathrm{dr}} \\ f_{cut} = \sum_{t=1}^{T_{cut}}\sum_{i=1}^{G_{CP}} P_{\mathrm{cut},t} c_{\mathrm{cut}} \\ f_q = \sum_{t=0}^{T}\sum_{j=1}^{G} P_{j,t} q_{\mathrm{j}}(t) \end{cases} \tag{26}$$

Where G is the number of load nodes, G_{IP}, G_{CP} and G_{RP} are industrial loads, commercial loads, residential loads node-set, c_{dr} is the industrial and residential loads DR cost price per unit of load volume, c_{cut} is the commercial and residential loads to cut down the cost of compensation per unit of load volume, and $P_{j,t}$ is the power consumption of j node at t moment.

4.4.3 Flowchart for solving the two-stage scheduling model

Figure 4 displays the flowchart outlining the two-stage VPP low-carbon economic scheduling model.

The model workstream is as follows:

1) Commence the process by inputting unit node parameters, load forecast data, carbon quota parameters and other essential example-based data.
2) Solve the first stage VPP economic scheduling model to obtain the output, carbon emissions, active power data transmitted by each line during the unit scheduling cycle. Simultaneously, calculate the carbon intensity of each node by utilizing the CEF method.

3) Develop electric-carbon coupling prices grounded in the carbon intensity for each node.
4) Enter the second stage virtual power plant low carbon scheduling model to solve for the optimized loadings.
5) The optimized load quantity is resubstituted into the upper model to re-do the day-ahead scheduling. The above process is repeated until the difference in the load-side demand response change between the two processes is less than the critical value, then the optimal scheduling scheme and results are outputted.

In this particular instance, the dichotomy is employed as a means of imposing constraints that effectively prevent the emergence of oscillatory non-convergence. Dichotomous iteration addresses oscillation issues by adopting a heuristic strategy known as equipartitioning. Its core principle lies in establishing a practical load-interval that consistently encompasses the optimal operational state. Subsequently, through iterative adjustments to either the lower or upper bounds, this interval range is progressively narrowed, until it converges to or falls below the predefined convergence threshold. This methodical narrowing process ensures that the system stabilizes and converges to an optimal solution. To further clarify the process, Figure 5 provides a schematic diagram that illustrates the steps involved in the dichotomous iteration process.

The detailed procedure for the dichotomy method is outlined below: if the kth iteration oscillates, the load corresponding to the electricity demand is $P_{\varphi,t}^{buy}$, set as the maximum value of the power demand at time t as $P_{\varphi,t}^{buy,\max}$, $P_{\varphi,t}^{buy,\max} = \max\left\{P_{\varphi,t}^{buy}, P_{\varphi-1,t}^{buy}\right\}$, and the minimum value of the electricity demand at time t as $P_{\varphi,t}^{buy,\min}$, $P_{\varphi,t}^{buy,\min} = \min\left\{P_{\varphi,t}^{buy}, P_{\varphi-1,t}^{buy}\right\}$, which will be set to be the load operation interval, and the optimal operational condition lies within this range.

Step 1: The average value of electricity consumption at moment t is $P_{t,ave}^{buy}$, $P_{t,ave}^{buy} = (P_{\varphi,t}^{buy,\max} + P_{\varphi,t}^{buy,\min})/2$.
Step 2: Adding constraints: $P_t^{buy} = P_{t,ave}^{buy}$, solving the two-layer model. This step splits the current running interval into two-halves and terminates the iteration if the convergence condition is satisfied. Otherwise $\varphi = \varphi + 1$, perform step 3.
Step 3: Adding constraints: $P_{\varphi,t}^{buy,\min} \le P_t^{buy} \le P_{\varphi,t}^{buy,\max}$, solving the two-layer model. This step obtains a new run interval containing the optimal state. If the convergence condition is satisfied, the iteration is terminated. Otherwise, perform step 4.
Step 4: If $P_t^{buy} = P_{\varphi,t}^{buy,\max}$, the optimal state is within $[P_{t,ave}^{buy}, P_{\varphi,t}^{buy,\max}]$, Update the lower bound, let $P_{\varphi,t}^{buy,\min} = P_{t,ave}^{buy}$; if $P_{\varphi,t}^{buy,\min} = P_t^{buy}$, update the upper bound, let $P_{\varphi,t}^{buy,\max} = P_{t,ave}^{buy}$. Then return to step 1 until the convergence condition is satisfied.

5 Case study

5.1 Basic data

The improved IEEE-14 node system is used for the arithmetic example analysis, the distribution of units is shown in Figure 6, and the distribution of multiple types of load nodes is shown in Table 1. The predicted power of WT and PV is shown in Figure 7. A period of 24 h and a step size of 1 h is set to solve the problem using the CPLEX simulation platform.

5.2 Simulation results analysis

To confirm the efficacy of the proposed low-carbon economy scheduling model, sets up and analyzes three operational scenarios through simulation. Scenario A is the two-stage low-carbon economic scheduling of VPP proposed in this paper. Scenario B adopts the traditional time-sharing price DR modeling in (Zhao et al., 2022) for VPP scheduling. Scenario C does not consider DR modeling for VPP scheduling.

By contrasting the carbon emissions and economical operating expenses of the previously discussed scenarios. Figures 8, 9 show that the main factor affecting the variation in carbon emissions is the amount of clean energy used during the scheduling period. The quantity of clean energy used determines how much displacement the thermal power unit can produce. As the use of renewable energy increases, thermal power output decreases, resulting in lower carbon emissions. Based on a combined analysis of Table 2 and Figures 8A,C, gas turbine power has a higher proportion and the clean energy consumption rate is lower when DR is ignored. In Scenario C, there is an increase in gas turbine output during peak load hours, which raises generation costs and carbon emissions. On the other hand, in Scenario A, consumers engage in DR by allocating a portion of the load to the clean energy unit that has a higher output. This lowers generation costs and carbon emissions while simultaneously encouraging the use of clean energy.

Through a comprehensive analysis involving Table 2 and Figures 8A,B, it becomes evident that the clean energy consumption rate is higher in the scheduling model proposed in this paper, leading to a reduction in gas turbine output. This is because, compared with conventional time-sharing tariffs, the electric-carbon coupling price based on load electric-carbon characteristics takes into account the differences in carbon emissions at the nodes to reasonably calculate the carbon price at different nodes, to formulate a reasonable price, which enables the users to be more actively involved in the DR, promotes the clean energy consumption and reduces carbon emissions.

The comparison of clean energy consumption rates under different scenarios in Figure 9 shows that the multi-type demand response improves the low-carbon incentive effect for the system. The time-sharing load-side electricity-carbon coupling price signal guides the users to consciously carry out low-carbon electricity consumption behaviors and thus reduces the amount of abandoned wind and light, the carbon emission and system operation cost, which demonstrates that the multi-type demand response model proposed in this paper can enhance the low-carbon economic benefit. Figures 9, 10 reveal that, in comparison to Scenario B and Scenario C, the new energy units in Scenario A are fully utilized, the carbon emissions of the three types of regions are all reduced, and the carbon emissions of the industrial regions in the three types of regions are greatly restricted, which is in line with the priority requirement of carbon restriction in the industrial and commercial regions in the context of the dual-carbon mechanism.

As seen in Figure 11, Scenario A contrasts the system load change curves before and after DR. During the 2 hours of the midday and evening peaks, the commercial load is somewhat reduced by the

electric power load. At the same time, a portion of the peak load is transferred to the load side valley by the DR model, which uses the linked price of carbon and electric power as the price signal. The results of the scheduling without DR indicate that the gas turbine production rises between 11:00 and 20:00, which raises the system's generating costs and carbon emissions. After DR, part of the peak shortfall load is shifted and curtailed to the 5:00–10:00 and 20:00–23:00 valley hours, where the load is mostly supplied by clean energy, thus reducing both carbon emissions and operating costs.

6 Conclusion

Based on the electric-carbon coupling relationship of distributed resources and the theory of CEF, this paper proposes a low-carbon optimal scheduling method for VPP considering the CEF and DR, making full use of the adjustable resources to enhance the low-carbon economic advantages of VPP as well as facilitating the utilization of clean energy sources, which is verified by the simulation of the improved IEEE-14 node system example. the following conclusions can be obtained:

The proposed two-stage optimal scheduling model for VPP considers both the cost of generation and carbon emissions in a comprehensive manner. Through the source-load-storage cooperative scheduling strategy, the load side consumes a higher proportion of renewable energy, leading to a significant reduction in carbon emissions. Additionally, the establishment of a DR model, which is based on the coupled price of electricity and carbon, and considers multiple types of loads, holds significant practical value for reducing emissions. This model not only meets the carbon reduction needs of diverse user categories but also addresses the dual requirements of low carbon and economy aligned with the dual carbon objective. Furthermore, it provides innovative ways to explore low-carbon measures tailored to specific load categories within the carbon trading market.

Data availability statement

The original contributions presented in the study are included in the article/Supplementary Material, further inquiries can be directed to the corresponding author.

Author contributions

YW: Conceptualization, Data curation, Formal Analysis, Investigation, Methodology, Software, Validation, Writing–original draft, Writing–review and editing. Jiantie Xu: Conceptualization, Formal Analysis, Funding acquisition, Project administration, Resources, Visualization, Writing–review and editing. WP: Data curation, Validation, Writing–review and editing. Hanyang Wang: Data curation, Validation, Writing–review and editing. ZZ: Data curation, Validation, Writing–review and editing.

Funding

The author(s) declare that financial support was received for the research, authorship, and/or publication of this article. The author(s) declare financial support was received for the research, authorship, and/or publication of this article. This work was supported by the State Grid Liaoning Electric Power Co., Ltd. Technology project–Research on day-ahead optimal scheduling strategy considering multi-virtual power plant P2P transactions under the joint electricity-carbon market (2023ZX-01).

Conflict of interest

Authors JX, WP, HW, and ZZ were employed by State Grid Liaoning Electric Power Co., Ltd. The authors declare that this study received funding from the State Grid Liaoning Electric Power Co., Ltd. The funder had the following involvement in the study: the research design, data collection and analysis, decision to publish, preparation of the manuscript, and provided solutions and assistance with the writing of the manuscript.

The remaining author declares that the research was conducted in the absence of any commercial or financial relationships that could be construed as a potential conflict of interest.

Publisher's note

All claims expressed in this article are solely those of the authors and do not necessarily represent those of their affiliated organizations, or those of the publisher, the editors and the reviewers. Any product that may be evaluated in this article, or claim that may be made by its manufacturer, is not guaranteed or endorsed by the publisher.

References

Cao, C., Xie, J., Yue, D., Zhao, J., Xiao, Y., and Wang, L. (2016). "A distributed gradient algorithm based economic dispatch strategy for virtual power plant," in *2016 35th Chinese control conference (CCC)* (Chengdu, China: IEEE), 7826–7831.

Cheng, Y., Zhang, N., Lu, Z., and Kang, C. (2019). Planning multiple energy systems toward low-carbon society: a decentralized approach. *IEEE Trans. Smart Grid* 10, 4859–4869. doi:10.1109/TSG.2018.2870323

Cheng, Y., Zhang, N., Wang, Y., Yang, J., Kang, C., and Xia, Q. (2019). Modeling carbon emission flow in multiple energy systems. *IEEE Trans. Smart Grid* 10, 3562–3574. doi:10.1109/TSG.2018.2830775

Cheng, Y., Zhang, N., Zhang, B., Kang, C., Xi, W., and Feng, M. (2020). Low-carbon operation of multiple energy systems based on energy-carbon integrated prices. *IEEE Trans. Smart Grid* 11, 1307–1318. doi:10.1109/TSG.2019.2935736

Da, C. (2016). *Study on factor decomposition and network stream analysis of carbon emission in power systems*. Hangzhou: Zhejiang University.

Huang, B., Li, Y., Zhan, F., Sun, Q., and Zhang, H. (2022). A distributed robust economic dispatch strategy for integrated energy system considering cyber-attacks. *IEEE Trans. Industrial Inf.* 18, 880–890. doi:10.1109/TII.2021.3077509

Kang, C., Chen, X., Su, J., Ai, Q., Ji, Y., Pan, W., et al. (2022). Scientific issues and research framework of a new power system scale-up flexible resource virtual power plant. *Automation Electr. Power Syst.* 46, 3–14. doi:10.7500/AEPS20220401007

Kang, C., Zhou, T., Chen, Q., Wang, Q., Sun, Y., Xia, Q., et al. (2015). Carbon emission flow from generation to demand: a network-based model. *IEEE Trans. Smart Grid* 6, 2386–2394. doi:10.1109/tsg.2015.2388695

Lei, R., Zhou, M., Wu, Z., Sha, Y., Zhang, Y., and Liu, X. (2020). "The optimal operation and revenue allocation method of virtual power plant considering carbon trading," in *2020 IEEE 4th conference on energy internet and energy system integration*, 2396–2402. doi:10.1109/ei250167.2020.9347001

Li, T., Huang, R., Chen, L., Jensen, C. S., and Pedersen, T. B. (2020). Compression of uncertain trajectories in road networks. *Proc. VLDB Endow.* 13, 1050–1063. doi:10.14778/3384345.3384353

Li, W., Liang, R., Luo, F., Feng, S., Yang, B., Liu, Z., et al. (2022). Response potential assessment of user-side flexible resources of regional power distribution networks based on sequential simulation of optimal operation. *Front. Energy Res.* 10, 1096046. doi:10.3389/fenrg.2022.1096046

Li, Y., Gao, D. W., Gao, W., Zhang, H., and Zhou, J. (2020). Double-mode energy management for multi-energy system via distributed dynamic event-triggered Newton-raphson algorithm. *IEEE Trans. Smart Grid* 11, 5339–5356. doi:10.1109/TSG.2020.3005179

Li, Y., Gao, D. W., Gao, W., Zhang, H., and Zhou, J. (2021). A distributed double-Newton descent algorithm for cooperative energy management of multiple energy bodies in energy internet. *IEEE Trans. Industrial Inf.* 17, 5993–6003. doi:10.1109/TII.2020.3029974

Li, Y., Zhang, H., Liang, X., and Huang, B. (2019). Event-triggered-based distributed cooperative energy management for multienergy systems. *IEEE Trans. Industrial Inf.* 15, 2008–2022. doi:10.1109/TII.2018.2862436

Li, Y., Zhou, L., Wang, D., Gao, Z., and Wu, X. (2022). Virtual power plant economic dispatching considering user classification. *Power Syst. Prot. Control* 50, 121–130. doi:10.19783/j.cnki.pspc.211449

Liu, Z., Huang, B., Hu, X., Du, P., and Sun, Q. (2023). Blockchain-based renewable energy trading using information entropy theory. *IEEE Trans. Netw. Sci. Eng.*, 1–12. doi:10.1109/TNSE.2023.3238110

Liu, Z., Huang, B., Li, Y., Sun, Q., Pedersen, T. B., and Gao, D. W. (2024). Pricing game and blockchain for electricity data trading in low-carbon smart energy systems. *IEEE Trans. Industrial Inf.* 20, 6446–6456. doi:10.1109/TII.2023.3345450

Liu, Z., Xu, Y., Zhang, C., Elahi, H., and Zhou, X. (2022). A blockchain-based trustworthy collaborative power trading scheme for 5G-enabled social internet of vehicles. *Digital Commun. Netw.* 8, 976–983. doi:10.1016/j.dcan.2022.10.014

Naughton, J., Wang, H., Cantoni, M., and Mancarella, P. (2021). Co-optimizing virtual power plant services under uncertainty: a robust scheduling and receding horizon dispatch approach. *IEEE Trans. Power Syst.* 36, 3960–3972. doi:10.1109/TPWRS.2021.3062582

Nguyen Duc, H., and Nguyen Hong, N. (2021). Optimal reserve and energy scheduling for a virtual power plant considering reserve activation probability. *Appl. Sci.* 11, 9717. doi:10.3390/app11209717

Sun, W., Xiang, Z., Yang, L., Wo, J., Ma, X., Fang, X., et al. (2023). "Low carbon scheduling of integrated energy systems considering stepped carbon trading and demand response," in *2023 3rd power system and green energy conference (PSGEC)*, 291–295.

Tang, J., Liu, J., Sun, T., Kang, H., and Hao, X. (2023). Multi-time-scale optimal scheduling of integrated energy system considering demand response. *IEEE Access* 11, 135891–135904. doi:10.1109/ACCESS.2023.3335242

Wang, S., and Wu, W. (2021). Aggregate flexibility of virtual power plants with temporal coupling constraints. *IEEE Trans. Smart Grid* 12, 5043–5051. doi:10.1109/TSG.2021.3106646

Wang, Y., and Teng, Y. (2023). "Economic dispatching model of virtual power plant and carbon emission under carbon trading mechanism," in *2023 IEEE international conference on control, electronics and computer Technology (ICCECT)*, 765–769.

Yang, C., Liu, J., Liao, H., Liang, G., and Zhao, J. (2023). An improved carbon emission flow method for the power grid with prosumers. *Energy Rep.* 9, 114–121. doi:10.1016/j.egyr.2022.11.165

Zahra, A., Hooshmand, R. A., and Soleymani, S. (2021). Optimal integration of demand response programs and electric vehicles in coordinated energy management of industrial virtual power plants. *J. Energy Storage* 41, 102951. doi:10.1016/j.est.2021.102951

Zhang, Z., Yang, X., Zhao, S., Wu, D., Cao, J., Gao, M., et al. (2022). Large-signal stability analysis of islanded DC microgrids with multiple types of loads. *Int. J. Electr. Power & Energy Syst.* 143, 108450. doi:10.1016/j.ijepes.2022.108450

Zhao, L., Wang, X., Ding, Y., Guo, Y., and Li, J. (2022). Optimal scheduling of multi-energy virtual power plant considering time-sharing tariff and participation of photovoltaic power plant. *Power Constr.* 43, 119–129. doi:10.12204/j.issn.10007229.2022.04.013

Zhou, T., Kang, C., Xu, Q., and Chen, Q. (2012). Preliminary investigation on a method for carbon emission flow calculation of power system. *Automation Electr. Power Syst.* 36, 44–49. doi:10.3969/j.issn.1000-1026.11.008

frontiers | Frontiers in Energy Research

TYPE Hypothesis and Theory
PUBLISHED 06 September 2024
DOI 10.3389/fenrg.2024.1413297

Check for updates

OPEN ACCESS

EDITED BY
Yushuai Li,
Aalborg University, Denmark

REVIEWED BY
Jay Zarnikau,
The University of Texas at Austin, United States
Yunting Yao,
Nanjing Normal University, China

*CORRESPONDENCE
Xu Wen,
2536692102@qq.com

RECEIVED 08 April 2024
ACCEPTED 01 July 2024
PUBLISHED 06 September 2024

CITATION
Wen X, Zhou Q, Luo B, Yang Y, Mao R and Fan D (2024), Impact of different reserve cost allocation mechanisms on market participants' revenues: a quantitative analysis.
Front. Energy Res. 12:1413297.
doi: 10.3389/fenrg.2024.1413297

COPYRIGHT
© 2024 Wen, Zhou, Luo, Yang, Mao and Fan. This is an open-access article distributed under the terms of the Creative Commons Attribution License (CC BY). The use, distribution or reproduction in other forums is permitted, provided the original author(s) and the copyright owner(s) are credited and that the original publication in this journal is cited, in accordance with accepted academic practice. No use, distribution or reproduction is permitted which does not comply with these terms.

Impact of different reserve cost allocation mechanisms on market participants' revenues: a quantitative analysis

Xu Wen*, Quan Zhou, Baosong Luo, Yang Yang, Rui Mao and Dong Fan

Southwest Subsection of State Grid, Chengdu, China

Insufficient flexibility is a major barrier to the development of new power systems. Leveraging the resource allocation function of the electricity market is a promising way to enhance the flexibility of power systems and promote the consumption of renewables. The reasonable allocation of ancillary service costs plays a pivotal role in this function. Towards the target of "who causes, who shares," various research related to cost allocation has been conducted. However, there is a lack of quantitative analysis of the impact of different cost allocation mechanisms on the market participants' revenues. Whether various cost allocation mechanisms can alleviate the insufficient flexibility problem of power systems needs to be validated. With this in mind, taking operating reserve ancillary services as an example, a long-term market operation simulation model with energy-reserve joint clearing is established in this paper based on the time series production simulation. According to this, the revenues of market participants under different reserve cost allocation mechanisms are quantified. Besides, a self-dispatch model for the energy storage (ES) equipped by renewables is established, based on which the impact of ES on the revenues of renewables under different cost allocation mechanisms is analyzed. Case studies based on practical data from a provincial power grid in China demonstrate that with the well-designed reserve cost allocation mechanism, the revenues of flexible resources can be ensured. Meanwhile, renewables are incentivized to reduce their fluctuations and uncertainties by equipping the ES. Hence, the insufficient flexibility problem of power systems can be alleviated from both supply and requirements perspectives.

KEYWORDS

cost allocation mechanisms, electricity market, market operation simulation, market revenue calculation, self-dispatch of energy storage (ES)

1 Introduction

In recent years, the large-scale integration of renewables has brought significant challenges to the safe and stable operation of power systems due to their inherent fluctuations and uncertainties. Regarding this, leveraging the resource allocation function of the electricity market plays a crucial role in enhancing the operational flexibility of power systems and promoting the consumption of renewables. The resource allocation function of the electricity market is twofold: it provides reasonable compensation to flexible resources that offer ancillary services, and thus, they are

incentivized to provide ancillary services to handle the variability of renewables (Fang et al., 2019); and it reasonably allocates the ancillary services costs to market participants that cause the requirements for services, and thus, they are incentivized to reduce their variability. The aforementioned resource allocation function can alleviate the impact of renewables from both the supply and requirements of ancillary services (Chen et al., 2015; Ela and Hytowitz et al., 2019; Yu et al., 2019).

The reasonable allocation of ancillary service costs is the key part of the resource allocation function (Gazafroudi et al., 2015; Buchholz et al., 2019), which affects the revenues of flexible resources and the penalties for market participants that cause the requirements for services. This issue has drawn global attention. In industrial practice, China mainly allocates the ancillary service costs in proportion to the generated or consumed energy of market participants. This method is easy to implement. However, the variability of market participants cannot be considered (Prica and Ilic, 2006). Australia allocates the ancillary service costs according to the deviation responsibility, for instance, the frequency regulation costs are allocated based on the deviation between the planned and actual energy of market participants (AEMO et al., 2018). This method can reflect the variability of market participants to some extent. However, the providers of ancillary services need to undertake service costs, which affects their market revenues (Morales-Espana et al., 2016). California allocates the ancillary service costs in proportion to the declared ancillary service requirements of market participants (Yu et al., 2019). The actual variability of market participants cannot be considered. Regarding the drawbacks of the methods used in industrial practices, researchers have proposed various cost allocation methods to achieve that target of "who causes, who shares." These methods include the method based on the Vickrey-Clarke-Groves (VCG) theory (Xiang et al., 2023), forecast accuracy (He et al., 2019), risk contribution theory (Liang et al., 2007), the Shapley value (Haring et al., 2014), and price components of ancillary services (Wang et al., 2020), etc. Among them, based on the contribution of renewables and load to the reserve requirement, reference Wang et al. (2020) derivates the reserve price component to achieve the natural allocation of reserve costs. If the contribution of renewables and load to the reserve requirement is accurate, this method can achieve the target of "who causes, who shares". In the following part of this paper, this method will be regarded as the ideal cost allocation mechanism and compared with other traditional cost allocation mechanisms.

In summary, toward the target of "who causes, who shares," various cost allocation methods have been proposed. Nevertheless, the impact of different cost allocation mechanisms on the market participants' revenues has not been quantitatively analyzed. How could different cost allocation mechanisms alleviate the insufficient flexibility problem of power systems is not clear. The necessity of a reasonable cost allocation mechanism needs to be further validated.

With this in mind, taking the operating reserve as the research object, the market participants' revenues under different cost allocation mechanisms are quantitatively analyzed in this paper based on the long-term market operation simulation. The effect of ensuring flexible resources' revenues and incentivizing renewables to reduce their variability of different cost allocation mechanisms is explored, which can give references for the design of the cost allocation mechanism. In this paper, the market participants include renewables, load, and thermal power units. The energy storage devices mentioned in this paper are equipped with renewables. Hence, they belong to renewable entities. The contributions of this paper are listed as follows:

1) Based on the time series production simulation, a long-term market operation simulation model with energy-reserve joint clearing is established in this paper. In the established model, the contributions of renewables and load to the reserve requirement are described according to their historical forecast errors. A self-dispatch model for energy storage (ES) equipped by renewables is established. The forecast errors of renewables can be reduced by the equipped ES, and thus, their contributions to the reserve requirement can be reduced. According to the market clearing prices and different cost allocation mechanisms, the market participants' revenue calculation model considering the equipped ES is constructed, which lays a foundation for analyzing how could different cost allocation mechanisms alleviate the insufficient flexibility problem of power systems.
2) Based on the practical data from a provincial power grid in China, a quantitative analysis of market participants' revenues is conducted under different cost allocation mechanisms, variability of renewables, and capacities of the equipped ES. Case studies demonstrate that compared with the method based on energy generation/consumption used in Chinese industry, the method based on "who causes, who shares" can ensure the revenues of flexible resources better (revenues are improved by 3.34%). Besides, under the method based on "who causes, who shares," the revenues of renewables can be greatly improved by equipping the ES (reflected in the 28.64% improvement in energy revenues and the 49.61% reduction of allocated reserve costs). While under the method based on energy generation/consumption, the allocated reserve costs of renewables will instead increase by 61.11% after the configuration of the ES, which affects the total revenues of renewables. Therefore, the reasonable cost allocation mechanism can alleviate the insufficient flexibility problem of power systems by ensuring the flexible resources' revenues and incentivizing renewables to reduce their variability.

2 Long-term market operation simulation model with energy-reserve joint clearing

To quantitatively assess the revenues of market participants under various reserve cost allocation strategies, a simulation of the power spot market's daily operations is required, utilizing extensive load and renewables data via time-series production simulation theory. This section outlines the energy-reserve market joint clearing model employed in this study, enabling the determination of market participants' operational modes through model resolution. Subsequently, Section 3 will evaluate the impacts of different reserve cost allocation mechanisms on market participants' revenues. The energy-reserve joint clearing model utilized in this study is detailed further below.

2.1 Energy-reserve joint market clearing model considering contributions of market participants to reserve requirement

2.1.1 Objective function

The market clearing model's objective function aims to minimize the system's operating costs:

$$\min\left\{\left[\sum_{k\in K}\left[\sum_{t\in T}\left[\sum_{g\in G}\left[b_{\mathrm{E},g}^{t,k}\times P_g^{t,k}+b_{\mathrm{R},g}^{t,k,\mathrm{UP}}\times R_g^{t,k,\mathrm{UP}}+b_{\mathrm{R},g}^{t,k,\mathrm{DN}}\times R_g^{t,k,\mathrm{DN}}+C_{g,\mathrm{U}}^{t,k}+C_{g,\mathrm{D}}^{t,k}\right]+C_r^{t,k}\right]\right]\right]\right\} \tag{1}$$

$$C_r^{t,k}=\left[\sum_{v\in V}r_v\left(P_v^{t,k,\mathrm{f}}-P_v^{t,k}\right)+\sum_{d\in D}r_d\left(P_d^{t,k,\mathrm{f}}-P_d^{t,k}\right)\right] \tag{2}$$

$$\begin{cases}C_{g,\mathrm{U}}^{t,k}\geq K_g\left(u_g^{t,k}-u_g^{t-1,k}\right)\\ C_{g,\mathrm{U}}^{t,k}>=0\end{cases} \tag{3}$$

$$\begin{cases}C_{g,\mathrm{D}}^{t,k}\geq M_g\left(u_g^{t,k}-u_g^{t-1,k}\right)\\ C_{g,\mathrm{D}}^{t,k}>=0\end{cases} \tag{4}$$

When $u_g^{t,k}$ is 0, the thermal power unit is shut down. When $u_g^{t,k}$ is 1, the thermal power unit is operational.

2.1.2 Operating constraints

2.1.2.1 Line power flow constraints

$$\left(\sigma_l^{t,k,l-}\right),P_l{}^{\min}\leq\sum_{j\in J}H_{lj}\left(A_{jg}P_g^{t,k}+A_{jv}P_v^{t,k}-P_d^{t,k}\right)\leq P_l{}^{\max},\left(\sigma_l^{t,k,l+}\right) \tag{5}$$

2.1.2.2 Power balance constraints

$$\sum_{v\in V}P_v^{t,k}+\sum_{g\in G}P_g^{t,k}=\sum_{d\in D}P_d^{t,k},\left(\sigma_b^{t,k}\right) \tag{6}$$

2.1.2.3 Reserve constraints

The aggregated frequency regulation capacity across all units must satisfy the system's overall frequency regulation requirements.

$$\sum_{g\in G}R_g^{t,k,\mathrm{UP}}\geq R_{sys}^{t,k,\mathrm{UP}},\left(\lambda_{\mathrm{R}}^{t,k,\mathrm{UP}}\right) \tag{7}$$

$$\sum_{g\in G}R_g^{t,k,\mathrm{DN}}\geq R_{sys}^{t,k,\mathrm{DN}},\left(\lambda_{\mathrm{R}}^{t,k,\mathrm{DN}}\right) \tag{8}$$

$$R_{sys}^{t,k,\mathrm{UP}}=\pi_dP_d^{t,k,\mathrm{UP}}+\pi_vP_v^{t,k,\mathrm{UP}} \tag{9}$$

$$R_{sys}^{t,k,\mathrm{DN}}=\pi_dP_d^{t,k,\mathrm{DN}}+\pi_vP_v^{t,k,\mathrm{DN}} \tag{10}$$

where the ratio $\pi_{di/vi}$ is determined by the maximum ratio between the historical forecast errors of market members and their corresponding predicted power generation capacity/load demand (the system reserves capacity to address the maximum forecast error of market members). It is noted that the focus of this paper is not to accurately quantify the operating reserve requirement of the power system. Instead, this paper aims to quantitatively analyze the impact of different cost allocation mechanisms on the market participants' revenues, thus, demonstrating the effectiveness of the cost allocation mechanism that obeys the principle of "who causes, who shares." Therefore, the offset of prediction errors of renewables and load is ignored and the ratio $\pi_{di/vi}$ is assumed to be accurate, based on which the reserve cost allocation that obeys the principle of "who causes, who shares" can be achieved. Besides, so far, there still lacks a cost allocation mechanism that can achieve the target of "who causes, who shares" considering the impact of conventional generators, renewables, and load. Therefore, to achieve a reasonable cost allocation that obeys the principle of "who causes, who shares" and simplify the analysis, this paper does not consider the impact of conventional generators on the reserve requirement. The reasonable cost allocation mechanism that considers conventional generators is worthy of future research but out of the scope of this paper.

Except for the constraints illustrated above, constraints related to the upper/lower output limits of thermal power units, the upward/downward ramping limits of thermal power units, and the operating status of the last period on day k being the same as the first period on day $(k+1)$ are common constraints for thermal power unit operation. Additionally, the constraints related to the curtailment of renewable energy units and load are also considered. Due to space limitations, these constraints are not illustrated in detail.

The market clearing model outlined in this section enables the daily determination of scheduling and operation plans for various market participants. This forms the basis for calculating subsequent earnings for market participants.

2.2 Self-dispatch model for energy storage equipped by renewables

An effective alternative cost allocation mechanism should incentivize renewable sources to reduce their forecast errors through the deployment of ES systems. This requires that the market revenues of renewable sources, post-storage deployment, exceed their pre-storage revenues, with a growth rate higher than that of renewable sources without storage deployment. To analyze whether different cost allocation mechanisms can motivate renewable sources to voluntarily deploy storage, this section develops a self-dispatch model for renewables with integrated storage. This model can reflect, through historical operation data of renewable sources, the extent to which proper storage operation planning can reduce the daily maximum forecast error. As discussed in Section 2.1, the reduction in the maximum forecast error reduces the reserve impact of renewable sources, thereby decreasing the overall system reserve requirements and total reserve costs.

2.2.1 Objective function

The objective function for the self-dispatch model of renewables with integrated ES, as developed in this study, aims to minimize the maximum prediction error across all operational periods for renewable sources as detailed in the Eqs 11, 12.

$$\min\left\{\max\left(\left|e^{t,k}\right|\right)\right\} \tag{11}$$

$$e^{t,k}=P_v^{t,k,\mathrm{f}}-P_v^{t,k,\mathrm{a}}+\left(\chi_{es,\mathrm{cha}}^{t,k}P_{es,\mathrm{cha}}^{t,k}-\chi_{es,\mathrm{dis}}^{t,k}P_{es,\mathrm{dis}}^{t,k}\right) \tag{12}$$

$\chi_{es,\mathrm{cha}}^{t,k}=1$ Indicates the charging state, and 0 signifies the absence of charging; similarly, $\chi_{es,\mathrm{dis}}^{t,k}=1$ denotes the discharging state, with 0 indicating no discharging. $P_{es,\mathrm{cha/dis}}^{t,k}$ quantifies the power associated with charging or discharging the ES system.

2.2.2 Operating constraints

In the self-dispatch model for renewables with integrated ES, the operational constraints of ES systems include the following:

(1) ES state mutually exclusive constraint

An ES unit can either be in a charging or discharging state at any given time, as detailed in Eq. 13.

$$\chi_{es,\mathrm{cha}}^{t,k} + \chi_{es,\mathrm{dis}}^{t,k} \le 1 \tag{13}$$

(2) Charge/discharge power constraints for ES devices as detailed in the Eqs 14, 15.

$$0 \le P_{es,\mathrm{cha}}^{t,k} \le \chi_{es,\mathrm{cha}}^{t,k} P_{es,\mathrm{cha}}^{t,k,\max} \tag{14}$$

$$0 \le P_{es,\mathrm{dis}}^{t,k} \le \chi_{es,\mathrm{dis}}^{t,k} P_{es,\mathrm{dis}}^{t,k,\max} \tag{15}$$

(3) ES constraints

The energy levels within the storage system must remain within its permissible limits, as specified in Eq. 16:

$$\kappa_{es}{}^{\min} E_{cap} \le E_{es}^{t,k} \le \kappa_{es}{}^{\max} E_{cap} \tag{16}$$

The initial energy level for each day is set based on the final energy level from the preceding day, as outlined in Eq. 17.

$$E_{es}^{24,k} = E_{es}^{1,k+1} \tag{17}$$

The constraint governing changes in ES is detailed in Eq. 18.

$$E_{es}^{t,k} = (1-\alpha_{es})E_{es}^{t-1} + \left(P_{es,\mathrm{cha},i}^{t,k}\delta_{es,\mathrm{cha}} + P_{es,\mathrm{dis}}^{t,k}/\delta_{es,\mathrm{dis}}\right)\Delta t \tag{18}$$

2.2.3 Objective function linearization

The objective function depicted in Eq. 11 is non-linear, hindering the model's solvability. To address this issue, the study linearizes the objective function by introducing an ancillary variable z, thereby transforming it into a linear form devoid of absolute values and the max function. Consequently, the objective function now aims to minimize the value of z, with two additional constraints, as specified in Eq. 19, incorporated into the model.

$$\min z \quad s.t \begin{cases} z \ge e^{t,k} \\ z \ge -e^{t,k} \end{cases} \tag{19}$$

The constraints in Eq. 19 necessitate that the ancillary variable z must be at least as large as the absolute value of the prediction error for renewables in each historical period, ensuring $z \ge \max(|e^{t,k}|)$. Thus, minimizing z equates to reducing the maximum prediction error of renewables across all operational periods. Consequently, the optimization problem, when substituting the original objective function depicted in Eq. 11 with that in Eq. 19, remains equivalent to the original problem.

By implementing the self-dispatch model for renewables integrated with ES, renewables operators can optimally utilize ES systems. This optimization allows for the adjustment of discrepancies between actual and forecasted outputs through strategic charging or discharging of the storage system. Consequently, this reduces the maximum prediction error associated with renewable sources, diminishing their impact on system reserve requirements and enhancing their competitive position in the market. With ES in place, the reserve requirements attributed to the variance in renewables production decrease. As a result, the overall bidding cost of the energy unit is reduced, improving its likelihood of success in market clearing.

3 Total revenues calculation of market participants under different reserve cost allocation mechanisms

3.1 Energy revenues calculation of market participants

Regarding power revenue, the market clearing prices discussed here mainly consist of energy and start-stop prices. Thermal power units earn revenue from both energy and start-stop operations, while renewables sources (considered units with minimal start-stop costs) generate income similarly. On the other hand, the load incurs both energy and start-stop expenses. As explained in Section 2.1, the model for energy-reserve joint clearing introduces a binary variable to indicate the start-stop status of units, which introduces non-convexity into the model. To accurately formulate energy and start-stop prices, this study uses the approach outlined in the reference Wang et al. (2023), converting the original non-convex model into a convex one through the application of artificial constraints.

The clearing model delineated in Section 2.1 is designated as $\boldsymbol{m}1$. Building upon the solution outcomes of $\boldsymbol{m}1$, the price-assisted optimization model $\boldsymbol{m}2$ is developed. In $\boldsymbol{m}2$, the integer variable and $u_g^{t,k}$ from $\boldsymbol{m}1$ are relaxed into continuous variables with values spanning from 0 to 1, as illustrated in Eq. 20. Additionally, an artificial bundle is introduced as depicted in Eq. 21.

$$0 \le u_g^{t,k} \le 1, \forall g, \forall t, \forall k \tag{20}$$

$$\sum_{v\in V} P_v^{t,k} + \sum_{g\in G} PU_g^{t,k} u_g^{t,k} = \sum_{d\in D} P_d^{t,k}, \left(\varsigma_{en}^{t,k}\right) \tag{21}$$

where: $\varsigma_{en}^{t,k}$ represents the dual multiplier of the artificial constraint, and $PU_g^{t,k}$ is determined based on the solution results of $\boldsymbol{m}1$. Specifically, when the optimal start-stop state in $\boldsymbol{m}$ 1, $u_g^{t,k^*} = 1$, is active, $PU_g^{t,k}$ it corresponds to the optimal output value of the M1 thermal power unit P_g^{t,k^*}. Conversely, when $u_g^{t,k^*} = 0$ it is inactive, $PU_g^{t,k}$ it is set to the negative maximum output of the thermal power unit.

In conclusion, Eqs 1–10, and Eqs 19–21 form the $\boldsymbol{m}2$ pricing auxiliary optimization model within the framework of linear programming. The inclusion of Constraint (21) ensures that, even when the integer variable $u_g^{t,k}$ is relaxed to a continuous variable, its optimal value aligns with the optimal solution of the original model, $\boldsymbol{m}1$. Consequently, the optimal solution of the price-assisted optimization model $\boldsymbol{m}2$ coincides with that of the original model $\boldsymbol{m}1$. Utilizing model $\boldsymbol{m}2$ facilitates the derivation of energy and start-stop prices (detailed derivation is beyond the scope of this discussion but can be found in reference (Wang et al., 2023),

enabling the calculation of power revenue for each market participant.

The energy price for thermal power units is detailed in Eq. 22.

$$\gamma_{en,g}^{t,k} = \sigma_b^{t,k} + \sum_{l\in L}\left(\sigma_l^{t,k,l-} - \sigma_l^{t,k,l+}\right)H_{\lg} \tag{22}$$

The start-stop price for thermal power units is detailed in Eq. 23.

$$\gamma_{st,g}^{t,k} = \varsigma_{en}^{t,k} PU_g^{t,k} \tag{23}$$

The income from electricity for thermal power units is presented in Eq. 24.

$$H_{en,g}^{t,k} = \sum_{t\in T}\left(\gamma_{en,g}^{t,k} P_g^{t,k} + \gamma_{st,g}^{t,k} u_g^{t,k}\right) \tag{24}$$

For load d, the electricity price, comprising both energy and start-stop components, is indicated in Eq. 25.

$$\gamma_d^{t,k} = \sigma_b^{t,k} + \sum_{l\in L}\left(\sigma_l^{t,k,l-} - \sigma_l^{t,k,l+}\right)H_{ld} + \varsigma_{en}^{t,k} \tag{25}$$

The cost incurred by load d for electrical energy is depicted in Eq. 26.

$$E_{en,d}^{t,k} = \gamma_d^{t,k} P_d^{t,k} \tag{26}$$

Similarly, the electricity price for renewables units v, which includes the energy and start-stop components, is specified in Eq. 27.

$$\gamma_v^{t,k} = \sigma_b^{t,k} + \sum_{l\in L}\left(\sigma_l^{t,k,l-} - \sigma_l^{t,k,l+}\right)H_{lv} + \varsigma_{en}^{t,k} \tag{27}$$

The income from electricity for renewables units v is documented in Eq. 28.

$$E_{en,v}^{t,k} = \gamma_v^{t,k} P_v^{t,k} \tag{28}$$

3.2 Reserve revenues calculation of market participants under different reserve cost allocation mechanisms

The energy-reserve joint clearing model, as delineated in Section 2.1, quantifies the influence of renewables and load on reserve requirements. This study posits that this influence is precisely characterized and, on this premise, computes the reserve revenue for market participants across various reserve cost allocation mechanisms. Subsequently, it evaluates the efficacy of these mechanisms. It is noted that the focus of this paper is not to propose an ideal reserve cost allocation. This paper aims to demonstrate the necessity of reasonable cost allocation mechanisms that obey the principle of "who causes, who shares" by comparing market revenues under different cost allocation mechanisms.

3.2.1 Mechanism based on "who causes, who shares"

As outlined in Section 2.1, this study excludes the influence of thermal power unit outages on system reserve requirements. Consequently, under the "who cause, who share" allocation mechanism, thermal power units are exempt from reserve costs, while the revenue generated from providing reserve services is distributed between renewable sources and load entities. Thus, thermal power units accrue reserve revenue, whereas renewable sources and load entities incur the reserve costs.

As highlighted in the introduction, accurately characterizing the impact of renewables and load on requirements for reserve services enables the application of the method from reference (Wang et al., 2020) to fulfill the market allocation principle of "who cause, who share." Building on the premise that the impact of renewables and load on reserve requirements, as described in Section 2.1, is precisely articulated, this study employs the approach detailed in reference (Wang et al., 2020) to calculate the reserve price components for thermal power units, as well as renewables sources and load. This approach facilitates the natural redirection of reserve costs via price signals, thereby achieving the "who cause, who share" objective. The pricing and earnings related to reserves for each market participant are presented below [the detailed derivation process is elaborated in reference (Wang et al., 2020)].

The reserve revenue for thermal power units is detailed in Eq. 29.

$$H_{s,g}^{t,k} = \lambda_{\mathrm{R}}^{t,k,\mathrm{UP}} R_g^{t,k,\mathrm{UP}} + \lambda_{\mathrm{R}}^{t,k,\mathrm{DN}} R_g^{t,k,\mathrm{DN}} \tag{29}$$

By integrating this with the electricity revenue, the total revenue for thermal power units is computed as presented in Eq. 30.

$$H_g^{t,k} = H_{en,g}^{t,k} + H_{s,g}^{t,k} \tag{30}$$

The reserve price components for renewables unit v are outlined in Eq. 31, encompassing both the upper and lower reserve price components.

$$\rho_v^{t,k} = \pi_v \lambda_{\mathrm{R}}^{t,k,\mathrm{UP}} + \pi_v \lambda_{\mathrm{R}}^{t,k,\mathrm{DN}} \tag{31}$$

The reserve costs attributed to renewables unit v are specified in Eq. 32, consisting of the reserve price components for renewables and their output power.

$$S_{\mathrm{w},v}^{t,k} = \rho_v^{t,k} P_v^{t,k} \tag{32}$$

The overall revenue of renewables is determined by aggregating the electricity revenue and the reserve costs for renewables units, as indicated in Eq. 33.

$$E_v^{t,k} = E_{en,v}^{t,k} - S_{\mathrm{w},v}^{t,k} \tag{33}$$

The reserve price component for load d, detailed in Eq. 34, comprises both the upper and lower reserve price components.

$$\rho_d^{t,k} = \pi_d \lambda_{\mathrm{R}}^{t,k,\mathrm{UP}} + \pi_d \lambda_{\mathrm{R}}^{t,k,\mathrm{DN}} \tag{34}$$

The reserve cost incurred by load d, specified in Eq. 35, includes the reserve price component associated with renewables and the load requirements.

$$S_{\mathrm{w},d}^{t,k} = \rho_d^{t,k} P_d^{t,k} \tag{35}$$

By holistically assessing the electrical energy cost and reserve cost for load d, the aggregate cost payable by the load is computed, as presented in Eq. 36.

$$E_v^{t,k} = -E_{en,d}^{t,k} - S_{\mathrm{w},d}^{t,k} \tag{36}$$

3.2.2 Mechanisms based on the proportion of energy generation/consumption

The allocation method, predicated on the ratio of power generation to consumption, distributes the total reserve cost among market participants based on their respective shares of total power generation and consumption within the network. This approach is detailed in Eqs 37, 38, exemplified by the reserve cost allocation for day k, and represents a prevalent method within the Chinese industry.

$$Z_s^k = \sum_{t\in T}\sum_{g\in G} H_{s,g}^{t,k} \tag{37}$$

$$S_{p,d/v/g}^k = \left(\frac{\sum_{t\in T} P_{d/v/g}^{t,k}}{\sum_{t\in T}\left(\sum_{d\in D} P_d^{t,k} + \sum_{v\in V} P_v^{t,k} + \sum_{g\in G} P_g^{t,k}\right)}\right) Z_s^k \tag{38}$$

Within this distribution mechanism, thermal power units, renewable sources, and loads are all required to contribute towards the reserve costs. Consequently, the aggregate revenue of thermal power units is derived from their electricity sales revenue, reserve revenue, and the reserve costs they incur, as illustrated in Eq. 39.

$$H_g^{t,k} = H_{en,g}^{t,k} + H_{s,g}^{t,k} - S_{p,g}^{t,k} \tag{39}$$

The total revenue calculations for renewables sources and loads, akin to those presented in Eqs 33, 36, respectively, will not be reiterated here.

3.2.3 Mechanism based on types of market participants

The apportionment method, which accounts for the type of market entity, initially allocates the total reserve cost among different types of market entities in predetermined proportions. Subsequently, it distributes the reserve cost to individual market participants based on their share of electricity generation/consumption. This approach is a prevalent method of cost distribution within the Chinese industry.

The total reserve cost allocated to various market entities by this method is detailed in Eq. 40.

$$W_{d/v/g}^k = \alpha_{d/v/g} Z_s^k \tag{40}$$

In the Chinese industrial sector, the allocation ratio for thermal power units $\alpha_{d/v/g}$ is set at 10%, while the ratios for renewable energy and load are both set at 45%.

Taking thermal power units as an example, the reserve cost allocated to thermal power units will be further allocated to each thermal power unit according to the ratio of power generation between thermal power units, as shown in Eq. 41. The apportionment of the reserve cost between the load subject and the renewables subject is similar to that of the thermal power unit, which will not be described here.

$$S_{x,g}^{t,k} = \left(\frac{\sum_{t\in T} P_g^{t,k}}{\sum_{t\in T}\sum_{g\in G} P_g^{t,k}}\right) W_g^k \tag{41}$$

Under this apportionment mechanism, the total revenue of thermal power is similar to Eq. 39, and the total revenue of renewables and the total revenue of load are similar to Eqs 33, 36, which will not be repeated here.

3.3 Total revenues calculation of renewables with equipped energy storage

Section 3.1 determines the electricity revenue generated by renewable sources, while Section 3.2 assesses the reserve costs allocated to renewables under various distribution mechanisms. The overall revenue of renewables is derived from combining electricity revenue and reserve costs. Additionally, for renewables entities equipped with supporting ES systems, it is imperative to account for the investment and operational costs of these storage solutions to precisely evaluate the revenue implications for renewables entities following the implementation of ES under diverse cost allocation mechanisms.

The costs associated with ES discussed in this paper encompass investment costs, maintenance costs, and life loss costs, as detailed in references (Li and Xu et al., 2018; Ahmadi et al., 2018; Li et al., 2021). These costs are distributed across each moment and day within the sequential production simulation.

The life loss cost, allocated per period, is detailed in Eq. 42.

$$C_{es}^{t,k} = \sum_{es\in ES} \varepsilon_{es} \cdot \left(P_{es,\mathrm{cha}}^{t,k} + P_{es,\mathrm{dis}}^{t,k}\right) \tag{42}$$

The parameter ε_{es} can be obtained by fitting the energy storage life cycle curve.

The investment cost allocated per period is outlined in Eq. 43.

$$C_{cap}^{t,k} = \frac{\sum_{es\in ES} C_{cp,es} f (1+f)^{w_{es}} / \left[(1+f)^{w_{es}-1}\right]}{R \times L} \tag{43}$$

The maintenance cost for each period of ES is detailed in Eq. 44.

$$C_{ma}^{t,k} = \left(P_{es,\mathrm{cha}}^{t,k} + P_{es,\mathrm{dis}}^{t,k}\right) E_{es,om}^{t,k} \tag{44}$$

Upon accounting for ES costs, the total revenue of renewables entities, inclusive of supporting ES, comprises electricity revenue, reserve costs, and ES costs. This is exemplified in Eq. 45, utilizing the "who cause, who share" principle for reserve cost allocation.

$$E_v^{t,k} = E_{en,v}^{t,k} - S_{w,v}^{t,k} - \left(C_{es}^{t,k} + C_{cap}^{t,k} + C_{ma}^{t,k}\right) \tag{45}$$

Since the energy storage is equipped with renewables, the costs of the energy storage are added to the costs of corresponding renewables.

4 Case studies

4.1 Case description

The operational data from a provincial power grid in China, spanning January 2020 to December 2020, serves as the basis of the load and renewables data utilized in case studies. Meanwhile, to improve the penetration of renewables, the renewables data are proportionally expanded to achieve a 30% penetration rate. In addition, the prediction errors of renewables and load are generated according to the assumption that the prediction errors

TABLE 1 Operation parameters of thermal power units.

Unit index	Energy bid price /$·(MW·h)$^{-1}$	Reserve bid price /$·(MW·h)$^{-1}$	Maximum output /MW	Minimum output /MW	Ramping capability /[MW·(5 min)$^{-1}$]
1	28.50	36.61	70.00	15.00	10.00
2	40.39	38.30	75.00	15.00	10.00
3	36.32	26.32	80.00	10.00	10.00
4	38.27	22.35	60.00	10.00	10.00
5	36.30	25.45	50.00	10.00	10.00
6	23.47	39.74	30.00	15.00	10.00
7	35.64	41.85	60.00	15.00	10.00
8	30.47	34.52	40.00	15.00	10.00

TABLE 2 Earnings of market players under different reserve cost allocation mechanisms.

Cost allocation mechanism	M1			M2			M3		
Market entity	Energy revenue	Reserve revenue	Total revenue	Energy revenue	Reserve revenue	Total revenue	Energy revenue	Reserve revenue	Total revenue
W1	1,611,317	−128,433	1,482,884	1,611,317	−12,673	1,598,644	1,611,317	−16,410	1,594,907
W2	2,015,401	−60,993	1,954,408	2,015,401	−33,645	1,981,756	2,015,401	−40,768	1,974,633
G	14,172,753	1,114,357	15,287,110	14,172,753	603,496	14,776,249	14,172,753	614,356	14,787,109

follow a normal distribution with a mean of zero (Holttinen et al., 2008). By amalgamating the prediction error data with the practical data, the predicted renewables and load are obtained. The predicted data are used as input for the market clearing model, while the prediction error data are used to form the operating reserve requirement of the power system.

The IEEE 30-node system serves as the basis of the power system's topology in case studies. In addition, two wind turbines are added in nodes 5 and 50, and two thermal power units are added in nodes 8 and 19. The practical renewables and load data are scaled to fit the parameters of the IEEE 30-node system. This paper focuses on the evaluation of market participants' revenues under various reserve cost allocation mechanisms and explores the mechanisms' effectiveness. For the sake of simplicity, this paper denotes the three cost allocation methods introduced in Section 3.2 as M1, M2, and M3, respectively. The scheduling interval used in the dispatch model introduced in Section 2 is 1 h. The operating parameters of the thermal power units in the modified IEEE 30-node system are detailed in Table 1.

4.2 Analysis of simulation results

4.2.1 Analysis of market participants' revenues under different reserve cost allocation mechanisms

To effectively analyze the impact of the reserve cost allocation mechanism on market participants' revenue, this section assumes that the two introduced typhoon motor groups, labeled W1 and W2, have identical installed capacities and forecasted outputs. However, the standard deviation of the forecast error for W1 is 30% of its actual output, while for W2, it is 20%. Neither wind turbine incorporates ES. Table 2 presents the revenue of each market entity under various standby cost allocation mechanisms, with "G" representing all thermal power units.

Data from Table 2 indicates that, under the allocation mechanism M1, thermal power units enjoy the highest total revenue. This outcome is attributed to the fact that in mechanism M1, thermal power units do not induce additional reserve requirements (as the model does not consider shutdowns of thermal units), thus exempting them from bearing the costs associated with reserve capacity. Conversely, under mechanisms M2 and M3, thermal units incur higher reserve costs, diminishing their reserve revenue in comparison to M1, which in turn affects their overall profitability. Consequently, compared to mechanisms M2 and M3, thermal units' total revenue under M1 increased by 3.46% and 3.38%, respectively. Therefore, mechanism M1 more effectively ensures the profitability of thermal power units, encouraging them to offer reserve services. In contrast, under mechanisms M2 and M3, despite providing reserve services, the associated costs dampen their enthusiasm for offering ancillary services.

A comparison of the energy revenue between wind power units reveals that W2's energy revenue is 25.07% higher than that of W1. This is because W2 exhibits less variability, leading to lower system reserve requirements per unit of output (i.e., a lesser impact on reserve requirements), thereby reducing the operational costs associated with its output. Hence, compared to W1, which has

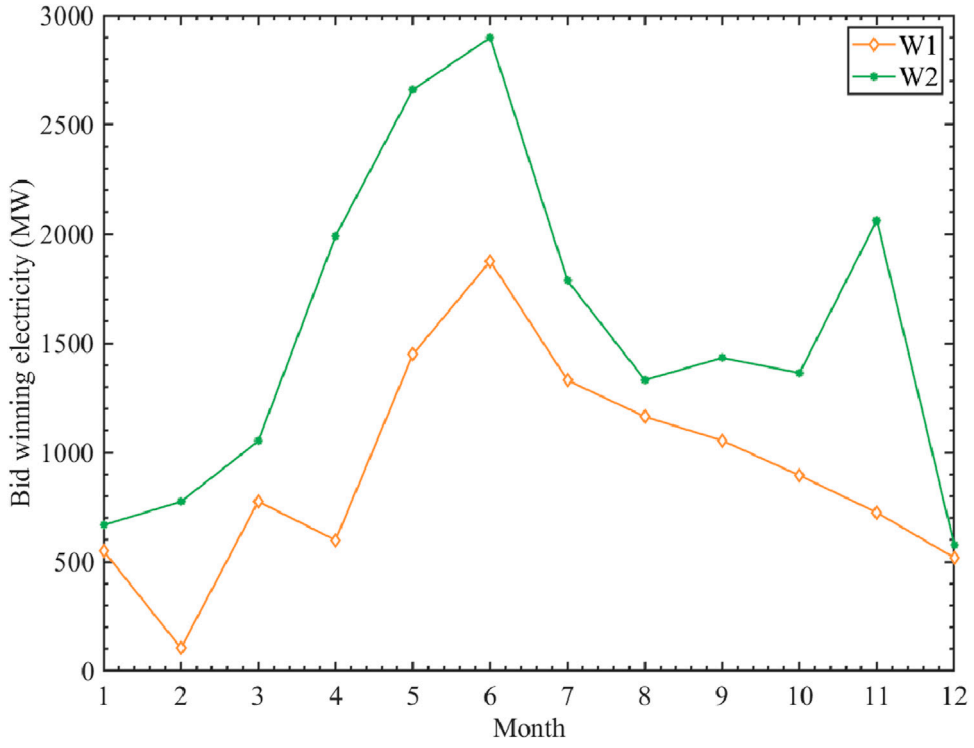

FIGURE 1
Comparison of scalars in fans with different bearing coefficients.

more significant fluctuations, the market prefers to accommodate W2, as evidenced by its substantially higher accepted bid volume (an increase of 66.21%, as shown in Figure 1), ultimately resulting in higher energy revenue for W2.

An analysis of the reserve costs associated with wind turbines reveals that under the M1 allocation mechanism, W2 incurs a lower reserve cost, constituting only 47.44% of W1's reserve cost, attributed to its minimal impact on reserve requirements. Conversely, traditional cost allocation mechanisms M2 and M3 allocate reserve costs based on bid quantities, resulting in W2 incurring higher reserve costs, 165.45% and 148.43% greater than W1, respectively. Besides, under traditional cost allocation mechanisms M2 and M3, W2 with fewer uncertainties undertakes more reserve costs than that allocated to W1. Hence, these mechanisms do not obey the principle of "who causes, who shares" and are regarded as unfair (Gazafroudi et al., 2017; Xiang et al., 2023). By contrast, the M1 mechanism is more favorable for renewable sources with smaller fluctuations and uncertainties, as it imposes lower reserve costs on them, thereby incentivizing the reduction of their fluctuations and uncertainties characteristics.

Regarding the total revenue of wind turbines, under allocation mechanism M1, W2 achieves not only a higher energy revenue than W1 but also incurs a lower reserve cost, resulting in a total revenue increase of 31.79% compared to W1. In contrast, under mechanisms M2 and M3, the elevated reserve costs borne by W2 lead to a relative decrease in its total revenue increase to only 23.96% and 23.81%, respectively, when compared to W1. Analysis of the total revenue across both turbines under all three mechanisms reveals that W1 and W2 secure higher revenues under M2 and M3. This outcome is attributable to the distribution of reserve costs among thermal power units in M2 and M3, thereby reducing the wind turbines' reserve costs and enhancing their total revenue.

In conclusion, the M1 allocation mechanism is more effective in ensuring the revenue stability of power supply regulation while also enabling renewable sources with lower fluctuations and uncertainties to gain a competitive edge in the market (relative to the revenue increase of newer, high-fluctuation energy sources). This approach incentivizes renewable entities to minimize their fluctuations and uncertainties characteristics.

4.2.2 Incentive effect of different reserve cost allocation mechanisms on configuring energy storage by renewables

To further assess the validity of various reserve cost allocation mechanisms, this section will evaluate the impact of ES configurations with differing capacities and maximum charge/discharge rates in wind turbine W1. It will also examine the revenue variations of two wind turbines to understand the motivational effects of these mechanisms on the integration of ES into renewable sources. It is posited that both wind turbines, W1 and W2, have identical installed capacities, predicted outputs, and actual outputs, with the forecast error's standard deviation being 20% of the actual output.

Table 3 illustrates the revenue shifts for new energy entities given an energy storage configuration of 30 MW charging/discharging power and 200 MWh capacity.

Table 3 demonstrates that equipping wind turbine W1 with ES significantly mitigates its fluctuations and uncertainties characteristics and enhances its market competitiveness, leading to an increase in its

TABLE 3 Revenues of each market entity under different reserve cost allocation mechanisms after new ES is configured.

Market entity	Cost allocation mechanism	M1		M2		M3	
	Does W1 incorporate ES?	Without ES	With ES (30 MW/ 200 MWh)	Without ES	With ES (30 MW/ 200 MWh)	Without ES	With ES (30 MW/ 200 MWh)
W1	Energy Revenue	1,574,131	2,007,110	1,574,131	2,007,110	1,574,131	2,007,110
	Reserve Revenue	−134,826	−67,944	−18,637	−30,024	−23,768	−36,365
	ES Cost	0	39,169	0	39,169	0	39,169
	Total Revenue	1,439,304	1,899,997	1,555,493	1,937,916	1,560,363	1,941,747
W2	Energy Revenue	1,574,131	1,461,887	1,574,131	1,461,887	1,574,131	1,461,887
	Reserve Revenue	−134,826	−117,943	−18,637	−16,423	−23,768	−21,177
	Total Revenue	1,439,304	1,343,943	1,555,493	1,445,463	1,560,363	1,440,710
G	Energy Revenue	10,322,660	10,296,755	10,322,660	10,296,755	10,322,660	10,296,755
	Reserve Revenue	1,015,278	843,756	544,914	468,326	555,175	482,421
	Total Revenue	11,337,939	11,140,512	10,867,575	10,765,082	10,877,826	10,779,177

bid-winning capacity. Conversely, this results in a reduction in both the bid-winning capacity and capacity income of thermal power units. Furthermore, analyzing the revenue of thermal power units after integrating ES into W1 under the three allocation mechanisms reveals an increase in reserve revenue for the thermal motor group under M1 by 44.49% and 42.82% compared to M2 and M3, respectively, with total revenue seeing an uptick of 3.36% and 3.24%. This indicates that in scenarios involving renewables configurations with ES, M1 more effectively safeguards the market revenue of thermal power units compared to the conventional mechanisms M2 and M3.

An analysis of W1's market revenue reveals that integrating ES leads to a significant improvement in energy revenue, with a 27.51% increase in bid power compared to configurations without ES. Regarding reserve costs, the M1 allocation mechanism sees a reduction in W1's fluctuations and uncertainties characteristics due to ES installation, thereby decreasing its impact on reserve requirements and reducing its reserve costs by 49.61%. Despite the higher investment cost for ES, W1's overall revenue post-integration increases by 32.01%. Conversely, under the M2 and M3 mechanisms, W1 incurs higher reserve costs (61.09% and 53.00% increases, respectively) due to enhanced bid-winning power, resulting in overall revenue growth rates of only 24.58% and 24.44%, respectively, which are lower than those observed under M1. In summary, the M1 mechanism more effectively promotes the enhancement of overall revenue for renewable sources equipped with ES by encouraging a reduction in fluctuations and uncertainties through strategic ES allocation, in comparison to M2 and M3.

Analysis of W2's market revenue indicates that in scenarios lacking ES support, W1, and W2 exhibit identical market revenues across all three reserve cost allocation mechanisms due to their matching operating parameters. However, upon integrating ES, W1 enhances its market competitiveness and bid capacity, inversely affecting W2's bid capacity. Consequently, W2's energy revenue decreases by 9.46% in comparison to scenarios where W1 is not equipped with ES. Regarding reserve costs, under the M1 mechanism, W2 incurs higher reserve costs owing to its pronounced fluctuations and uncertain characteristics. Nevertheless, W1's adoption of ES leads to a system-wide reduction in reserve costs, thereby diminishing W2's reserve expenses by 12.52% relative to scenarios excluding ES. Ultimately, W2's total revenue declines by 7.38%; under M2 and M3 mechanisms, due to its lesser bid capacity, W2's reserve costs are lower than W1's and are further reduced by 11.88% and 13.10%, respectively, compared to scenarios without W1's ES, culminating in a total revenue reduction of 7.07% and 7.66%. This comparison underlines that traditional mechanisms M2 and M3, where W1 incurs higher reserve costs post-ES integration, may deter renewable sources from adopting ES solutions.

This study aims to examine the impact of the M1 allocation mechanism on incentivizing renewable sources to actively integrate ES. Figure 2 presents a comparative analysis of the overall revenue across various renewables units under M1, focusing on configurations of W1 with diverse ES capacities and maximum powers.

Figure 2 illustrates that, under the M1 allocation mechanism, as ES capacity and maximum power enhance, W1's total revenue progressively increases. In contrast, W2's total revenue exhibits a corresponding decline. Notably, when the ES parameters reach 50 MW/300 MWh, W1's total revenue surges by 46.73% relative to scenarios lacking ES, whereas W2's total revenue diminishes by 15.97%. This pattern underscores that, within the M1 framework, renewable sources equipped with storage markedly boost their revenue, whereas those without storage experience a revenue downturn. Hence, the M1 mechanism effectively motivates the strategic integration of ES among renewable sources.

In conclusion, the M1 allocation mechanism outperforms traditional mechanisms M2 and M3 by more effectively securing power supply revenue adjustments and incentivizing renewable sources to integrate ES. Consequently, there is a compelling need

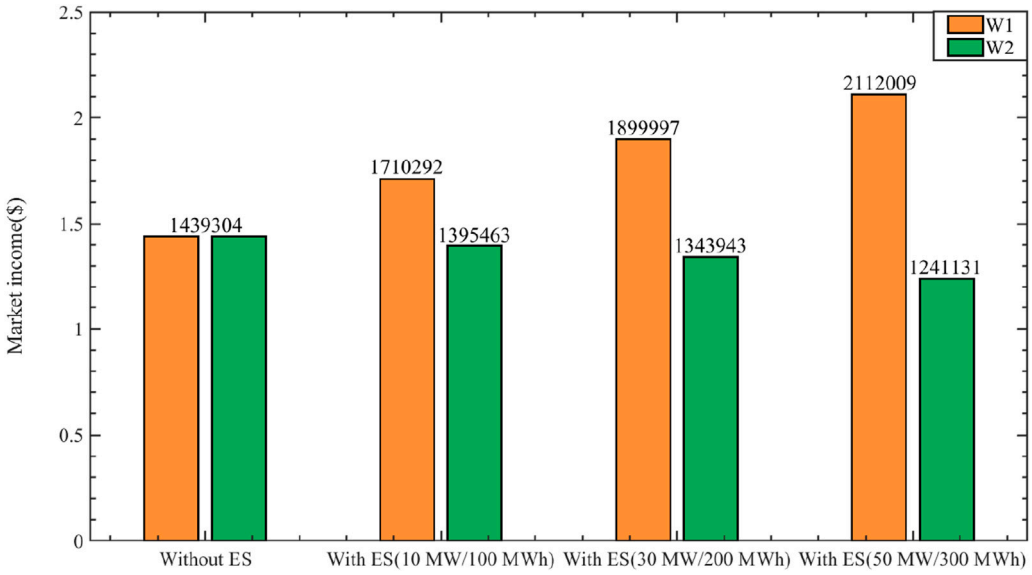

FIGURE 2
Overall revenues of renewables under the M1 allocation mechanism when supporting ES parameters change.

to develop a market-driven allocation mechanism aligned with the principle of "who causes, who shares." This study presupposes that renewable sources and loads can precisely forecast the system's reserve requirements, thereby achieving the cost allocation principle. However, this assumption may not hold in real-market operations, necessitating further investigation by market operators. Such research is crucial for enhancing the power system's flexibility through a well-designed cost-allocation mechanism for auxiliary services.

5 Conclusion

This study addresses the challenge of enhancing power network flexibility, which is compromised by the high influx of renewable sources. We explore a viable reserve cost allocation mechanism to tackle this challenge. We develop a comprehensive simulation model that combines long-period market operations with energy-reserve joint clearing. This model encapsulates the impact of renewable source prediction errors on system reserve requirements. Furthermore, we formulate a self-dispatch model for the equipped ES to accurately reflect changes in prediction error post-storage implementation. By incorporating market clearing mechanisms, we establish a model for calculating the total revenue of market entities under various reserve cost allocation schemes. This sets the stage for an in-depth analysis of how different mechanisms can alleviate the system's flexibility shortfall. Using real data from a provincial power grid in China, we conduct a comparative analysis of the revenues to market participants under diverse reserve cost allocation frameworks. This analysis helps to illustrate the potential of these mechanisms to enhance system flexibility. The key findings are as follows:

(1) In contrast to the traditional allocation mechanisms that are widely used in the Chinese industry, under the mechanism that obeys the principle of "who causes, who shares," the regulating resources that do not cause the need for the reserve need not undertake reserve costs. As a result, the market revenues of regulating resources can be ensured.
(2) Besides, under the mechanism that obeys the principle of "who causes, who shares," the reserve costs allocated to renewables can be greatly reduced by equipping ESs. As a result, their market revenues can be significantly improved (including the costs of ESs). By contrast, the market revenues of renewables without equipped ESs are decreased.

In summary, this research demonstrates that the "who causes, who shares" allocation mechanism not only effectively ensures and stabilizes the revenue of power suppliers but also motivates renewable entities to diminish their fluctuations and uncertainties traits through the adoption of ES. This approach holds significant potential for enhancing the power system's flexibility and addressing its current limitations.

Data availability statement

The original contributions presented in the study are included in the article/Supplementary Material, further inquiries can be directed to the corresponding author.

Author contributions

XW: Formal Analysis, Methodology, Writing–original draft, Writing–review and editing. QZ: Writing–original draft. BL: Writing–original draft. YY: Writing–review and editing. RM: Writing–original draft. DF: Writing–review and editing.

Funding

The authors declare that financial support was received for the research, authorship, and/or publication of this article. This work is supported by the Science and Technology Project of the Southwest Subsection of State Grid. Project Name: Research on the Multi-dimensional Value Evaluation and Benefit Sharing Mechanism of Clean Energy in Southwest Power Grid toward the Target of "Carbon Peaking and Carbon Neutrality" (SGSW0000JYJS2310064).

Conflict of interest

Authors XW, QZ, BL, YY, RM, and DF were employed by Southwest Subsection of State Grid.

The authors declare that this study received funding from Southwest Subsection of State Grid. The funder had the following involvement in the study: Data Collection and Data Analysis.

Publisher's note

All claims expressed in this article are solely those of the authors and do not necessarily represent those of their affiliated organizations, or those of the publisher, the editors and the reviewers. Any product that may be evaluated in this article, or claim that may be made by its manufacturer, is not guaranteed or endorsed by the publisher.

References

AEMO RegulationFCAS contribution factor procedure[EB/OL]. Available at: http://www.aemo.com.au/Stakeholder-Consultation/Consultations/Causer-Pays-Procedure-Consultation.

Ahmadi, A., Nezhad, A. E., and Hredzak, B. (2018). Security-constrained unit commitment in presence of lithium-ion battery storage units using information-gap decision theory. *IEEE Trans. Ind. Inf.* 15, 148–157. doi:10.1109/tii.2018.2812765

Buchholz, W., Dippl, L., and Eichenseer, M. (2019). Subsidizing renewables as part of taking leadership in international climate policy: the German Case. *Energy Policy* 129, 765–773. doi:10.1016/j.enpol.2019.02.044

Chen, Y., Leonard, R., Keyser, M., and Gardner, J. (2015). Development of performance-based two-part regulating reserve compensation on MISO energy and ancillary service market. *IEEE Trans. Power Syst.* 30 (1), 142–155. doi:10.1109/tpwrs.2014.2320519

Ela, E., and Hytowitz, R. B. (2019). *Ancillary services in the United States: technical requirements, market Designs and price trends*. Palo Alto,CA, USA: EPRI.

Fang, X., Hodge, B. M., Du, E. S., Kang, C., and Li, F. (2019). Introducing uncertainty components in locational marginal prices for pricing wind power and load uncertainties. *IEEE Trans. Power Syst.* 34 (3), 2013–2024. doi:10.1109/tpwrs.2018.2881131

Gazafroudi, A. S., Afshar, K., and Bigdeli, N. (2015). Assessing the operating reserves and costs with considering customer choice and wind power uncertainty in pool-based power market. *Int. J. Elect. PowerEnergy Syst.* 67, 202–215. doi:10.1016/j.ijepes.2014.11.007

Gazafroudi, A. S., Shafie-khah, M., Abedi, M., Hosseinian, S. H., Dehkordi, G. H. R., Goel, L., et al. (2017). A novel stochastic reserve cost allocation approach of electricity market agents in the restructured power systems. *Electr. Power Syst. Res.* 152, 223–236. doi:10.1016/j.epsr.2017.07.012

Haring, T., and Andersson, G. (2014). "Cost allocation in ancillary service markets," in 2014 47th Hawaii international conference on system sciences, 06-09 January 2014, Waikoloa, HI, USA.

He, Y., Zhou, L., and Pang, Y., (2019). Design of frequency modulation auxiliary service cost allocation mechanism based on triggered liability under new power reform [J].*Automation Electr. power Syst.*, 43(18): 88–94+144. doi:10.1109/ICGEA.2017.7925458

Holttinen, H., Milligan, M., Kirby, B., Acker, T., Neimane, V., and Molinski, T. (2008). Using standard deviation as a measure of increased operational reserve requirement for wind power. *Wind Eng.* 32 (4), 355–377. doi:10.1260/0309-524x.32.4.355

Li, Z., Wu, L., and Xu, Y. (2021). Risk-averse coordinated operation of a multi-energy microgrid considering voltage/var control and thermal flow: an adaptive stochastic approach. *IEEE Trans. smart grid* 2021 (12-5), 3914–3927. doi:10.1109/TSG.2021.3080312

Li, Z., and Xu, Y. (2018). Optimal coordinated energy dispatch of a multi-energy microgrid in grid-connected and islanded modes. *Appl. Energy* 210, 974–986. doi:10.1016/j.apenergy.2017.08.197

Liang, J. (2007). Improvement of CPS performance index and frequency control strategy of guangdong power grid. *Guangdong Power Transm. Transformation Technol.* 2007 (1), 12–15. doi:10.1109/POWERCON.2018.8601873

Morales-España, G., Baldick, R., García-González, J., and Ramos, A. (2016). Power-capacity and ramp-capability reserves for wind integration in power-basedUC. *IEEETrans. Sustain. Energy* 7 (2), 614–624. doi:10.1109/tste.2015.2498399

Prica, M., and Ilic, M. (2006). "Peak-load pricing based planning for distribution networks under change," in Power Engineering Society General Meeting, 2006. IEEE. doi:10.1109/PES.2006.1709296

Wang, Y., Yang, Z., Yu, J., et al. (2020). Revisit the electricity price formulation: a formal definition, proofs, and examples. *Energy* 200, 117542.

Wang, Y., Yang, Z., Yu, J., and Liu, S. (2023). Pricing in non-convex electricity markets with flexible trade-off of pricing properties. *Energy* 274, 127382. doi:10.1016/j.energy.2023.127382

Xiang, M., Yang, Z., Yu, J., and Wang, G. (2023). Determination and cost allocation for regulation reserve with renewables: a data-driven assisted approach. *IEEE Trans. Sustain. Energy.* 14(2), 813–825. doi:10.1109/tste.2022.3226255

Yu, J., Liu, Y., Yang, J., et al. (2019). Analysis of development of California ancillary service market and its enlightenment to China's power market. *Power Sys. Technol.* 43(008), 2711–2717. doi:10.13335/j.1000.3673.pst.2019.0254

Nomenclature

g, G	Index and set for generators
v, V	Index and set for renewables
d, D	Index and set for load
es, ES	Index and set for energy storage
j, J	Index and set for buses
l	Index for branches
k, K	Index and set for the day
t, T	Index and set for dispatch intervals
$b_{\mathrm{E},g}^{t,k}$	Energy bid of generator g in the tth dispatch interval ($/MWh)
$b_{\mathrm{R},g}^{t,k,\mathrm{UP/DN}}$	Regulation-up/down mileage bid of genera-tor i in the tth dispatch interval ($/MWh)
$P_g^{t,k}$	Planned output of thermal power units
$R_g^{t,k,\mathrm{UP/DN}}$	Upper/lower reserve capacity by thermal power units
$C_r^{t,k}$	The cost associated with renewables curtailment and load shedding
$r_{v/d}$	The per-unit cost of renewables curtailment/load shedding
$P_{v/d}^{t,k,\mathrm{f}}$	The forecasted output of renewable and predicted load demand
$P_{v/d}^{t,k}$	The actual output of renewable and actual load demand
$C_{g,\mathrm{U/D}}^{t,k}$	Startup and shutdown costs of thermal power units
K_g	The unit startup costs of thermal power units
M_g	The unit shutdown costs of thermal power units
$u_g^{t,k}$	The binary variable indicates the operational status of thermal power units
$H_{l,j}$	The transfer distribution factors between injection power and active power flow
A_{jg}	The correlation matrix between thermal power unit indices and node indices
A_{jv}	The correlation matrix between renewable unit indices and node indices
$P_l^{\mathrm{max\,/\,min}}$	Maximum/minimum transmission power
$\sigma_l^{t,k,l+/-}$	Dual multipliers of line flow constraints
$\sigma_b^{t,k}$	Dual multipliers of power balance constraints
$R_{sys}^{t,k,\mathrm{UP/DN}}$	System upward/downward reserve requirements
$\pi_{di/vi}$	The impact of load/renewable on system reserve requirements
$\lambda_{\mathrm{R}}^{t,k,\mathrm{UP/DN}}$	Dual multipliers of system upward/downward reserve requirement constraints
$\lvert e^{t,k}\rvert$	Forecast errors in renewables
$P_v^{t,k,\mathrm{a}}$	The historical actual output of renewable
$\chi_{es,\mathrm{cha/dis}}^{t,k}$	Integer variables for the charging/discharging state of energy storage
$P_{es,\mathrm{cha/dis}}^{t,k}$	Charging/discharging power of energy storage
$P_{es,\mathrm{cha/dis}}^{t,k,\,\mathrm{max}}$	Maximum charging/discharging power of energy storage
$\kappa_{es}^{\mathrm{min\,/\,max}}$	The maximum/minimum energy coefficients allowed for energy storage
E_{cap}	Maximum energy capacity of energy storage equipment
$E_{es}^{t,k}$	Energy capacity of energy storage
α_{es}	The natural decay rate of energy storage
$\delta_{es,\mathrm{cha/dis}}$	Charging/discharging efficiency of energy storage
Δt	Time granularity of each dispatch period
$S_{v/d}^{t,k}$	Reserve costs are borne by renewable/load
$S_{\mathrm{p},d/v/g}^{k}$	Reserve costs that each market member needs to bear
Z_s^k	Total reserve revenue of all thermal power units on the kth day
$\alpha_{d/v/g}$	Allocation coefficients of various market entities
$W_{d/v/g}^{k}$	Total reserve costs that each market entity needs to bear
ε_{es}	Power degradation cost per unit for energy storage
R	Number of periods per day in long-term simulations
L	Total number of simulated days
$C_{cp,\ es}$	Initial investment costs
W_{es}	Annual interest rate lifespan of energy storage units
f	Annual interest rate
$E_{es,om}^{t,k}$	Maintenance cost per unit of power for energy storage

Frontiers in
Energy Research

Advances and innovation in sustainable, reliable and affordable energy

Explores sustainable and environmental developments in energy. It focuses on technological advances supporting Sustainable Development Goal 7: access to affordable, reliable, sustainable and modern energy for all.

Discover the latest Research Topics

See more →

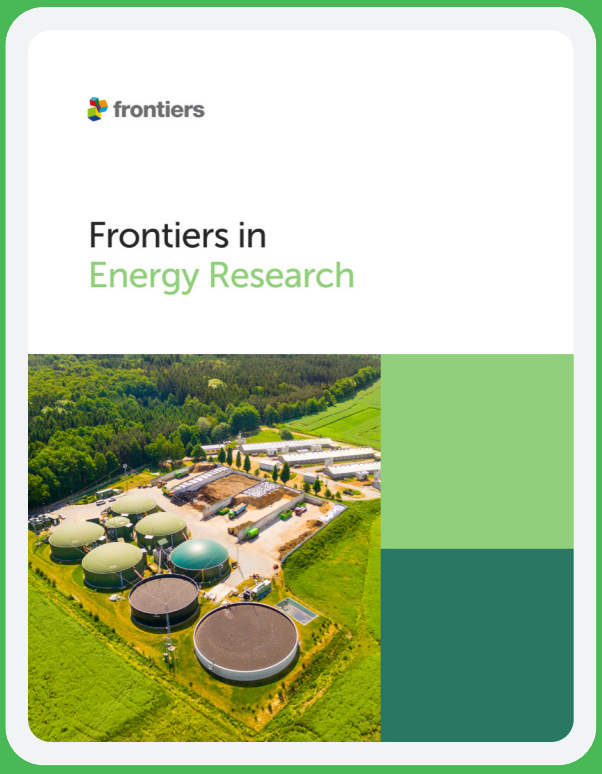

Frontiers

Avenue du Tribunal-Fédéral 34
1005 Lausanne, Switzerland
frontiersin.org

Contact us

+41 (0)21 510 17 00
frontiersin.org/about/contact